CORA Cork Open Research Archive
Cartlann Taighde Oscailte Chorcaí

Title	Bandwidth enhanced sub-GHz wristwatch antennas for wireless body sensor network applications
Authors	Kumar, Sanjeev
Publication date	2021-08-22
Original Citation	Kumar, S. 2021. Bandwidth enhanced sub-GHz wristwatch antennas for wireless body sensor network applications. PhD Thesis, University College Cork.
Type of publication	Doctoral thesis
Rights	© 2021, Sanjeev Kumar. - https://creativecommons.org/licenses/by-nc-nd/4.0/
Download date	2026-11-07 03:24:37
Item downloaded from	https://hdl.handle.net/10468/12522

UCC
University College Cork, Ireland
Coláiste na hOllscoile Corcaigh

Ollscoil na hÉireann, Corcaigh

National University of Ireland, Cork



Bandwidth Enhanced Sub-GHz Wristwatch Antennas for Wireless Body Sensor Network Applications

Thesis presented by

Sanjeev Kumar, M.S. by Research

for the degree of

Doctor of Philosophy

University College Cork

School of Electrical and Electronic Engineering

Head of School: Dr. Jorge Oliveira

Supervisors: Dr. John Buckley,

Dr. Brendan O'Flynn

August 2021

Table of Contents

List of Figures ..... **v**

List of Tables ..... **x**

List of Symbols (with SI units) ..... **xiii**

Acknowledgements ..... **xv**

Abstract ..... **xviii**

List of Publications ..... **xx**

Chapter 1: Introduction **1**

1.1 Motivation of this Work 2

1.2 Aim and Objectives 5

1.3 Organisation of the Thesis 6

Chapter 2: Background Theory **8**

2.1 Background 8

2.2 Antenna Parameters 8

2.3 The Hertzian Dipole 13

2.4 Electrically Small Antennas 13

2.5 Radiation Efficiency Measurement 15

2.6 Link Budget 16

2.7 Antenna-Human Body Interaction 17

2.8 Planar Inverted-F Antennas 19

2.9 Dielectric Characterization Technique 20

2.10 Conclusions 22

Chapter 3: Literature review **23**

3.1 Background 23

3.2 State-of-the-Art Smartwatch Devices 23

3.3 Wearable Antennas 25
3.4 Frequency of Operation for Wrist-Worn Antennas 26
3.5 Wrist-Worn Antennas for Frequencies above 1 GHz 27
3.6 Wrist-Worn Antennas for Sub-GHz Bands 34
3.7 Performance Comparison of State-of-the-Art Sub-GHz Wrist-Worn Antennas43
3.8 Gaps in the State-of-the-Art and Research Hypothesis 50
3.9 Conclusions 50
Chapter 4: A Bandwidth Enhanced 915 MHz Wristwatch Antenna 52
4.1 Background 52
4.2 Target Wristwatch Device for Antenna Integration 53
4.3 Antenna Design Concept 54
4.4 Antenna Design and Simulations 55
4.5 Antenna Measurements 66
4.6 Performance Evaluation of the Developed Antenna 69
4.7 Conclusions 71
Chapter 5: Development of Bandwidth Enhanced 915/868 MHz Wristwatch-Integrated Antennas 72
5.1 Background 72
5.2 Target Wristwatch Device for Antenna Integration 73
5.3 915/868 MHz PIFA Antenna Design Concept 75
5.4 Development of a 915 MHz Wristwatch-Integrated Antenna 76
5.5 Development of an 868 MHz Wristwatch-Integrated Antenna 98
5.6 Conclusions 106
Chapter 6: A Bandwidth Enhanced 915 MHz Wristwatch Antenna using an Optimized Feed Structure 108
6.1 Background 108
6.2 Antenna Design 109

6.3 Antenna Simulations 110
6.4 Antenna Measurements 123
6.5 Performance Evaluation of the Proposed Antenna 128
6.6 Conclusions 130
Chapter 7: Conclusions and Future Work 131
7.1 Contributions to the state-of-the-art 132
7.2 Future Work 134
Bibliography 136

List of Figures

Figure 1.1: Overview of a typical WSN system for health monitoring.....1

Figure 2.1: One-port network describing voltage reflection coefficient, Γ [59]. 9

Figure 2.2: Two-port S-parameter network [60]. 10

Figure 2.3: Electrically small antenna (ESA) and radian sphere [69, 70]. 14

Figure 2.4: Antenna efficiency measurement: (a) in a Wheeler cap, and (b) in free-space. 15

Figure 2.5: A dosimetric assessment system (DASY) SAR measurement setup [81]. 18

Figure 2.6: PIFA evolution: (a) Quarter-wavelength monopole, (b) Inverted-L antenna (c) Inverted-F antenna (d) Planar inverted-F antenna.....20

Figure 2.7: The DAK-TL-3.5 block diagram [87].....21

Figure 2.8: Dielectric measurement setup using a DAK-TL-3.5 system. 21

Figure 3.1: The market trend for global wearable devices from 2018 to 2022 [13]. 24

Figure 3.2: Application of smartwatches in everyday life [89]: (a) SpO_2 measurement, (b) electrocardiogram (ECG) monitoring, (c) Workout and activity tracking [89].....25

Figure 3.3: 2.4/5.5 GHz 3-D Printed diversity bracelet antenna [99]. 27

Figure 3.4: Dual-band, 2.4 and 5.2 GHz smartwatch antenna structure [100].....28

Figure 3.5: Antennas structures: (a) Multiband (1.575, 2.4, 5.2 and 5.8 GHz) smartwatch antenna [98], (b) 2.4 GHz metal frame wristwatch loop antenna [103].....29

Figure 3.6: Geometry of the 2.4 GHz cavity-backed annular slot antenna [29]. 30

Figure 3.7: Two element MIMO PIFA wristwatch antenna [106]. 31

Figure 3.8: Configuration of the internal shorted monopole (IFA) antenna [105]. 32

Figure 3.9: A low profile 2.4 GHz smartwatch ILA antenna using a miniature high impedance surfaces (HIS) structure [112]. 33

Figure 3.10: Number of Sub-GHz wrist-worn antennas reported in the literature. 35

Figure 3.11: Geometry of the wristwatch antennas [45]: (a) Dipole antenna, (b) Monopole antenna 1 and (c) Monopole antenna 2. 35

Figure 3.12: (a) Configuration of the monopole antenna on a flexible substrate, (b) Arrangement when the antenna is mounted on an ABS bracelet [44]. ...36

Figure 3.13: (a) Metal frame loop antenna [43], (b) Configuration of the wristwatch antenna reported in [47]. 37
Figure 3.14: (a) Geometry of the proposed 915 MHz RFID tag antenna, d = 26, S_l = 24, S_W = 6, S_g = 3, Unit: mm, (b) Antenna attached to a human wrist [34]. 38
Figure 3.15: (a) Diversity PIFA antenna [50], (b) Metal frame PIFA antenna [49]. 39
Figure 3.16: Configuration of the three-antenna system [42]. 40
Figure 3.17: (a) Antenna structure, (b) Configuration of the casing watch [40]. 41
Figure 3.18: Geometry of the meandered 915 MHz PIFA [28]. 42
Figure 3.19: (a, b) Configuration of the wristwatch IFA, (c) Wristwatch model [46]. 42
Figure 4.1: Wristwatch enclosure device placed on a phantom arm [131]. 53
Figure 4.2: (a) Conventional single-element PIFA topology [84], (b) Proposed dual-radiator PIFA antenna design concept. 54
Figure 4.3: Antenna-1 topology and simulated S_{11} response for varying L_2. 56
Figure 4.4: Antenna-2 antenna topology and simulated S_{11} response. 57
Figure 4.5: Antenna-3 (proposed) topology and simulated S_{11} response 58
Figure 4.6: Simulated S_{11} response for varying element Rad_1 end length, L_1 60
Figure 4.7: Simulated S_{11} response for varying the width, W_1 of element Rad_1. 60
Figure 4.8: Simulated S_{11} response for varying distance L_2. 61
Figure 4.9: Final configuration of the developed 915 MHz wristwatch antenna. 62
Figure 4.10: Simulated 3D Realized Gain pattern of the antenna at 915 MHz. 63
Figure 4.11: Simulated surface magnitude current distribution at 915 MHz. 64
Figure 4.12: Simulated surface vector current distribution at 915 MHz. 64
Figure 4.13: SAR distribution on the phantom arm at 915 MHz. 65
Figure 4.14: Photograph of the fabricated antenna prototype. 66
Figure 4.15: Simulated versus measured S_{11} response of the AUT. 67
Figure 4.16: AUT measurement setup in the AMS-8050 anechoic chamber [63]. 67
Figure 4.17: Simulated and measured radiation characteristics of the proposed antenna at 915 MHz (a) *XY*- plane (b) *YZ*- plane and (c) *XZ*- plane. 68
Figure 5.1: Wristwatch sensor device showing various internal components. 73
Figure 5.2: Exploded view of the wristwatch wireless sensor device. 74
Figure 5.3: (a) Conventional single-element PIFA topology [84], (b) Proposed dual-radiator PIFA antenna design concept. 75

Figure 5.4: Wristwatch model placed on a Speag SHO-GFPC-V1 phantom arm [145]. 76
Figure 5.5: Configuration of Antenna-1 in system within a wristwatch device, where the ground planes are highlighted in green for clarity. 77
Figure 5.6: Antenna-1 topology and corresponding EM simulated S_{11} response. 78
Figure 5.7: Antenna-2 topology and corresponding EM simulated S_{11} response. 79
Figure 5.8: EM Simulated complex S_{11} response of Antenna-1 and Antenna-2. 80
Figure 5.9: Antenna-3 topology and corresponding EM simulated S_{11} response. 81
Figure 5.10: EM Simulated complex S_{11} response of Antenna-1 and Antenna-3. 82
Figure 5.11: Configuration of the proposed antenna in system within a wristwatch device, where the ground planes are highlighted in green for clarity. 83
Figure 5.12: EM Simulated S_{11} response showing effects of varying parameter L_1. 84
Figure 5.13: EM Simulated S_{11} response showing effects of varying parameter L_2. 85
Figure 5.14: EM Simulated S_{11} response showing effects of varying parameter W_3. 86
Figure 5.15: EM Simulated S_{11} response showing effects of varying parameter W_4. 86
Figure 5.16: EM Simulated complex S_{11} response for varying parameter W_4. 87
Figure 5.17: (a) Proposed antenna topology, (b) 3-branch equivalent circuit model and (c) Single-branch equivalent circuit model. 88
Figure 5.18: Circuit Simulated and measured S_{11} responses for the proposed antenna. ...88
Figure 5.19: EM Simulated surface current distribution of the antenna at 915 MHz. 90
Figure 5.20: EM Simulated surface current distribution on the ground planes at 915 MHz. 90
Figure 5.21: EM Simulated SAR distribution on the phantom arm at 915 MHz.....91
Figure 5.22: E-field distribution in the *YZ*-plane at 915 MHz 92
Figure 5.23: EM Simulated 3D Realized Gain radiation pattern at 915 MHz. 92
Figure 5.24: Photograph of the fabricated 915 MHz antenna. 93
Figure 5.25: EM Simulated versus measured S_{11} response of the 915 MHz antenna. 94
Figure 5.26: Device under test (DUT) measurement setup in an AMS-8050 anechoic chamber. 95
Figure 5.27: Simulated and measured radiation characteristics of the antenna at 915 MHz in (a) *XY*-plane, (b) *YZ*-plane and (c) *XZ*-plane. 96
Figure 5.28: Cross section-view of the metallization of the antenna track. 100
Figure 5.29: Photograph of the proposed laser direct structuring (LDS) printed antenna. 100

Figure 5.30: Measured S_{11} response of the proposed 868 MHz antenna. 101
Figure 5.31: (a) Measured antenna realized gain (3D) at 868 MHz, (b) Coordinate system of the wristwatch device placed on a phantom arm. 101
Figure 5.32: Clinical trial test devices. 104
Figure 5.33: Wristwatch sensor device worn by a patient in a clinical setting. 105
Figure 5.34: Smartphone application for SpO2 and heart rate measurements (a) smartphone app in a user's hand, (b) screenshot of the measured plots. 105
Figure 6.1: Geometry of the proposed wristwatch-integrated antenna placed on a phantom arm. 109
Figure 6.2: (a) Antenna topology presented in Chapter 5 [52], (b) Proposed antenna topology with optimized feed developed in this work. 111
Figure 6.3: (a) Geometry of the proposed antenna, (b) Equivalent circuit model. 111
Figure 6.4: Simulated S_{11} response showing the impedance bandwidth enhancement. 112
Figure 6.5: Single-branch equivalent circuit model for the 915 MHz antenna in Chapter 5. 113
Figure 6.6: (a) proposed antenna geometry, (b) Equivalent transmission line (TL) model. 114
Figure 6.7: Inverted microstrip topology. 115
Figure 6.8: Simulated TL model S_{11} response for varying L_{SH}. 116
Figure 6.9: Simulated TL model S_{11} response for varying L_4. 117
Figure 6.10: Simulated TL model S_{11} response for varying L_5. 118
Figure 6.11: EM Simulated S_{11} response of the proposed antenna. 119
Figure 6.12: Surface current distribution at (a) 912 MHz and (b) 936 MHz. 121
Figure 6.13: E-field distribution in the *YZ*-plane at 915 MHz. 121
Figure 6.14: Simulated 3D Realized Gain radiation pattern at 915 MHz. 122
Figure 6.15: Simulated SAR distribution on the phantom arm at 915 MHz. 123
Figure 6.16: Photograph of the fabricated antenna. 124
Figure 6.17: Internal components of the wristwatch device. 124
Figure 6.18: Simulated (TL and EM models) and measured S_{11} response of the antenna. 125
Figure 6.19: Device under test (DUT) measurement setup in an AMS-8050 anechoic chamber. 126

Figure 6.20: Simulated and measured radiation patterns of the antenna at 915 MHz: (a) *XY*-plane, (b) *YZ*-plane and (c) *XZ*-plane.....127

List of Tables

Table 2.1: Sub-GHz band impedance bandwidth specifications. 11

Table 2.2: Parameters for link budget calculation at f_0 = 915 MHz. 17

Table 3.1: On-phantom performance of state-of-the-art Sub-GHz wrist-worn antennas. 44

Table 3.2: -10 dB impedance requirements for several Sub-GHz bands. 45

Table 3.3: Challenges with reported state-of-the-art Sub-GHz wrist-worn antennas. 49

Table 4.1: Performance comparison of the 3 iterations. 59

Table 4.2: Final design parameters of the proposed antenna. 63

Table 4.3: The EM simulated performance summary of the proposed antenna. 66

Table 4.4: Comparing on-phantom performance of the developed antenna with the literature. 70

Table 5.1: Performance comparison of the 3 iterations. 83

Table 5.2 Final design parameters of the proposed 915 MHz antenna. 87

Table 5.3: The EM simulated performance summary of the proposed 915 MHz antenna. 93

Table 5.4: Comparing on-phantom performance of the developed 915 MHz antenna with the literature. 97

Table 5.5: Comparing on-phantom performance of the developed 868 MHz LDS printed antenna with the literature. 103

Table 6.1: Final Optimized TL Parameters of the Proposed Antenna. 118

Table 6.2: Final optimized EM model parameters of the proposed antenna. 119

Table 6.3: Comparing EM and TL models S_{11} computation time. 120

Table 6.4: The EM simulated performance summary of the proposed 915 MHz antenna. 123

Table 6.5: Comparing on-phantom performance of the developed antenna with the literature. 129

Table 7.1: Performance summary of the Sub-GHz wristwatch antennas developed in this thesis. 132

Glossary of Terms

ABS	Acrylonitrile Butadiene Styrene
ASA	Acrylonitrile Styrene Acrylate
AUT	Antenna Under Test
BLE	Bluetooth Low Energy
CAD	Computer Aided Design
DAK	Dielectric Assessment Kit
DUT	Device Under Test
EM	Electromagnetic
ESA	Electrically Small Antenna
FCC	Federal Communications Commission
FEM	Finite Element Method
FSPL	Free Space Path Loss
FR-4	Flame Retardant - 4
GPS	Global Positioning System
HFSS	High Frequency Structure Simulator
HIS	High Impedance Surface
IEEE	Institute of Electrical & Electronics Engineers
ICNIRP	International Commission on Non-Ionizing Radiation Protection
ILA	Inverted-L Antenna
IoT	Internet of Things
ISM	Industrial, Scientific and Medical
LDS	Laser Direct Structuring
LoRaWAN	Long Range Wide Area Network
LTE	Long Term Evolution
MAPS	Multi-Axis Positioning System
MICS	Medical Implant Communication System

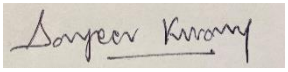
MIMO	Multiple-Input and Multiple-Output
PIFA	Planar Inverted-F Antenna
PCB	Printed Circuit Board
RF	Radio Frequency
RFID	Radio Frequency Identification
Rx	Radio Receiver
SAR	Specific Absorption Rate
Sigfox	A French global network operator
SpO_2	Saturation of Peripheral Oxygen
Tx	Radio Transmitter
UWB	Ultra Wide Band
VNA	Vector Network Analyzer
WBSN	Wireless Body Sensor Network
Wi-Fi	Wireless Fidelity
WLAN	Wireless Local Area Network
WSN	Wireless Sensor Network

List of Symbols (with SI units)

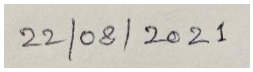
C	Capacitance (F)
D	Antenna directivity (dBi)
ε_r	Relative electrical permittivity
E	Electric field (V/m)
η	Antenna radiation efficiency (%)
f_0	Resonant frequency (Hz)
G	Antenna gain (dBi)
G_R	Antenna realized gain (dBi)
L	Inductance (H)
L_M	Mutual inductance (H)
λ_0	Free-space wavelength (m)
Q	Quality factor
R_R	Antenna radiation resistance (Ω)
R_L	Antenna loss resistance (Ω)
ρ	Mass density (kg/m^3)
σ	Electrical conductivity (S/m)
$tan\delta$	Dielectric material loss tangent
t_{CU}	Copper thickness (m)
Γ	Voltage reflection coefficient
U	Radiation intensity (Watt/steradian)
Z_A	Antenna input impedance (Ω)

Declaration

This is to certify that the work I am submitting is my own and has not been submitted for another degree, either at University College Cork or elsewhere. All external references and sources are clearly acknowledged and identified within the contents. I have read and understood the regulations of University College Cork concerning plagiarism.



Signed: ……..



Date: ……..

Acknowledgements

A number of funded programs have supported the work that is presented in this thesis. I would like to acknowledge the support of Enterprise Ireland and IDA for funding innovation partnership project under Grant IP20170559. I want to acknowledge Science Foundation Ireland (SFI) Connect Centre for co-funding this work under project “Future Networks and Communications under (Grant 13/RC/2077)”. Furthermore, the support of Enterprise Ireland for funding the “Holistics DTIF project” under Grant EIDT20180291-A is also greatly acknowledged. I would also like to acknowledge Insight Centre for Data Analytics for co-funding this work under Grant SFI/12/RC/2289. I also acknowledge Vistamilk for supporting this work under Grant SFI 16/RC/3835 as well as European Regional Development Fund (ERDF) under Ireland’s European Structural and Investment Funds Programmes 2014-2020 for supporting this work.

I would like to express my sincere gratitude to my supervisors Dr. John Buckley and Dr. Brendan O’Flynn for giving me this opportunity of working on this interesting research topic. Their unfailing support, guidance and valuable advice has helped me immensely throughout my PhD journey. I am especially thankful to John for all his expert advice, encouragement and never-ending patience with this work. His active involvement and the drive towards perfection has shaped my research mind-set. John’s insight and enthusiasm has always motivated me to never lose hope and excel in my life. Brendan has always supported me throughout this thesis and I greatly appreciate all his advice, support and encouragement. I cannot thank my supervisors enough for all their effort behind each and every important step of this journey and without their constant support and encouragement this thesis would not have been possible

My sincere appreciation also goes to my thesis advisor Dr. Aidan Quinn for his valuable advice and support with this research work. A special thanks to Professor William G. Scanlon for being an excellent constructive critic and for his valuable feedback on this work. I would also like to acknowledge Dr. Kevin McCarthy of University College Cork for teaching me the concept of radio frequency IC design that greatly helped me in carrying out the work described in this thesis.

I would like to acknowledge the support of all the members of the Wireless Sensor Network Group, especially to Dinesh R. Gawade, Adhurim Hajzeraj, John Barton, Dr. Roy B V B Simorangkir, Dr. Mariusz Wilk, Dr. Melusine Pigeon, Dr. Su Zhen, Dr. Salvatore Tedesco, Marco Belcastro, Rose Lenihan, Nadeem Rather, Javier Torres and all my postgraduate colleagues. I would also like to thank Ken Rodgers, Declan Casey, and Donal O'Sullivan for their time and help with antenna fabrication, and Tim Hannon, Robert Newberry, Matthew Rodencal and Gary Dunlop of Sanmina Corporation for their support with this work.

I would also like to acknowledge all members of other departments in Tyndall for their help including the Graduate Studies, IT, HR and Finance departments.

I am extremely grateful to my friends Dr. Vaibhav Kumar, Dr. Arpit Rana, Ghanshyam Verma, Dr. Swatchith Lal, Kankana Paul, Dr. Bill Charteris, Adolfo Di Serio, Arindam Samanta, Dr. Deepak, Dr. Pramod and Mukesh for being a constant source of support, motivation and for always believing in me. I would also like to thank Paul Roseingrave, Ray O'Cinneide and Mary Kent for their constant encouragement and motivation.

I would also like to pay a special thanks to Professor Raghuvir Tomar of the LNMIIT, Jaipur, India who has always been a source of inspiration and has provided me with valuable suggestions and guidance during my studies.

I would like to express my sincere thanks to my thesis examiners Professor Vincent Fusco of Queen's University Belfast and Dr. Kevin McCarthy of University College Cork for their expertise, time and effort in examining this thesis.

Finally, I would like to deeply thank my parents, Birendra Singh and Meena Singh and my brothers for all their unconditional love, support and sacrifices over the years. I would sincerely like to thank Anju Singh for her love, support and motivation, and for standing by my side all through despite the geographical boundaries. Without their inspiration and support, this work would not have been possible.

To my parents and to the memory of my beloved grandfather

Abstract

With recent advances in wearable wireless sensor technology, the demand for smart wristwatches is growing rapidly due to their widespread adoption in applications such as smart health monitoring, security and fitness tracking. At the present time, the majority of wristwatch devices use the 2.45 GHz band due to the widespread availability of Bluetooth and Wi-Fi wireless technologies. Recently, the use of Sub-GHz frequencies for wearable systems has also gained interest due to the emergence of wireless technologies such as LoRaWAN and Sigfox that have the potential for long-range wireless communications. However, the design of antennas for Sub-GHz wristwatch devices poses challenges due to issues such as practical size constraints and the requirement for the use of electrically small antennas. In addition, the presence of the human body in close proximity to the antenna also poses design challenges due to its effect on the key antenna characteristics.

This thesis presents the development of four new Sub-GHz wristwatch antennas, with the key focus on addressing the bandwidth limitation challenge associated with state-of-the-art Sub-GHz wristwatch antennas. The research hypothesis for this work focuses on the use of a dual-radiator approach to enhance antenna bandwidth performance. In the first contribution, a novel 915 MHz wristwatch planar inverted-F antenna (PIFA) is designed using a dual-radiator approach for impedance bandwidth enhancement. The approach of using dual radiators has not been reported previously for Sub-GHz wristwatch antennas. This antenna demonstrates the highest peak realized gain and the second highest radiation efficiency for Sub-GHz wristwatch antennas reported in the literature.

In the second contribution, a new 915 MHz wristwatch PIFA design printed on a flexible PCB substrate is reported, which also uses a dual-radiator design approach. This antenna features one of the most compact Sub-GHz wristwatch antenna designs and the achieved performance compares well to the literature in terms of impedance bandwidth, peak realized gain and radiation efficiency. In addition, a second iteration of this antenna is also designed for operation in the 868 MHz band. This 868 MHz antenna is directly printed on the inside surface of a plastic enclosure using laser direct structuring (LDS) technology and demonstrates a similar impedance and radiation performance as that of the 915 MHz antenna.

Finally, in the third contribution, a significant enhancement of the impedance bandwidth is achieved using a modified feed structure to excite dual resonant responses that can be independently tuned to maximize the impedance bandwidth by 107 % when compared to the first generation 915 MHz antenna. The excitation of two adjacent resonant frequencies has not been previously reported for Sub-GHz wristwatch antennas in the literature. An equivalent circuit model for this antenna is also derived to explain the impedance bandwidth enhancement mechanism. Another key contribution of this work includes the development of a new equivalent transmission line model to accurately predict the antenna impedance characteristics with greatly reduced computation time compared to electromagnetic (EM) simulation. The outcomes of this thesis contribute to advancing the state-of-the-art in bandwidth enhanced Sub-GHz wristwatch antennas for wireless body sensor network applications.

List of Publications

A. The following peer-reviewed publications have emanated from the research work presented in this thesis:

Journal Publications:

[P1] **S. Kumar**, R. Newberry, T. Hannon, J. Barton, M. Rodencal, M. Pigeon, W. G. Scanlon, B. O'Flynn, and J. L. Buckley, "A Bandwidth-Enhanced Sub-GHz Wristwatch Antenna Using an Optimized Feed Structure," *IEEE Antennas and Wireless Propagation Letters,* vol. 20, no. 8, pp. 1389-1393, 2021.

[P2] **S. Kumar**, J. L. Buckley, J. Barton, M. Pigeon, R. Newberry, M. Rodencal, A. Hajzeraj, T. Hannon, K. Rogers, D. Casey, D. O'Sullivan, and B. O'Flynn, "A Wristwatch-Based Wireless Sensor Platform for IoT Health Monitoring Applications," *MDPI Sensors Journal,* vol. 20, no. 6, p. 1675, 2020.

Conference Publications:

[P3] **S. Kumar**, J. L. Buckley, J. Barton, R. Newberry, G. Dunlop, M. Rodencal, C. Webster, M. Pigeon, W. G. Scanlon, and B. O'Flynn, "A 915 MHz Wristwatch-Integrated Antenna for Wireless Health Monitoring," *14th European Conference on Antennas and Propagation (EuCAP)*, pp. 1-5, 2020.

[P4] **S. Kumar**, J. L. Buckley, J. Barton, R. Newberry, G. Dunlop, M. Rodencal, C. Webster, and B. O'Flynn, "A Bandwidth Enhanced 915 MHz Antenna for IoT Wrist-Watch Applications," *13th European Conference on Antennas and Propagation (EuCAP)*, pp. 1-5, 2019.

B. Related publications:

[P5] D. R. Gawade, S. Ziemann, **S. Kumar**, D. Iacopino, M. Belcastro, D. Alfieri, K. Schuhmann, M. Anders, M. Pigeon, J. Barton, B. O'Flynn, and J. L. Buckley, "A Smart Archive Box for Museum Artifact Monitoring Using Battery-Less Temperature and Humidity Sensing," *MDPI Sensors Journal,* vol. 21, no. 14, p. 4903, 2021.

[P6] **S. Kumar**, J. L. Buckley, A. D. Serio, and B. O'Flynn, "Comparative Analysis of Circuit and Finite Element Models for a Linear Wire Dipole Antenna," *29th Irish Signals and Systems Conference (ISSC)*, pp. 1-6, 2018.

[P7] **S. Kumar**, J. Buckley, J. Barton, and B. O'Flynn, "Performance analysis of a novel flexible NFC Tag for IoT applications," *12th Smart Systems Integration Conference,* pp. 432-435, 2018.

[P8] D. R. Gawade, R. B. V. B. Simorangkir, D. Zorbas, **S. Kumar**, S. Ziemann, D. Iacopino, J. Barton, K. Schuhmann, M. Anders, B. O'Flynn, and J. L. Buckley, "A Museum Artefact Monitoring Testbed using LoRaWAN," *26th IEEE Symposium on Computers and Communications (ISCC),* pp. 1-3, 2021.

[P9] R. B. V. B. Simorangkir, D. R. Gawade, **S. Kumar**, B. O'Flynn, J. L. Buckley, T. Hannon, P. Donovan, and R. Newberry, "Screen Printed Epidermal Antenna for IoT Health Monitoring," *Asia-Pacific Microwave Conference (APMC),* 2021 (*Accepted*).

[P10] R. B. V. B. Simorangkir, B. Mohamadzade, A. Lalbakhsh, **S. Kumar**, J. L. Buckley, and B. O'Flynn, "Conformal Antenna with Monopolar-Broadside Pattern Reconfigurability Realized with Polymer-Conductive Textile Composite," *European Microwave Conference (EuMC),* 2021 (*Accepted*).

Chapter 1: Introduction

The last few decades have witnessed a significant advancement in wearable Internet-of-Things (IoT) technology. The IoT is a network of internet-connected physical objects that typically contain embedded sensors, actuators and firmware to wirelessly communicate and exchange data with other wireless devices and systems over the internet [1].

Figure 1.1 shows a typical wireless sensor network (WSN) system for health monitoring, where a wristwatch-based wireless sensor node is shown. A wireless radio transceiver with one or more integrated antennas is a key component of a wireless sensor node because the radio transceiver enables sensor nodes to wirelessly communicate with external devices such as smartphones [2]. Further, the sensor data stored in a smartphone can be wirelessly forwarded to the data cloud repository via a wireless network such as Wi-Fi [3] or cellular networks [3]. Once the measured data is available on the data cloud repository, the measured information can be easily accessed at a nurse station for further analysis of health records and planning treatments.

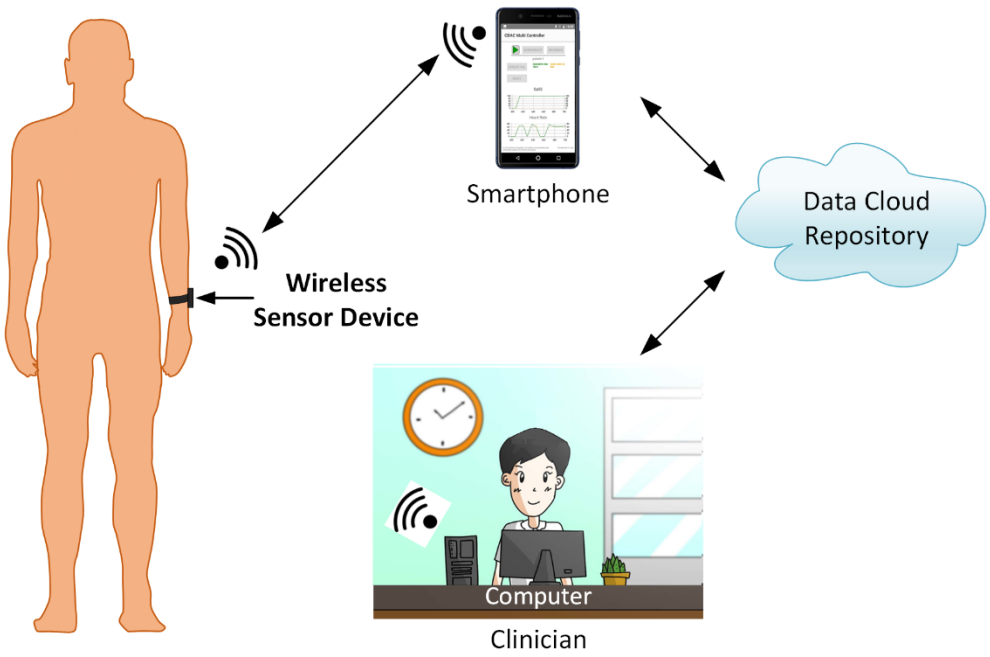


Figure 1.1: Overview of a typical WSN system for health monitoring.

When a WSN is specifically used for wireless networking of wearable and implantable sensors, the WSN is referred to as a wireless body sensor network (WBSN) [4]. In recent years, WBSN technology has gained much attention because of its widespread usage in a growing range of applications such as smart health monitoring, security, sports, fitness tracking, localization and proximity alerting [5, 6]. Furthermore, due to recent advances in WBSN and wearable technologies, smart wearable devices have started to appear in an ever-increasing number of applications, such as smartwatches [7], wristbands [8], smart clothing [9] and smart glasses [10] to name but a few. However, of these different groups of wearable devices, smartwatches are the most popular form factor for wearables mainly because of their ability to be worn seamlessly and conveniently on the human body and help the users to collect, analyze and wirelessly transfer real-time personal data to external monitoring devices [6]. Nowadays, smartwatches play a significant role in wireless tracking of human physiological activities and estimating various health parameters, such as activity levels, sleep patterns, heart rate, blood oxygen saturation (SpO_2) level and electrocardiogram (ECG) [11, 12]. Because of the aforementioned reasons, currently, smartwatches with wireless sensing capabilities are dominating the global wearables market and a similar trend is predicted for the near future [13].

1.1 Motivation of this Work

At the present time, the majority of wristwatch devices use the 2.45 GHz license free industrial, scientific and medical (ISM) band [14] due to the widespread availability of Bluetooth and Wi-Fi wireless technologies. However, wireless technologies are emerging such as long-range wide area network (LoRaWAN) [15] and SigFox [16] operating in the Sub-GHz ISM bands such as 915 MHz (902−928 MHz) in North America and 868 MHz (863−870 MHz) in Europe [17]. These technologies enable wireless communication over long range at low power consumption compared to the 2.45 GHz band [18].

Wireless communications at 2.45 GHz has reduced wireless communication range compared to Sub-GHz frequencies because of increased free space path loss and poor radio frequency (RF) penetration through walls and buildings [19].

Radio waves propagating at higher frequencies through walls and buildings have more interaction with material molecules compared to lower frequencies and thus experience greater RF attenuation compared to lower frequencies [20].

Power consumption is a key concern for wireless sensor devices because the sensor nodes generally incorporate low capacity small batteries to power the sensor device [21]. Because of the ubiquitous use of the license-free 2.45 GHz ISM band, wireless communications at 2.45 GHz can lead to co-existence issues [22] that may degrade wireless performance. Therefore, multiple re-transmissions of the same information may be required, which leads to increased power consumption in the 2.45 GHz band [22, 23]. On the other hand, Sub-GHz bands such as 868 and 915 MHz are less congested mainly because of a restricted duty cycle (typically ≤ 1 % [24]) and can circumvent the co-existence issues of the 2.45 GHz band [18, 19] particularly when high data rates are not required. In addition, because of the reduced RF attenuation through walls and other obstacles at Sub-GHz frequencies, a radio transceiver operating at Sub-GHz bands requires less power to achieve a similar communication range as at 2.45 GHz [25].

In recent times, many emerging wristwatch-based applications require long-range wireless communications for increased coverage. For example, patient health monitoring in a hospital building may require a wireless communication range to cover the entire hospital building [26]. LoRaWAN wireless technology uses Sub-GHz frequencies to meet the above-mentioned long-range wireless communications with low power operation and extended battery life [18].

The wireless transmission and reception capabilities of wireless sensor devices such as smartwatches are enabled by the integration of one or more antennas. There has therefore been an upsurge of research interests in developing antennas for wrist-worn devices [27-30]. However, the design of wristwatch antennas for the Sub-GHz bands is challenging mainly because of the practical size constraints of wrist-worn devices [31].

Wristwatch antennas operating at Sub-GHz frequencies require a large form factor compared to the antennas operating at 2.45 GHz. However, considering end user convenience, wrist-worn devices are also required to have a compact size, which leads to the requirements of designing electrically small antennas (ESAs).

ESAs have fundamental performance limitations in terms of impedance bandwidth, antenna gain and radiation efficiency [31] and therefore it is challenging to design high-performance antennas that can be accommodated within a small size device. Another challenge in the design of wristwatch antennas concerns the presence of the human body in the immediate vicinity of the antenna.

The electromagnetic (EM) coupling between an antenna and the human body can lead to antenna impedance mismatch issues [32, 33]. This impedance mismatch results in power loss at the input terminal and ultimately reduces the power radiated from the antenna. In addition, human body tissues constitute a lossy RF medium and absorb EM radiation and thus degrade the radiation efficiency and gain of the antenna [32]. These antenna design issues lead to reduced wireless communication range, increased power consumption and ultimately increased design cost when considering such electrically small antennas operating in the Sub-GHz bands.

The challenges with current state-of-the-art Sub-GHz wristwatch antennas are summarized below:

- Several Sub-GHz band wrist-worn antennas have been reported in the literature; however, the majority of antennas have a limited -10 dB impedance bandwidth of less than 20 MHz [30, 34-41] or achieve a wider impedance bandwidth of greater than 20 MHz either by substantially increasing the antenna size [42-50] or at the cost of compromised radiation performance [36, 42-45, 47, 48].
- The majority of wristwatch antennas developed by other researchers assume an ideal environment close to the antenna element and do not take into account the effects of nearby internal components within a practical wristwatch device, These include printed circuit boards (PCBs), battery, sensor assemblies, connectors and metal screws.
- Very few Sub-GHz wristwatch antennas [44, 46] designed previously by other researchers report all the key antenna parameters, such as impedance bandwidth, gain, efficiency and SAR figures.

The above issues signify the need for developing new Sub-GHz wristwatch-integrated antenna solutions with improved impedance characteristics while at the same time maximizing radiation performance which are designed with a system-level approach to optimise antenna performance.

The Sub-GHz wristwatch-integrated antennas designed and demonstrated in this thesis are described in [51-54] which report on the design, simulation and test of all the key parameters associated with optimised antenna development and explain the wrist-worn antenna characteristics.

In addition, the proposed antennas have been designed to take into account all internal components and assemblies within a practical wristwatch sensor device to ensure accurate EM modelling of the entire assembly.

The motivation of this work is to address the design challenges associated with Sub-GHz operation in a highly constrained form factor and develop novel wristwatch antenna designs with improved impedance and radiation performance for Sub-GHz band WBSN applications when compared with the current state-of-the-art in this research domain.

1.2 Aim and Objectives

The aim is to address the aforementioned research challenges and develop novel Sub-GHz wristwatch antennas with improved impedance characteristics while at the same time maximizing radiation performance. The main objectives of this research work are as follows:

- Uncover the main design challenges associated with the state-of the art Sub-GHz wristwatch antennas.
- Present new antenna designs, develop accurate EM models and characterize the performance of the proposed antennas through measurements and experiments.
- Develop novel equivalent circuit and transmission line models to enable accurate and rapid intuition of the impedance characteristics of the antennas.
- Perform optimization and parametric analysis of the proposed antennas to achieve desired performance when deployed on the body.

- Achieve minimum required impedance bandwidth of 26 MHz for 915 MHz band operations as defined by the IEEE 802.15.4 standard [55] as well as maximizing radiation performance compared to the literature. In addition, an associated objective is to design antennas with reduced RF power absorbed by the human body.
- Explore the feasibility of designing wristwatch antennas using novel manufacturing techniques such as laser direct structuring (LDS) technology to deposit the metal antennas to the plastic housing of a wristwatch form factor device.
- Contribute to the advances in the development of next generation antenna solutions for wristwatch-based WBSN technology.

1.3 Organisation of the Thesis

The remainder of the thesis is organised as follows:

Chapter 2: In this chapter, the fundamentals of antenna theory and key performance parameters used to explain the impedance and radiation characteristics of the proposed novel antennas are described. The electromagnetic interaction between wearable antennas and the lossy human body tissue is also outlined.

Chapter 3: A comprehensive overview of state-of-the-art wrist-worn antennas in the literature is presented. This chapter investigates the design techniques and performance of several wrist-worn antennas, with a particular focus given to Sub-GHz band antennas. A number of limitations, design challenges and gaps in current state-of-the-art Sub-GHz wristwatch antennas are identified and the research hypothesis is formulated. The need for developing new wristwatch-integrated antenna designs with improved performance in terms of impedance characteristics while at the same time maximizing radiation performance is highlighted.

Chapter 4: A bandwidth enhanced novel 915 MHz planar inverted-F antenna (PIFA) wristwatch antenna using a dual-radiator approach is presented. The use of dual-radiator approach enables the impedance matching of the antenna over the required -10 dB impedance bandwidth of greater than 26 MHz and thus improves the impedance bandwidth of the antenna. The antenna element was integrated into a simplified wristwatch model and the impedance and radiation performances were characterized [51].

Chapter 5: The development of two new bandwidth enhanced wristwatch-integrated compact PIFA antennas operating at 915 MHz and 868 MHz bands are presented. First, a novel dual-radiator based 915 MHz antenna printed on a low-cost flexible polyimide substrate is presented [52].

The dual-radiator topology is implemented to enhance the impedance bandwidth of the antenna by enabling the impedance matching over a -10 dB impedance bandwidth of greater than 26 MHz and to improve radiation performance of the antenna. In addition to the above, a second iteration [53] of this antenna is designed for operation in the 868 MHz band. This 868 MHz antenna is directly printed on the inside surface of a plastic wristwatch enclosure using laser direct structuring (LDS) technology and has been fully integrated into a demonstrator wristwatch device.

Chapter 6: The feed structure of the flexible 915 MHz antenna presented in Chapter 5 is further optimized to significantly increase the impedance bandwidth performance of the antenna. With the optimized feed, the new antenna excites two closely located resonant frequencies that can be independently tuned to maximize the impedance bandwidth of the antenna. An equivalent circuit model for the proposed antenna is also derived to explain the impedance bandwidth enhancement approach. In addition, a new equivalent transmission line model for the proposed antenna is developed to accurately predict the antenna impedance characteristics with greatly reduced computation time compared to EM simulation [54].

Chapter 7: In this chapter, the key conclusions and findings of this thesis are presented and suggestions for future research work are outlined.

Chapter 2: Background Theory

2.1 Background

This chapter presents an overview of the key performance parameters that are used to describe the impedance and radiation characteristics of an antenna. The design challenges associated with the continued trend for antenna miniaturization is discussed with a key focus on antenna gain and impedance bandwidth performance. As the performance of wearable antennas needs to be optimised to operate efficiently in the presence of the human body, the electromagnetic (EM) interaction between the antenna and the human body is also outlined.

2.2 Antenna Parameters

According to *IEEE standard for definitions of terms for antennas* (IEEE Std 145-2013), an antenna is defined as "that part of a transmitting or receiving system that is designed to radiate or to receive electromagnetic waves" [56]. In a wireless communication system, an antenna serves as a transitional structure between a guided wave and free space.

In the following sub-sections, several key antenna performance parameters are introduced which are used to analyze antenna performance throughout the thesis.

2.2.1 Antenna Impedance

Antenna input impedance (Z_A) is defined as "the impedance presented by an antenna at its terminals" [56]. In other words, Z_A represents the ratio of voltage to current at a pair of terminals where the antenna structure is excited [57].

The input impedance of an antenna is a complex quantity with both real and imaginary components and can be expressed as follows

$$Z_A(\Omega) = R_A + jX_A, \tag{2.1}$$

where, R_A denotes the resistive component of antenna impedance and X_A represents the reactive component. The quantities R_A and X_A are frequency dependent.

The resistive component R_A consists of two terms, namely, undesired loss resistance R_L and desired radiation resistance R_R.

Thus, the input impedance of the antenna can be expressed as

$$Z_A\,(\Omega) = (R_L + R_R) + jX_A \tag{2.2}$$

The imaginary part of the input impedance X_A determines the amount of power stored in the near field of the antenna [58]. To ensure that maximum power is transferred from the source or generator to the antenna or from the antenna to a load, the input impedance of the antenna needs to be conjugately matched to the load or source impedance [57].

2.2.2 Voltage Reflection Coefficient

The voltage reflection coefficient (Γ) of an antenna measures the amount of RF energy reflection from the antenna. The antennas demonstrated in this thesis can be represented by a 1-port network shown in Figure 2.1, where a transmission line of characteristic impedance Z_0 is terminated in a load impedance Z_A, representing the antenna impedance. The amplitude of the voltage wave incident on port-1 (P_1) is denoted by the quantity $V^+$and the amplitude of the voltage wave reflected from Port-1 is denoted as V^-[59].

The ratio of the reflected voltage amplitude V^- to the incident voltage amplitude V^+ is defined as the voltage reflection coefficient, Γ [59] and is expressed as follows

$$\Gamma = \frac{V^-}{V^+} = \frac{Z_A - Z_0}{Z_A + Z_0}. \tag{2.3}$$

A key requirement of antenna design is to minimize Γ so as to maximize the RF power delivered to the antenna over the required band of the antenna operation.

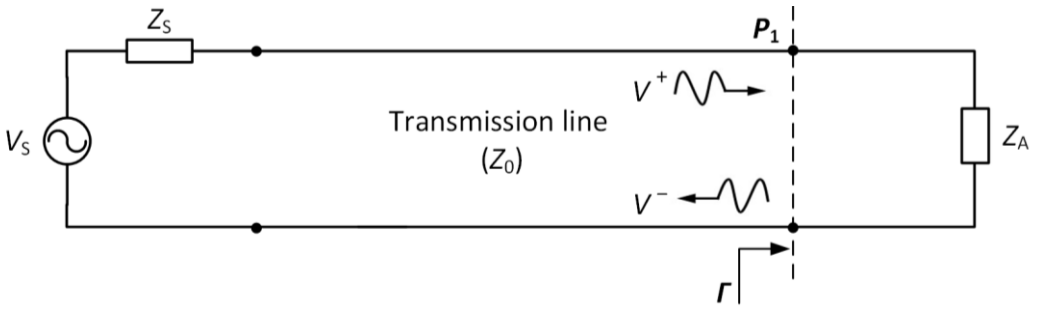


Figure 2.1: One-port network describing voltage reflection coefficient, Γ [59].

2.2.3 S-parameters

Scattering or *S*-parameters are used at radio frequencies to describe the input-output relationship between the ports of an *n*-port network, where *n* is the number of ports [60]. In Figure 2.2, a two-port network is shown, where the incident and reflected voltage wave variables are represented as a_n and b_n, respectively. At lower frequencies, terminating the ports in open or short circuit standards is conveniently used to determine the impedance and admittance parameters [60]. However, at high frequencies, it is difficult to provide ideal open or short circuit terminations due to the presence of parasitics and it is convenient to use *S*-parameters to determine the input-output relationship between the ports by terminating the required port in the characteristic impedance of the system denoted Z_0, which is typically 50 Ω [60].

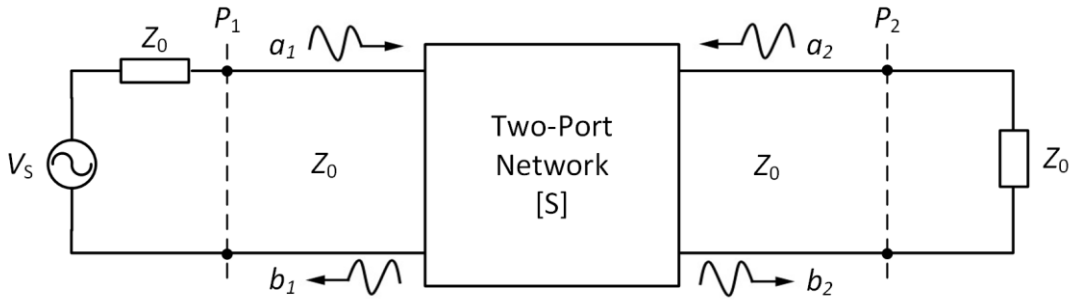


Figure 2.2: Two-port S-parameter network [60].

Consider the two-port network shown in Figure 2.2, the traveling voltage wave variables *a* and *b* are related to the S-parameters as follows

$$b_1 = S_{11}a_1 + S_{12}a_2 \tag{2.4}$$

$$b_2 = S_{21}a_1 + S_{22}a_2 \tag{2.5}$$

In equations (2.4) and (2.5), the variables a_1 and a_2 represent the incident voltage waves at ports P_1 and P_2, respectively, while b_1 and b_2 respectively represent the reflected voltage waves from ports P_1 and P_2. Driving the input port P_1 and terminating the output port P_2 in Z_0, there will be no reflected wave from port P_2 (i.e., $a_2 = 0$) because of a perfect impedance match at P_2 and thus, the parameters S_{11} (reflection coefficient, Γ) and S_{21} (transmission coefficient) can be expressed as

$$S_{11} = \left.\frac{b_1}{a_1}\right| \text{ where, } a_{2=0} \tag{2.6}$$

$$S_{21} = \left. \frac{b_2}{a_1} \right| \text{where}, a_{2=0} \tag{2.7}$$

S-parameters of the antennas developed in this thesis were measured using Rohde & Schwarz *ZVRE* [61] and Anritsu MS2038C [62] vector network analyzers (VNA). The Anritsu MS2038C is a portable VNA, whereas the Rohde & Schwarz *ZVRE* VNA is connected to an AMS-8050 [63] anechoic chamber measurement setup.

2.2.4 Impedance Bandwidth of an Antenna

According to the *IEEE standard for definitions of terms for antennas* (IEEE Std 145-2013), the bandwidth of an antenna is defined as "the range of frequencies within which the performance of the antenna conforms to a specified standard with respect to some characteristic" [56]. In this thesis, a -10 dB impedance bandwidth definition is used which signifies the frequency range over which less than 10 % of the incident power is reflected from the antenna and greater than 90 % of the incident power is delivered to the antenna input terminal.

In this thesis, Sub-GHz wristwatch antennas have been developed for 915 MHz (North America) and 868 MHz (Europe) band operations. As summarized in Table 2.1, wireless communications operating at 915 MHz require a -10 dB impedance bandwidth of 26 MHz [55], and for 868 MHz operations, the required impedance bandwidth is 7 MHz [64].

Table 2.1: Sub-GHz band impedance bandwidth specifications.

Frequency band (MHz)	Frequency range (MHz)	-10 dB impedance bandwidth (MHz)
915	902 – 928	26
868	863 – 870	7

2.2.5 Antenna Directivity and Gain

The directivity (*D*) of an antenna is defined as "the ratio of the radiation intensity in a given direction from the antenna to the radiation intensity of an isotropic source" [57] and expressed as follows

$$D = \frac{U}{U_0} = 4\pi \frac{U}{P_{rad}}, \tag{2.8}$$

where, U is the radiation intensity in a given direction, $U_0 = P_{rad}/4\pi$ is the radiation intensity of an isotropic source [57] and P_{rad} is the total power radiated by the antenna.

The radiation intensity (U, Watt/steradian) in a given direction is defined as the *total power* radiated per unit solid angle. The directivity of the antenna is generally expressed in dBi and describes only the directional properties of the antenna [57].

Antenna gain (G) is another key parameter describing the radiation performance of an antenna. The gain is closely related to the directivity and takes into account both directional performance and the radiation efficiency of the antenna [57].

The gain of an antenna is defined as "the ratio of the intensity, in a given direction, to the radiation intensity that would be obtained if the *power accepted* by the antenna were radiated isotropically" [57].

$$G = 4\pi \frac{\text{Radiation intensity, } U}{\text{total input (accepted) power}} = 4\pi \frac{U}{P_{in}} \tag{2.9}$$

In practice, the gain (typically in dBi) of an antenna is expressed as realized gain (G_R), which also takes into account the impedance mismatch loss factor of the antenna [56].

2.2.6 Radiation Efficiency

The radiation efficiency (η_{rad}) is defined as the ratio of the total power radiated (P_{rad}) by the antenna to the total power accepted (P_{in}) by the antenna at its input terminals [57]. The radiation efficiency is related to the radiation resistance (R_R) and loss resistance (R_L) of the antenna and commonly given as follows [65]

$$\eta_{\text{rad}} = \frac{P_{\text{rad}}}{P_{\text{in}}} = \frac{R_{\text{R}}}{R_{\text{R}} + R_{\text{L}}}, \tag{2.10}$$

where, R_R (in Ω) represents the amount of power radiated from the antenna and R_L (in Ω) is the inherent conductor and dielectric losses of the antenna. The radiation efficiency relates the gain and directivity of the antenna as follows

$$G = \eta_{\text{rad}} \times D, \tag{2.11}$$

where, the gain and directivity are computed in the direction of maximum radiation [57].

2.3 The Hertzian Dipole

The Hertzian dipole is an antenna consisting of a short length of linear conductor that carries a uniform alternating current along its length [65]. In order to ensure that the current distribution is uniform, the antenna is assumed to be electrically short ($\Delta l << \lambda_0$), where, Δl represents the total length of the Hertzian dipole and λ_0 represents the free-space wavelength at the nominal operating frequency f_0. The concept of a Hertzian dipole is useful in analysing linear wire antennas of finite length by treating the antenna as a cascade of several Hertzian dipoles [65].

It is shown in equation (2.10) that the radiation efficiency of an antenna is defined by the ohmic and radiation resistances of the antenna. In [65], the expression for the radiation resistance (R_R) of the Hertzian dipole is defined as

$$R_R(\Omega) = 80\pi^2 \left(\frac{\Delta l}{\lambda_0}\right)^2 \tag{2.12}$$

Therefore, to maximize radiation resistance R_R, it is necessary to maximize the ratio of the dipole length to the free-space wavelength. This is especially challenging when designing antennas of small size.

2.4 Electrically Small Antennas

An electrically small antenna (ESA) is defined as an antenna whose dimensions are a small fraction of the free-space wavelength λ_0 at the operating frequency f_0 [66]. Wheeler described the ESA as an antenna whose maximum dimensions are less than a *radianlength*, $\lambda_0/2\pi$ [67]. An ESA can also be described using a quantity referred to as the *wave number*, $k = 2\pi/\lambda_0$, which represents the phase change per wavelength and is the inverse of the radianlength definition [68]. An ESA is an antenna having $ka < 1$, where a (in m) is the radius of the smallest sphere (*radiansphere*) circumscribing the antenna [57]. This situation is illustrated in Figure 2.3, where an ESA, in this case a dipole antenna, is surrounded by a sphere of radius a [69, 70].

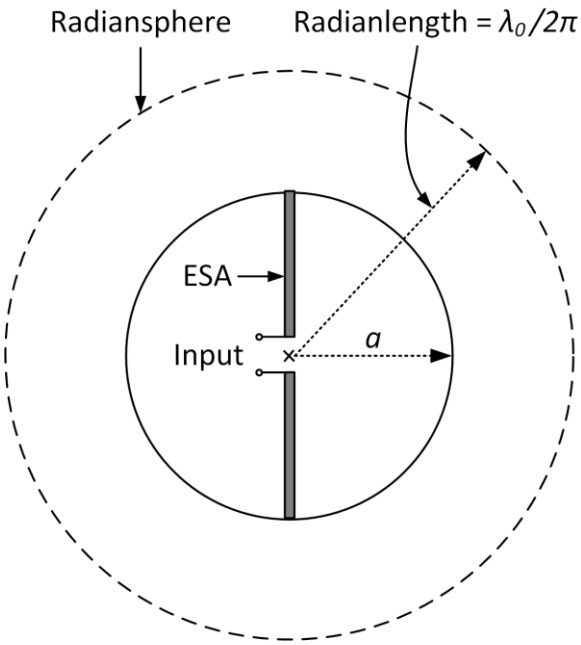


Figure 2.3: Electrically small antenna (ESA) and radian sphere [69, 70].

The performance characteristics of an ESA, such as impedance bandwidth, gain and efficiency are fundamentally limited by the antenna size [31, 71]. This is primarily because the radiation resistance (R_R), and hence the power radiated from the antenna, decreases with decreasing antenna size [65, 72]. Thus, for an ESA, the ohmic losses of the antenna need to be minimized in order to maximize antenna radiation efficiency, as described in Section 2.2.6 [65].

For a linearly polarized ESA, the minimum quality factor, Q_{MIN} [65, 73] can be expressed as

$$Q_{\text{MIN}} = \frac{1}{(ka)^3} + \frac{1}{ka} \tag{2.13}$$

This expression shows that as the quantity a decreases, the value of Q_{MIN} increases, resulting in greater RF energy storage with less power radiated from the antenna.

In addition, the impedance bandwidth (BW) of an antenna [60] is inversely proportional to the quality factor (Q) and is given by

$$BW = \frac{f_C}{Q} \tag{2.14}$$

In equation (2.14), the term f_C denotes the centre frequency of operation and the term *BW* represents the -3 dB impedance bandwidth of the antenna [60]. Equation (2.14) shows that antenna bandwidth and *Q*-factor are intimately linked and decreasing the antenna size also leads to bandwidth reduction.

Furthermore, for an ESA, the maximum achievable gain, G_{MAX} is also limited by the quantities *k* and *a* and is expressed as [65]

$$G_{\mathrm{MAX}} = (ka)^2 + 2(ka) \tag{2.15}$$

2.5 Radiation Efficiency Measurement

Many antenna radiation efficiency measurement techniques have been reported in the literature. Some of the most commonly used methods include the Wheeler cap and directivity/gain methods [74].

2.5.1 Wheeler Cap Method

In this method, proposed by Wheeler [70], a hollow conductive shield or 'Wheeler cap' is placed over the antenna under test as depicted in Figure 2.4(a). The radius of the cap is chosen to be a radianlength ($\lambda_0/2\pi$) in extent. This dimension ensures that the near-field of the antenna is not disturbed and at the same time, ensures that all radiated power from the antenna is reflected. S_{11} measurements are performed with and without the cap in place to derive values for the radiation and loss resistances $R_R + R_L$ from which the antenna efficiency can then be estimated [65]. The Wheeler cap method is one of the most popular radiation efficiency measurement methods for small antennas due to its simplicity, speed, repeatability, and accuracy [74].

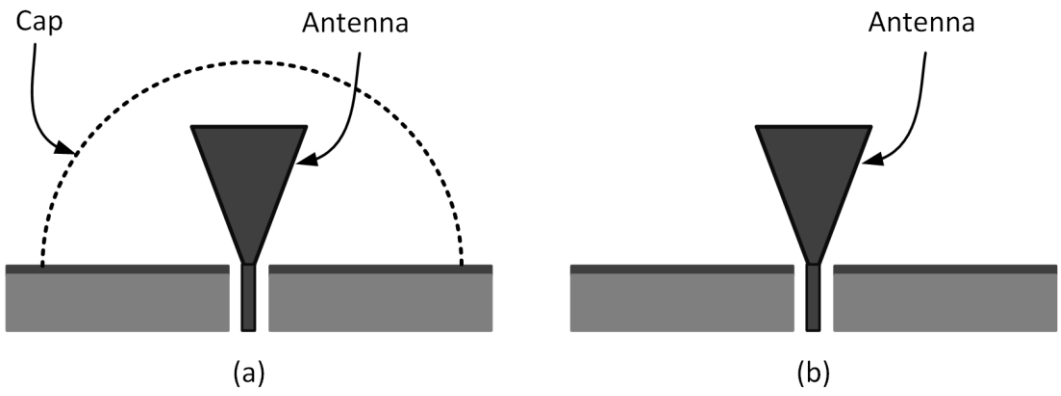


Figure 2.4: Antenna efficiency measurement: (a) in a Wheeler cap, and (b) in free-space.

2.5.2 Directivity/Gain Method

The second method for radiation efficiency measurement of an antenna is based on direct measurement of the gain and directivity characteristics of the antenna in an anechoic chamber environment [74]. This method works by measuring the antenna under test against a calibrated reference antenna, commonly a reference dipole antenna with known gain, directivity and efficiency figures [74]. The radiation efficiency of the antennas developed in this thesis was measured with the above approach using an AMS-8050 compact anechoic chamber [63].

2.6 Link Budget

A link budget for a free-space wireless communication system, consisting of a radio transmitter and receiver, describes the relationship between the received power, P_R and the transmitted power, P_T and can be written as [75]

$$P_{\mathrm{R}}(\mathrm{dBm}) = P_{\mathrm{T}}(d\mathrm{Bm}) + G_{\mathrm{T}}(\mathrm{dBi}) + G_{\mathrm{R}}(\mathrm{dBi}) + 20\ log\left(\frac{\lambda_0}{4\pi d}\right) \tag{2.16}$$

In equation (2.16), parameter P_R is the received power (dBm), P_T is the power delivered to the transmitting antenna (dBm), G_T is the transmitter antenna gain (dBi), G_R represents the gain of the receiving antenna (dBi), λ_0 is the wavelength at the specified operating frequency (m) and d denotes the distance between the transmitter and receiver (m).

Table 2.2 summarizes the parameters required for the link budget calculation. In this thesis work, an AT86RF212B radio transceiver from Microchip Technology has been employed [76], with transmit power = 5 dBm and minimum receiver sensitivity = -110 dBm. Furthermore, the link budget calculation at f_0 = 915 MHz assumes the use of an omni-directional antenna with a peak realized gain G_R = 0 dBi. The distance between the transmitter and receiver is denoted d and is assumed to be 3 m for this calculation. The difference between the minimum receiver sensitivity and the receiver power is denoted as the link margin and is calculated in Table 2.2.

Table 2.2: Parameters for link budget calculation at f_0 = 915 MHz.

Parameters	Specification	Value
Transmitter power, P_T (dBm)	for AT86RF212B radio XCVR [76]	5
Transmitter antenna gain, G_T (dBi)	For the antenna in chapter 5	-4.9
Receiver antenna gain, G_R (dBi)	Assumed	0
Free-space path loss (dB)	$20\ log(\lambda_0/4\pi d)$, d = 3 m	-41.2
Minimum receiver sensitivity (dBm)	AT86RF212B radio XCVR [76]	110
Calculated link margin (dBm)	**P_R – receiver sensitivity**	**68.9**

In this case, the calculated link margin is approximately 68.9 dB which is almost 50 dB larger than the minimum recommended link margin of 20 dB [77] for establishing reliable wireless communications.

2.7 Antenna-Human Body Interaction

When an antenna is placed in close proximity to the human body, the electromagnetic coupling between the antenna and the human body can alter the impedance and radiation characteristics of the antenna [32, 33]. The relative permittivity of human body tissue is large compared to the permittivity of free space, and therefore the dielectric loading caused by the human body may lead to antenna detuning [32]. In addition, human body tissues have a high water content that makes the body tissue moderately conductive and causes RF losses at radio frequencies [32]. Therefore, due to the high relative electrical permittivity and lossy nature of the human body tissue, the coupling between an antenna and the human body leads to antenna impedance variation and deterioration of antenna gain and radiation efficiency [32, 33].

The RF losses associated with the human body tissue and electromagnetic (EM) radiation is represented by a standard parameter called specific absorption rate (SAR). The SAR parameter is a measure of the rate at which power is absorbed by the human body when exposed to electromagnetic (EM) radiation and is given as follows [78]

$$SAR = \frac{\sigma\,|E^2|}{\rho}\ (\mathrm{W/kg}), \tag{2.17}$$

In equation (2.17), σ represents the electrical conductivity of the tissue specified (S/m), E is the RMS electric field strength (V/m) and ρ is the mass density of the tissue (kg/m^3). Defining σ and ρ of the phantom arm is important as these parameters are essential for evaluating the SAR figure of the antenna, as shown in equation (2.17).

According to IEEE Std C95.1 safety guidelines, the SAR limit for the human head region must not be greater than 1.6 W/kg averaged over 1 g of human tissue [79]. However, if the SAR is evaluated on the human wrist, a limit of 4.0 W/kg averaged over 10 g of wrist tissue is applied according to IEEE Std C95.1 safety [79] and International Commission on Non-Ionizing Radiation Protection (ICNIRP) guidelines [80]. The SAR limit for the human wrist is higher compared to the head region mainly because different body parts respond differently to the RF-induced rise in the body temperature [80].

2.7.1 SAR measurement techniques

SAR measurement techniques are based on direct measurement of the electric field strength produced by the antenna under test when immersed in a tissue equivalent phantom.

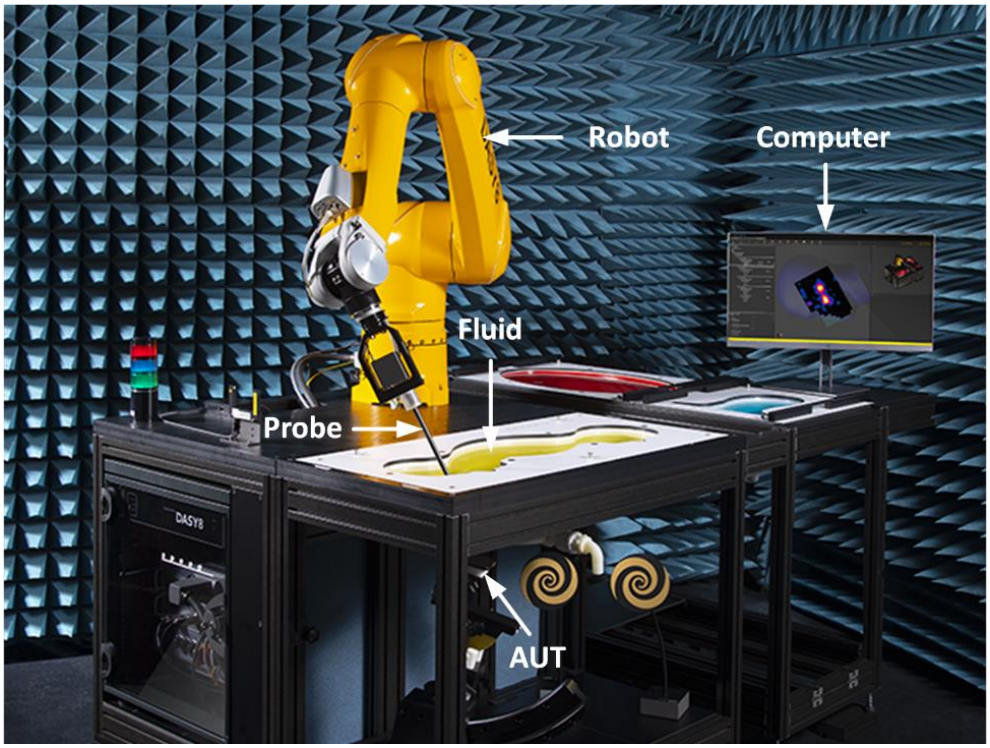


Figure 2.5: A dosimetric assessment system (DASY) SAR measurement setup [81].

This technique uses an E-field probe that is immersed in a EM phantom containing a tissue-equivalent fluid that mimics the RF dielectric properties of human tissue. The probe position is varied in a controlled manner to yield a three dimensional measurement of SAR in the desired region of the human body [82]. An example of a commercial SAR measurement system is the Dosimetric Assessment System (DASY) from SPEAG [81] is shown in Figure 2.5. The DASY system is a robot-based, high precision electromagnetic (EM) near-field scanning platform that can be used for precise SAR measurements in the frequency range of 3 kHz to 110 GHz [81].

The above commercial SAR measurement systems require expensive instrumentation and the measurements are time-consuming to complete [83]. SAR analysis is therefore more readily achieved using EM simulation methods. For the above reasons, simulated SAR figures are reported in the literature.

2.8 Planar Inverted-F Antennas

In this thesis, variants of a planar inverted-F antenna (PIFA) topology have been used to design the Sub-GHz wristwatch antennas developed in this work [84]. The PIFA antennas are a commonly used solution for wearable wireless devices mainly because of their potential to be realized in a compact form factor and their ability to reduce the backward radiation towards the human wrist due to the use of a finite size ground plane between the radiator and human tissue [40, 65].

In Figure 2.6, the evolution of a PIFA antenna is depicted, where the symbol *S* denotes the source excitation and the symbol *G* denotes ground. A PIFA antenna has evolved from a vertical wire quarter-wavelength monopole antenna, as illustrated in Figure 2.6(a) [84]. However, a conventional vertical wire monopole requires a monopole element of quarter-wavelength placed orthogonal to the ground plane and is therefore not suitable for the integration into compact wearable devices, such as a smartwatch. An ILA enables integration of the antenna in a compact device, but the bending of the wire parallel and close to the ground plane introduces additional capacitance to the input impedance of the antenna, which leads to antenna impedance mismatch. The additional capacitance associated with the ILA is compensated by adding a shorting pin that contributes shunt inductance to the input impedance of the antenna.

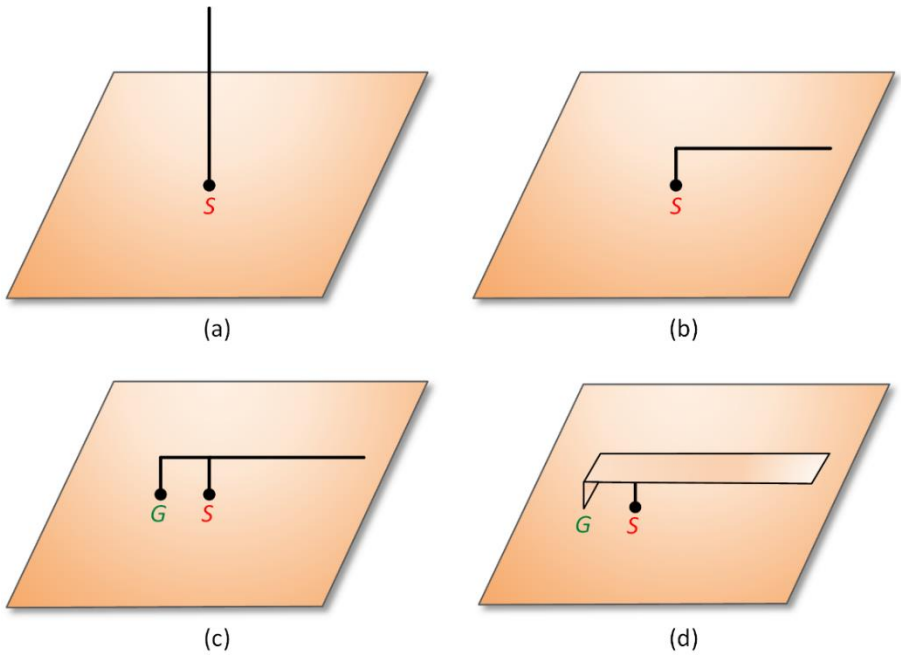


Figure 2.6: PIFA evolution: (a) Quarter-wavelength monopole, (b) Inverted-L antenna (c) Inverted-F antenna (d) Planar inverted-F antenna.

As depicted in Figure 2.6(c), the modified version of ILA takes a shape of an inverted-F and so this antenna topology is referred to as an Inverted-F antenna (IFA). The input impedance matching of an IFA is achieved by adjusting the value of the shunt inductance, which can be controlled by changing the position of the shorting pin and/or varying the width of the feed and shorting pin [85]. Finally, as shown in Figure 2.6(d), when the radiating wire of the IFA is replaced by a conducting plate, the antenna configuration is referred to as a PIFA [84].

2.9 Dielectric Characterization Technique

In order to characterize the RF dielectric properties of materials, open-ended coaxial probes are commonly used [86]. The open-end of the probe is placed in direct contact with the sample to be measured. The fringing fields at the open-end of the probe changes with varying material type as does the measured reflection coefficient at the input of the probe. These effects enable the frequency dependant dielectric properties of the material (ε_r and tanδ) to be computed.

A block diagram for a commercial dielectric measurement system is shown in Figure 2.7 and the lab setup is shown in Figure 2.8. This system uses a dielectric assessment kit, DAK-TL-3.5 from SPEAG [87].

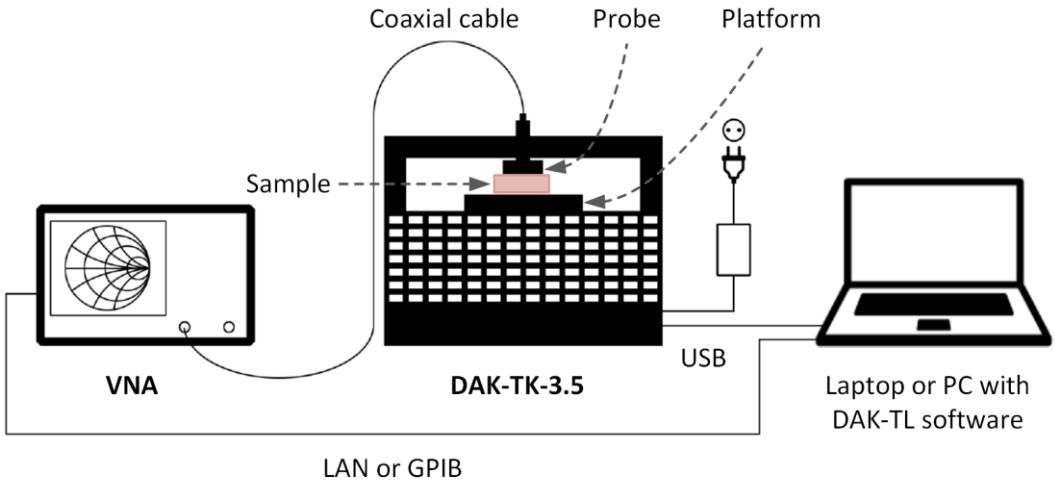


Figure 2.7: The DAK-TL-3.5 block diagram [87].

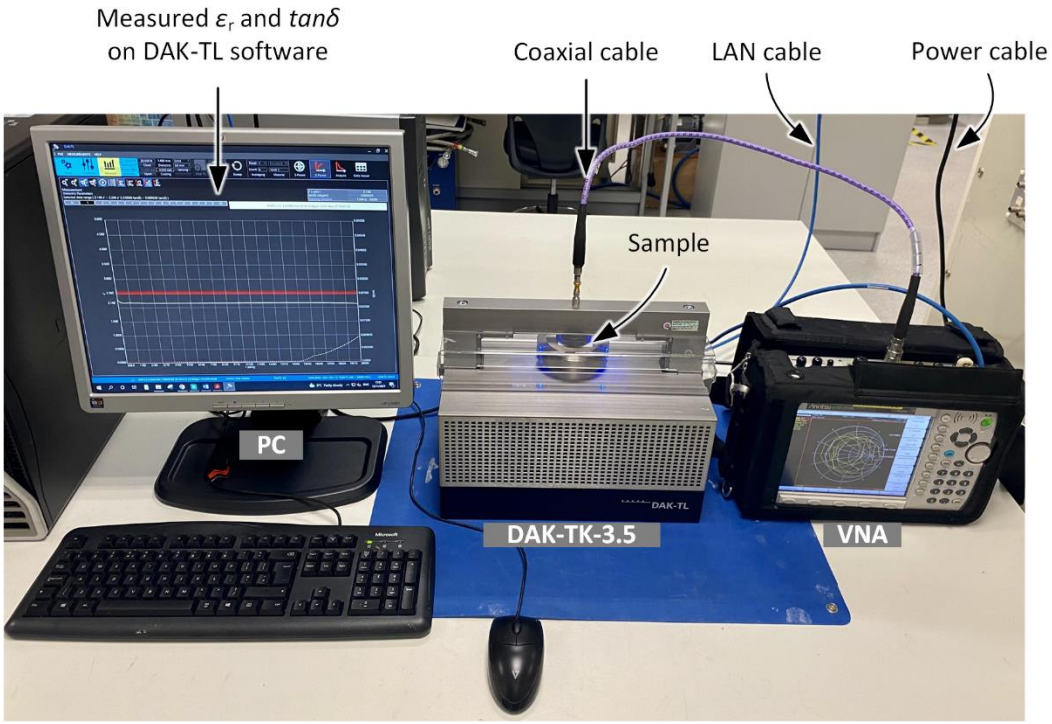


Figure 2.8: Dielectric measurement setup using a DAK-TL-3.5 system.

This system is fully automated and is suitable for the measurement of dielectric properties of materials with a thickness range of 0.1 to 10 mm over a frequency range of 200 MHz to 20 GHz.

In order to measure the dielectric properties of the sample material, the system is first calibrated by applying a short, open and load termination at the face of the coaxial probe. The system performs an automatic calibration from 200 MHz to 2 GHz. The dielectric material sample is then placed beneath the probe as shown.

The system then measures the frequency dependant dielectric properties (ε_r and tanδ). In this work, the measured dielectric properties for the ASA material were recorded as ε_r = 2.9 and tanδ = 0.033 at 915 MHz.

2.10 Conclusions

In this chapter, a brief introduction to the key antenna parameters that describe both the impedance and radiation performance of an antenna was presented. The key antenna parameters, such as reflection coefficient, antenna gain, impedance bandwidth, radiation efficiency and specific absorption rate (SAR) described have been used repeatedly in the remaining chapters of this thesis to characterize the performance of the developed antennas. The concept of the Hertzian dipole and the fundamental limitations of electrically small antennas (ESA) were also discussed. In addition, the popular techniques for the measurement of radiation efficiency, SAR and dielectric characterisation were also described. This chapter also described the effects of the presence of the human body in the immediate vicinity of an antenna. In Chapters 4, 5 and 6 of this thesis, variants of a planar inverted-F antenna (PIFA) topology have been realized for developing wristwatch antennas and in this chapter, the evolution of a PIFA from a monopole antenna was also outlined.

Chapter 3: Literature review

3.1 Background

This chapter presents a comprehensive review of the state-of-the-art in wrist-worn antennas reported in the literature. To begin, a brief introduction to state-of-the-art smartwatch devices is presented. A detailed review of the literature for wrist-worn antennas operating at different frequencies (e.g., 868 MHz, 915 MHz, 1575 MHz, 2450 MHz and 5200 MHz) is discussed with a particular focus placed on Sub-GHz wrist-worn antennas. A performance comparison of Sub-GHz wristwatch antennas is conducted to help identify areas for improvement for new antenna designs. Key design challenges associated with state-of-the-art Sub-GHz wristwatch antennas are also outlined and the need for developing new Sub-GHz wristwatch-integrated antenna designs are highlighted.

3.2 State-of-the-Art Smartwatch Devices

The Internet of Things (IoT) is a network of internet-connected physical objects that can contain embedded sensors, actuators and firmware to wirelessly communicate and exchange data with other wireless devices and systems over the internet [1]. In recent times, the demand for smart wearable devices is growing due to the increasing number of IoT applications in smart health monitoring, security, fitness tracking, localization and proximity alerting [5, 6]. In recent years, a variety of wearable devices such as smartwatches, wristbands, smart clothing and smart glasses are used as platforms to realize these applications [5, 27].

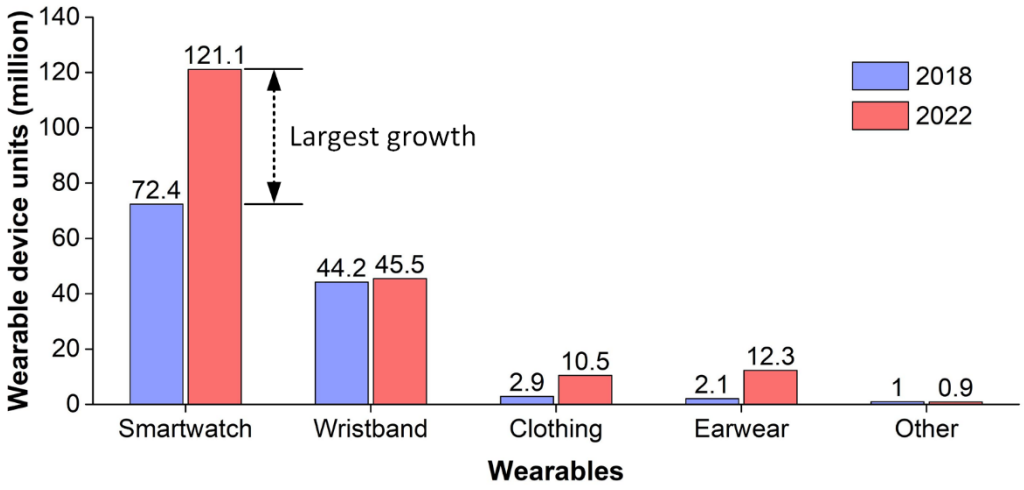


Figure 3.1: The market trend for global wearable devices from 2018 to 2022 [13].

In 2020, the market for smart wearable devices stood at 266.3 million units and is projected to reach 776.23 million units by the year 2026, that will represent a compound annual growth rate (CAGR) of 19.48 % during the period of 2021-2026 [88].

Figure 3.1 shows the global market trend for wearable devices from 2018 to 2022. It is observed that among the various existing wearable devices (e.g., smartwatches, wristbands, smart clothing and smart earwear), smartwatches are shown to have the largest growth with a growth of greater than 48 million units between 2018 to 2022. This is due to the fact that users are familiar with the concept of wearing wristwatches that can be worn conveniently on the human body. Such devices can be used to help users collect, analyze and wirelessly transfer personal data relating to health, navigation and workout activities [6]. Figure 3.1, in this context, shows that at the present time, smartwatches are the most preferred wearable IoT device amongst users and it is predicted that smartwatches will continue to dominate the global wearable market in the near future, i.e., "*the future global wearables market is all about the wrist*" [13].

As illustrated in Figure 3.2, smartwatches play a significant role in human activity monitoring for sleep and workout patterns as well as estimating health parameters such as heart rate and blood oxygen saturation (SpO_2) level and heart-related parameters using electrocardiogram (ECG) techniques [11, 12, 89]. Smartwatches enabled with sensing and wireless communication capabilities are becoming increasingly available as commercial products in a variety of configurations in recent times.

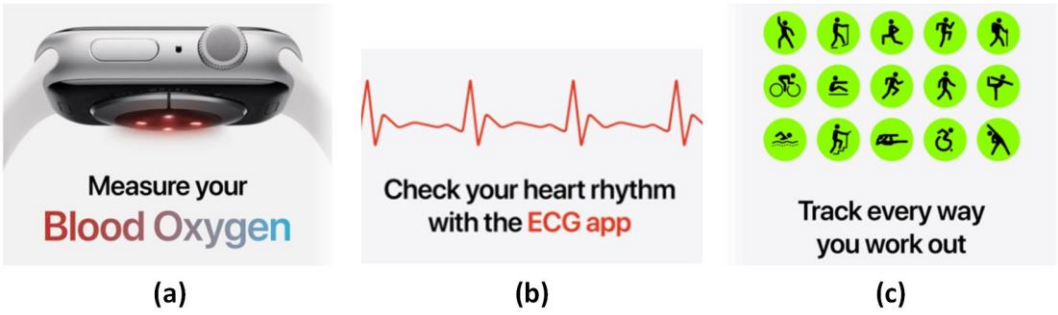


Figure 3.2: Application of smartwatches in everyday life [89]: (a) SpO_2 measurement, (b) electrocardiogram (ECG) monitoring, (c) Workout and activity tracking [89].

For example, the Huawei GT 2 Pro Watch [90], Apple watch series 6 [89], Garmin Vivoactive 4 [91], Fitbit sense [92], Samsung galaxy watch active [93] and Fossil Gen 5 [94] are some of the popular smartwatches available to users at the present time.

The wireless transmission and reception capabilities of smartwatches are made possible by using integrated radio transceivers and antennas. Because of the limited real-estate available within a typical wearable device, smartwatches generally incorporate a small battery with finite capacity [95]. The communication range of a wireless device depends on the antenna gain [53]. It was shown in Chapter 2 that a low efficiency antenna has reduced gain [65] with limited wireless communications range [53]. Maximizing antenna efficiency is therefore required to improve wireless communication range performance and extend battery lifetime [74].

3.3 Wearable Antennas

A wearable antenna can be described as an antenna that is designed to be incorporated in clothing or worn on the human body [27]. In recent years, wearable antennas have gained attention in a growing range of application domains, such as defence, security, healthcare, proximity alert, sports and fitness monitoring [5, 96].

Wearable antennas have key requirements to enable compact, flexible, conformal, low cost, lightweight and seamless antenna integration into wearable devices. To ensure the users' convenience and comfort, it is desired to have a small, compact form factor for such wearable devices.

For instance, a point of reference would be the Apple Watch Series 6 [89] smartwatch, a leader in the market in 2021. This watch device measures 44 mm × 38 mm × 10.7 mm. Small form factors for these devices are very desirable features for users. Therefore, high levels of integration are required to implement such devices, with decreasing space available to integrate key components such as antennas. This creates a requirement to integrate electrically small antennas. However, as discussed in Chapter 2, electrically small antennas have fundamental performance limitations in terms of impedance bandwidth, antenna gain and radiation efficiency [31].

It is challenging to design high-performance antennas that can be accommodated within a small sized device, in particular at lower frequencies. In addition, as also discussed in Chapter 2, the design of wearable antennas is further complicated by the presence of the human body. The presence of the human body in close proximity to the antenna can lead to EM energy absorption in the body tissues that can lead to a reduction in antenna gain and radiation efficiency [32, 33].

3.4 Frequency of Operation for Wrist-Worn Antennas

In the literature, wrist-worn antennas are reported that operate in a range of frequencies, and for the purposes of this review, these antennas have been categorised under two categories, namely (a) wrist-worn antennas for Sub-GHz bands and (b) wrist-worn antennas for frequencies above 1 GHz. The Sub-GHz bands category includes wristwatch antennas for the following frequencies: 13.56 MHz (Industrial, Scientific and Medical; ISM) [97], 402–405 MHz (Medical Implant Communication System; MICS) [40], 433 MHz (ISM), 868 MHz (ISM in Europe) [41] and 915 MHz (ISM in North America) [28]. Wrist-worn antennas for frequencies above the 1 GHz category include antennas for the following frequencies: 1.575 GHz (Global Positioning System; GPS) [98], 2.45 (ISM; IEEE 802.15.1, IEEE 802.15.4 and IEEE 802.11a/b/g) [99], 5.2 GHz (IEEE 802.11a/b/g) [100], 5.8 GHz (ISM; IEEE 802.11ac) [98] and 3.1–10.6 GHz (Ultra Wide Band; UWB) [101]. In the following section, a review of the previous related research on the design of wrist-worn antennas operating at frequencies above 1 GHz is presented.

3.5 Wrist-Worn Antennas for Frequencies above 1 GHz

The majority of wrist-worn antennas reported in the literature are designed to operate at frequencies above 1 GHz (e.g., 1.575 GHz, 2.45 GHz, 5.2 GHz and 5.8 GHz) because of the widespread availability of GPS, Bluetooth and Wi-Fi wireless technologies. In recent years, a variety of antenna topologies have been reported for use in wrist-worn devices. These antenna topologies include dipoles [99, 102], monopoles [100], loops [103], slots [29, 104], Inverted-L antennas (ILA) [98, 100], planar Inverted-F antennas (PIFA) [105, 106] and a combination of two or more antenna topologies [107].

Dipole antennas are popularly used in bracelet-based wireless devices [99], where the radiating elements of a dipole can be incorporated into the strap and extended to meet the half-wavelength requirement of a dipole at the operating frequency. For example, as shown in Figure 3.3, a 3-D printed conformal diversity antenna is reported in [99]. This diversity antenna solution consists of three dipole-type antennas with two resonant arms. Each dipole arm has two sections: the longer section of length L = 24 mm is resonant at 2.4 GHz and the shorter section of length S = 9 mm is resonant at 5.5 GHz. The metallic layers of the diversity antennas are deposited on a polylactic acid (PLA) bracelet of 70 mm diameter. The -10 dB impedance bandwidth of this antenna system ranges from 2.24 GHz to 3.14 GHz for the lower band and from 4.6 GHz to 7 GHz for the higher band. Furthermore, this diversity antenna achieves an on-phantom measured peak realized gain of 2.0 dBi and 1.3 dBi at 2.4 GHz and 5.5 GHz, respectively [99].

Inverted-L antennas (ILA) in conjunction with parasitic elements have also been widely used for smartwatch devices operating at 1.575 GHz, 2.4 GHz, 5.2 GHz and 5.8 GHz [98, 100].

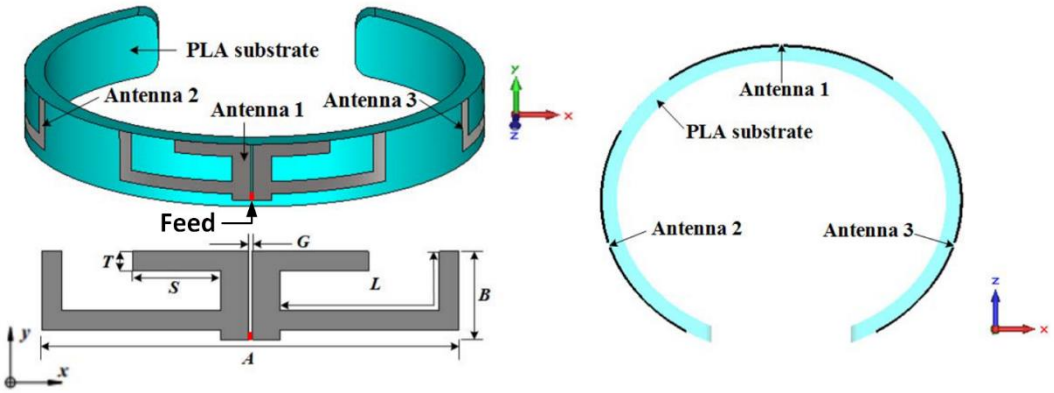


Figure 3.3: 2.4/5.5 GHz 3-D Printed diversity bracelet antenna [99].

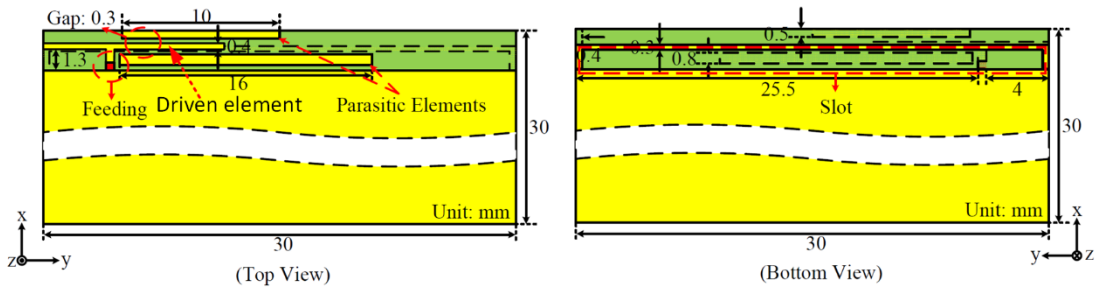


Figure 3.4: Dual-band, 2.4 and 5.2 GHz smartwatch antenna structure [100].

For example, as shown in Figure 3.4, a T-shaped dual-band planar smartwatch ILA with a total size of 30 mm × 30 mm is reported in [100]. The antenna operates in the 2.4 and 5.2 GHz frequency bands and incorporates two parasitic elements on the top layer and a slot on the bottom layer of an FR-4 substrate. The parasitic elements are excited via mutual coupling with the driven element and create two adjacent resonant frequencies to enhance the impedance bandwidth for both the 2.4 and 5.2 GHz bands. The enhanced impedance bandwidth makes the wristwatch antenna more robust to variations arising from different users and wrist-antenna spacing, which can affect the input impedance of the antenna [33]. The two adjacent resonant frequencies in the 2.4 GHz band are located respectively at 2.4 and 2.5 GHz, and in the 5.2 GHz band, the two resonant frequencies are located at 5.2 and 5.35 GHz. The slot in the ground plane mainly controls the S_{11} magnitude for both bands. This antenna achieves a -10 dB impedance bandwidth of 160 MHz for the 2.4 GHz band and 230 MHz for the 5.2 GHz band.

As shown in Figure 3.5(a), a multi-band (1.575, 2.4, 5.2 and 5.8 GHz) smartwatch ILA is reported in [98], which is printed on a 0.5 mm thick FR-4 substrate with a total size of 30 mm × 30 mm. This antenna incorporates a parasitic element on the back side of the substrate that enhances the impedance bandwidth by exciting two adjacent resonant frequencies at 1.6 and 2.45 GHz in the lower band, and 5.0 and 5.9 GHz in the upper band. This ILA reports a -6 dB impedance bandwidth of 1.21 GHz for the lower band and 1.81 GHz for the upper band and achieves a peak realized gain of -3.9 dBi and a radiation efficiency of 86.8 % at 1.575 GHz in free-space.

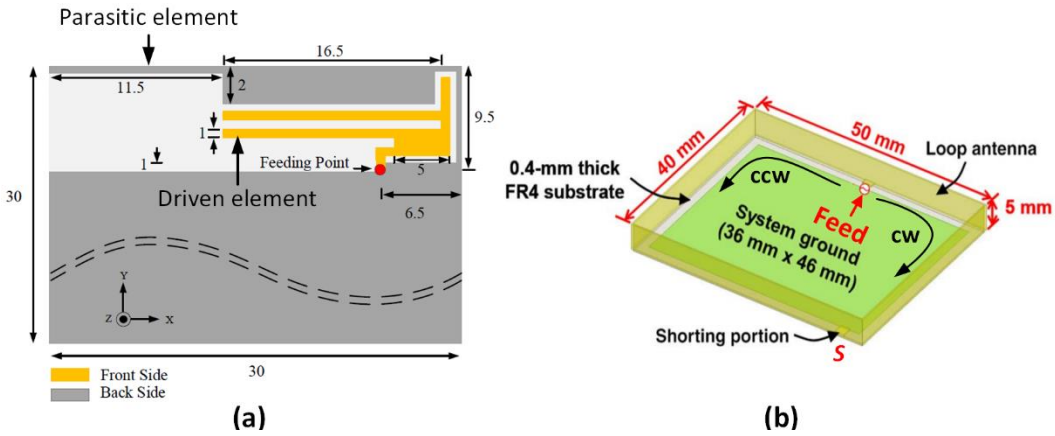


Figure 3.5: Antennas structures: (a) Multiband (1.575, 2.4, 5.2 and 5.8 GHz) smartwatch antenna [98], (b) 2.4 GHz metal frame wristwatch loop antenna [103].

Metal frame antennas are another commonly used solution for wristwatch devices operating above 1 GHz (e.g., 1.575, 2.4 GHz) because the metallic frame itself can be made resonant, with no additional space requirement for antenna integration [103, 104]. An example of a metal frame loop antenna is shown in Figure 3.5(b), where the antenna has a total size of 50 mm × 40 mm × 5 mm and is designed for 2.4 GHz Bluetooth operation [103]. The antenna is fed using a balanced feed and the loop structure is shorted to the ground system at point *S*. Starting from the feed port, as depicted in Figure 3.5(b), the shorting location is placed at a one-wavelength distance at 2.4 GHz, clockwise or counter-clockwise from the feed point location. The location of the shorting portion determines the one-wavelength current path required for resonance and the resonant frequency of the antenna can be tuned by varying the position of the shorting portion. This metal frame loop antenna achieves a -10 dB impedance bandwidth of approximately 160 MHz, a peak realized gain of -0.89 dBi and a radiation efficiency of 26 % at 2.442 GHz.

Slot antennas are also used for wristwatch applications [29, 104]. A slot antenna uses a half-wavelength long slot cut on a conductive metal sheet and operates in an analogous manner to a linear dipole antenna [72]. The main advantages of a slot antenna are that it is simple to fabricate and has a low profile. A slot antenna inherently radiates equally on both sides of the conductive metal sheet on which the slot is cut [72]. However, for wristwatch applications, a loop antenna is desired not to radiate towards the human wrist as it can lead to EM energy absorption in the wrist.

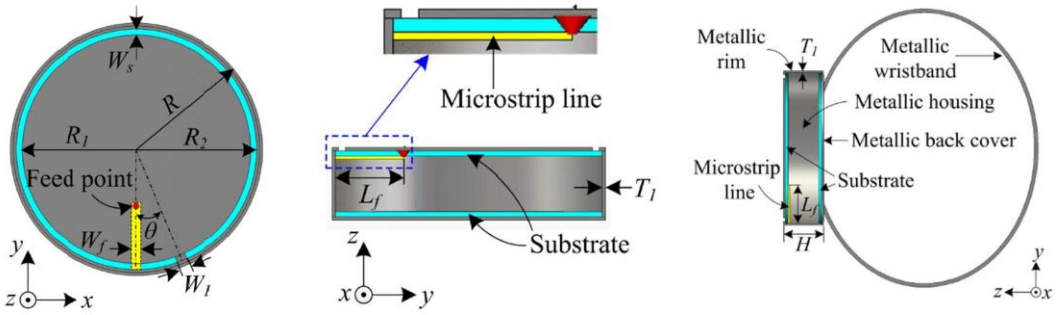


Figure 3.6: Geometry of the 2.4 GHz cavity-backed annular slot antenna [29].

The radiation towards the human wrist is alleviated in the reported case by including a metallic cavity or a reflective conductive sheet at the back of the slot to suppress backward radiation and the resulting structure is called a cavity-backed slot antenna [108]. A cavity-backed annular slot smartwatch antenna designed for 2.45 GHz Bluetooth and Wi-Fi applications is reported in [29] and shown in Figure 3.6. This cavity-backed annular slot antenna is cylindrical in shape and occupies a total volume of $\pi \times 21^2 \times 10$ mm^3. The top and bottom surfaces of the cavity are realized using a 0.8 mm thick Rogers 4050B substrate [29]. Along the top surface of the metallic cavity, an annular slot with a width W_S = 1 mm is created and the inner portion of the slot is shorted to the system ground using a shorting strip of width W_1 = 1.7 mm. The slot antenna is fed with a 50 Ω unbalanced microstrip feed line that is printed on the opposite side of the top substrate and the angle Θ between the microstrip feed line and shorting strip mainly determines the resonant frequency of the antenna. This annular slot antenna reported in [29] shows a -10 dB impedance bandwidth of approximately 80 MHz, a peak realized gain of 2.6 dBi and a radiation efficiency of 66 % at 2.45 GHz.

It was described in Chapter 2 that the specific absorption rate (SAR) is a measure of the rate at which RF power is absorbed by the human body when exposed to electromagnetic (EM) radiation [78]. The RF power absorption is potentially harmful to the human tissue and a maximum permissible limit of the SAR value is defined by the Federal Communications Commission (FCC) [109] and the International Commission on Non-Ionizing Radiation Protection (ICNIRP) guidelines [80]. For example, for wrist-worn wireless devices, the SAR level should not exceed a limit of 4.0 W/kg averaged over 10 g of wrist tissue, as defined by FCC and ICNIRP guidelines [80, 109].

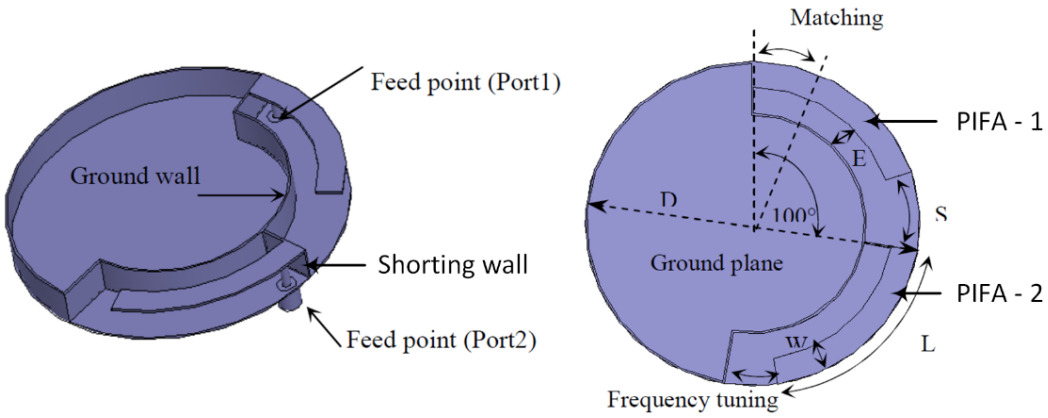


Figure 3.7: Two element MIMO PIFA wristwatch antenna [106].

The annular slot antenna [29] shown in Figure 3.6 demonstrated a low 10 g SAR figure of 0.0365 W/kg, for 15.8 dBm input power to the antenna, making the antenna a good candidate for practical wearable applications.

Planer Inverted-F antennas (PIFA) are another commonly used solution for wristwatch applications mainly because of their potential to be realized in a compact form factor and their ability to reduce the backward radiation towards the human wrist due to the use of a finite size ground plane between the radiator and human tissue [28, 110, 111].

An example of a circular-type PIFA wristwatch antenna is shown in Figure 3.7 where the design in which a MIMO antenna system using two curved PIFAs is reported [106]. The wristwatch device operates in the 2.45 GHz Wi-Fi band (2.4-2.483 GHz) and has a total volume of $\pi \times 25^2 \times 5$ mm^3. Each individual PIFA is fed by a 50 Ω coaxial cable and is connected to the ground plane by a shorted wall of width $W + E$. The second PIFA is tilted by 100° relative to the first one so as to reduce the mutual coupling between the radiating elements and the vertical curved ground plane is used to improve the isolation between the two ports. The resonant frequency of the antenna can be tuned by adjusting the length of the individual radiating elements, while the impedance matching can be improved by varying the position of the feed point relative to the shorted wall. This PIFA antenna achieves a -10 dB impedance bandwidth of approximately 160 MHz, a peak realized gain of -2.4 dBi and a radiation efficiency of 44 % at 2.45 GHz.

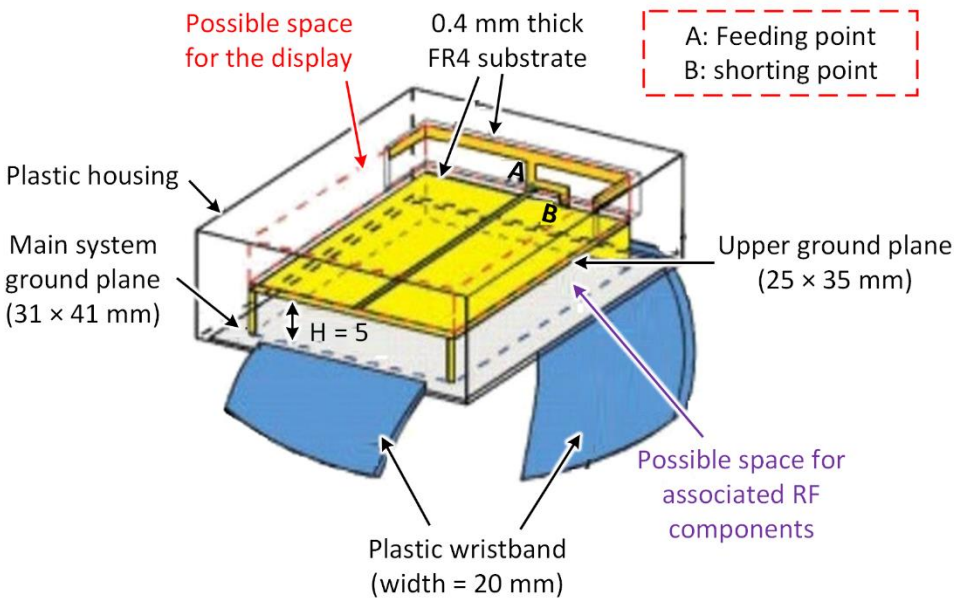


Figure 3.8: Configuration of the internal shorted monopole (IFA) antenna [105].

Figure 3.8 shows a 2.4 GHz internal shorted monopole or inverted-F antenna (IFA) embedded within a wristwatch plastic enclosure [105]. The antenna is printed on a 0.4 mm thick FR-4 substrate with overall dimensions of 43 mm × 33 mm × 10 mm, including the enclosure. The antenna consists of two ground planes, with a 50 Ω microstrip feed line printed on the opposite side of the upper ground plane. This antenna is fed at point *A* and a shorting section between points *A* and the upper ground plane at point *B* is used for impedance matching. The resonant frequency of this antenna can be tuned by adjusting the end lengths of the T-shaped monopole to obtain resonance at 2.4 GHz. This IFA antenna achieves a -10 dB impedance bandwidth of approximately 270 MHz and a radiation efficiency of 50 % at 2.442 GHz.

High impedance surfaces (HIS) have been employed for wristwatch antennas to improve radiation performance by minimizing the power radiated towards the human wrist [112, 113]. A HIS structure is designed in such a way that the image current in the HIS flows in-phase and parallel to the original current in the radiating antenna element and thereby a HIS minimizes the radiation towards the human wrist [112].

An example of a 2.4 GHz wristwatch antenna designed using a miniature HIS is shown in Figure 3.9, where the antenna, including the HIS structure occupies a total volume of 38 mm x 38 mm x 3 mm [112]. The antenna stackup in [112] consists of two structures, both printed on FR-4 substrates and separated by a 0.6 mm thick foam insulator.

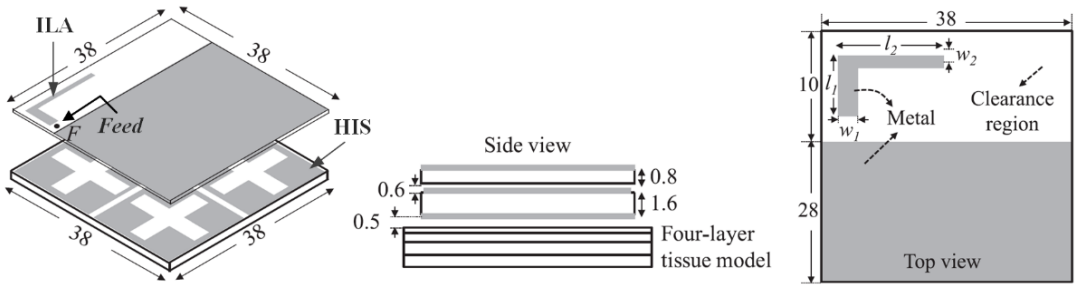


Figure 3.9: A low profile 2.4 GHz smartwatch ILA antenna using a miniature high impedance surfaces (HIS) structure [112].

The top structure of the antenna represents an Inverted-L antenna (ILA), while the bottom structure represents a compact-size HIS comprising a grid of 2 x 2 unit-cells. The ILA element does not have a conductor on the opposite side; however, the HIS structure is backed by a conductive sheet. As explained above, the HIS structure ensures that the antenna radiates away from the human wrist and makes the antenna robust against the dielectric loading effect due to nearby human tissue [112]. This ILA achieves a -10 dB impedance bandwidth of approximately 400 MHz, a peak realized gain of 2.2 dBi and a radiation efficiency of 39 % at 2.4 GHz. The use of a HIS structure reduces the SAR level from 13.5 W/kg (without HIS) to 0.29 W/kg, i.e., more than 90 % reduction in SAR.

To summarize, in the above section, several wrist-worn antennas operating at frequencies above 1 GHz (e.g., 1.575 GHz, 2.4 GHz, 5.2 GHz and 5.8 GHz) are reviewed. It is observed that the dipole topology is mostly used for wristband and bracelet antennas because the radiating elements can be extended to the strap to meet the half-wavelength requirement for a dipole [99]. Metal frame loop [103], slot [29] and ILA [98, 100] antennas have also been used for wristwatch applications. At 2.4 GHz, cavity-backed annular slot [29] and metal frame loop antennas were developed; however, these antennas required a perimeter of one-wavelength at the nominal operating frequency, which is substantial for a practical size Sub-GHz wristwatch (e.g., 328 mm at 915 MHz). It is observed that PIFA and IFA are the most widely used antenna topologies for wristwatch applications mainly because of their potential to be realized in a compact form factor along with their capability to reduce backward radiation towards the human wrist (i.e., reduced SAR) due to the use of a finite size ground plane [28, 110, 111].

At higher frequencies greater than 1 GHz (e.g., 2.45 GHz, 5.2 GHz, 5.8 GHz), parasitic elements have been used for wristwatch antennas to achieve enhanced impedance bandwidth by exciting dual resonant modes [98, 100]. High impedance surface (HIS) structures have also been employed at 2.45 GHz to improve the performance of a wristwatch antenna by ensuring that the image current in the HIS flows in-phase and parallel to the original current distribution in the radiating element thereby minimises the power radiated towards the human wrist [112]. However, the HIS structure is electrically large and is not practical for realization in a compact, practical-size wristwatch device operating at Sub-GHz frequencies.

3.6 Wrist-Worn Antennas for Sub-GHz Bands

The use of Sub-GHz frequencies for wearable systems have received increased interest due to the emergence of wireless technologies such as LoRaWAN [15] and SigFox [16] that have the potential for long-range wireless communications with low power operation and increased battery life [25, 28, 53]. Therefore, in this section a detailed review of the state-of-the-art Sub-GHz wrist-worn antennas is presented.

Figure 3.10 depicts the number of research papers reporting the use of Sub-GHz wrist-worn antennas over the last four decades in this very active research domain. To the author's knowledge, one of the first Sub-GHz wrist-worn antenna was reported in the literature in 1984 [114]. This was a wristwatch radio device designed to operate in the FM frequency band (88 – 108 MHz) [115]. This device implemented a loop antenna topology and was embedded in the watch strap to receive the weather information.

It can be seen from Figure 3.10 that the last decade has witnessed a growing interest in the development of Sub-GHz wrist-worn antennas. This is mainly because of emerging wireless technologies, such as LoRaWAN and SigFox that operate at Sub-GHz band frequencies (e.g., 868, 915 MHz) [17, 18]. In this section, a comprehensive review of wrist-worn antennas operating at Sub-GHz band frequencies (e.g., f_0 = 403 MHz, 868 MHz and 915 MHz) is presented.

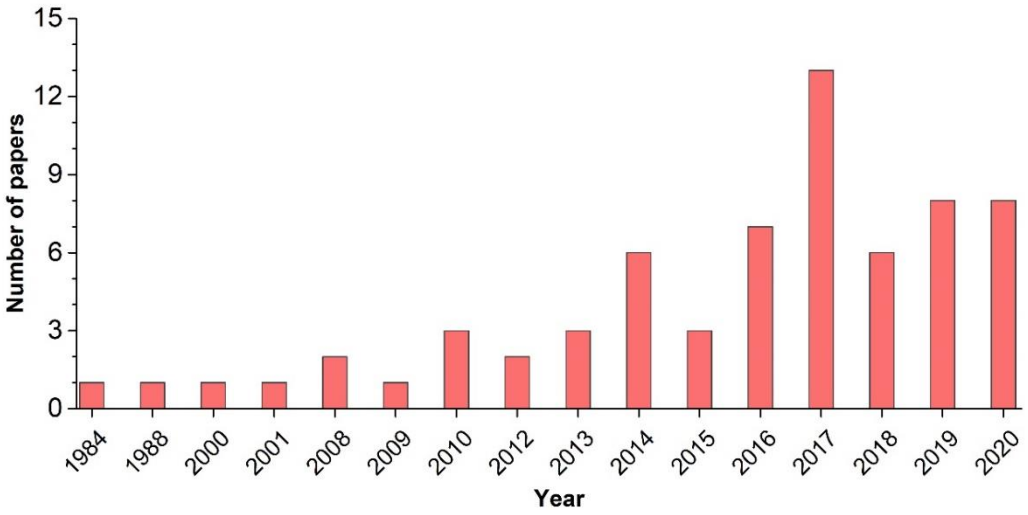


Figure 3.10: Number of Sub-GHz wrist-worn antennas reported in the literature.

Different variants of dipole and monopole antennas have been used for wrist-worn applications, as shown in Figure 3.11. For a wrist-worn dipole antenna, the radiating element can be incorporated into the wristband of a watch/bracelet in order to take advantage of the additional real-estate provided by this configuration [45].

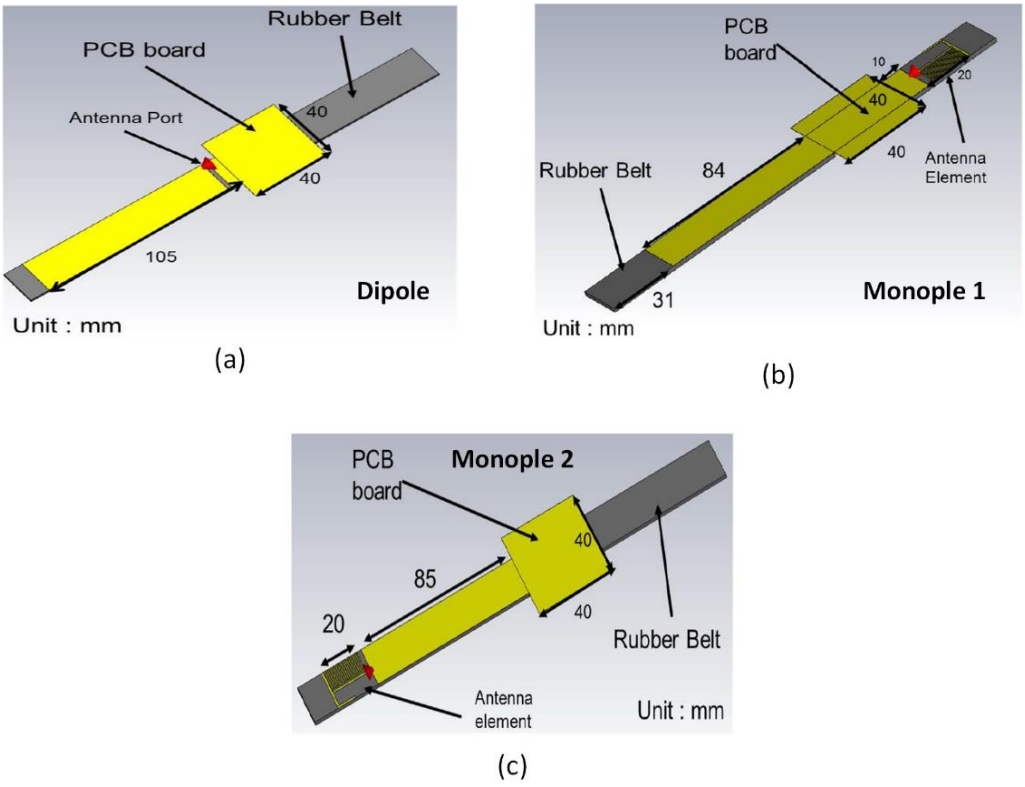


Figure 3.11: Geometry of the wristwatch antennas [45]: (a) Dipole antenna, (b) Monopole antenna 1 and (c) Monopole antenna 2.

For example, in [45], a dipole and two types of monopole smartwatch antennas using a metallic strap operating in the frequency range 0.7 GHz to 2.7 GHz are presented. As shown in Figure 3.11, all antenna designs are realized using a copper metallic strip that is integrated into the rubber strap. The two dipole arms are formed using the metal conductor integrated in the strap and also the PCB board ground-plane, as shown in Figure 3.11(a). Monopole 1 and monopole 2 have a similar configuration, but are realized at different locations on the rubber belt, as shown in Figure 3.11 (b and c). The dipole antenna shows a -10 dB impedance bandwidth of approximately 160 MHz at a frequency f_0 = 750 MHz, but the dipole has a radiation efficiency of less than 9 % at 750 MHz and less than 6.3 % at 900 MHz. The close proximity of the radiating elements to the lossy human wrist tissue leads to an absorption of RF power in the human body and therefore limits the radiation efficiency of the antenna.

As mentioned in Chapter 2, specific absorption rate (SAR) is a measure of the rate at which RF power is absorbed by the human body when exposed to EM radiation [78]. For 24 dBm input power, the dipole antenna in [45] demonstrated a 10 g SAR value of 0.18 W/kg at 900 MHz, which is less than 5 % of the maximum limit of 4.0 W/kg [79, 80]. An example of a monopole wrist-worn conformal bracelet antenna designed to operate at 850 MHz is shown in Figure 3.12 [44]. This antenna is printed on a 0.035 mm thin, flexible Kapton substrate with ε_r = 3.8 and is mounted on a 2 mm thick Acrylonitrile Butadiene Styrene (ABS) plastic bracelet with ε_r = 2.8. This monopole bracelet antenna [44] achieves a -10 dB impedance bandwidth of approximately 160 MHz, with a peak realized gain of -8.3 dBi and a radiation efficiency of 7 % at 850 MHz.

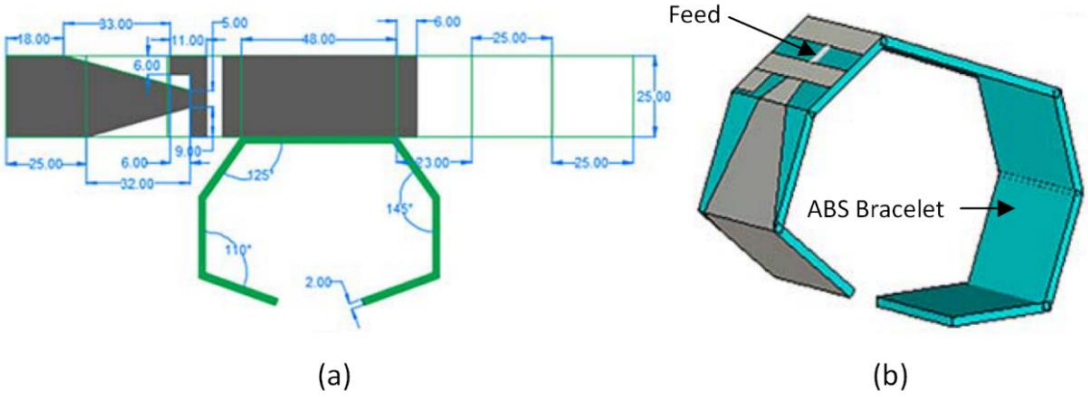


Figure 3.12: (a) Configuration of the monopole antenna on a flexible substrate, (b) Arrangement when the antenna is mounted on an ABS bracelet [44].

In addition, for 23 dBm input power, the antenna in [44] exhibits a 10 g SAR value of 3.75 W/kg at f_0 = 850 MHz. This high SAR value is attributed to the closeness (2 mm) of the antenna to the lossy human wrist tissue.

Loop antennas have also been employed for Sub-GHz wristwatch applications. For instance, in [43], a cellular metal frame loop antenna is reported and is shown in Figure 3.13(a). The antenna operates in two frequency bands (880–960 MHz and 1500–2200 MHz) with a total dimension of 40 mm × 30 mm × 10 mm. As shown in Figure 3.13(a), the grounding points for low band grounding denoted LG and high band grounding denoted HG are used to control the resonant frequencies of the antenna. The low band mode (880–960 MHz) has a half-wavelength resonant length measuring from feed to point LG through HG. In the low band, the antenna exhibits a -10 dB impedance bandwidth of 180 MHz, but at the cost of low radiation efficiency of less than 6 % at f_0 = 920 MHz.

As shown in Figure 3.13(b), a variant of a loop antenna using an annular ring, in conjunction with two rectangular patches for 915 MHz wristwatch applications is reported in [47]. The annular ring is internally loaded with two rectangular patches to lower the resonant frequency and to improve the impedance matching of the antenna The antenna shown in Figure 3.13(b) is made from a copper sheet and is placed 3 mm away from a simplified cylindrical human phantom model of a radius of 26 mm. This antenna achieves a -10 dB impedance bandwidth of approximately 100 MHz, with a peak realized gain of -8 dBi at the resonant frequency, f_0 = 915 MHz.

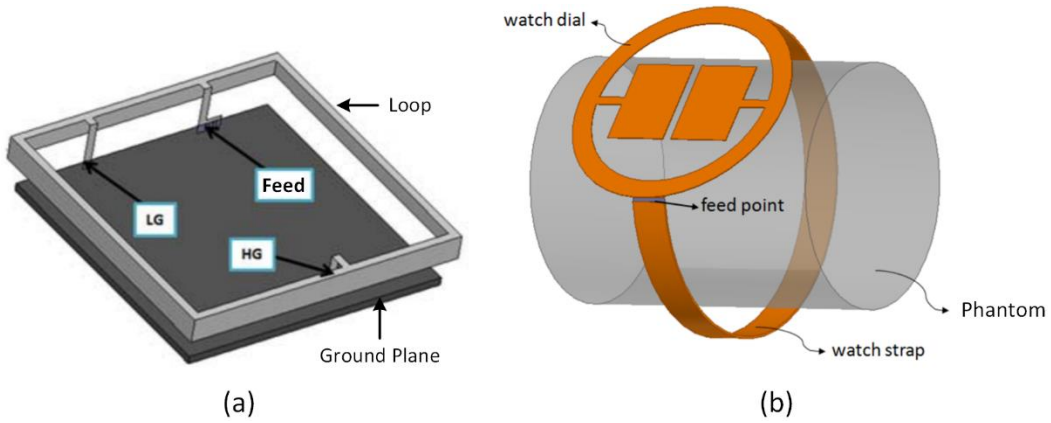


Figure 3.13: (a) Metal frame loop antenna [43], (b) Configuration of the wristwatch antenna reported in [47].

Microstrip patch antennas have also been used for Sub-GHz wristwatch antennas. For example, a low profile flexible 915 MHz RFID-tag slotted patch antenna is presented in [34] and depicted in Figure 3.14. The geometry of the proposed antenna is shown in Figure 3.14(a-b) and Figure 3.14(c) shows the arrangement when the antenna is attached to a human wrist. The bottom conductive surface (ground plane) of the PVC flexible substrate is metalized with adhesive copper tape that is shorted to the two rectangular copper areas on the left and right sides of the top of the PVC substrate. The copper shapes on the top surface of the PVC substrate are then soldered to the left and right edges of the slotted patch, as shown in Figure 3.14(b). Two T-shaped slots have been etched on a 0.4 mm FR-4 substrate that is placed on a 1.4 mm thick foam substrate. Varying the physical parameters (S_l, S_w and S_g) of the T-shaped slots affects the input impedance to provide conjugate matching for the tag chip and adjust the resonant frequency of the antenna.

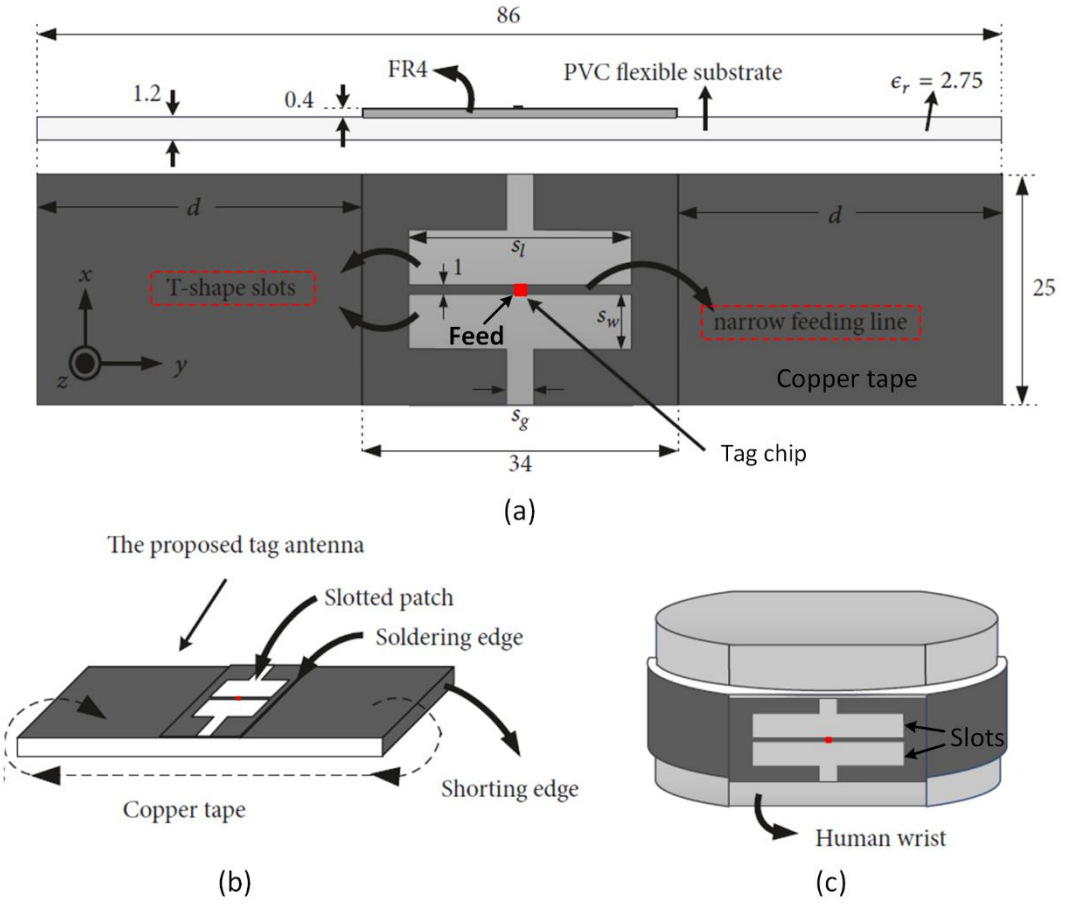


Figure 3.14: (a) Geometry of the proposed 915 MHz RFID tag antenna, d = 26, S_l = 24, S_W = 6, S_g = 3, Unit: mm, (b) Antenna attached to a human wrist [34].

This RFID tag antenna achieves a -10 dB impedance bandwidth of 19 MHz, which does not meet the required impedance bandwidth of 26 MHz for 915 band operation [55]. At f_0 = 915 MHz, this antenna achieves a peak realized gain of -6.87 dBi. This antenna is designed to work when integrated into a wristband and is not ideal for integration into a practical size wristwatch device where the antenna is not envisaged to be part of the strap.

Planar inverted-F antennas (PIFA) are the most widely used topology for Sub-GHz wristwatch antennas because of their suitability for integration in low-profile, compact size wristwatch devices. In addition, the ground plane of the PIFA acts as a shield for backward radiation towards the human wrist and minimizes the losses associated with human wrist tissue [40, 65].

A wrist-worn dual-band diversity PIFA antenna operating at 880 MHz and 1.8 GHz is reported in [50]. As shown in Figure 3.15(a), the antenna comprises two PIFA-type radiating patches (Radiating patch 1 and 2), where dual-resonant operation is achieved by creating an L-shaped slot in the radiating patches. Both the radiating elements share a common ground plane and a gap in the ground plane is used to improve the isolation between the two radiating elements. This antenna has a -10 dB impedance bandwidth of 28 MHz and achieves a radiation efficiency of 83.7 % at 880 MHz. However, the antenna has a large size of 188 mm × 30 mm × 6 mm and is not an ideal solution for the integration into a practical wristwatch device.

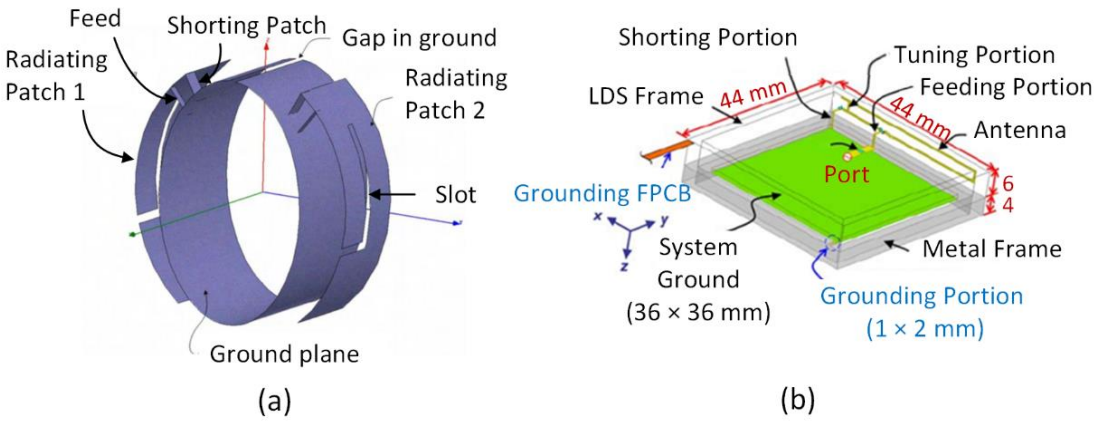


Figure 3.15: (a) Diversity PIFA antenna [50], (b) Metal frame PIFA antenna [49].

A watch frame PIFA antenna capable of operating in the 746–787 MHz and 1710–2170 MHz bands is reported in [49]. As shown in Figure 3.15(b), the wristwatch frame of the antenna comprises a top metal and a bottom laser direct structure (LDS) frame, together occupying a total volume of 44 mm × 44 mm × 6 mm. The antenna is printed inside the LDS frame made of plastic with a relative electrical permittivity ε_r = 2.92 and a loss tangent $tan\delta$ = 0.007 and the metallic part of the frame is connected to the PCB system ground. For this antenna, the lower frequency band (746–787 MHz) operation is achieved by the LDS antenna in conjunction with the grounding flexible printed circuit board, denoted FPCB (connected to the metal frame) and an impedance matching capacitor. On the other hand, the higher frequency band operation (1710–2170 MHz) was accomplished with the help of a position adjustable tuning portion. This watch frame PIFA antenna achieves a -10 dB impedance bandwidth of 35 MHz by incorporating a lumped capacitor (3.9 pF) in series with the feedline to match the input impedance of the antenna. This antenna has a peak realized gain of -5.4 dBi and a radiation efficiency of 13 % at f_0 = 767 MHz.

As shown in Figure 3.16, a wrist wearable three-antenna system for long term evolution (LTE) cellular and global positioning system (GPS) applications is reported [42]. The antenna system is integrated within an ABS plastic enclosure with ε_r = 2.7 and $tan\delta$ = 0.005. The antenna geometry measures a total size of 93 mm x 37 mm x 5 mm. The ground of the chassis is extended to the wristband of the watch device in order to increase the electrical length of the antenna (ANT1) and incorporates a matching circuit to achieve resonance for LTE low-band (699-862 MHz) operation.

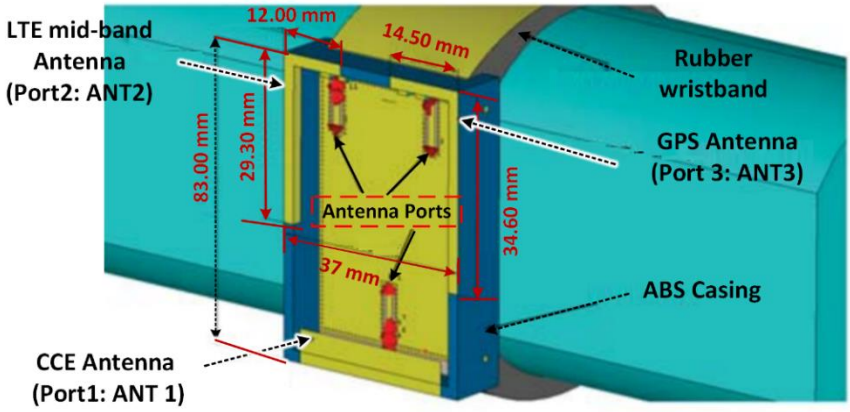


Figure 3.16: Configuration of the three-antenna system [42].

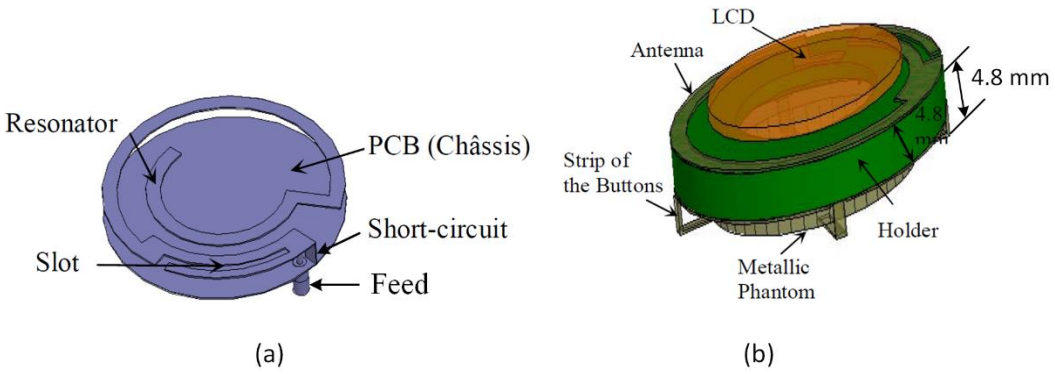


Figure 3.17: (a) Antenna structure, (b) Configuration of the casing watch [40].

The two Inverted-F antennas located on the top edge of the wristwatch case, denoted ANT2 and ANT3 in Figure 3.16, are used for the LTE mid-band (1710-2155 MHz) and GPS bands (1563-1605.7 MHz), respectively. The LTE low-band antenna (ANT1) has a radiation efficiency of 7.9 % at 780 MHz and achieves a -10 dB impedance bandwidth of 105 MHz using an impedance matching network.

A spiral-shaped PIFA antenna for the MICS band (402-405 MHz) and Bluetooth (2.4-2.483 GHz) applications is reported in [40]. As shown in Figure 3.17(a), the antenna has a circular ground plane with a spiral resonator located 5 mm above the ground plane. The total spiral length is approximately one quarter-wavelength at 402.5 MHz and a quarter-wavelength slot on the surface of the radiator is added to excite a resonance at 2.4 GHz. In Figure 3.17(b), the configuration of the wristwatch case is depicted, where the holder of the antenna is made of Epoxy FR-4 substrate with $\varepsilon_r = 4.4$, $tan\delta = 0.01$ and the LCD is made of a silicon substrate with $\varepsilon_r = 11.9$. When placed on the user's arm, the proposed antenna shows a -6 dB impedance bandwidth of 5.2 MHz, a peak realized gain of -12 dBi and a radiation efficiency of 3.6 % in the MICS band.

As shown in Figure 3.18, a grounded coplanar waveguide (GCPW) fed meandered 915 MHz PIFA antenna for wristwatch applications is reported in [28]. The antenna is realized using a standard FR-4 substrate material and has a compact size of 44 mm × 28 mm × 1.6 mm. This antenna achieves a peak realized gain of -6.1 dBi at 915 MHz and with the help of a π-type matching network, a -10 dB impedance bandwidth of 55 MHz is achieved.

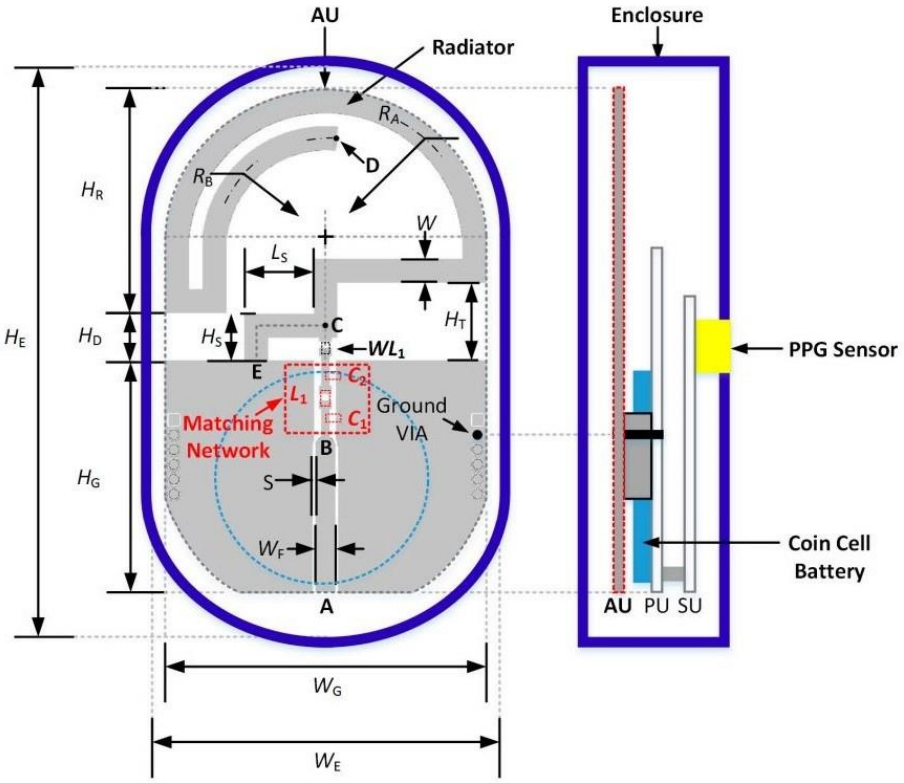


Figure 3.18: Geometry of the meandered 915 MHz PIFA [28].

Figure 3.19 shows an inverted-F type wristwatch antenna operating in the 810–960, 1370–1450 and 1710–2630 MHz bands [46]. The proposed antenna has multiple radiating elements that are excited at different resonant frequencies, including 866 MHz, 1437 MHz, 1960 MHz and 2300 MHz. At 866 MHz, the antenna exhibits a -10 dB impedance bandwidth of approximately 105 MHz, a peak realized gain of -4.4 dBi and a radiation efficiency of 26 %.

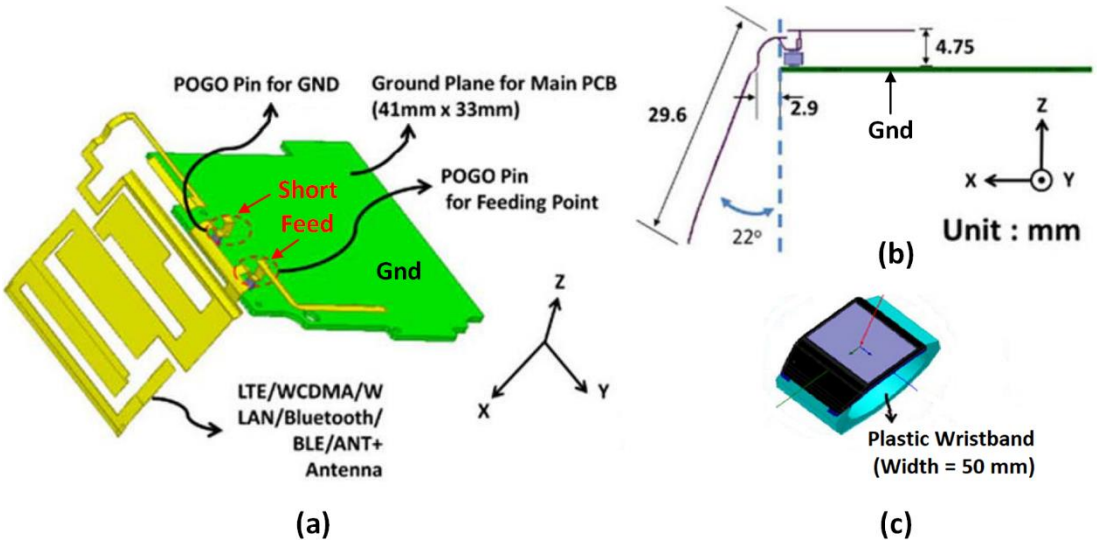


Figure 3.19: (a, b) Configuration of the wristwatch IFA, (c) Wristwatch model [46].

Furthermore, for 22.96 dBm input power, this antenna exhibits a 10 g SAR value of 0.78 W/kg at 836.5 MHz. However, the radiating part of the antenna in [46] is extended to the strap of the wristwatch device. Note that the width of the watch strap also has a wide dimension of 50 mm, which is not ideal for a practical wristwatch device in terms of comfort.

3.7 Performance Comparison of State-of-the-Art Sub-GHz Wrist-Worn Antennas

Table 3.1 summarizes the key performance characteristics of the 23 state-of-the-art Sub-GHz wrist-worn antennas discussed in detail in Section 3.6. Note that all the antennas listed in Table 3.1 were characterised using a phantom arm; however, the dielectric constant (ε_r) and electrical conductivity (σ) of the phantom arms used are different for different antennas. For instance, the phantom arm model used for the antenna in [28] has ε_r = 32.5, σ = 0.5 S/m, and the phantom arm used in [34] has ε_r = 41.3, σ = 0.87 S/m at 915 MHz.

For the ease of reading, each reference is assigned a row number.

In Table 3.1, the columns denoted (A) to (I) respectively include, row number, publication reference, antenna topology, antenna dimensions (*L* = length, *W* = width, *h* = height in mm), f_0 = resonant frequency in MHz, *BW* = measured -10 dB impedance bandwidth in MHz, Gain = measured peak realized gain in dBi at f_0, η = measured radiation efficiency in % at f_0 and SAR = simulated specific absorption rate in W/kg at f_0.

Table 3.1: On-phantom performance of state-of-the-art Sub-GHz wrist-worn antennas.

A	B	C	D			E	F	G	H	I
Row	Ref.	Antenna Topology	Dimensions (mm)			f_0 (MHz)	-10 dB *BW* (MHz)	*Gain* (dBi) @ f_0	*h* (%) @f_0	*SAR* (W/kg) @f_0
			L	*W*	*h*					
1	[43]	Loop	40	30	10	920	180	NA	6.4	NA
2	[44]	Dipole	127	25	2	850	160	-8.3	7	3.75
3	[45]	Dipole	145	40	NA	900	160	NA	6.3	0.18
4	[42]	IFA[4]	93	37	5	780	105[1]	NA	7.9	NA
5	[46]	PIFA[4]	64.8	45.6	4.75	866	105	-4.4	26	0.78
6	[47]	Loop	201	56	0.2	900	100	-8[5]	NA	NA
7	[28]	PIFA[4]	44	28	1.6	915	55[1]	-6.09	NA	NA
8	[48]	Dipole[4]	220	10	0.25	922.5	44	-11.2	NA	NA
9	[49]	PIFA[4]	44	44	10	767	35[1]	-5.4	13	NA
10	[50]	PIFA[5]	188	30	6	880	28	NA	83.7	NA
11	[116]	Helix	40	40	14.4	890	23	NA	NA	NA
12	[34]	Patch	86	25	1.6	915	19[3]	-6.87[5]	NA	NA
13	[36]	Helical	110	29	1.55	868	17	-13[5]	NA	NA
14	[37]	Monopole	100	15	0.6	911	14	-5.35	NA	NA
15	[38]	Monopole	40	15	1.8	911	7.5	-5.86	NA	NA
16	[39]	IFA[4]	45	30	5.5	846	7[5]	NA	14.8	NA
17	[40]	PIFA[4]	$\pi \times 25^2 \times 5$			402.5	5.2[2,3]	-12	3.6	NA
18	[30]	PIFA	$\pi \times 25^2 \times 5$			402.5	4.22[2,3]	-9.2	6.9	NA
19	[41]	Loop[5]	50	35	3	868	3.5	-1.44	NA	0.0002
20	[35]	Spiral[5]	$\pi \times 16^2$			915	3[3]	-1.04	NA	NA
21	[117]	PIFA	76.1	13.6	9.5	866	NA	-6.6	8.6	NA
22	[118]	Patch[5]	120	29	0.64	867	NA	-13	NA	NA
23	[119]	PIFA	90	20	3	923	NA	-5	NA	NA

This table is sorted in decreasing order of -10 dB bandwidth in column F

Important Notes:

[1] Antenna requires the use of an impedance matching network

[2] Only the -6 dB impedance bandwidth is reported

[3] Antenna does not meet the -10 dB bandwidth requirements for the targeted band

[4] Antenna was fully integrated in a wristwatch device

[5] Only simulated results are reported

NA = Information not reported

In the following sections, Table 3.1 is studied in detail to analyze the key performance parameters of the state-of-the-art Sub-GHz wrist-worn antennas reported in the literature and in the following chapters, the developed antennas in this thesis are compared against Table 3.1 to determine their relative performance.

3.7.1 Antenna Topology

As summarized in Column C of Table 3.1, different antenna topologies (e.g., dipole, monopole, loop, helical, patch and PIFA) have been used for Sub-GHz wristwatch applications. However, the majority of Sub-GHz wristwatch antennas are designed using the PIFA topology, mainly because of its capability to be integrated into a low-profile, compact size wristwatch device. In addition, the finite ground plane of the PIFA acts as a shield for backward radiation towards the human wrist and minimizes the losses that can be caused by human tissue [40, 65].

3.7.2 -10 dB Impedance Bandwidth

First, the impedance bandwidth of the antennas in Table 3.1 is investigated because the main focus of this thesis is on bandwidth improvement. Note that the antennas listed in Table 3.1 are sorted in the decreasing order of -10 dB impedance bandwidth, column F. The -10 dB impedance requirements of the various Sub-GHz bands have been summarized in Table 3.2.

Table 3.2: -10 dB impedance requirements for several Sub-GHz bands.

Frequency band (MHz)	Frequency range (MHz)	-10 dB impedance bandwidth (MHz)	Reference
915	902 – 928	26	[55]
868	863 – 870	7	[64]
920	920 – 928	8	[55]
402.5	402 – 405	3	[30]
866	865 – 867	2	[120]
866	865 – 867	2	[120]
922.5	920 – 925	5	[121]
864	864 – 870	6	[120]
923	915 – 928	13	[120]
433	433.05 – 434.79	1.74	[120]

It is observed from Table 3.1 that the four antennas in rows 1 to 4 achieve the best -10 dB impedance bandwidth performance. Those four antennas achieve a -10 dB impedance bandwidth of more than 100 MHz, but at the cost of a radiation efficiency of

less than 8 %. The PIFA antenna in row 5 has a -10 dB impedance bandwidth of 105 MHz. However, this antenna uses a wrist strap that has a width of 50 mm which is considerably wider than a standard wristwatch strap, for example an Apple smartwatch, whose strap measures a total width of 24 mm [89].

The antennas in rows 4, 7 and 9 achieve a -10 dB impedance bandwidth of 55, 35 and 105 MHz, respectively, but these antennas use impedance matching networks for impedance bandwidth enhancement. However a key disadvantage of introducing an impedance matching network is the addition of RF losses in the matching components as well as the increase in cost and design complexity [122]. The dipole antenna in row 8 has a -10 dB impedance bandwidth of 44 MHz, but this antenna has a peak realized gain of less than -11 dBi at 922.5 MHz. The PIFA antenna in row 10 achieves a -10 dB impedance bandwidth of 28 MHz, but this antenna occupies a size of 188 mm × 30 mm × 6 mm, which is substantial for integration into a practical wristwatch device, such as an Apple watch [89].

Table 3.1 shows that many of the antennas in the literature have a limited -10 dB impedance bandwidth of less than 20 MHz, as for the antennas in rows 12 to 20. For example, the 915 MHz wristwatch antennas in rows 12 and 20 respectively achieve a -10 dB impedance bandwidth of 19 and 3 MHz, but do not meet the fundamental minimum bandwidth requirements for use in the 915 MHz ISM band of 26 MHz (902-928 MHz) as defined by IEEE 802.15.4 standard [55]. Furthermore, the antennas reported in row 17 and 18 are designed for the MICS band, but they do not meet the minimum required -10 dB impedance bandwidth of 3 MHz for the MICS band (402 – 405 MHz) operation [30].

From the above impedance bandwidth analysis of the 23 published work, a gap in the state-of-the-art relating to the limited impedance bandwidth was identified. It was concluded that the majority of antennas have limited -10 dB impedance bandwidth of less than 20 MHz (rows 12 to 20) or achieve a wider impedance bandwidth of greater than 20 MHz either by designing the antenna using an impractical size (rows 1-6, 8-11) wristwatch device or at the cost of impaired radiation performance (rows 1-4, 6, 8, 13). Therefore, the need for developing new compact antenna designs with enhanced impedance bandwidth while at the same time maximizing radiation performance was identified.

The research hypothesis for this work focuses on the use of a dual-radiator approach to enhance the antenna characteristics when compared to the state-of-the-art Sub-GHz wristwatch antenna. This research hypothesis is based on the fact that the impedance bandwidth of an antenna can be enhanced by: (a) modifying the input impedance to improve the impedance matching of the antenna over the required band [123, 124] and (b) by enabling the excitation of two closely located resonant frequencies creating two resonances that can be independently tuned to maximize the impedance bandwidth of the antenna [125].

3.7.3 Peak Realized Gain at f_0

Having studied the -10 dB impedance bandwidth performance for a total of 23 Sub-GHz wristwatch antennas, the peak realized gain performance, as summarized in Column G of Table 3.1 is now analyzed. The 915 MHz spiral antenna in row 20 has the highest peak realized gain of -1.04 dBi. However, this antenna has a -10 dB impedance bandwidth of only 3 MHz and does not meet the minimum 26 MHz requirement for 915 MHz band operation. The 868 MHz loop antenna in row 19 demonstrates the second highest peak realized gain of -1.44 dBi, but this antenna achieves a -10 dB impedance bandwidth of only 3.5 MHz. The 868 MHz helical antenna in row 13 has a peak realized gain of -13 dBi at 868 MHz, which is the lowest gain performance for the 23 papers reviewed.

It is observed that out of 23 antennas reviewed in Table 3.1, only 4 antennas as in rows 5, 19, 20 and 23 achieve a peak realized gain of greater than -5 dBi, and 6 antennas reported in rows 1, 3, 4, 10, 11, 16 do not report the peak realized gain figures at all.

3.7.4 Radiation Efficiency at f_0

Having studied the -10 dB impedance bandwidth and peak realized gain requirements, in this section the radiation efficiency performance, as listed in Column H of Table 3.1, is next investigated. It is observed that more than 50 % (12 out of 23) of the Sub-GHz wristwatch antennas do not report radiation efficiency performance figures, either measured or simulated.

The PIFA antenna in row 10 achieves the highest radiation efficiency of 83.7 % for all 23 antennas but this antenna occupies a considerable size of 188 mm × 30 mm × 6 mm, which is not suitable for integration into a practical wristwatch device [89].

The majority of Sub- antennas (rows 1-4, 17-18, 21) have a radiation efficiency of less than 9 % and only 4 antennas (rows 5, 9, 10, 16) out of 23 antennas analyzed achieve a radiation efficiency of greater than 10 %.

3.7.5 Specific Absorption Rate (SAR) at f_0

Table 3.1 column (I) summarizes the SAR performance figures for the 23 antennas analyzed. As described in Chapter 2, the SAR parameter is a measure of the rate at which RF power is absorbed by the human body when exposed to EM radiation [78] and for wrist-worn wireless devices, the SAR level should not exceed a limit of 4.0 W/kg averaged over 10 g of wrist tissue [79, 80]. Therefore, the SAR figure is an important parameter to consider when designing a wristwatch antenna. However, it is found that the majority of Sub-GHz wrist-worn antennas described in the literature do not report the SAR performance and out of 23 antennas reviewed, the SAR performance is only reported for 4 antennas (rows 2, 3, 5 and 19).

3.7.6 Wristwatch Model

This analysis of the literature also has found that the majority of Sub-GHz wristwatch antennas, with the exception of antennas in rows (4, 5, 7, 9, 16, 17) do not consider the potential performance effects of internal wristwatch components in close proximity to the antenna, something that is inevitable in a practical wristwatch device. The internal components of a practical wristwatch device typically include printed circuit boards (PCBs), battery, sensor assemblies, connectors and metal screws for example.

Based on the above literature review, the challenges and issues (relating to impedance bandwidth, peak realized gain, radiation efficiency and SAR) with the state-of-the-art Sub-GHz wrist-worn antennas are summarized in Table 3.3 on the next page.

Table 3.3: Challenges with reported state-of-the-art Sub-GHz wrist-worn antennas.

	No.	Challenges	References	Remark
Bandwidth Related Challenges	1	-10 dB impedance bandwidth (*BW*) requirements not met	[30, 34, 35, 40]	4 out of 23 papers do not meet *BW* requirements for targeted band
	2	*BW* figures not reported	[117-119]	3 out of 23 papers do not report bandwidth or S_{11} response
	3	*BW* < 20 MHz	[30, 34-41]	9 out of 23 papers have *BW* < 20 MHz
	4	*BW* > 20 MHz, but with substantial antenna size	[42-50]	9 out of 23 antennas have an impractical size for a wristwatch device [89]
	5	*BW* > 20 MHz, but with impaired radiation performance	[36, 42-45, 47, 48]	7 out of 23 antennas have either efficiency < 8 % or Gain < -8 dBi
Gain, Efficiency and SAR related challenges	6	Peak realized gain less than -5 dBi	[35, 41, 46, 119]	Only 4 out of 23 papers have Gain > -5 dBi
	7	Antenna gain figure not reported	[39, 42, 43, 45, 50, 116]	6 out of 23 papers do not report antenna gain
	8	Radiation efficiency (η) less than 10 %	[39, 46, 49, 50]	Only 4 out of 23 papers have η > 10 %
	9	Radiation efficiency (η) not reported	[28, 34-38, 41, 47, 48, 116, 118, 119]	More than 50 % papers do not report η
	10	SAR figures not reported	[28, 30, 34-40, 42, 43, 47-50, 116-119]	Only 4 out of 23 papers report SAR figures
	11	Enclosure and internal components of a wristwatch device are not considered	[30, 34-38, 41, 43-45, 47, 48, 50, 116-119]	Only 6 out of 23 papers use a physical wristwatch device

3.8 Gaps in the State-of-the-Art and Research Hypothesis

From the above review of the 23 antennas, it was concluded that the majority of antennas have limited -10 dB impedance bandwidth of less than 20 MHz [30, 34-41] or achieve a wider impedance bandwidth of greater than 20 MHz either by designing the antenna using an impractical sized wristwatch device [42-50] or at the cost of impaired radiation performance [36, 42-45, 47, 48].

Several gaps in the state-of-the-art relating to the limited impedance bandwidth are identified in Table 3.2 and the need for developing new compact antenna designs with enhanced impedance bandwidth while at the same time maximizing radiation performance is concluded. The work presented in this thesis aims at addressing the above challenges identified in the literature by designing new, performance improved wristwatch antennas. The research hypothesis for this work focuses on the use of a dual-radiator approach to enhance the antenna performance characteristics when compared to the state-of-the-art Sub-GHz wristwatch antennas.

3.9 Conclusions

This chapter has presented a comprehensive review of wrist-worn antennas reported in the literature. First, the wrist-worn antennas operating at frequencies above 1 GHz was discussed. Furthermore, a detailed review of Sub-GHz wrist-worn antennas was conducted and the associated design challenges were outlined. In the literature, several types of antenna topologies (e.g., dipole, monopole, ILA, metal frame loop, slot, helical, patch and PIFA) have been used for wristwatch devices. However, it was observed that, planar inverted-F antennas (PIFA) are the most widely used antenna topology for wristwatch devices due to their compact and low profile characteristics and the ability to minimize backward radiation towards the human wrist tissue [40, 65]. At higher frequencies (e.g., 2.4, 5.2 and 5.8 GHz), dual-radiator approaches have been used to enhance the impedance bandwidth of wristwatch antennas [98, 100]. However, this literature review also concludes that a dual-radiator approach has not been used previously for Sub-GHz wristwatch antennas.

A performance comparison of Sub-GHz wristwatch antennas reported in the literature was performed to highlight the characteristics and limitations of such antennas and a number of design challenges were identified. In particular, a gap in the state-of-the-art relating to the limited impedance bandwidth of Sub-GHz wristwatch antennas was identified and the need for developing new antenna designs with improved performance was identified. The aim of this thesis is to address the challenges identified in this chapter. The performance characteristics of the developed Sub-GHz wristwatch antennas in this thesis are later compared against the state-of-the-art wristwatch antennas, as was summarized in Table 3.1.

Chapter 4: A Bandwidth Enhanced 915 MHz Wristwatch Antenna

4.1 Background

As has been discussed in the literature review in Chapter 3, the emergence of wrist-worn wireless devices equipped with physiological sensors is part of a growing application space for consumer electronic and Medtech devices. Such devices with wireless capability can play a significant role in healthcare applications such as the bio-physiological measurement of heart rate, temperature and arterial oxygen saturation (SpO_2) [28, 126, 127]. At the present time, the majority of wristwatch devices use the 2.4 GHz band due to the widespread availability of Bluetooth and Wi-Fi wireless technology [28] and the ability to seamlessly interface these devices with smartphone technology for data analytics and visualisation. However, in the last decade, Sub-GHz band (915/868 MHz) frequencies have also shown potential for future IoT wristwatch applications. Sub-GHz frequencies are increasingly of interest for IoT applications due to emerging wireless technologies such as LoRaWAN [15] and SigFox [16] that have the potential for long-range wireless communications with low power consumption and increased battery life, when compared with the 2.45 GHz band [19, 128].

It was also concluded in the literature review, Chapter 3, that Sub-GHz wristwatch antennas can have impedance bandwidth figures of less than 20 MHz [30, 34-41] and limited radiation performance with less than 8 % efficiency [42-45]. The limited impedance bandwidth and radiation performance of Sub-GHz wristwatch antennas are mainly attributed to the practical size constraints of wrist-worn devices, resulting in electrically small antenna designs with limited radiation performance [31, 67]. In this work, a new bandwidth enhanced 915 MHz wristwatch antenna is developed, which aims at achieving the minimum required -10 dB impedance bandwidth of 26 MHz for the 915 MHz band operation [55].

In addition, the proposed antenna design aims to improve on the peak realized gain and radiation efficiency performance when compared to similar wristwatch antennas reported in the literature.

4.2 Target Wristwatch Device for Antenna Integration

The antenna proposed in this work is designed for integration into an off-the-shelf wristwatch assembly [129] shown in Figure 4.1. The wristwatch enclosure is made of an acrylonitrile butadiene styrene (ABS) plastic material with a relative electrical permittivity $\varepsilon_r = 2.8$ and a loss tangent $tan\delta = 0.004$ at 1 GHz [130]. The overall dimension of the wristwatch enclosure is 50 mm × 35 mm × 15 mm. Figure 4.1 also shows a cylindrical homogeneous phantom arm (IXB-63) from IndexSAR [131] used during electromagnetic (EM) simulation. The phantom arm has a length of 200 mm with 63 mm diameter. The electrical properties are specified as ε_r = 35.76 with an electrical conductivity σ = 0.58 S/m and mass density ρ = 1764 kg/m^3 at 915 MHz [131]. The wristwatch strap used in this work is made of silicone rubber with ε_r = 2.95 and $tan\delta$ = 0.001 at 1 GHz [132]. Figure 4.1 also shows the antenna structure integrated into the wristwatch device, which is excited using an unbalanced coaxial feed at points *S* (source) and *G* (ground). The next section describes the design and evolution of the antenna in detail.

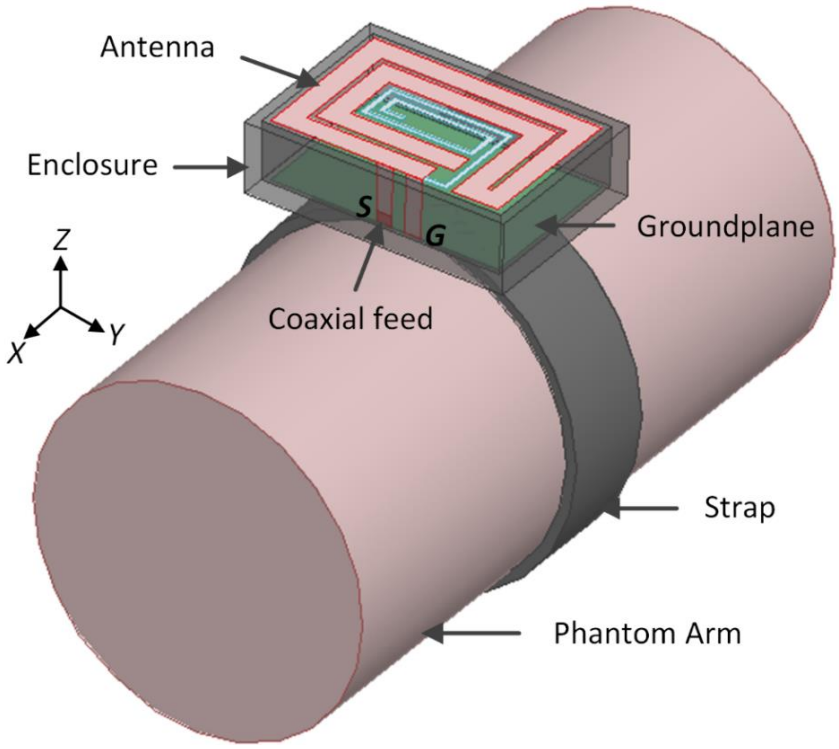


Figure 4.1: Wristwatch enclosure device placed on a phantom arm [131].

4.3 Antenna Design Concept

The proposed wristwatch antenna is a modified planar inverted-F antenna (PIFA) topology. A PIFA topology was selected because it can be readily incorporated into a compact wristwatch housing, compared to other antennas topologies, such as dipole, conventional monopole, loop and patch antennas, which require a larger space compared to a PIFA antenna [57]. In addition, the PIFA topology ensures reduced backward radiation towards the user's wrist due to the presence of the plane between the radiator and human tissue, which minimizes the losses in human tissue [40, 65]. A simplified view of a conventional quarter-wavelength single element (Rad_1) PIFA antenna topology is illustrated in Figure 4.2(a) [133]. With the goal to enhance the impedance bandwidth, this work proposes a dual-radiator (Rad_1 and Rad_2) based PIFA structure similar to the topology shown in Figure 4.2(b). For the proposed antenna, element Rad_1 is connected to the feed point *S*, whereas element Rad_2 is connected to ground *G* and is excited via mutual inductive coupling with Rad_1.

The following sections outline the benefits of the proposed antenna design. The inclusion of element Rad_2 improves the impedance bandwidth by enabling impedance matching of the antenna over a wider bandwidth compared to the single element PIFA. Furthermore, as both the elements Rad_1 and Rad_2 are shown to be resonant at 915 MHz, along with the impedance bandwidth enhancement, the proposed antenna structure also demonstrates an improved peak realized gain and radiation efficiency when compared to a single element PIFA. A conventional PIFA is a variant of a quarter-wavelength monopole antenna that is resonant at odd multiples of the free-space quarter-wavelength or $\lambda_0/4$, $3\lambda_0/4$, $5\lambda_0/4$ etc [134, 135].

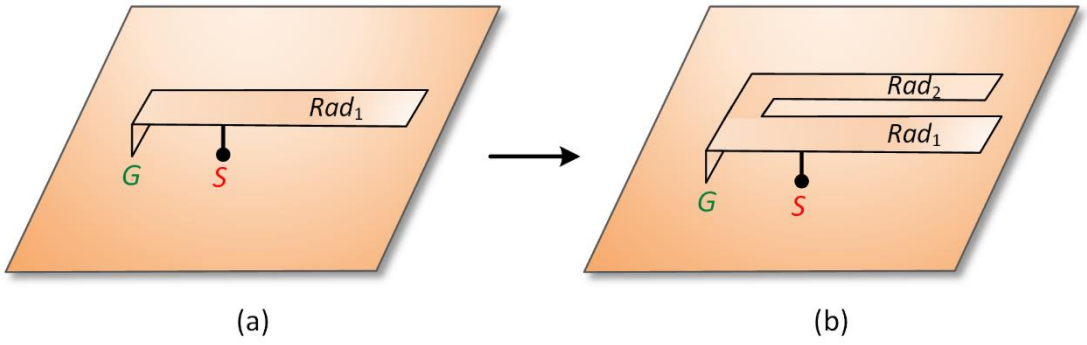


Figure 4.2: (a) Conventional single-element PIFA topology [84], (b) Proposed dual-radiator PIFA antenna design concept.

For the proposed dual-radiator PIFA shown in Figure 4.2(b), element Rad_2 has a free-space electrical length of approximately $\lambda_0/4$ and is resonant at a fundamental frequency of 915 MHz, similar to a conventional PIFA.

Element Rad_1 has an electrical length of approximately 0.38 λ_0 with a fundamental resonant frequency of f_0 = 510 MHz. This length is approximately 0.13 λ_0 greater than the theoretical quarter-wavelength of $\lambda_0/4$. This increase in electrical length can be explained by the capacitive loading effect of the meandered structure. This capacitive loading effect due to meandering is consistent with that of a similar PIFA antenna structure operating at 2.45 GHz as reported in [136]. The antenna structure in [136] has a second resonance at twice the fundamental frequency or approximately 5.5 GHz. For the antenna reported in this work, a similar response is observed with the antenna being resonant at a frequency of approximately $2f_0$ = 915 MHz.

4.4 Antenna Design and Simulations

Having described the antenna design concept, the development of a variant of a dual-radiator PIFA topology operating at 915 MHz is now presented. The proposed antenna topology was achieved after three design iterations, denoted as Antenna-1, Antenna-2 and Antenna-3. This antenna design evolution aims at improving the impedance bandwidth as well as the radiation performance of each antenna to arrive at the final design. The performance characteristics of all three antennas were simulated and analyzed using Ansys HFSS [137], as described below in detail.

4.4.1 Antenna-1

The starting point for the antenna design was a single element PIFA structure, as shown in Figure 4.3. The total size ($L \times W \times h$) of the antenna including the finite ground plane is 43.5 mm × 28.5 mm × 10.3 mm and is excited at point '*S*' using a 50 Ω unbalanced coaxial feed. The antenna structure was realized using a 0.35 mm copper plate. Element Rad_1 extends from the feed point *S* to the end of the element at point *A* and has a total length of 68.5 mm, which corresponds to a free-space electrical length of 0.21 λ_0 at 915 MHz. The separation L_2 between the feed point and the shorting plate determines the magnitude of the shunt inductance that is used to balance the net capacitance of the radiating element to the ground plane and thus controls the impedance matching of the antenna.

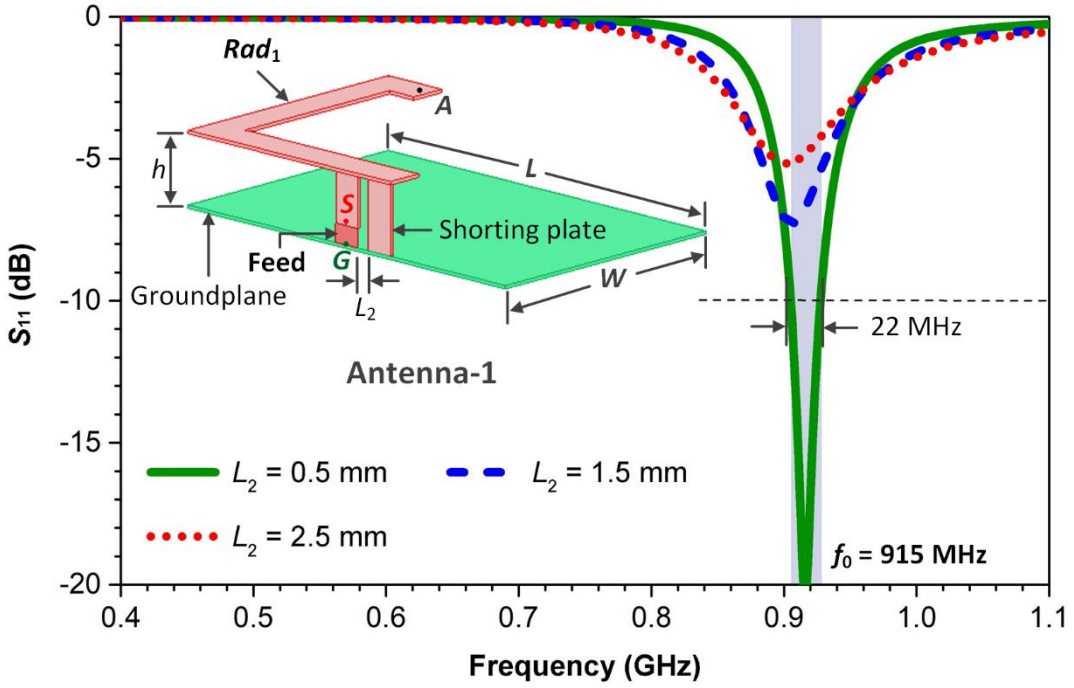


Figure 4.3: Antenna-1 topology and simulated S_{11} response for varying L_2.

It can be seen from Figure 4.3 that the impedance matching of the antenna improves with reducing values of L_2 and the antenna is best matched for L_2 = 0.5 mm at the resonant frequency f_0 = 915 MHz. The S_{11} response shows that Antenna-1 has a -10 dB impedance bandwidth of 22 MHz, which did not meet the minimum required impedance bandwidth of 26 MHz for 915 band operation [55]. Furthermore, Antenna-1 has a simulated peak realized gain of -1.4 dBi and a radiation efficiency of 41.8 % at 915 MHz.

4.4.2 Antenna-2

With the aim to improve the impedance and radiation performance of the antenna, the second antenna (Antenna-2) was designed. For Antenna-2, only the structure of the radiating element Rad_1 was modified and all other design parameters were maintained as described above for Antenna-1. The total length of element Rad_1 was increased to excite a second resonance at 915 MHz. The structure of Antenna-2 is illustrated in Figure 4.4, where element Rad_1 has a total length of 224 mm, which corresponds to a free-space electrical length of 0.68 λ_0 at 915 MHz. For this total length (224 mm) of Rad_1, the antenna has a fundamental resonant frequency f_{01} = 510 MHz and a second resonant frequency f_{02} = 915 MHz, as illustrated in Figure 4.4.

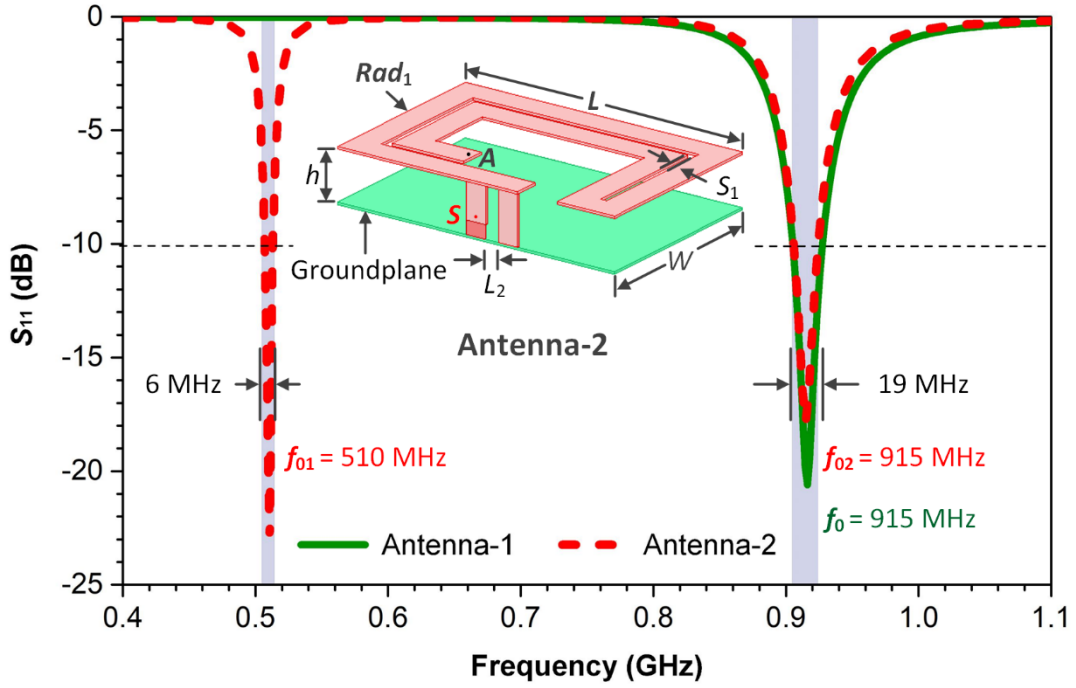


Figure 4.4: Antenna-2 antenna topology and simulated S_{11} response.

Furthermore, the distance L_2 was also optimized to 2 mm (L_2 was 0.5 mm for Antenna-1) to achieve the maximum impedance bandwidth for Antenna-2.

The S_{11} response shows that Antenna-2 achieved a -10 dB impedance bandwidth of 19 MHz, which is slightly (3 MHz) less than Antenna-1 and does not meet the minimum required impedance bandwidth of 26 MHz for 915 band operation [55]. However, the simulated results for Antenna-2 achieved a peak realized gain of -1.1 dBi and a radiation efficiency of 42.5 % at 915 MHz, which are respectively, 0.3 dB and 0.7 % higher than Antenna-1. Therefore, Antenna-2 was further optimized with the goal to enhance the impedance bandwidth and the radiation performance of the antenna.

4.4.3 Antenna-3 (Proposed Antenna)

With the aim to enhance the impedance bandwidth to achieve the minimum required −10 dB impedance bandwidth of 26 MHz for the 915 MHz band operation, Antenna-3 (the final proposed antenna) was designed.

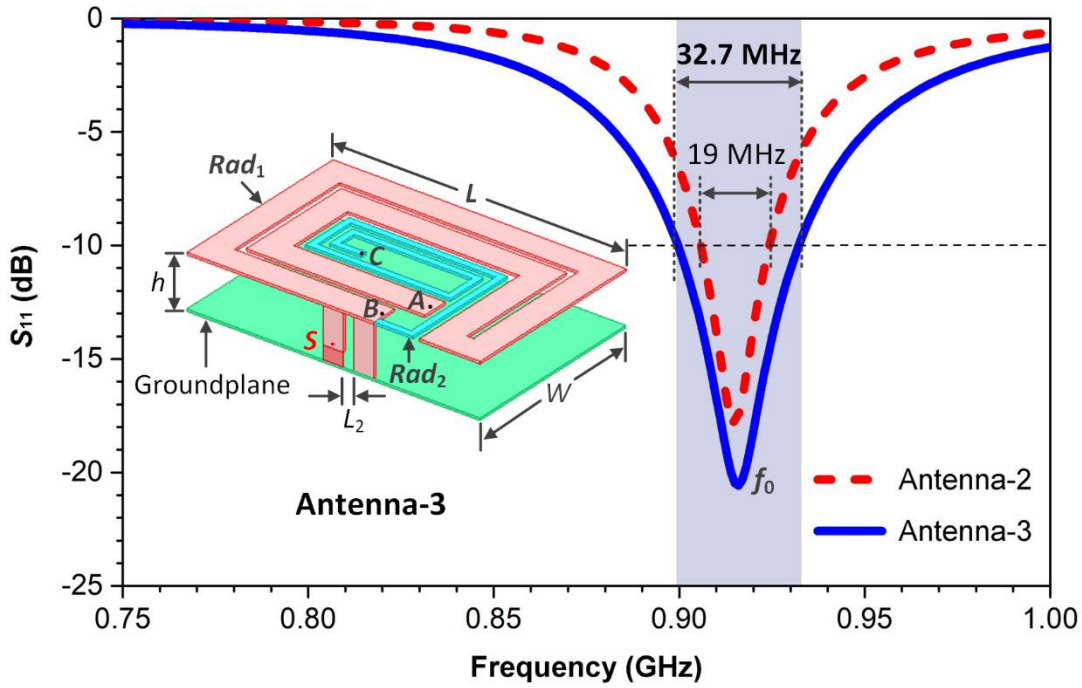


Figure 4.5: Antenna-3 (proposed) topology and simulated S_{11} response

The structure of the proposed antenna is illustrated in Figure 4.5, where a second element (Rad_2) has been incorporated in the design. Element Rad_2 was included in the design with the aim to enhance the impedance bandwidth of the antenna by improving the impedance matching over the required band of 26 MHz [123, 124].

The total length of element Rad_1 is 239 mm, which corresponds to a free-space electrical length of approximately 0.73 λ_0 at 915 MHz. Element Rad_2 extends between points *B* to *C* and has a total length of 96 mm, which corresponds to a free-space electrical length of approximately 0.29 λ_0 at 915 MHz. Figure 4.5 also shows the simulated S_{11} response of the proposed antenna, where the impedance bandwidth enhancement with the inclusion of element Rad_2 is highlighted. Without element Rad_2 (Antenna-2), the antenna has a −10 dB impedance bandwidth of 19 MHz. However, with the inclusion of element Rad_2 in the design, Antenna-3 (proposed antenna) achieved a −10 dB impedance bandwidth of 32.7 MHz, which is 72 % higher than Antenna-2. Furthermore, the simulated results for the proposed antenna achieved a peak realized gain of −0.78 dBi and a radiation efficiency of 46.8 % at 915 MHz, which are respectively 0.32 dB and 4.3 % higher than Antenna-2.

4.4.4 Antenna Design Evolution Summary

The impedance and radiation performance of the three antennas described above are summarized in Table 4.1. It can be seen from the table that the proposed antenna (Antenna-3) has achieved a -10 dB impedance bandwidth of 32.7 MHz, which is approximately 25 % higher than the required impedance bandwidth for 915 MHz band operation [55].

Table 4.1: Performance comparison of the 3 iterations.

Antenna Design Evolution	- 10 dB impedance Bandwidth (MHz)	Peak realized Gain at 915 MHz (dBi)	Radiation Efficiency at 915 MHz (%)
Antenna-1	22	-1.4	41.8
Antenna-2	19	-1.1	42.5
Antenna-3	32.7	-0.78	46.8

4.4.5 Parametric Analysis of the Proposed Antenna

A parametric analysis of the proposed antenna (Antenna-3) was conducted in order to study the key antenna parameters that affect the impedance response and optimize the antenna geometry for 915 MHz operation. For this purpose, the effect of key parameters, such as the end length of element Rad_1 (L_1), the width of element Rad_1 (W_1) and the distance (L_2) of the feed point from the shorting plate was investigated (see Figure 4.6). In this section, the vertical shaded strip on the S_{11} response plots represents the minimum required -10 dB impedance bandwidth of 26 MHz for 915 MHz band operation.

The influence of the end length L_1 of element Rad_1 that determines the total length of element Rad_1 was first studied. As shown in Figure 4.6, parameter L_1 was varied between 5 mm to 20 mm while keeping all other parameters fixed as listed in Table 4.2 at the end of this section. Figure 4.6 shows the resulting S_{11} response, where it can be seen that L_1 mainly controls the resonant frequency of the antenna. The resonant frequency continuously decreases with increasing L_1 and the antenna is resonant at f_0 = 915 MHz for L_1 = 22.5 mm. This resonant behaviour is expected as the electrical length of element Rad_1 increases with increasing the end length L_1.

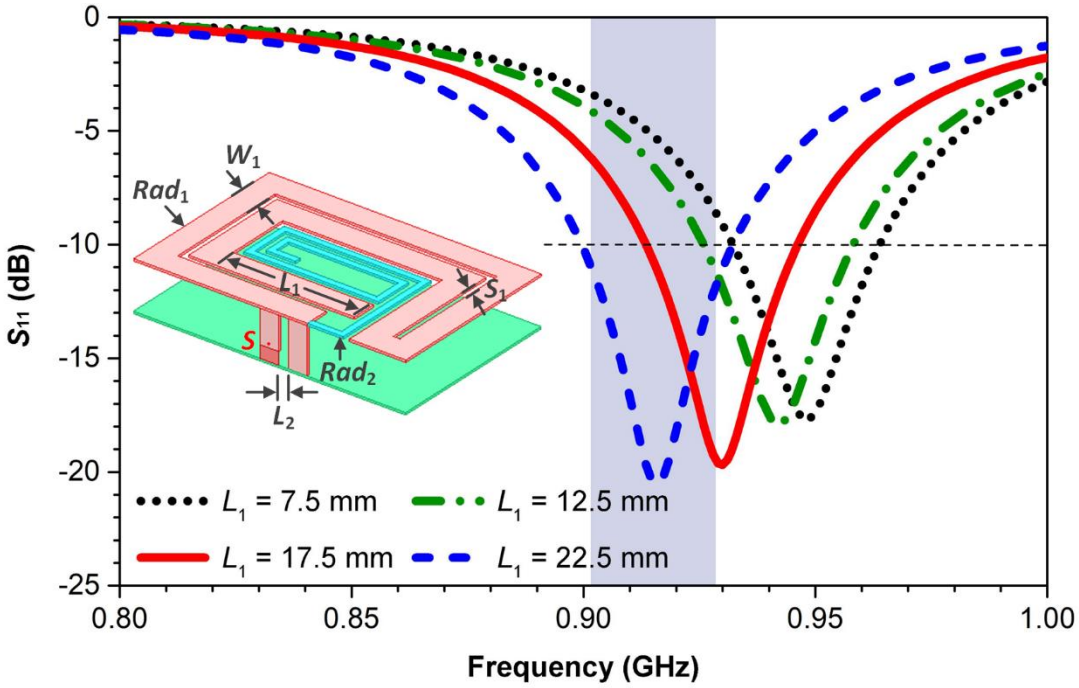


Figure 4.6: Simulated S_{11} response for varying element Rad_1 end length, L_1.

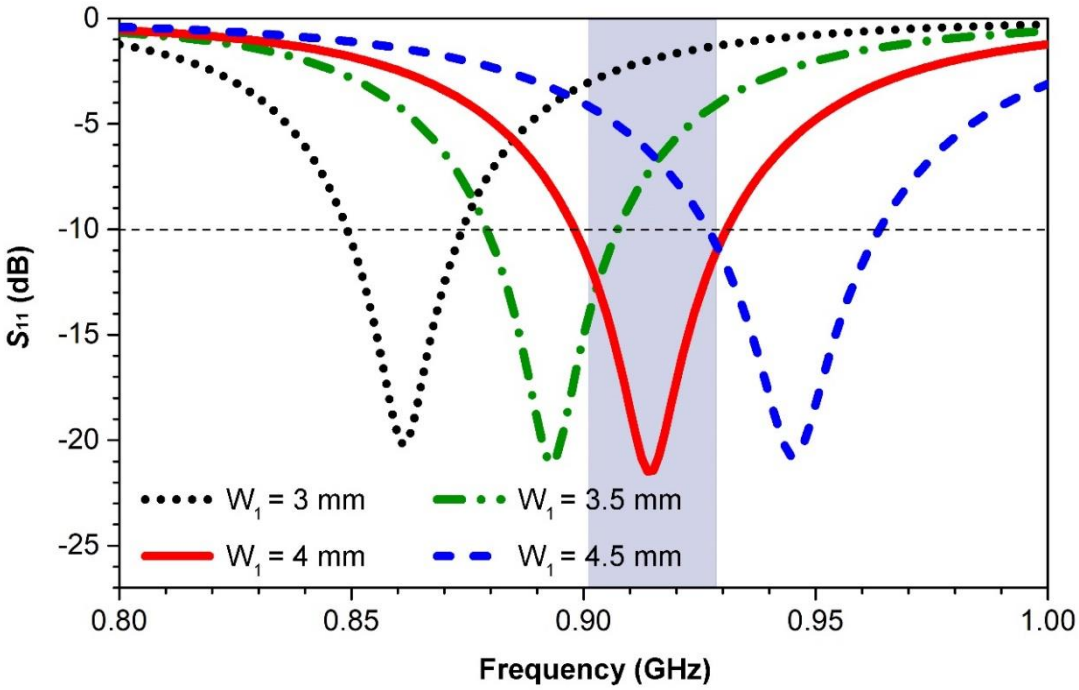


Figure 4.7: Simulated S_{11} response for varying the width, W_1 of element Rad_1.

Secondly, the influence of the width W_1 of element Rad_1 was investigated while keeping parameter L_1 = 22.5 mm and all previous parameters unchanged, with the results presented in Figure 4.7. The resonant frequency increases continuously as W_1 increases from 3 mm to 4.5 mm and the antenna is resonant at 915 MHz for W_1 = 4 mm.

It is observed that varying the width W_1 has a large effect on the resonant frequency. This large variation in resonant frequency is attributed to the fact that varying the width W_1 also increases the separation (S) between the consecutive arms of element Rad_1, as the relation $(2 \times W_1) + S$ has been equated to a constant, such that the total length of Rad_1 remains constant. Therefore, the resonant response in Figure 4.7 varies by a large amount as parameters W_1 and S vary together and therefore have a more pronounced effect. The impedance bandwidth of the antenna also increases with increasing the width W_1 of element Rad_1. With increasing width W_1, the amount of electric fringing fields radiated from element Rad_1 will increase and lead to a decreased quality factor or improvement in the impedance bandwidth of the antenna, as explained in [138, 139].

Finally, the effect of parameter L_2 on the resonant response of the antenna was investigated. Parameter L_2 is defined as the distance of the feed point (S) location from the shorting plate. Parameter L_2 was varied from 2.5 mm to 5.5 mm in 1 mm increments by moving the shorting plate towards right while keeping the other parameters constant, as listed in Table 4.2. The resulting S_{11} response for varying L_2 is shown in Figure 4.8. The resonant frequency increases continuously with increasing L_2 and the antenna is resonant at 915 MHz for L_2 = 2.5 mm.

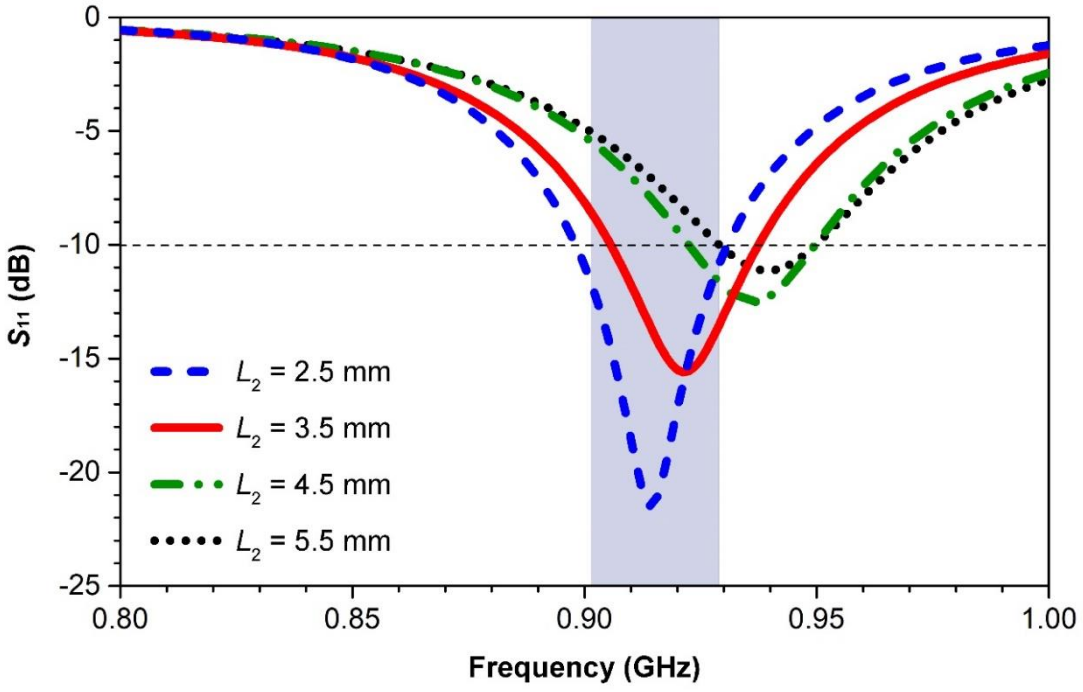


Figure 4.8: Simulated S_{11} response for varying distance L_2.

The separation L_2 between the feed point and the shorting plate determines the magnitude of the shunt inductance that is used to balance the capacitance of the radiating element Rad_1 that is in close proximity to the ground plane and thus controls the impedance matching of the antenna. For L_2 = 2.5 mm, the input impedance is best matched to 50 Ω and has the highest -10 dB impedance bandwidth of 32.7 MHz.

It is concluded from the above parametric analysis that the parameters L_1, W_1 and L_2 provide a sufficient degree of freedom to tune the resonant frequency of the antenna at 915 MHz and control the -10 dB bandwidth and impedance matching of the antenna. The final dimensions of the proposed antenna obtained after the above parametric analysis are listed in Table 4.2.

The final configuration of the proposed 915 MHz PIFA wristwatch antenna, which was developed after the parametric study is shown in Figure 4.9. The developed antenna consists of dual-radiators, denoted Rad_1 and Rad_2 and the antenna is excited at point '*S*' using a 50 Ω unbalanced coaxial feed.

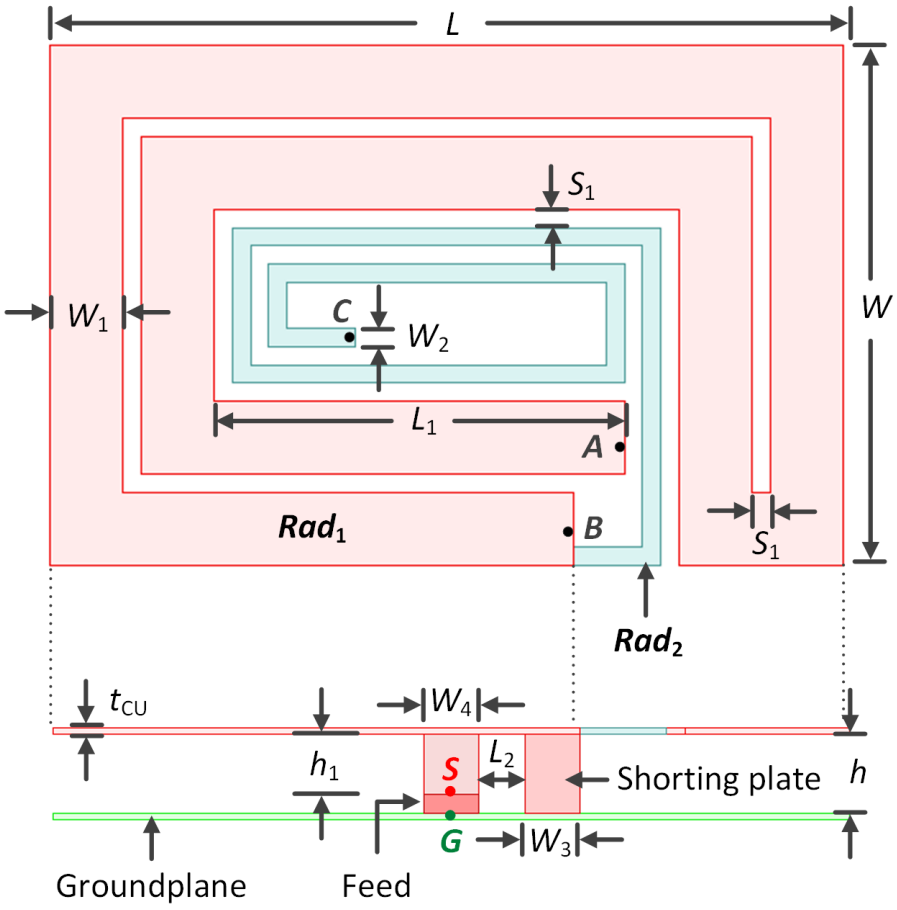


Figure 4.9: Final configuration of the developed 915 MHz wristwatch antenna.

Table 4.2: Final design parameters of the proposed antenna.

Parameter Name	Value (mm)	Parameter Name	Value (mm)
L	43.5	W_3	3
L_1	22.5	W_4	3
L_2	2.5	t_{CU}	0.35
W	28.5	h	10.3
W_1	4	h_1	8.3
W_2	1	S_1	1

4.4.6 Simulated 3D Radiation Pattern of the Antenna

The simulated 3D realized gain pattern of the antenna is shown in Figure 4.10. It can be observed that the radiation pattern is similar to a PIFA antenna [40]. The finite ground plane of the antenna helps minimize the power radiation towards the human phantom arm [40, 65]. The antenna has omnidirectional radiation characteristics in the *XY*-plane. The antenna exhibits nulls in the *YZ*- and *XZ*-planes. These nulls are expected due to the shielding effect of the PIFA ground plane in combination with the body absorption of energy in the negative *Z*-axis normal to the PIFA ground plane. As shown in Figure 4.10, the proposed antenna achieved a simulated peak realized gain of −0.78 dBi at 915 MHz.

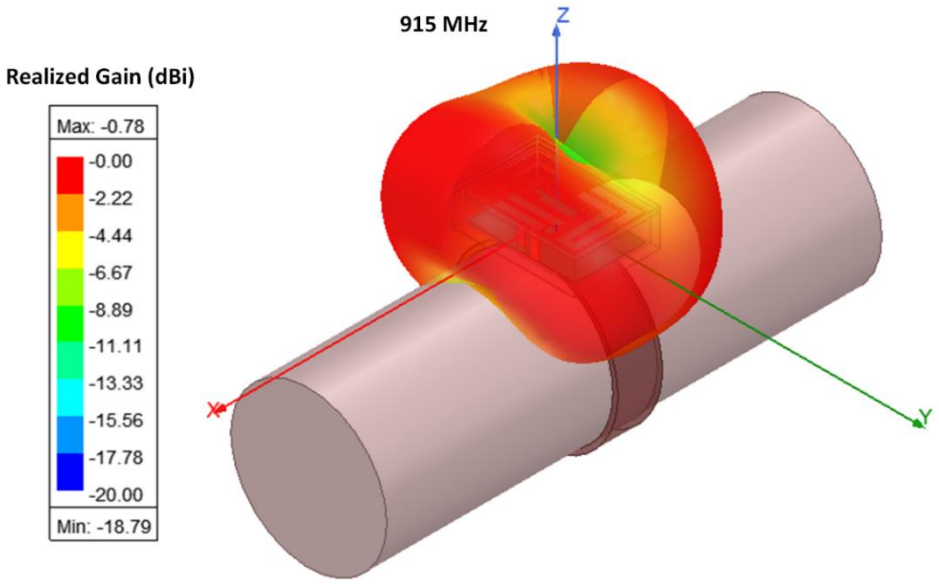


Figure 4.10: Simulated 3D Realized Gain pattern of the antenna at 915 MHz.

4.4.7 Surface Current Distribution

Figure 4.11 shows the surface current magnitude on elements Rad_1 and Rad_2 at 915 MHz. Large magnitude currents are observed on elements Rad_1 and Rad_2, indicating that both the elements are resonant at f_0 = 915 MHz. The surface current in vector form at 915 MHz is shown in Figure 4.12. As can be seen in Figure 4.12, from point S to P_1 the current path has an approximate electrical length of $\lambda_0/4$ and from P_1 to A, the approximate electrical length is $\lambda_0/2$ at 915 MHz. Therefore, the total electrical length of element Rad_1 from point S to point A is approximately $3\lambda_0/4$ at 915 MHz.

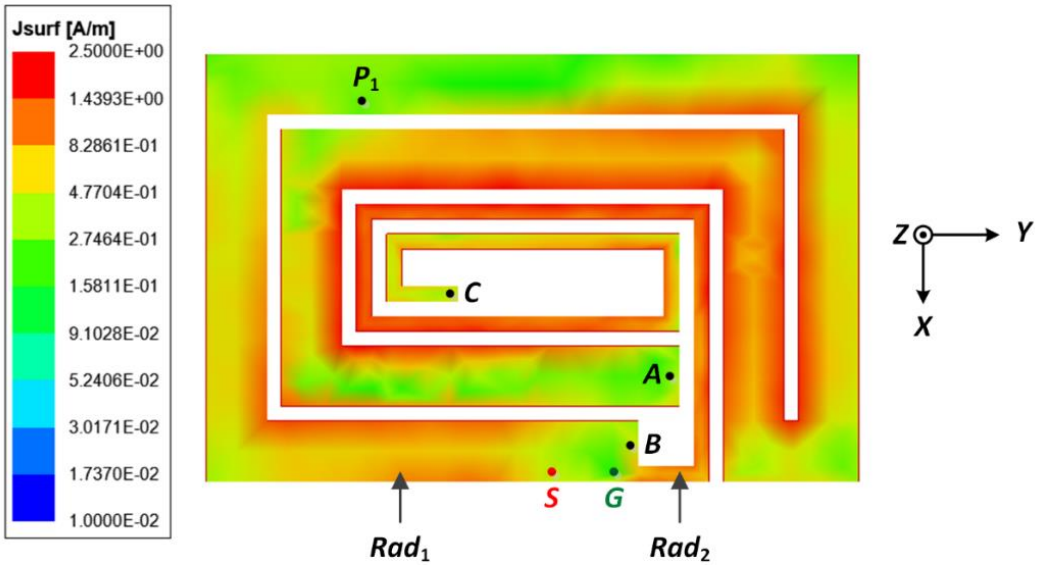


Figure 4.11: Simulated surface magnitude current distribution at 915 MHz.

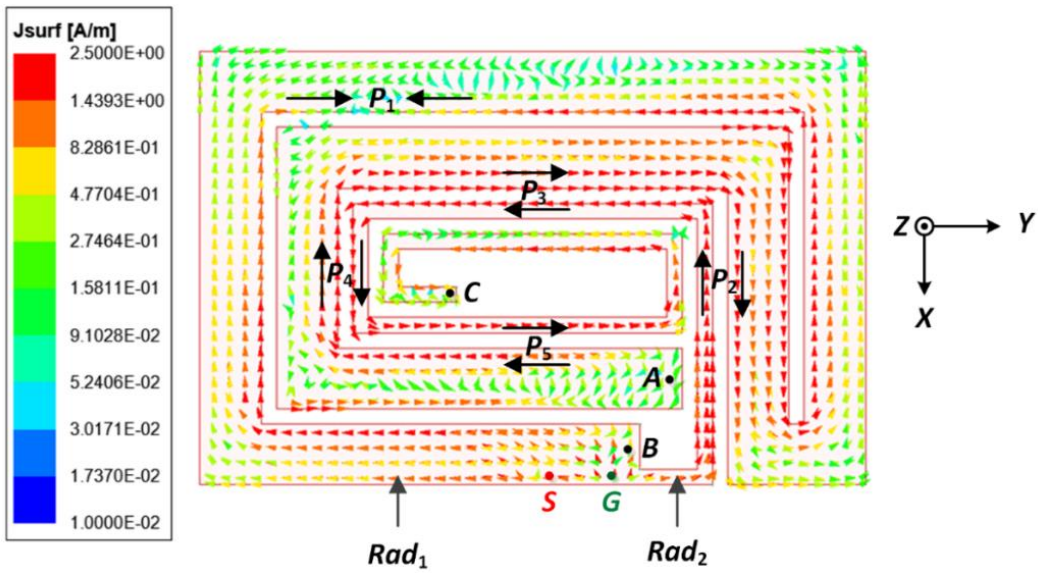


Figure 4.12: Simulated surface vector current distribution at 915 MHz.

Element Rad_2 is connected to ground and the current in element Rad_2 is excited through the mutual inductive coupling with element Rad_1 [140]. The direction of current flow through element Rad_2 is opposite to element Rad_1, as shown at points P_2, P_3, P_4 and P_5. Element Rad_2 has an approximate free-space electrical length of $\lambda_0/4$ at 915 MHz. The current distribution on element Rad_2 has a maximum near point *B* and the surface current is reduced to the minimum value at the end of element Rad_2 at point C, which is expected for a PIFA structure [141, 142].

4.4.8 Specific Absorption Rate (SAR) Evaluation

The Specific Absorption Rate (SAR) [29, 80] parameter is a measure of the rate at which power is absorbed by the human body when exposed to electromagnetic (EM) radiation [78]. The simulated SAR for the developed antenna was evaluated using an IndexSAR IXB-060 phantom arm [131] and simulated using Ansys HFSS [137]. According to the Federal Communications Commission (FCC) [109] and the International Commission on Non-Ionizing Radiation Protection (ICNIRP) guidelines [80], for limbs, the standard SAR exposure level should not exceed 4.0 W/kg, averaged over 10 g of tissue mass.

In Figure 4.13, the simulated SAR for the proposed antenna at 915 MHz is illustrated. The obtained peak 10 g SAR for an input power of 1 mW was 0.004 W/kg. This SAR figure is less than 0.1 % of the legal SAR limit of 4 W/kg for general public limb-wearable applications, as defined in [80, 109].

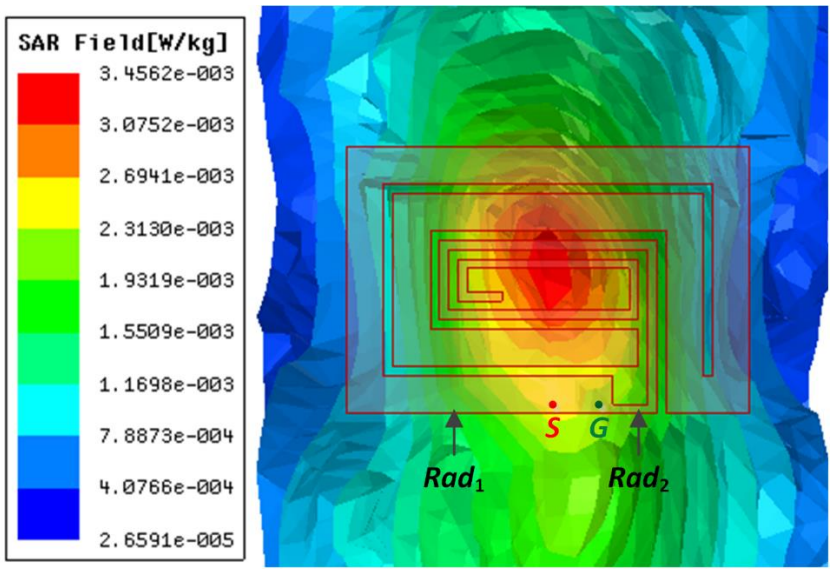


Figure 4.13: SAR distribution on the phantom arm at 915 MHz.

The EM simulated performance characteristics of the proposed antenna for the final design parameters listed in Table 4.2 are summarized in Table 4.3.

Table 4.3: The EM simulated performance summary of the proposed antenna.

-10 dB impedance bandwidth (MHz)	Peak realized gain at 915 MHz (dBi)	Radiation Efficiency at 915 MHz (%)	SAR at 915 MHz at 1 mW (W/kg)
32.7	-0.78	46.8	0.004

4.5 Antenna Measurements

To validate the antenna design, the measured impedance and radiation characteristics of the proposed antenna are now presented. The fabricated prototype of the proposed antenna is shown in Figure 4.14. The copper radiator was fabricated using a Bridgeport GX-480 milling machine [143]. The ground plane of the antenna makes a contact with the shorting plate on closing the lid of the plastic enclosure.

The S_{11} measurements of the antenna were taken after placing the antenna under test (AUT) on an IXB-63 phantom arm from IndexSAR [131]. The S_{11} response of the antennas was measured using a Rohde & Schwarz *ZVRE* vector network analyzer (VNA) [61]. The simulated and measured S_{11} responses of the antenna are shown in Figure 4.15.

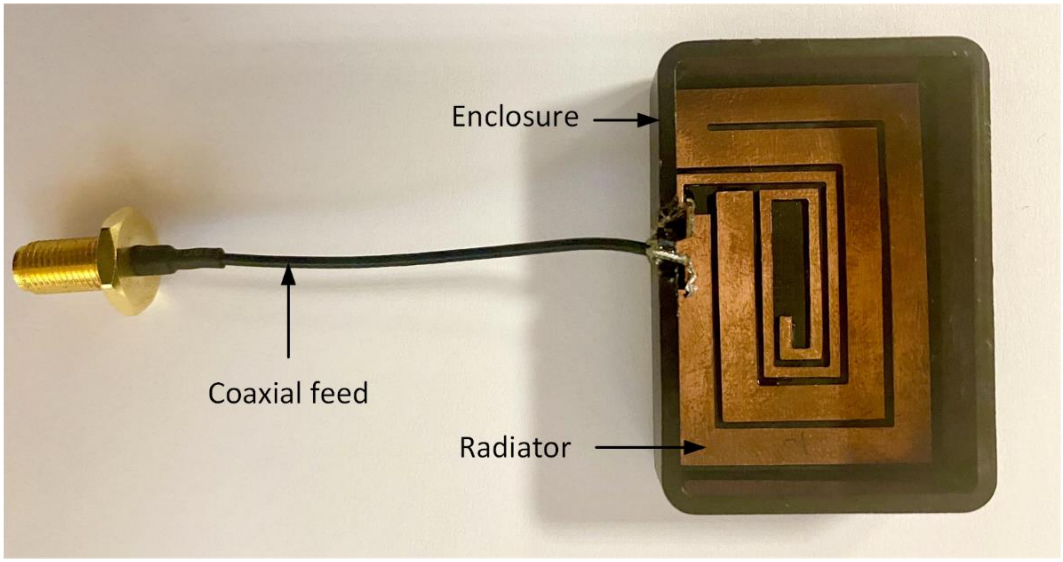


Figure 4.14: Photograph of the fabricated antenna prototype.

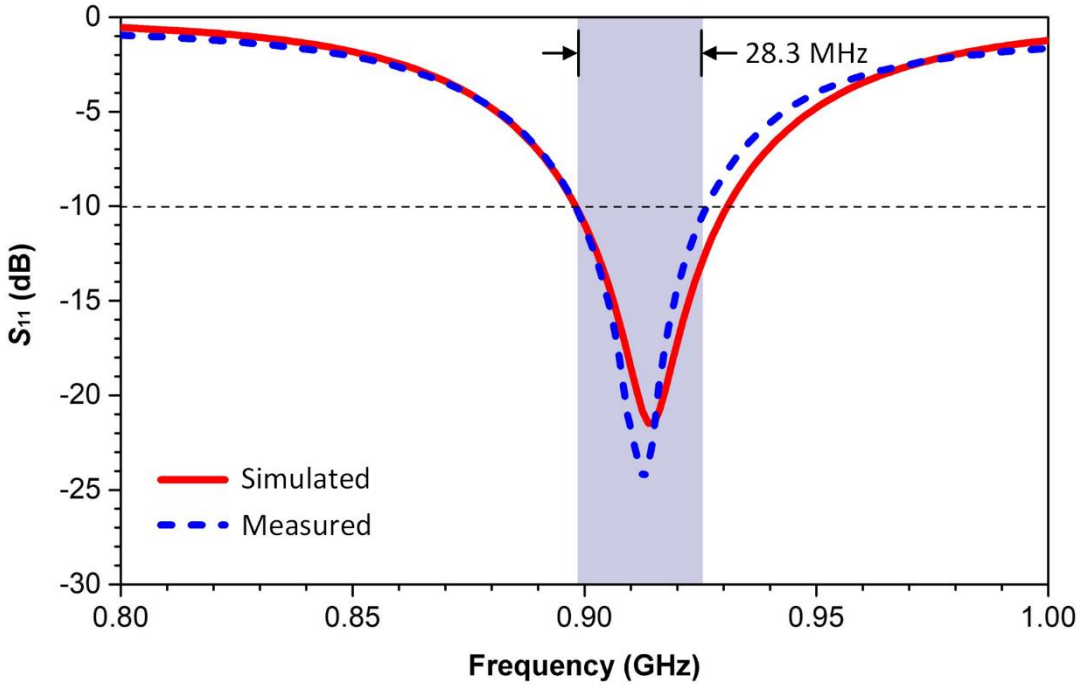


Figure 4.15: Simulated versus measured S_{11} response of the AUT.

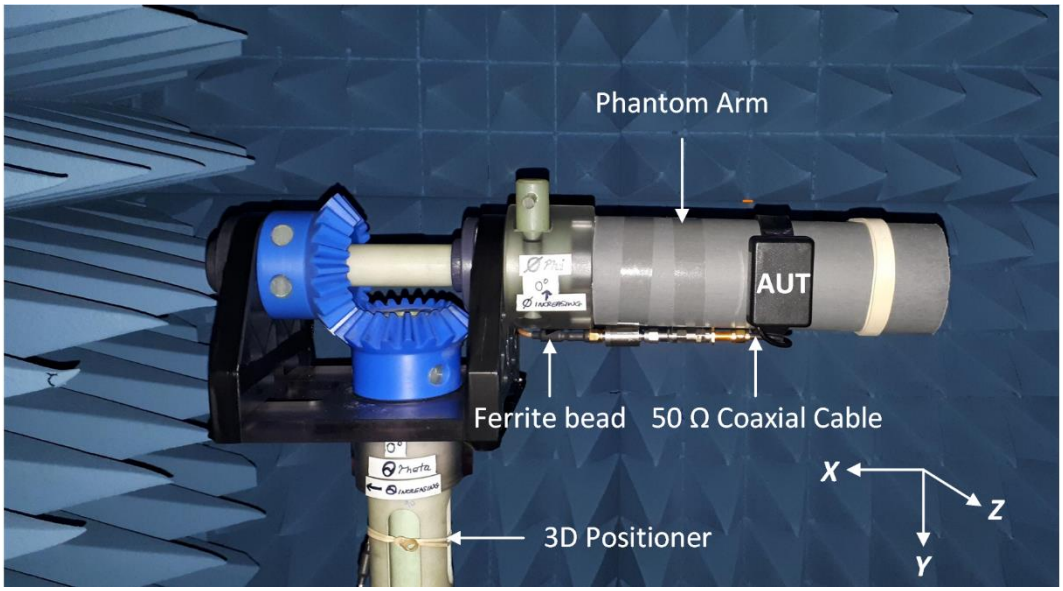


Figure 4.16: AUT measurement setup in the AMS-8050 anechoic chamber [63].

The proposed antenna has a measured -10 dB impedance bandwidth of 28.3 MHz and meets the minimum bandwidth requirements for use in the 915 MHz ISM band of 26 MHz [55]. In Figure 4.15, a slight discrepancy between the simulated and measured S_{11} responses is most likely attributed to the measurement setup and fabrication tolerances. In addition, the possible difference between the relative electrical permittivity (ε_r) of the ABS plastic enclosure material used in simulation and ε_r of the off-the-shelf wristwatch enclosure [129] used in the measurement.

The radiation pattern measurements of the AUT were performed in an AMS-8050 antenna measurement system [63]. The anechoic chamber measurement setup of the AUT is illustrated in Figure 4.16. The AUT was placed on an IXB-63 phantom [131] and the antenna was excited using an unbalanced 50 Ω coaxial cable. Since the coaxial cable can affect the antenna radiation properties, ferrite beads were incorporated in the measurement setup to suppress the effects of coaxial cable currents on the measured antenna radiation characteristics.

The measured and simulated radiation characteristics of the AUT at 915 MHz are shown in Figure 4.17. For the co-polarized case, the *XY*-plane exhibits an omnidirectional radiation pattern, as illustrated in Figure 4.17(a). The radiation characteristics in the *YZ*-plane are shown Figure 4.17(b) and in the *XZ*-plane is shown in Figure 4.17(c). For the co-polarized case, the antenna has a PIFA-like radiation characteristic in the YZ-plane [40]. The antenna exhibits nulls in the *YZ*- and *XZ*-planes for the co-polarized radiations.

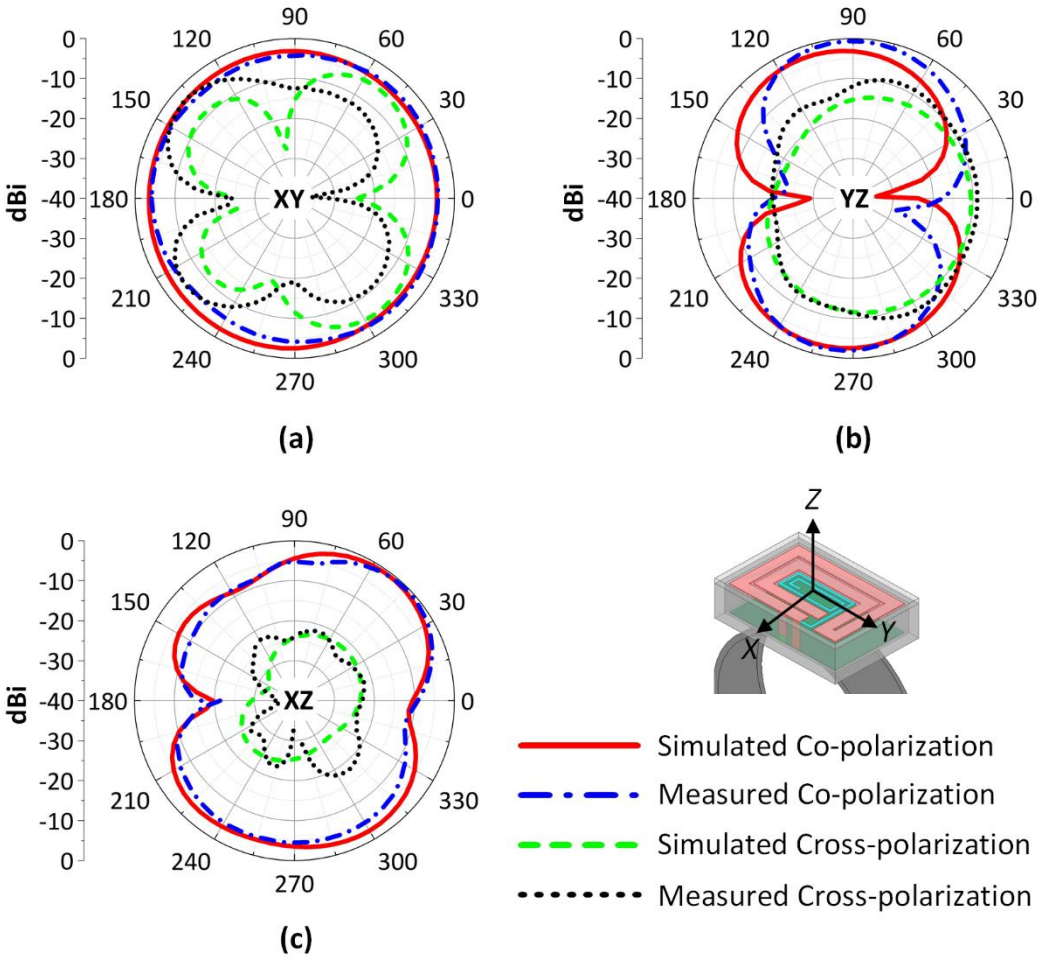


Figure 4.17: Simulated and measured radiation characteristics of the proposed antenna at 915 MHz (a) *XY*- plane (b) *YZ*- plane and (c) *XZ*- plane.

These radiation nulls are expected because of the shielding effect of the finite PIFA ground plane in combination with body absorption of energy in the axis normal to the PIFA ground plane.

The omnidirectional radiation pattern of the wristwatch antenna in the *XY*-plane is beneficial to maximize the signal strength at the radio receiver. For the intended application, the test protocol for clinical trials (described in Section 5.5.4 of Chapter 5) specifies that the patient's arm should remain horizontal during measurement as the patient is typically seated or in a laying down position during trials. The radio receiver used for clinical trials, was positioned at a distance of approximately 3 metres from the wristwatch device. The receiver features a linearly polarized antenna that is co-polarized in the above configuration. However, if patient's arm is rotated to a vertical position for example, the radiation nulls of the wristwatch antenna, along the *Z*-axis, can result in cross-polarization effects with up to 25 dB reduction in signal delivered to the receiver, as can be seen from Figure 4.17. However, during clinical trials, reliable wireless communications was demonstrated for all configurations of the patient's arm position up to a distance of 5 m in an indoor clinical lab environment.

Furthermore, the slight discrepancy in the simulated and measured radiation characteristics is attributed to the combined effects of the measurement setup, losses in the ferrite-beaded cable that was not included in the simulation and the possible difference between ε_r of the ABS plastic enclosure material used in simulation and ε_r of the off-the-shelf wristwatch enclosure [129] used in the measurement.

4.6 Performance Evaluation of the Developed Antenna

Table 4.4 summarizes the key performance characteristics of the newly developed 915 MHz wristwatch antenna described in this work (row 11) and the results are compared with the current state-of-the-art Sub-GHz wrist-worn antennas to identify performance improvements, compared with other works in the literature.

Table 4.4: Comparing on-phantom performance of the developed antenna with the literature.

A	B	C	D			E	F	G	H	I
Row	Ref.	Antenna Topology	Dimensions (mm)			f_0 (MHz)	-10 dB *BW* (MHz)	*Gain* (dBi) @ f_0	*h* (%) @f_0	*SAR* (W/kg) @f_0
			L	*W*	*h*					
1	[43]	Loop	40	30	10	920	180	NA	6.4	NA
2	[44]	Dipole	127	25	2	850	160	-8.3	7	3.75
3	[45]	Dipole	145	40	NA	900	160	NA	6.3	0.18
4	[42]	IFA[4]	93	37	5	780	105[1]	NA	7.9	NA
5	[46]	PIFA[4]	64.8	45.6	4.75	866	105	-4.4	26	0.78
6	[47]	Loop	201	56	0.2	900	100	-8[5]	NA	NA
7	[28]	PIFA[4]	44	28	1.6	915	55[1]	-6.09	NA	NA
8	[48]	Dipole[4]	220	10	0.25	922.5	44	-11.2	NA	NA
9	[49]	PIFA[4]	44	44	10	767	35[1]	-5.4	13	NA
10	[50]	PIFA[5]	188	30	6	880	28	NA	83.7	NA
11	**This Work**	**PIFA**	**43.5**	**28.5**	**10.3**	**915**	**28.3**	**-0.57**	**46.8**	**0.0034**
12	[116]	Helix	40	40	14.4	890	23	NA	NA	NA
13	[34]	Patch	86	25	1.6	915	19[3]	-6.87[5]	NA	NA
14	[36]	Helical	110	29	1.55	868	17	-13[5]	NA	NA
15	[37]	Monopole	100	15	0.6	911	14	-5.35	NA	NA
16	[38]	Monopole	40	15	1.8	911	7.5	-5.86	NA	NA
17	[39]	IFA[4]	45	30	5.5	846	7[5]	NA	14.8	NA
18	[40]	PIFA[4]	$\pi \times 25^2 \times 5$			402.5	5.2[2,3]	-12	3.6	NA
19	[30]	PIFA	$\pi \times 25^2 \times 5$			402.5	4.22[2,3]	-9.2	6.9	NA
20	[41]	Loop[5]	50	35	3	868	3.5	-1.44	NA	0.0002
21	[35]	Spiral[5]	$\pi \times 16^2$			915	3[3]	-1.04	NA	NA
22	[117]	PIFA	76.1	13.6	9.5	866	NA	-6.6	8.6	NA
23	[118]	Patch[5]	120	29	0.64	867	NA	-13	NA	NA
24	[119]	PIFA	90	20	3	923	NA	-5	NA	NA

This table is sorted in decreasing order of -10 dB bandwidth in column F

Important Notes:

[1] Antenna requires the use of an impedance matching network

[2] Only the -6 dB impedance bandwidth is reported

[3] Antenna does not meet the -10 dB bandwidth requirements for the targeted band

[4] Antenna was fully integrated in a wristwatch device

[5] Only simulated results are reported

NA = Information not reported

It can be seen from Table 4.4 that the wristwatch antenna developed in this work achieves the minimum required -10 dB impedance bandwidth of 26 MHz for 915 MHz operation. In addition, the developed antenna demonstrates the highest peak realized gain and the second highest radiation efficiency for Sub-GHz wristwatch antennas in the literature.

4.7 Conclusions

A novel bandwidth enhanced wristwatch planar inverted-F antenna (PIFA) operating at 915 MHz has been designed and demonstrated. The developed antenna incorporates two mutually coupled radiating elements denoted Rad_1 and Rad_2. Element Rad_2 was incorporated in the design to enhance the impedance bandwidth of the antenna. With the incorporation of element Rad_2, an improvement of greater than 70 % in the -10 dB impedance bandwidth was achieved when compared against a single element PIFA antenna without element Rad_2.

The prototype antenna achieved a measured -10 dB impedance bandwidth of 28.3 MHz, which meets the minimum bandwidth requirements for use in the 915 MHz ISM band of 26 MHz (902-928 MHz) [55]. In addition, the developed antenna achieved an on-phantom peak-realized gain of -0.57 dBi, which is the highest peak realized gain figure for any Sub-GHz wristwatch antenna reported in the literature. Furthermore, the developed antenna has a simulated radiation efficiency of 46.8 % at 915 MHz, which represented the second highest radiation efficiency for any Sub-GHz wristwatch antenna in the literature. In addition, for an input power of 1 mW, a low peak SAR figure of less 0.1 % of the legal SAR limit of 4 W/kg averaged over 10 g of limb tissue mass was demonstrated [80, 109].

The 915 MHz wristwatch antenna presented in this chapter has been published in [51]. The antenna developed and demonstrated in this work did not take into account the internal components, such as the battery, radio printed circuit board (PCB), SD card and sensor assemblies that are typically present in a practical wristwatch device.

In Chapter 5, a novel low-cost and compact bandwidth enhanced wristwatch antenna design is presented, where all internal components that are present in a physical wristwatch device are considered to ensure accurate EM modelling of the entire wristwatch device assembly.

Chapter 5: Development of Bandwidth Enhanced 915/868 MHz Wristwatch-Integrated Antennas

5.1 Background

In Chapter 4, the development of a first-generation bandwidth enhanced 915 MHz wristwatch antenna was described. However, this antenna assumed an ideal environment close to the antenna structure and did not take into account the effects of nearby internal components and assemblies that exist within a practical wireless wristwatch sensor. Such components include printed circuit board (PCBs) assemblies, battery, sensor assembly and connectors for example.

In this chapter, two new wristwatch-integrated compact antennas operating in the 915 MHz band (North America) and the 868 MHz band (Europe) are proposed and demonstrated. For the proposed antennas, key internal components associated with the wristwatch assembly and functionality are included in the EM model for accuracy. The developed compact antennas aim at achieving enhanced impedance bandwidth, while at the same time maximizing peak realized gain and radiation efficiency performance compared to the state-of-the-art in Sub-GHz wristwatch-integrated antennas. An antenna is an integral component in a wireless communication system and low-cost antennas are desired to minimize the overall cost of next-generation wireless sensor devices. Therefore, the 915 MHz antenna was fabricated using a low-cost flexible polyimide substrate PCB and the 868 MHz antenna was fabricated using a low cost laser direct structuring (LDS) technology. This chapter outlines the design, simulation, implementation and characterization of the proposed 915 and 868 MHz wristwatch antennas, as are presented in the following sections.

5.2 Target Wristwatch Device for Antenna Integration

The aim of this research work is to design compact Sub-GHz wristwatch antennas that can be accommodated within a practical wristwatch wireless sensor system. For the demonstrated prototype system, the wristwatch enclosure case shown in Figure 5.1 was used, which is a modified, off-the-shelf wristwatch assembly [144] and has maximum dimension of 53.9 mm × 44.8 mm × 17 mm. The wristwatch enclosure case uses an acrylonitrile styrene acrylate (ASA) material with a measured relative electrical permittivity ε_r = 2.9 and loss tangent $tan\delta$ = 0.033 at 915 MHz. The wristwatch strap is made of silicone rubber with a measured ε_r = 3 and $tan\delta$ = 0.0001 at 915 MHz. These dielectric properties of ASA plastic and silicone rubber were derived from the measurements taken using a dielectric assessment kit (DAK) from Speag [87]. Figure 5.1 also illustrates the key internal components that are present in a physical wireless sensor device as derived from CAD import of the mechanical design. The sensor device casing includes key internal components required for a functional wireless wristwatch device, including the antenna structure, sensor assembly, radio PCB, motherboard PCB, battery and SD card. The sensor assembly depicted in Figure 5.1 is responsible for the heart rate (HR) and arterial oxygen saturation (SpO_2) measurements required for the target device. The motherboard (processor) PCB is used to process the measured HR and SpO_2 data and transfer the processed data to a Sub-GHz radio transceiver (AT86RF212B) [76] mounted on the radio PCB. The key research focus of this chapter is to develop Sub-GHz antennas and the sensing and processing aspects of the wireless sensor device are not discussed in detail in this thesis work.

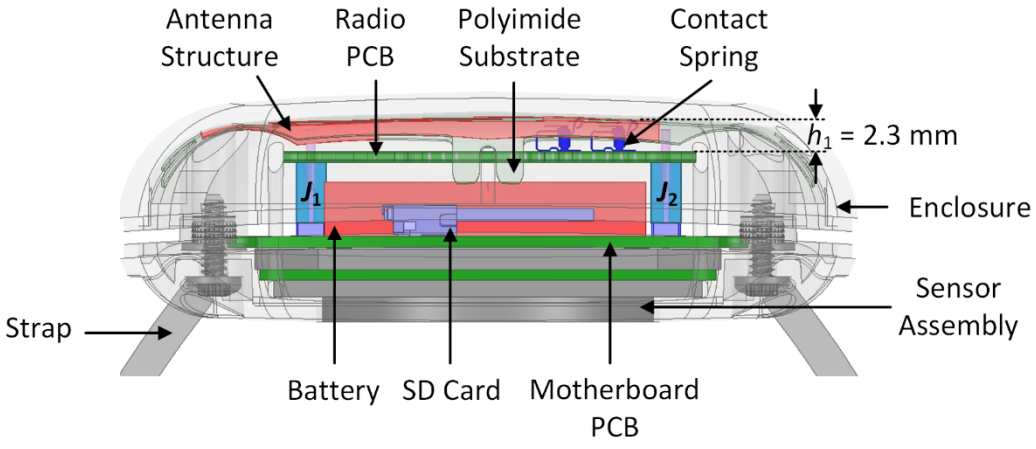


Figure 5.1: Wristwatch sensor device showing various internal components.

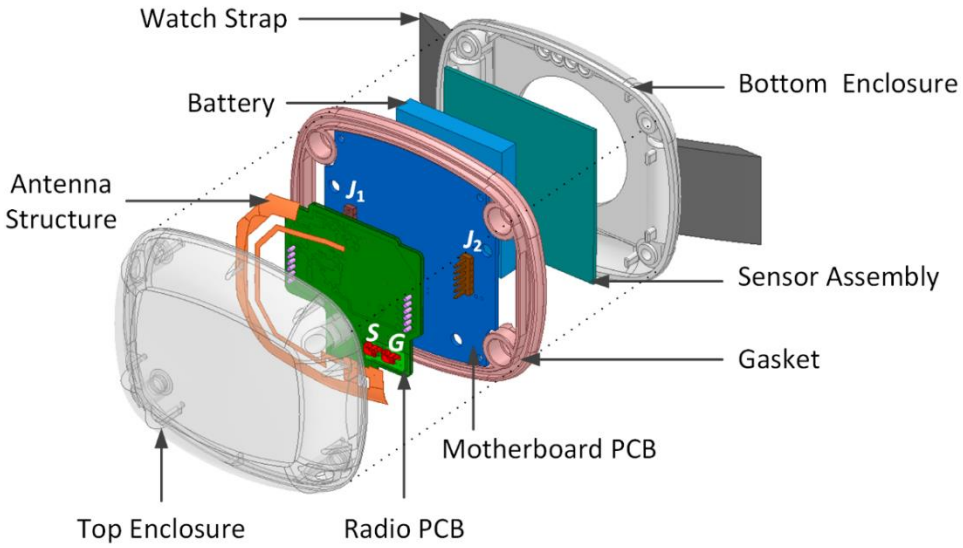


Figure 5.2: Exploded view of the wristwatch wireless sensor device.

In Figure 5.2, the exploded view of the wristwatch sensor device is illustrated to enable better visualization of the assembly. The connectors J_1 and J_2 have been used to join the motherboard PCB to the sensor assembly and the radio PCB. The contact springs denoted *S* (source) and *G* (ground) on the radio PCB are used to excite the antenna structure designed specifically for this system. Furthermore, the wristwatch casing contains an integrated rubber gasket to ensure a waterproof seal between the top and bottom enclosure assemblies. All the above components were included in the design to ensure accurate EM modelling of the entire wristwatch assembly and optimised RF performance characteristics. Note that the antenna EM simulation model includes electrical components such as printed circuit boards, connectors and battery. The dimensions of these components are an appreciable fraction (10 % or greater) of a free-space wavelength at 915 MHz and need to be modelled explicitly for accuracy. However, individual SMD components, with maximum dimensions of less than 0.3 % of a free-space wavelength at 915 MHz (e.g., inductors, capacitors, resistors, LEDs and microcontroller) do not have an appreciable effect and are therefore not included in simulation.

In terms of the phase response of the antenna to an incident plane wave, the effects of curvature of the antenna elements are negligible. The antenna element has an essentially flat configuration as the enclosure has a small change in height across its length. Since the height variation of the elements is approximately 0.006 λ_0 at 915 MHz,

this translates to a phase delay of 0.66 ps with negligible effects on the antenna response.

A large portion of the wristwatch sensor device is occupied by various electronics components such as the sensor assembly, battery, motherboard PCB and radio PCB, and only limited space is available for the antenna integration. The aim of this work was to design compact Sub-GHz antennas that can be accommodated within the size constrained wristwatch device model shown in Figure 5.2. The design of high performance Sub-GHz antennas that could fit into a small area contained within a wristwatch device is challenging because the key performance parameters of an antenna, such as gain, radiation efficiency and impedance bandwidth are fundamentally limited by the antenna size, as described in Chapter 2.

5.3 915/868 MHz PIFA Antenna Design Concept

A simplified view of a conventional quarter-wavelength single element (Rad_1) planar inverted-F antenna (PIFA) topology is illustrated in Figure 5.3(a) [84]. In order to enhance the impedance bandwidth this work proposes a dual-radiator (Rad_1 and Rad_2) based PIFA structure, where both elements are excited from the same source at point *S*, as shown in Figure 5.3(b). Element Rad_2 was included in the design with the aim to enhance the impedance bandwidth of the antenna by improving the impedance matching over the required band of 26 MHz [4, 5]. Furthermore, along with the impedance bandwidth enhancement, the proposed antenna design concept also exhibits improved peak realized gain and radiation efficiency when compared to a single element PIFA antenna. In the following section, the advantages of the proposed antenna design in terms of impedance and radiation performance improvements are described.

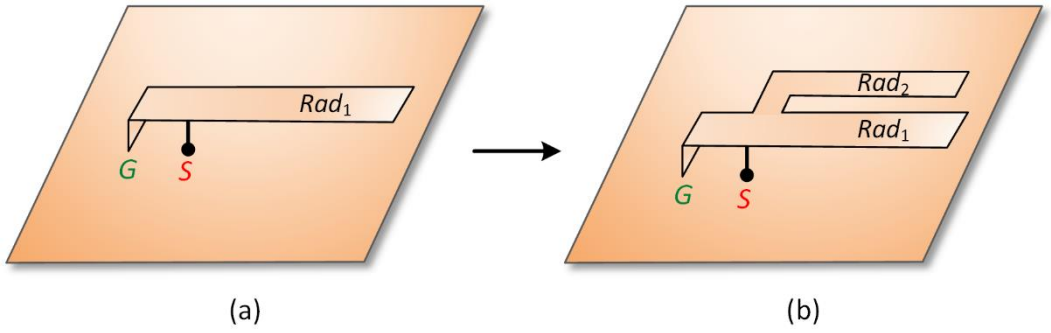


Figure 5.3: (a) Conventional single-element PIFA topology [84], (b) Proposed dual-radiator PIFA antenna design concept.

5.4 Development of a 915 MHz Wristwatch-Integrated Antenna

In this section, the development of a novel, bandwidth enhanced 915 MHz wristwatch-integrated antenna is presented. The new antenna design needs to meet the minimum required -10 dB impedance bandwidth of 26 MHz for 915 MHz band operation as defined by IEEE 802.15.4 standard [55], as well as achieve improved peak realized gain and radiation efficiency when compared to the state-of-the-art Sub-GHz wristwatch-integrated antennas reported in the literature.

5.4.1 915 MHz Antenna Design and Simulations

Having described the antenna design concept above, the implementation of the novel variant of a dual-radiator PIFA topology operating at 915 MHz is now presented. The electromagnetic (EM) simulation of the proposed antenna was performed using Ansys HFSS [137]. Figure 5.4 shows the EM simulation model, where the proposed 915 MHz antenna is integrated within a wristwatch device and placed on a commercial SPEAG SHO-GFPC-V1 phantom arm model Speag [145]. The phantom arm model consists of an outer silicone material with $\varepsilon_r = 30$, electrical conductivity $\sigma = 0.7$ S/m and a mass density $\rho = 1200$ kg/m^3 at 915 MHz [145]. The inner skeleton of the phantom arm has $\varepsilon_r = 30$ and $\sigma = 2.5$ S/m at 915 MHz.

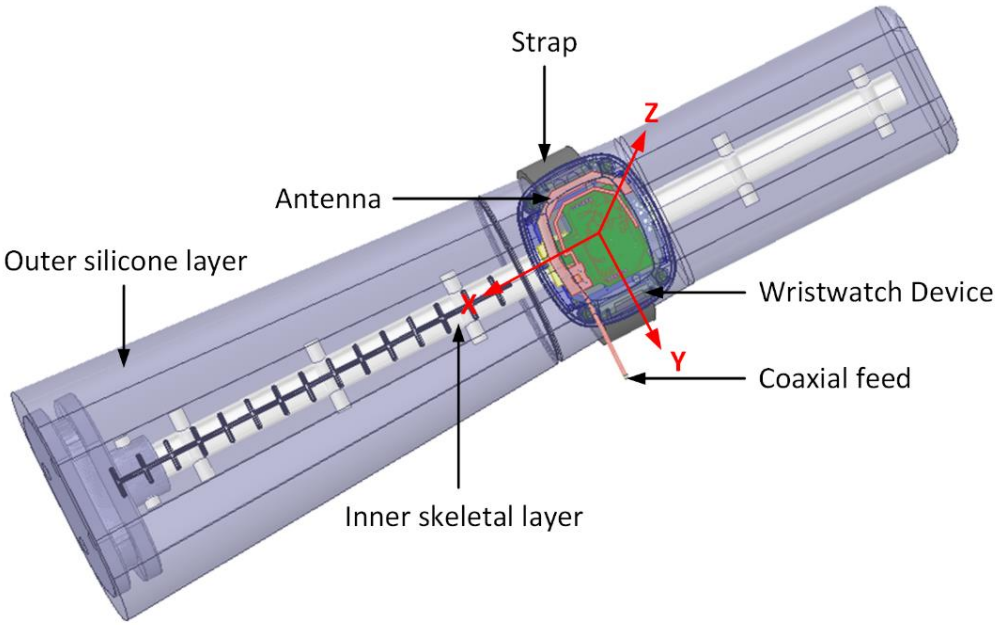


Figure 5.4: Wristwatch model placed on a Speag SHO-GFPC-V1 phantom arm [145].

In the following sections, the design of a 915 MHz wristwatch antenna is presented. The proposed antenna topology was achieved after three design iterations, denoted Antenna-1, Antenna-2 and Antenna-3. This antenna design evolution aimed at enhancing the impedance bandwidth to meet the minimum required -10 dB impedance bandwidth of 26 MHz for 915 MHz band operation, as well as improving the radiation performance when compared to the literature.

5.4.1.1 Antenna-1

The starting point for the design was a single element (Rad_1) planar inverted-F antenna (PIFA) structure (Antenna-1), as shown in Figure 5.5. The total length of Rad_1 (measured along the centre) from the feed point *S* to the end of the element at point *A* is 58.7 mm, which corresponds to a free space electrical length of 0.18 λ_0 at 915 MHz.

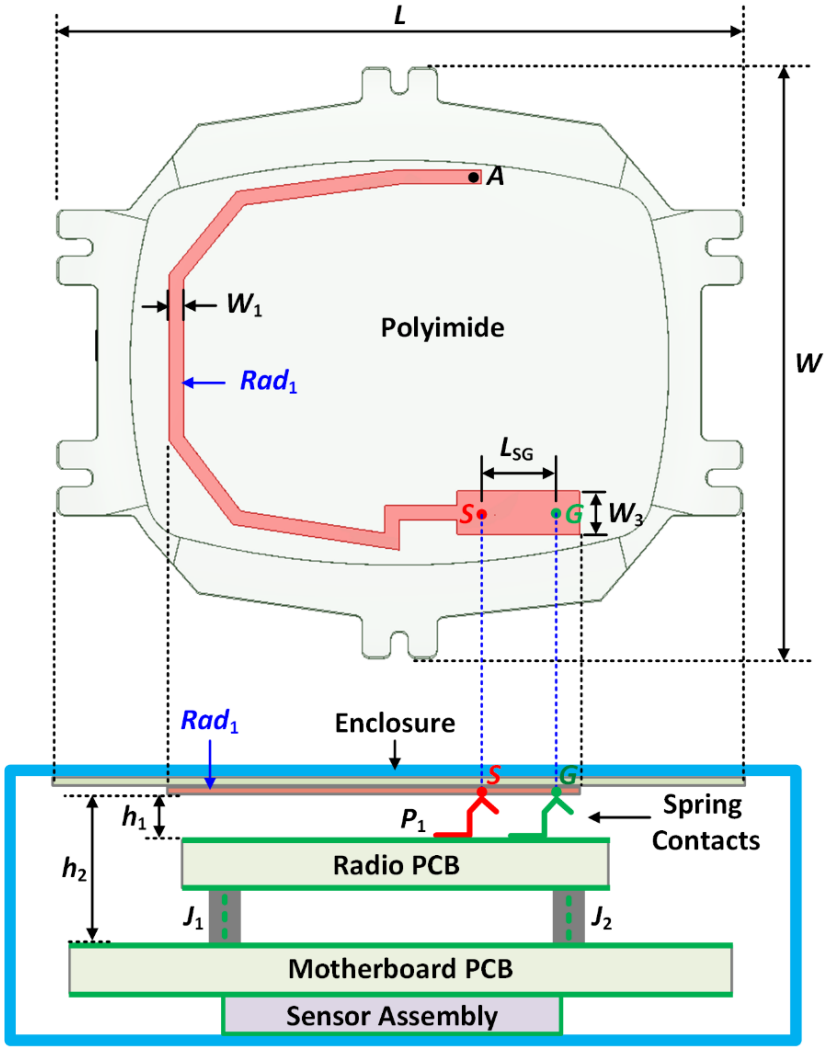


Figure 5.5: Configuration of Antenna-1 in system within a wristwatch device, where the ground planes are highlighted in green for clarity.

The antenna is printed on a low-cost, 0.11 mm thick flexible printed circuit polyimide substrate with a maximum size of L (48 mm) × W (41 mm). The flexible polyimide substrate uses 0.018 mm thick copper metallization and the polyimide dielectric has a measured ε_r = 3.1 and $tan\delta$ = 0.0245 at 915 MHz [87]. The dielectric properties of the polyimide substrate material were measured using a dielectric assessment kit (DAK) from Speag [87]. Figure 5.5 also illustrates the stack-up of various internal assemblies and components inside the wristwatch device. Such internal assemblies and components include a radio PCB, motherboard PCB, sensor assembly, connectors J_1 and J_2, and two spring contacts to connect to and feed the antenna. As shown in Figure 5.5, the Radio PCB feeds the antenna via spring contacts of height h_1 = 2.3 mm. The spring contacts that are mounted on the radio PCB excite the antenna by making contact at points S and G on the antenna structure when the wristwatch device is closed. The benefits of using spring contacts are that they eliminate the complexity of using a cable to feed the antenna. As shown in Figure 5.5, via the spring contacts, the antenna is excited at port P_1 with a 50 Ω unbalanced feed with a signal at point S and ground at point G. The metal section bridging points S and G implements a shunt inductive element that is used for impedance matching of the antenna by counteracting the capacitance of element Rad_1 that is in close proximity to the ground planes of the radio PCB beneath [146].

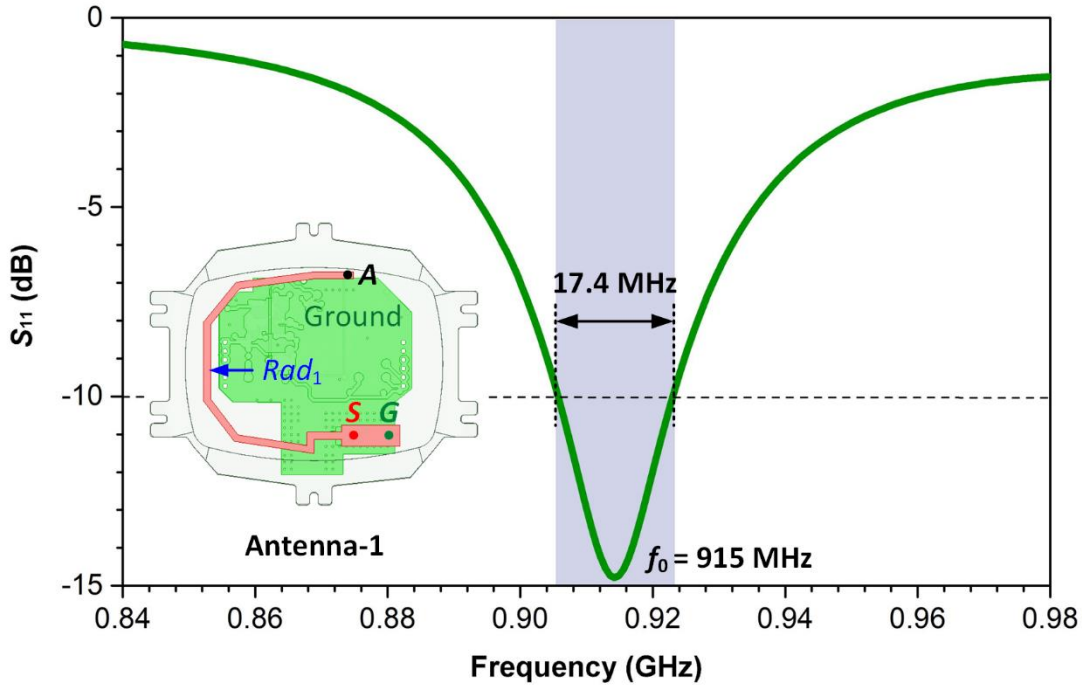


Figure 5.6: Antenna-1 topology and corresponding EM simulated S_{11} response.

In Figure 5.6, the antenna structure and the simulated S_{11} response for Antenna-1 is shown. As highlighted, Antenna-1 is resonant at f_0 = 915 MHz but has a limited -10 dB impedance bandwidth of 17.4 MHz that does not meet the minimum required impedance bandwidth of 26 MHz for 915 band operation [55]. Furthermore, Antennna-1 has a simulated peak realized gain of -5.4 dBi and a radiation efficiency of 14.2 % at 915 MHz.

5.4.1.2 Antenna-2

In order to improve the impedance bandwidth, the second antenna iteration (Antenna-2) was designed, as shown in Figure 5.7. For Antenna-2, the second element Rad_2 was incorporated in the design for the purpose of bandwidth enhancement. Both the elements, Rad_1 and Rad_2 were excited from the same source at point *S*. Elements Rad_1 and Rad_2 are extended beyond the ground plane with the aim to minimize the induction of image current on the ground planes.

As shown in Figure 5.7, Antenna-2 is resonant at f_0 = 915 MHz for an electical length of approximately $\lambda_0/4$ for both radiating elements Rad_1 and Rad_2, measured along the centre from the feed point *S* to the element ends *A* and *B*, respectively. Antenna-2 with two radiating elements achieves a -10 dB impedance bandwidth of 21.7 MHz which is 4.3 MHz or 24.7 % enhanced compared to the Iteration-1 antenna.

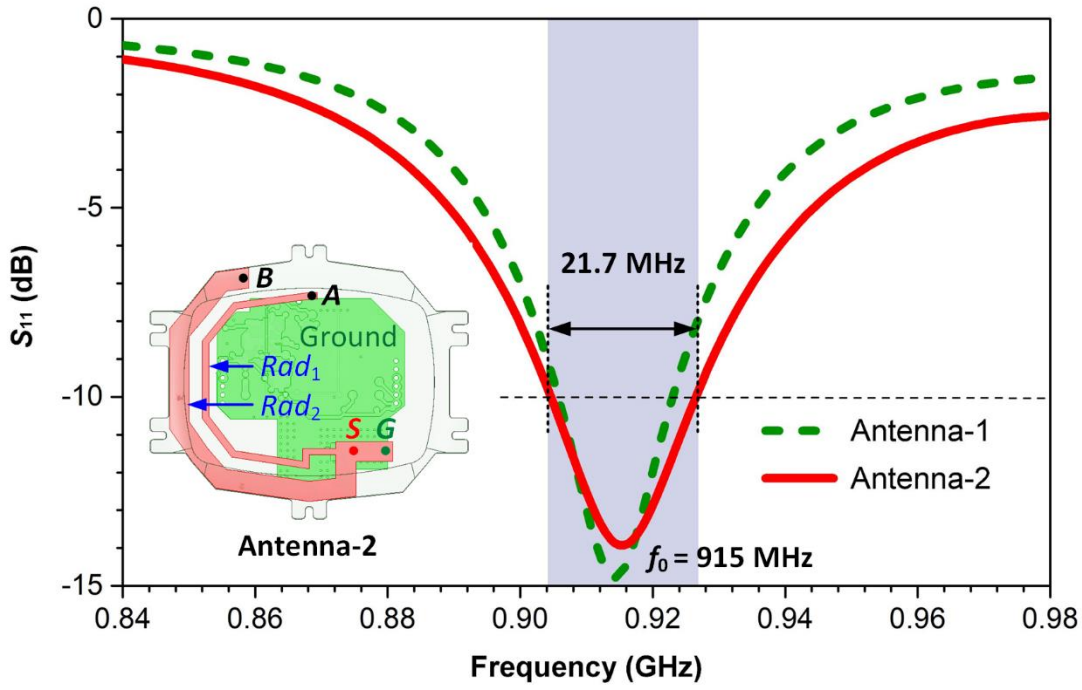


Figure 5.7: Antenna-2 topology and corresponding EM simulated S_{11} response.

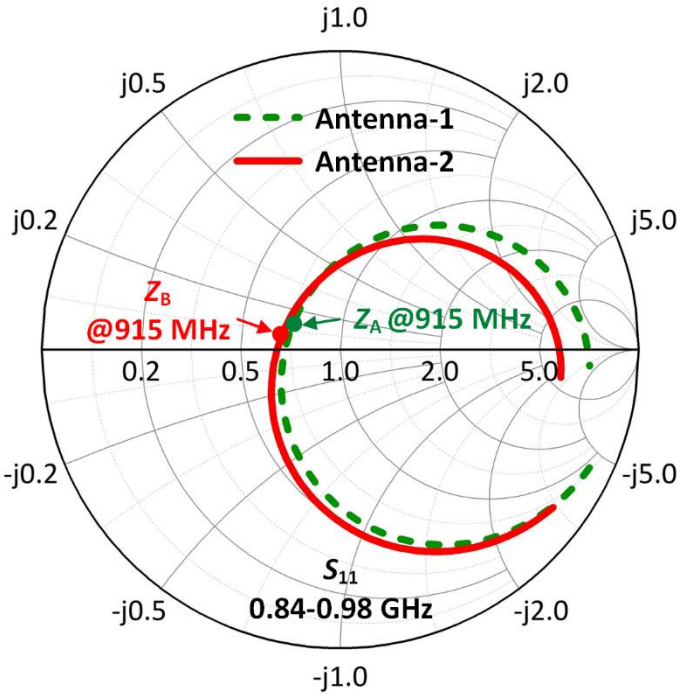


Figure 5.8: EM Simulated complex S_{11} response of Antenna-1 and Antenna-2.

This impedance bandwidth enhancement is explained by comparing the simulated input impedance response of Antenna-1 and Antenna-2 on the Smith chart from 0.84 to 0.98 GHz, as shown in Figure 5.8. At f_0 = 915 MHz, the input impedance for Antenna-1 is denoted Z_A and for Antenna-2 the input impedance is denoted Z_B.

A PIFA antenna can be represented as a series equivalent *RLC* circuit [147] with the quality factor (Q) given as in equation (5.1) [60, 65]:

$$Q = \frac{1}{R}\sqrt{\frac{L}{C}} \tag{5.1}$$

In equation (5.1), parameters *R*, *L* and *C* represent the lumped antenna resistance, inductance and capacitance, respectively.

The impedance bandwidth of an antenna is inversely proportional to the quality factor, as seen from equation (5.2) [59].

$$Q = \frac{f_C}{\mathrm{BW}} \tag{5.2}$$

where, f_C is the centre frequency of operation and *BW* represents the -3 dB impedance bandwidth [60].

When element Rad_2 is introduced, a net capacitive loading effect is observed that results in lowering Q and enabling the input impedance of Antenna-2 to be matched over a wide frequency range. Therefore, the -10 dB impedance bandwidth of Antenna-2 is enhanced to 21.7 MHz compared to 17.4 MHz bandwidth for Antenna-1. However, the achieved impedance bandwidth for Antenna-2 is still 4.3 MHz lower than the required impedance bandwidth of 26 MHz for 915 MHz band operation [55]. In addition, Antenna-2 has a simulated peak realized gain of -4.01 dBi and a radiation efficiency of 21.1 % at 915 MHz.

5.4.1.3 Antenna-3 (proposed antenna)

With the motivation to further enhance the bandwidth to meet the minimum required -10 dB impedance bandwidth of 26 MHz, Antenna-2 was further optimized to result in Antenna-3, as shown in Figure 5.9. The antenna structure shown in Figure 5.9 represents the final design that led to the proposed antenna structure with a -10 dB impedance bandwidth of 26.2 MHz. For the proposed antenna structure, an additional shunt inductive section between points C and G was added to further control the input impedance and thus enhance the impedance bandwidth of Antenna-3 compared to Antenna-2, as explained below.

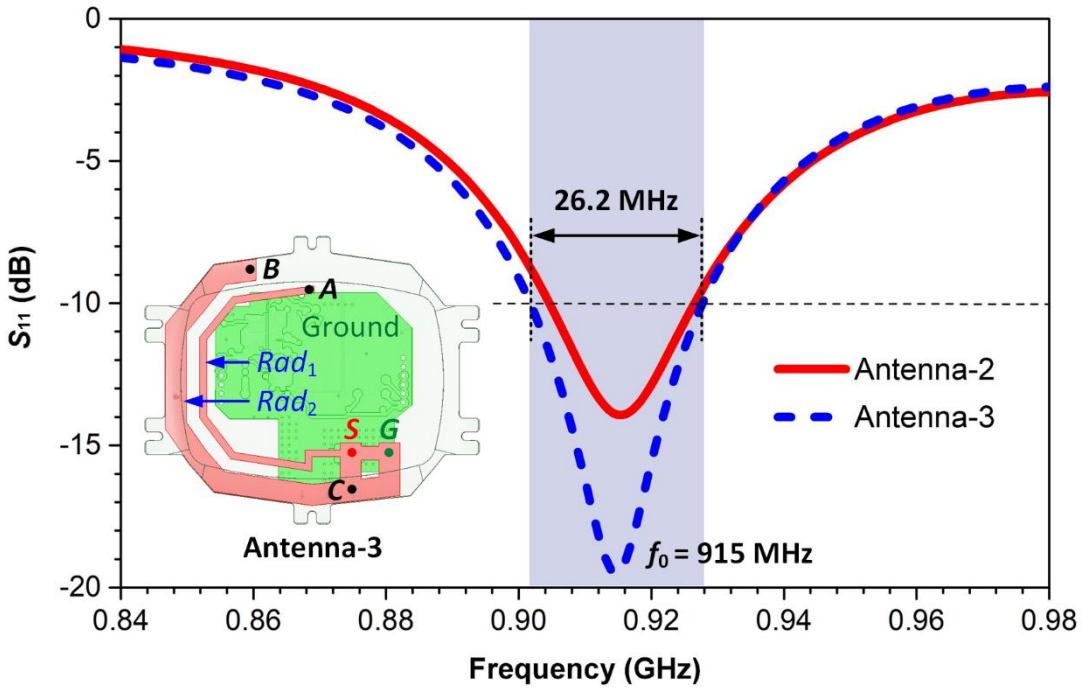


Figure 5.9: Antenna-3 topology and corresponding EM simulated S_{11} response.

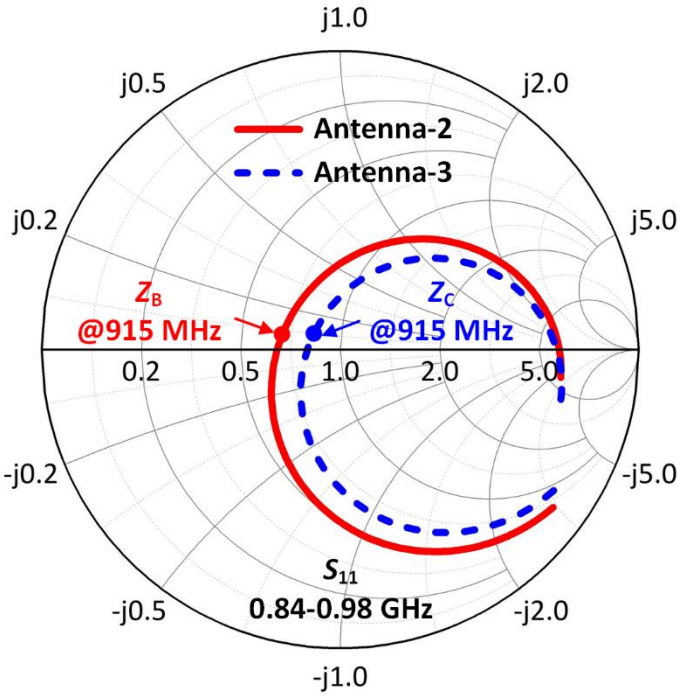


Figure 5.10: EM Simulated complex S_{11} response of Antenna-1 and Antenna-3.

This impedance bandwidth enhancement is explained by comparing the simulated input impedance response for Antenna-2 and Antenna-3 on the Smith chart from 0.84 to 0.98 GHz, as shown in Figure 5.10.

At f_0 = 915 MHz, the input impedance for Antenna-2 is denoted as Z_B and for Antenna-3 the input impedance is denoted as Z_C. As shown in Figure 5.10, introducing the conductive section between the points *C* and *G* increases the antenna resistance at 915 MHz, which leads to a reduced quality factor, as can be seen from equation (5.1).

Now from equation (5.2), it can be seen that the reduced quality factor results in improving the impedance bandwidth of Antenna-3. As shown in Figure 5.9, Antenna-3 has achieved a -10 dB impedance bandwidth of 26.2 MHz compared to 21.7 MHz for Antenna-2. In addition, the simulated results for the proposed antenna achieved a peak realized gain of -4.14 dBi and a radiation efficiency of 19.8 % at 915 MHz.

5.4.1.4 Antenna Design Evolution Summary

The impedance and radiation performance of the three antennas described above are summarized in Table 5.1 showing that Antenna-3 (proposed antenna) has achieved the required impedance bandwidth of 26 MHz for 915 MHz operation [55].

Table 5.1: Performance comparison of the 3 iterations.

Antenna Design Evolution	- 10 dB impedance Bandwidth (MHz)	Peak realized Gain at 915 MHz (dBi)	Radiation Efficiency at 915 MHz (%)
Antenna-1	17.4	-5.4	14.2
Antenna-2	21.7	-4.01	21.1
Antenna-3	26.2	-4.14	19.8

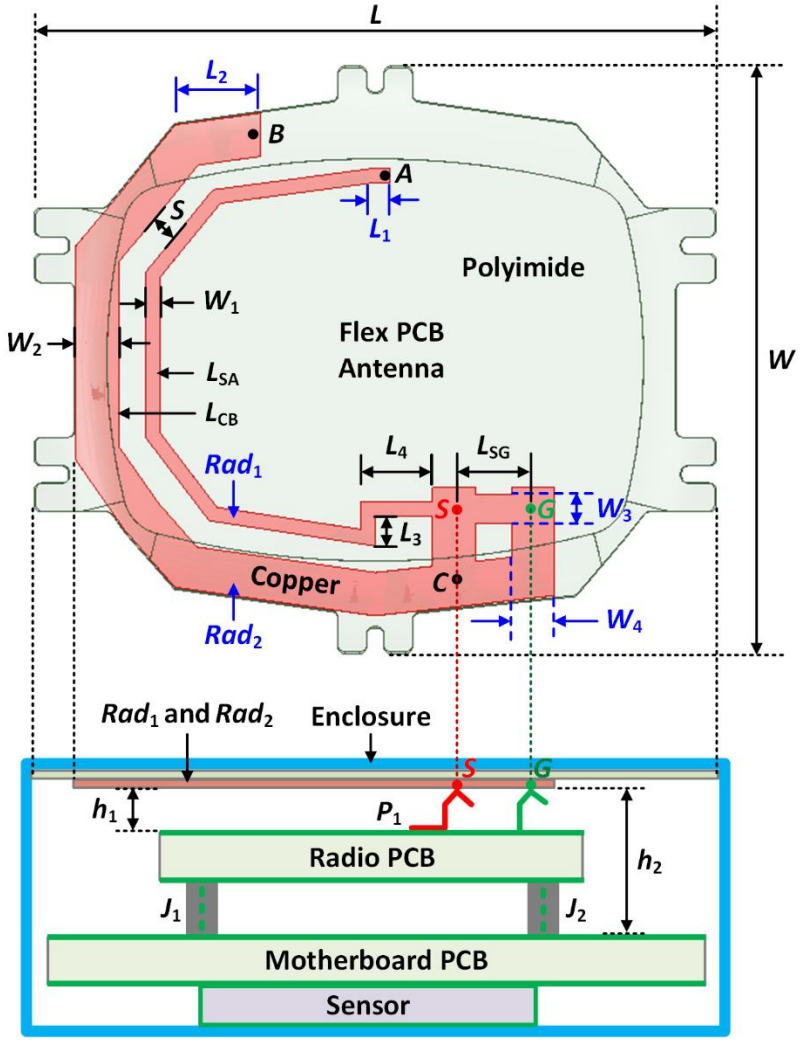


Figure 5.11: Configuration of the proposed antenna in system within a wristwatch device, where the ground planes are highlighted in green for clarity.

The final configuration of the proposed dual-radiator 915 MHz PIFA wristwatch antenna is shown in Figure 5.11.

5.4.1.5 Parametric Analysis of the Proposed 915 MHz Antenna

In order to optimize the antenna for 915 MHz operation (Antenna-3), the effects of several key parameters were investigated using EM simulations. Note that in the parametric analysis, only one parameter was varied at a time while the other parameters were kept constant, as listed in Table 5.2. In this section, the vertical shaded strip on the S_{11} response plots represents the minimum required -10 dB impedance bandwidth of 26 MHz for 915 MHz band operation.

First, the influence of parameter L_1 (end length of Rad_1) that determines the total length of Rad_1 was studied and the resulting S_{11} responses are presented in Figure 5.12. The results show that parameter L_1 mainly controls the resonant frequency with little effect on the impedance matching of the antenna. The resonant frequency decreases with increasing value of L_1 mainly because of the increase in the effective electrical length of element Rad_1 and the proposed antenna is resonant at 915 MHz for L_1 = 0.3 mm.

Secondly, the influence of parameter L_2 (end length of Rad_2) that determines the total length of Rad_2 was investigated and the resulting S_{11} response is summarized in Figure 5.13. Increasing the value of parameter L_2 primarily affects the resonant frequency of the antenna.

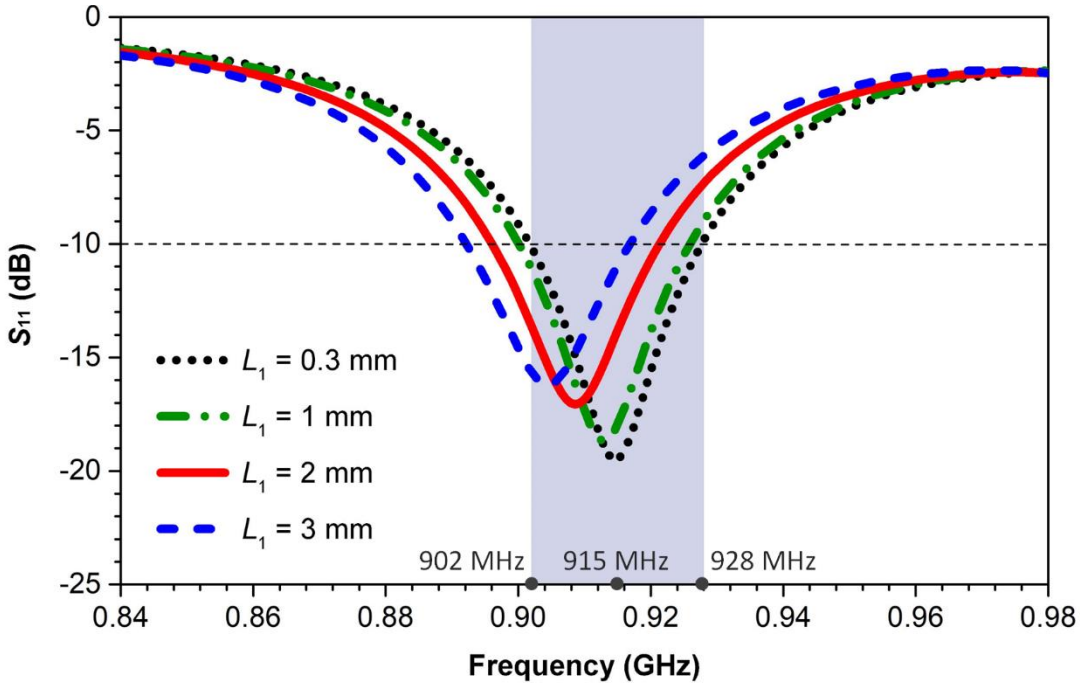


Figure 5.12: EM Simulated S_{11} response showing effects of varying parameter L_1.

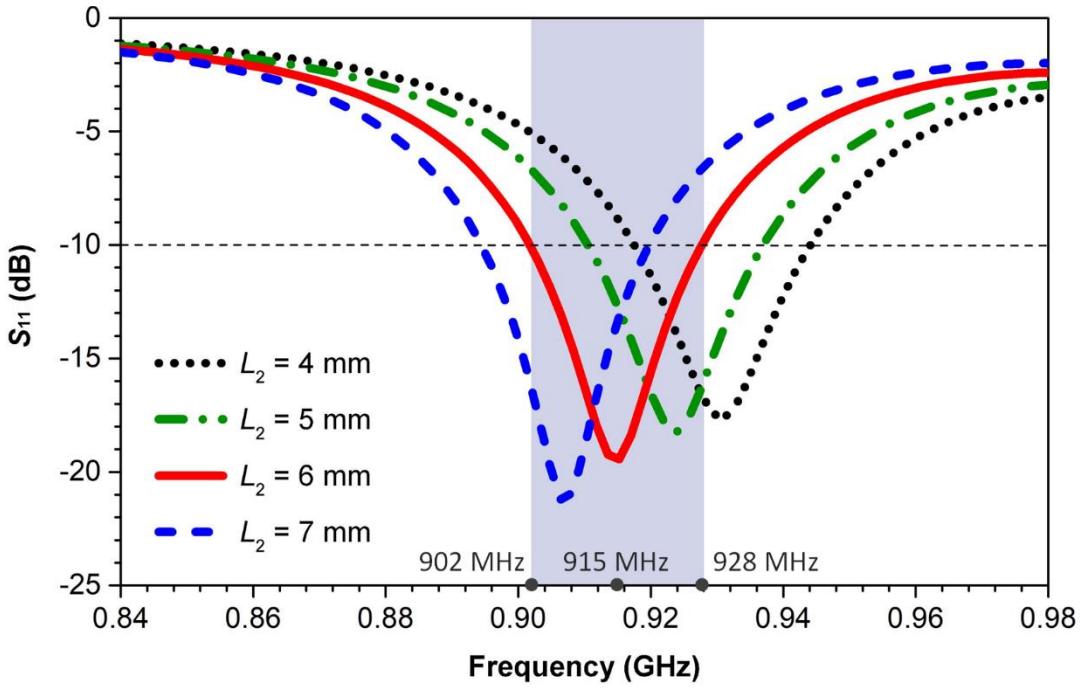


Figure 5.13: EM Simulated S_{11} response showing effects of varying parameter L_2.

With an increase in L_2, the effective electrical length of element Rad_2 increases and thus the resonant frequency decreases. The antenna is resonant at 915 MHz for L_2 = 6 mm. In addition, varying length L_2 also has an influence on the input impedance and thus affects the S_{11} magnitude (impedance matching) of the antenna.

Next, the effects of varying the width W_3 of the shunt inductive section between the feed point *S* and ground *G* were investigated and the resulting S_{11} response is illustrated in Figure 5.14. The S_{11} results show that parameter W_3 mainly controls the impedance matching with a small influence on the resonant frequency of the antenna. The input impedance is best matched to 50 Ω for W_3 = 2 mm, where the antenna is resonant at 915 MHz.

Lastly, the effects of varying width (W_4) of the second shunt section between point *C* and ground *G* were investigated and the S_{11} results are summarized in Figure 5.15. The resonant frequency increases with increasing W_4 because the effective inductance at the input port of the antenna decreases with increasing the width W_4, as shown on the Smith chart Figure 5.16. Varying parameter W_4 affects the input impedance and thus controls the impedance matching. As shown in Figure 5.16, the antenna is best matched to 50 Ω for W_4 = 3 mm.

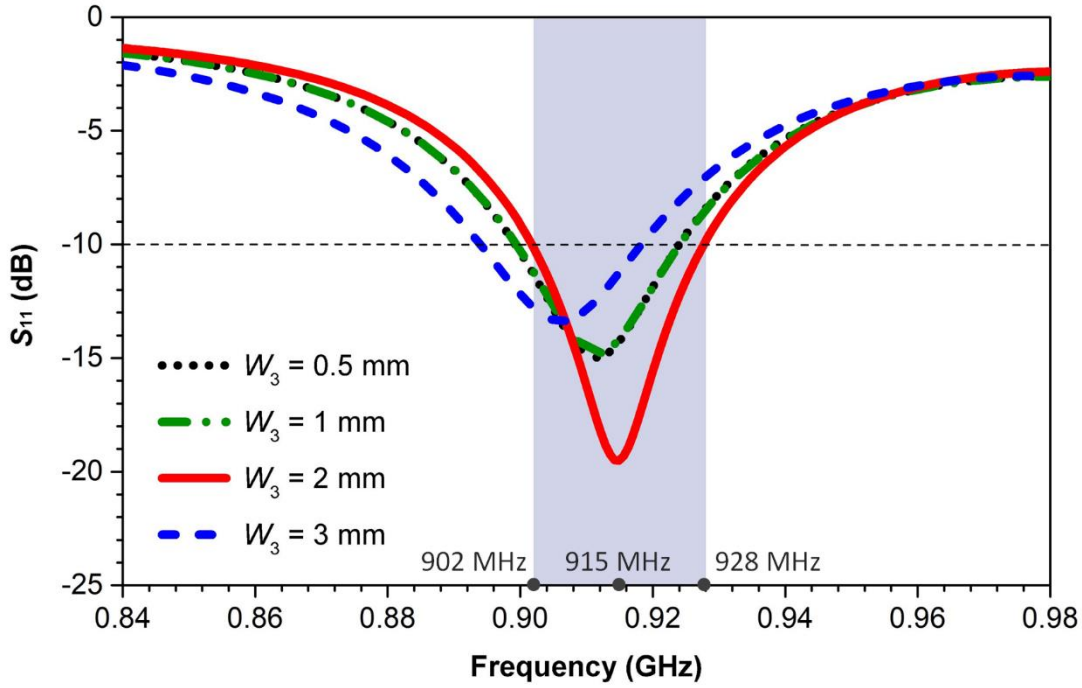


Figure 5.14: EM Simulated S_{11} response showing effects of varying parameter W_3.

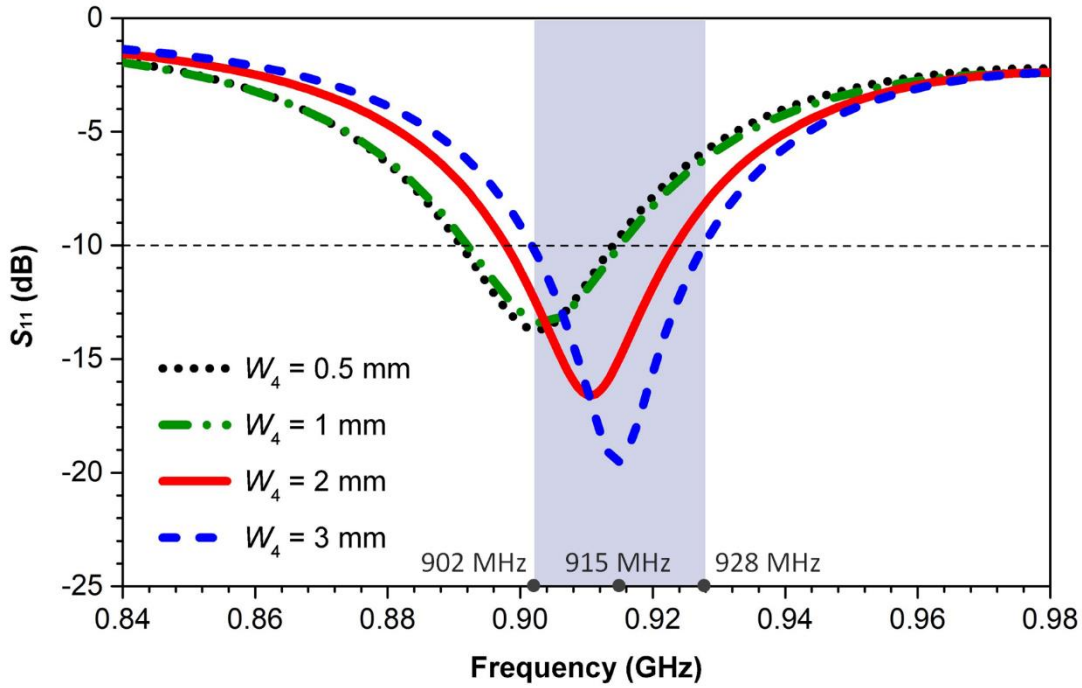


Figure 5.15: EM Simulated S_{11} response showing effects of varying parameter W_4.

This parametric study enabled the understanding of the methods to control the resonant frequency and impedance matching to optimizing the antenna for 915 MHz operation.

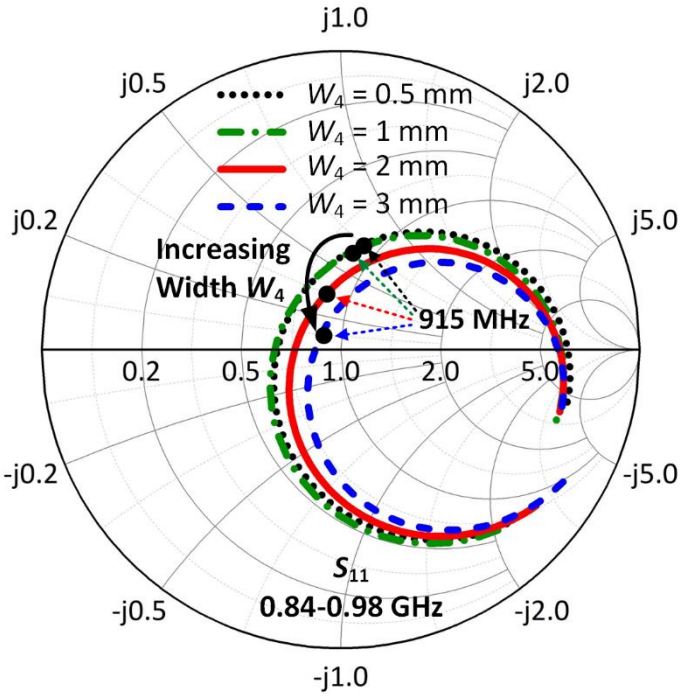


Figure 5.16: EM Simulated complex S_{11} response for varying parameter W_4.

The final design parameters of the proposed antenna are listed in Table 5.2. Also note that the width of the track between points *S* and *C* is fixed at 4 mm.

Table 5.2 Final design parameters of the proposed 915 MHz antenna.

Parameter Name	Value (mm)	Parameter Name	Value (mm)
L	48	W	41
L_{SA}	53.3	W_1	1
L_{CB}	58	W_2	3
L_1	0.3	W_3	2
L_2	6	W_4	3
L_3	2	S	2
L_4	5	h_1	2.3
L_{SG}	2.5	h_2	7.5

5.4.2 Equivalent Circuit Model of the Proposed 915 MHz Antenna

To better understand the resonant behaviour of the proposed antenna (Antenna-3) shown in Figure 5.17(a), an equivalent circuit model was developed using AWR Microwave Office [148].

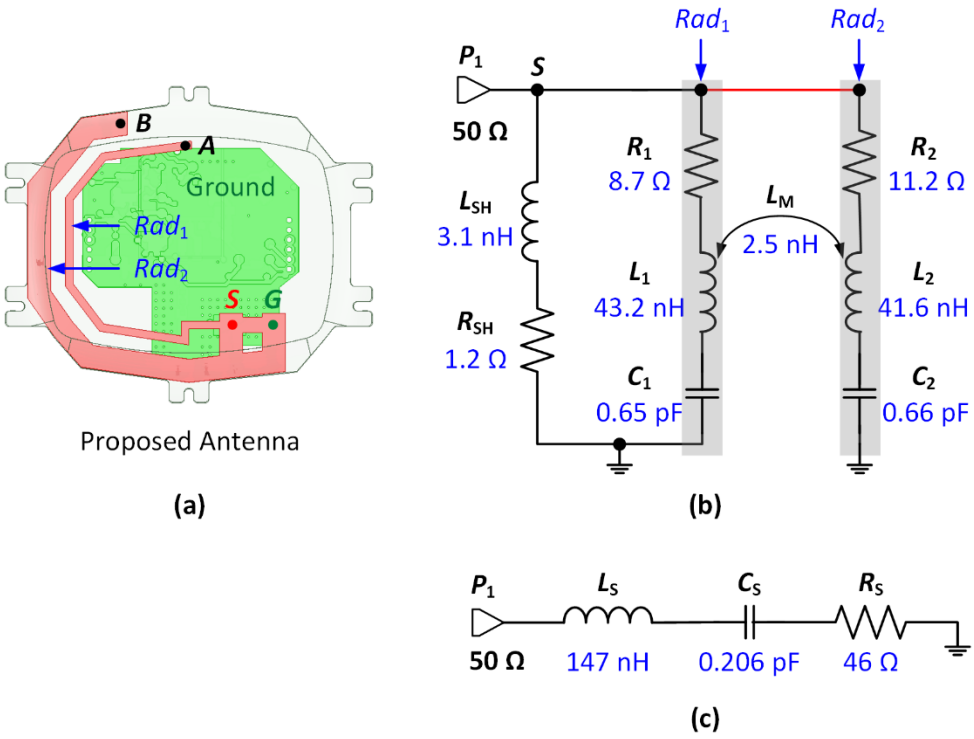


Figure 5.17: (a) Proposed antenna topology, (b) 3-branch equivalent circuit model and (c) Single-branch equivalent circuit model.

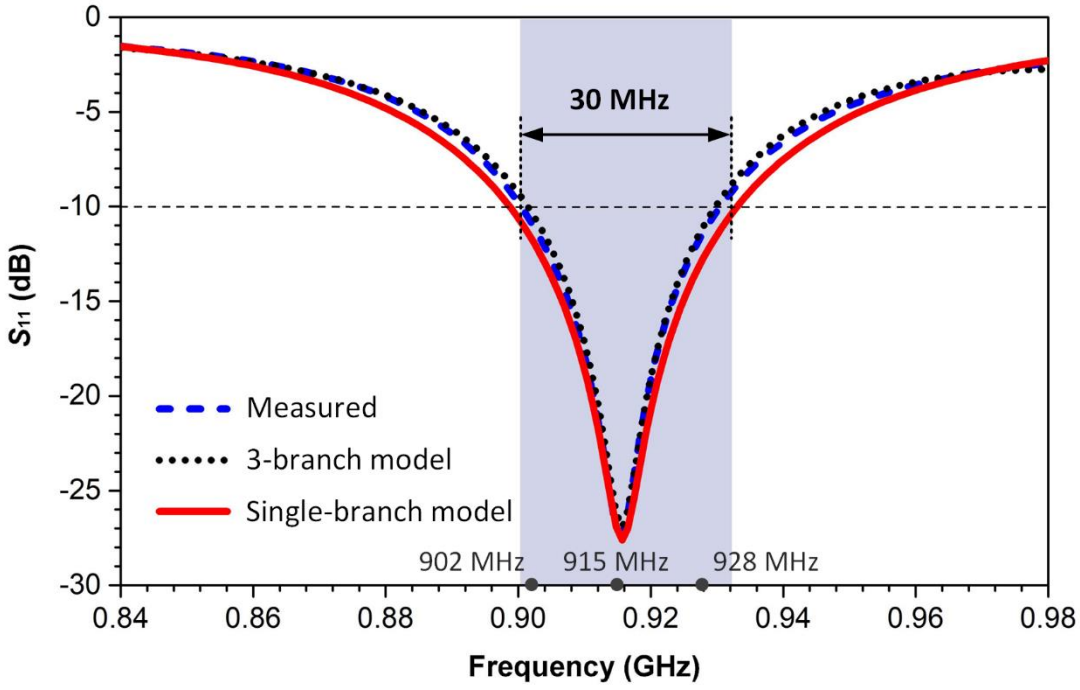


Figure 5.18: Circuit Simulated and measured S_{11} responses for the proposed antenna.

The proposed antenna can be represented by a 3-branch equivalent circuit model shown in Figure 5.17(b), where the first series $R_1L_1C_1$ branch represents element Rad_1 and the second series $R_2L_2C_2$ branch represents element Rad_2.

The third branch L_{SH} with resistance R_{SH} represents the effective shunt inductive section between excitation points *S* and ground *G*. The inductive coupling between elements Rad_1 and Rad_2 is modelled using a mutual inductance L_M. The red line connection in Figure 5.17(b) shows that both elements Rad_1 and Rad_2 are excited from the same source at point *S*. For the purpose of understanding the resonant behaviour, the 3-branch equivalent circuit in Figure 5.17(b) can be reduced to a lumped series $R_S L_S C_S$ circuit with a single resonant frequency, as shown in Figure 5.17(c). The resonant frequency for the single branch circuit is calculated to be $f_0 = 1/\left(2\pi\sqrt{L_S C_S}\right) = 914.6$ MHz, which is close to 915 MHz.

Note that the equivalent circuit component values shown in Figure 5.17(b, c) were derived from automatic parameter fitting or optimization against the S_{11} measured data (measurements described in Section 5.4.7 of this chapter) in AWR circuit simulator [148], and were not obtained from calculations based on the canonical form of the circuit. A random optimization method was chosen to vary the circuit parameters shown in Figure 5.17 in order to reduce the error between the measured and simulated S_{11} magnitude responses to a value of less than 0.01 (absolute value) with a frequency range from 0.84 GHz to 0.98 GHz.

Figure 5.18 compares the S_{11} response of the 3-branch and the single-branch equivalent circuit models with the measured response, where both the circuit models are resonant only at one frequency f_0. This equivalent circuit model analysis suggests that when the two radiating elements (Rad_1 and Rad_2) are excited from the same source point, the antenna is resonant at a single frequency and thus the 3-branch equivalent circuit model can be reduced to a single-branch $R_S L_S C_S$ circuit.

5.4.3 Surface Current Distribution of the 915 MHz Antenna

In Figure 5.19(a), the simulated surface current distribution of the proposed antenna is illustrated. At resonance, large magnitude currents are observed to flow on both elements Rad_1 and Rad_2 and reduce to zero at both open ends which is expected for a PIFA antenna [141]. A large current flow is also observed at point *a* along the shunt inductive tuning path between the signal (*S*) and ground (*G*) contacts. This is expected due to the low impedance (small resistive and inductive components) along this short inductive section.

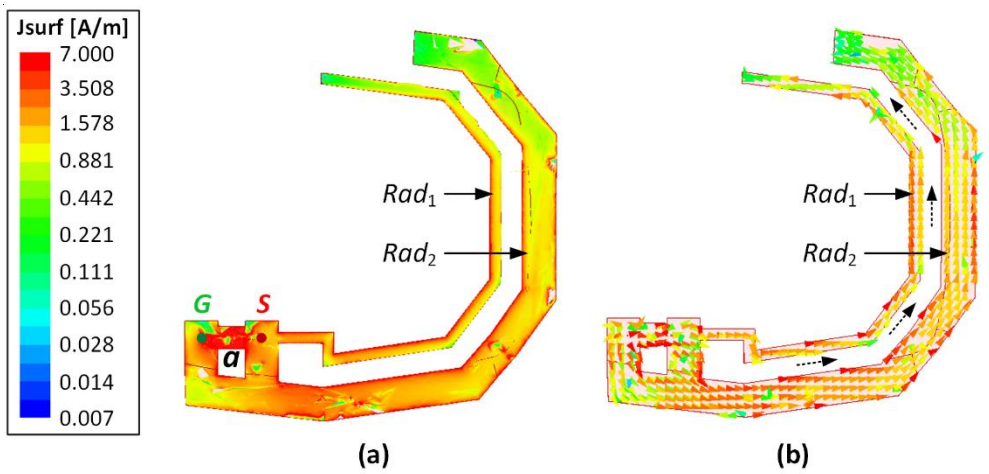


Figure 5.19: EM Simulated surface current distribution of the antenna at 915 MHz.

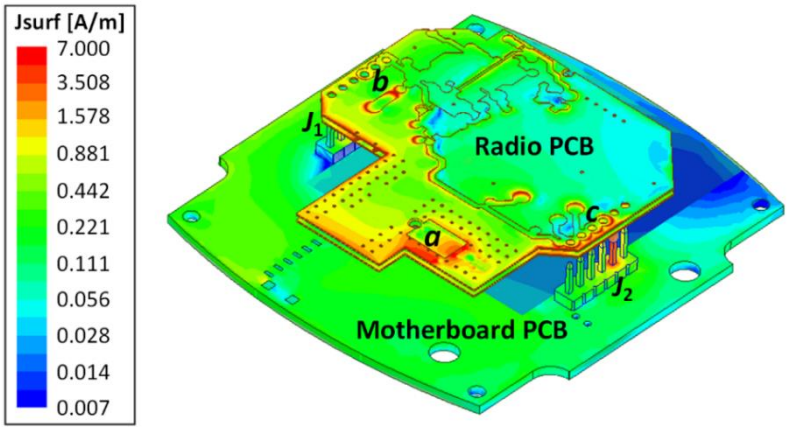


Figure 5.20: EM Simulated surface current distribution on the ground planes at 915 MHz.

Figure 5.19(b) shows the simulated surface current distributions in vector form at 915 MHz. The direction of current flow on both elements Rad_1 and Rad_2 are in the same direction because both elements are excited from the same feed point *S* and have approximately the same electrical length (quarter-wavelength).

In Figure 5.20, the simulated surface current distribution on the radio and motherboard ground planes at 915 MHz is illustrated. The radio PCB is located closer (2.3 mm) to the antenna as compared to the motherboard PCB (7.5 mm) and therefore large magnitude currents are observed on the radio PCB. On the radio ground plane, large magnitude currents are also observed along paths *a* to *b* and *a* to *c*. Electromagnetic coupling also exists between the antenna and motherboard ground PCB and these current paths (denoted *a*, *b* and *c*) represent the path of return current flow from the radio ground plane to the ground plane of the motherboard via the ground pin connections in connectors J_1 and J_2.

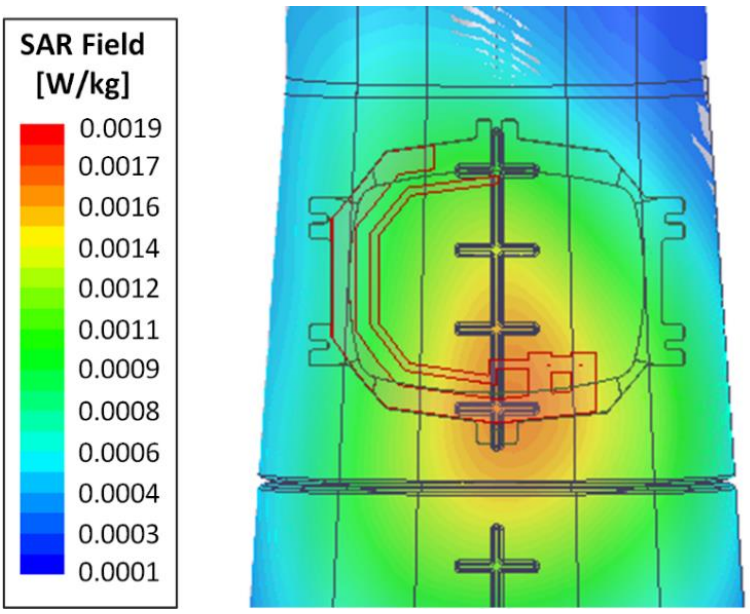


Figure 5.21: EM Simulated SAR distribution on the phantom arm at 915 MHz.

5.4.4 Specific Absorption Rate (SAR) Evaluation of the 915 MHz Antenna

The specific absorption rate (SAR) is a measure of the rate at which RF power is absorbed by the human body when exposed to electromagnetic (EM) radiation [78]. The RF power absorption is harmful to the human tissue and for wrist-worn wireless devices, a maximum permissible limit of 4 W/kg is defined by Federal Communications Commission (FCC) [109] and International Commission on Non-Ionizing Radiation Protection (ICNIRP) guidelines [80]. Figure 5.21 shows the simulated SAR distribution on a Speag SHO-GFPC-V1 phantom arm [145] at 915 MHz.

For an input power of 1 mW, a low peak SAR figure of 0.0019 W/kg averaged over 10 g of wrist tissue mass was obtained. This SAR figure is 3 orders of magnitude lower than the maximum permissible SAR limit of 4 W/kg averaged over 10 g of wrist tissue, as defined in [80, 109]. The radio and motherboard ground planes of the PIFA antenna provide shielding to EM radiation towards the human arm and play a critical role in achieving the low SAR figure.

5.4.5 Radiation Mechanism of the proposed 915 MHz antenna

In Figure 5.22, the E-field distribution at 915 MHz in the YZ-plane (passing through the ends of elements Rad_1 and Rad_2) is illustrated to explain the radiation mechanism of the proposed antenna.

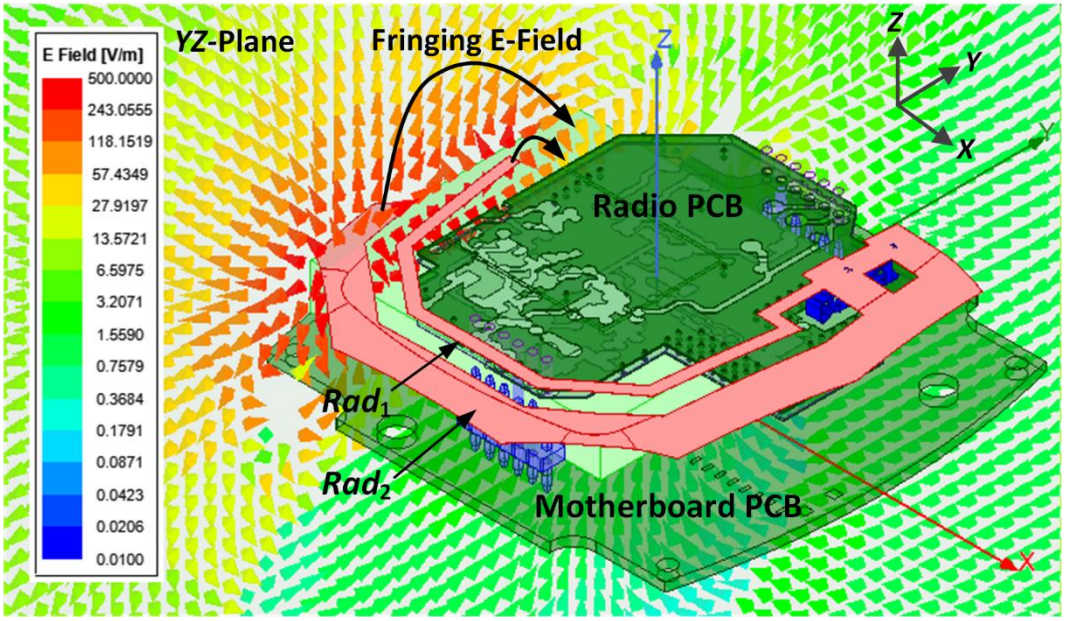


Figure 5.22: E-field distribution in the *YZ*-plane at 915 MHz

Fringing E-field originates from the end of the two radiating elements and terminates to the system ground planes, namely radio and motherboard PCB. Therefore, as illustrated in Figure 5.22, the fringing fields at the end of the elements are the main source of radiation for the proposed antenna [149-152].

5.4.6 Simulated 3D Radiation Pattern of the Proposed 915 MHz Antenna

Figure 5.23 shows the simulated 3D realized gain radiation pattern of the proposed antenna at 915 MHz.

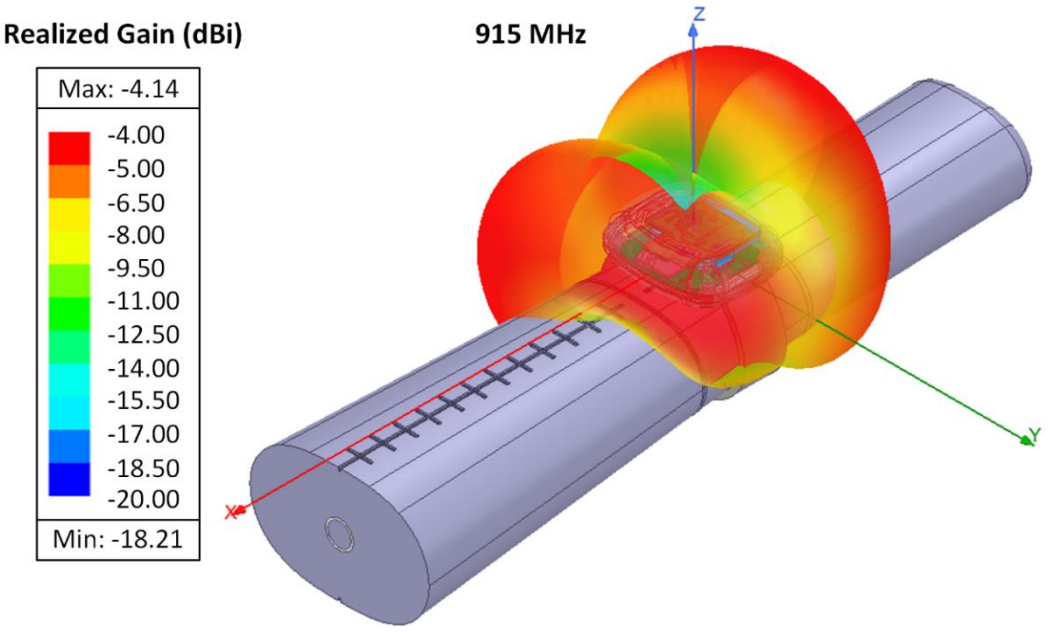


Figure 5.23: EM Simulated 3D Realized Gain radiation pattern at 915 MHz.

The radiation pattern is similar to a PIFA antenna [40] and the finite ground planes (radio and motherboard PCBs) of the PIFA minimize the power radiation towards the phantom arm. The antenna has omnidirectional radiation characteristics in the *XY*-plane. The antenna exhibits radiation nulls in the *YZ*- and XZ-planes. These nulls are expected due to the shielding effect of the finite PIFA ground planes and energy absorption of the wrist with the nulls in the axis normal to the PIFA ground planes (along the *Z*-axis). As depicted in Figure 5.23, the proposed antenna achieves a simulated peak realized gain of −4.14 dBi at 915 MHz.

The EM simulated performance characteristics of the proposed antenna for the final design parameters listed in Table 5.2 are summarized in Table 5.3.

Table 5.3: The EM simulated performance summary of the proposed 915 MHz antenna.

-10 dB impedance bandwidth (MHz)	Peak realized gain at 915 MHz (dBi)	Radiation Efficiency at 915 MHz (%)	SAR at 915 MHz at 1 mW (W/kg)
26.2	-4.14	19.8	0.0019

5.4.7 Measurements of the 915 MHz Wristwatch Antenna

In order to validate the simulated results, a prototype of the proposed 915 MHz antenna was fabricated and measured. A photograph of the fabricated antenna that is attached to the wristwatch enclosure using cyanoacrylate adhesive is shown in Figure 5.24.

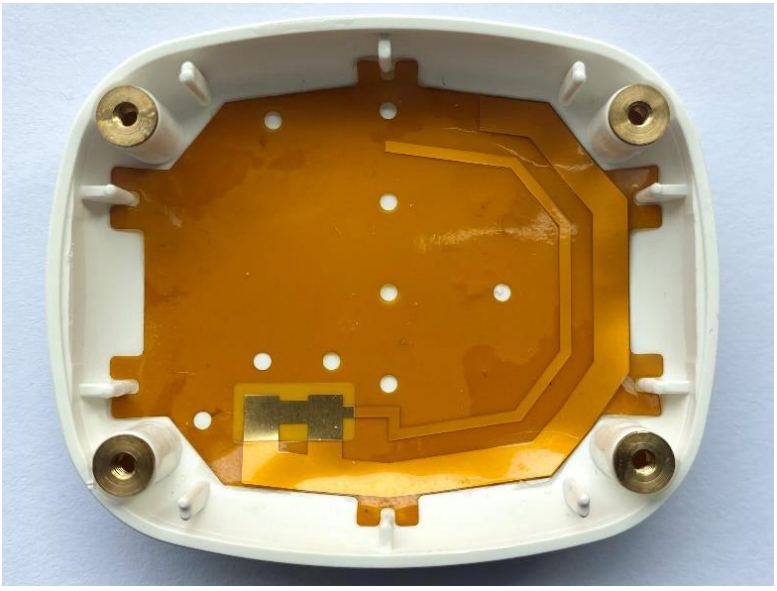


Figure 5.24: Photograph of the fabricated 915 MHz antenna.

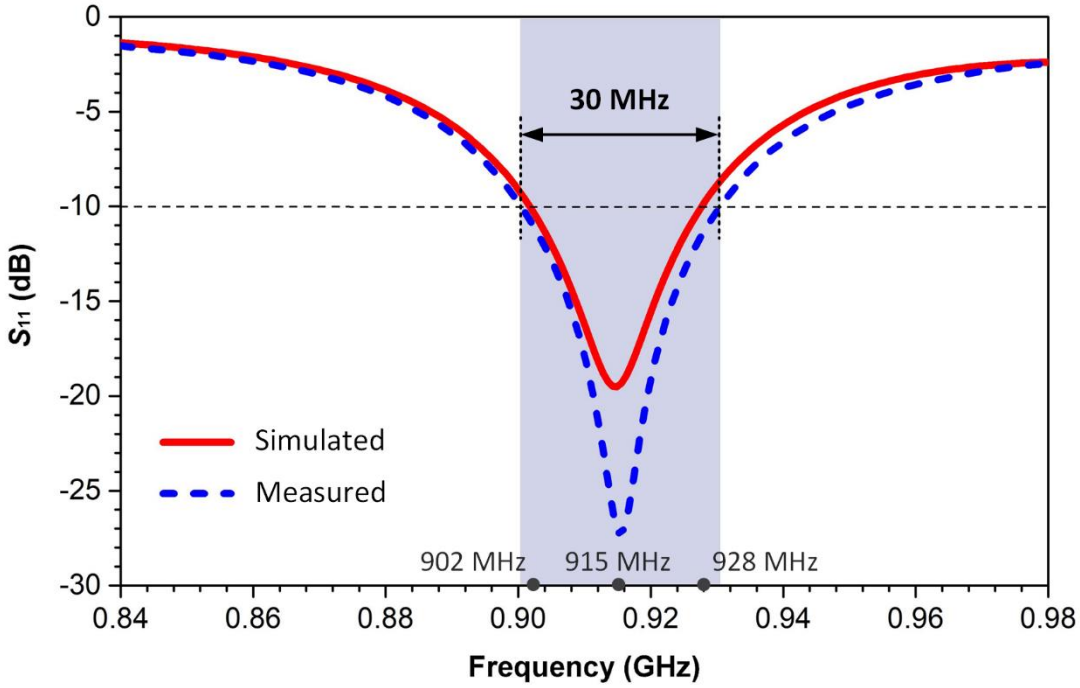


Figure 5.25: EM Simulated versus measured S_{11} response of the 915 MHz antenna.

For S-Parameter measurements, the fabricated antenna and all internal components such as radio and motherboard PCBs and sensor assembly were integrated inside the wristwatch device. The measurements of the device under test (DUT) were taken after placing the wristwatch on the Speag phantom arm [145].

The S_{11} response of the proposed antenna was measured using a Rohde & Schwarz *ZVRE* vector network analyzer [61]. Figure 5.25 shows the simulated and measured S_{11} responses of the antenna. Both simulated and measured responses are shown to be resonant at 915 MHz. The proposed antenna has a measured -10 dB impedance bandwidth of 30 MHz, which is slightly (3.8 MHz) higher than the simulated impedance bandwidth. The slight difference in the simulated and measured S_{11} responses is most likely attributed to the measurement setup and the possible losses in the ferrite-beaded cable used in measurement, which was not accounted for in simulation.

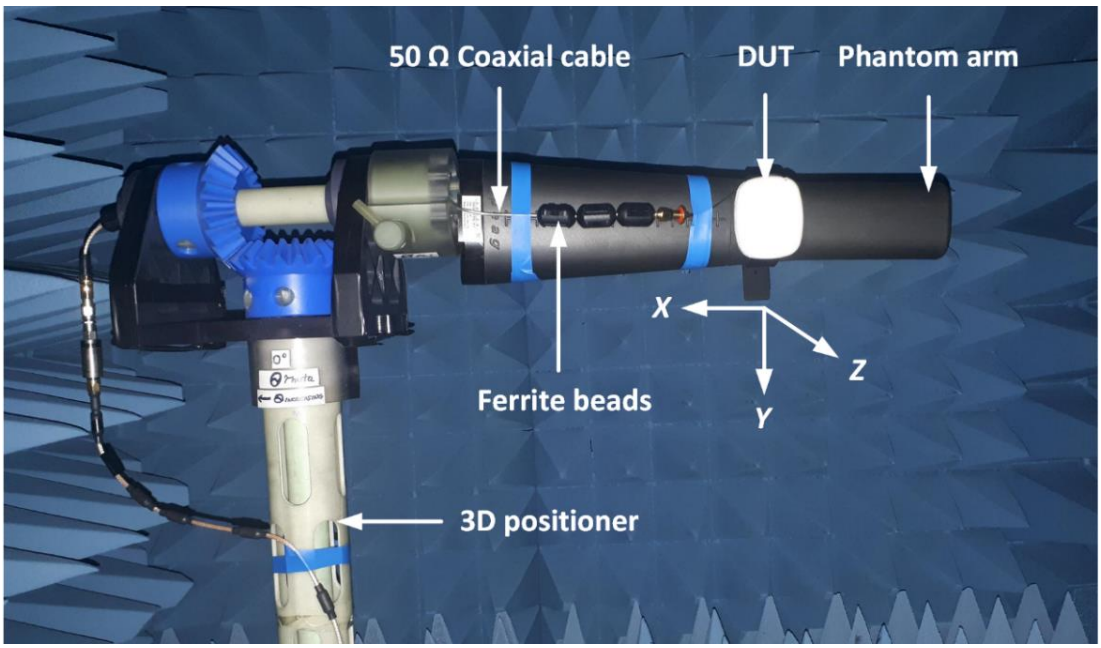


Figure 5.26: Device under test (DUT) measurement setup in an AMS-8050 anechoic chamber.

The radiation characteristics of the device under test (DUT) were measured using an AMS-8050 antenna measurement system [63]. Figure 5.26 illustrates the anechoic chamber measurement setup of the DUT. The rotation of the DUT in the chamber is controlled using the multi-axis positioning system (MAPS) or 3D antenna positioner. The wristwatch device was placed on an SHO-GFPC-V1 phantom arm [145] and was excited using an unbalanced 50 Ω coaxial cable. Since the coaxial cable can affect the antenna radiation properties, multiple ferrite beads have been incorporated in the measurement setup to suppress radiation from coaxial cable ground currents.

Figure 5.27 shows the simulated and measured radiation patterns of the proposed antenna at 915 MHz. For the co-polarized case, the antenna exhibits omnidirectional radiation characteristics in the *XY*-plane, as shown in Figure 5.27(a). The simulated and measured co-polarized radiation patterns correlate well in the *XY*-plane. In Figure 5.27(b), the radiation pattern in the *YZ*-plane is shown and Figure 5.27(c) depicts the radiation pattern in the *XZ*-plane. The co-polarized radiations have nulls in the *YZ* and *XZ*-planes. These nulls are expected due to the shielding effect of the PIFA ground plane (radio and motherboard PCBs) in combination with body absorption of energy in the axis normal to the PIFA ground plane. In the *YZ*- and *XZ*- planes, the discrepancy between the simulated and measured radiation patterns is observed at some angles.

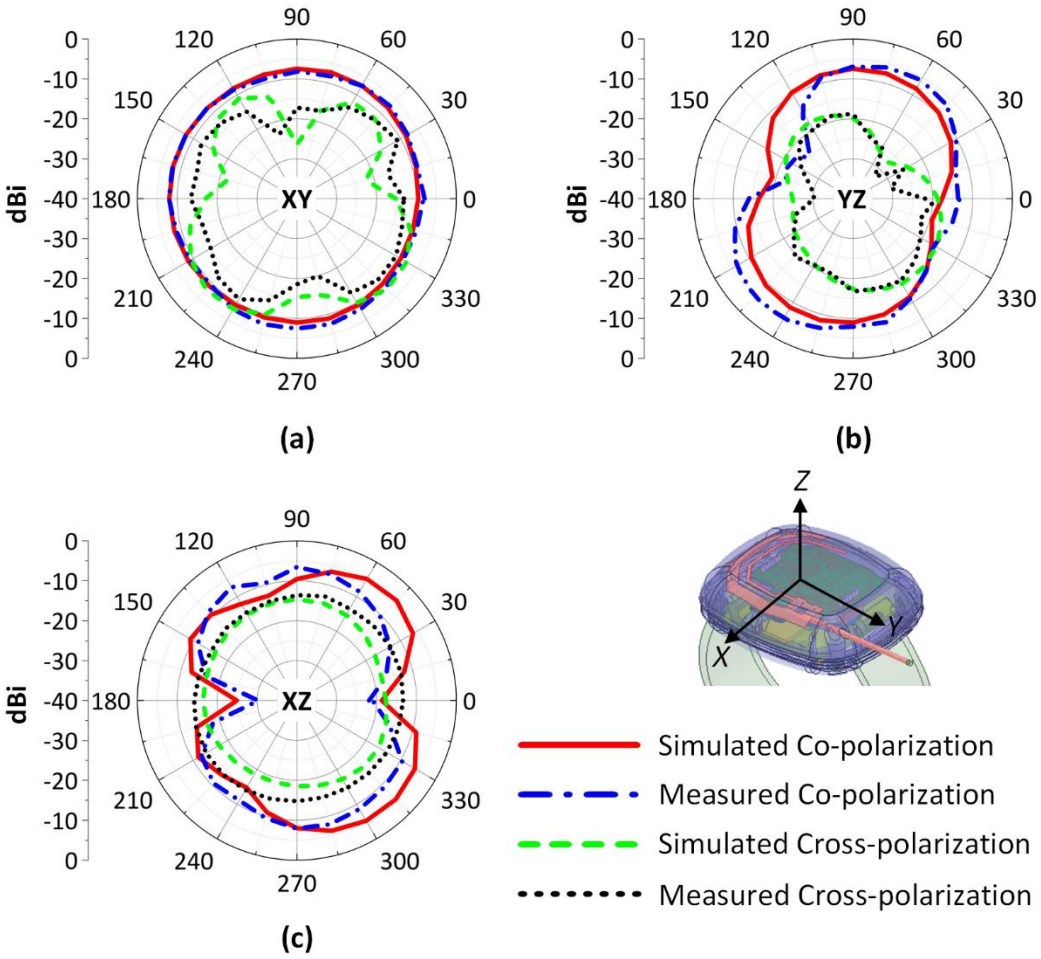


Figure 5.27: Simulated and measured radiation characteristics of the antenna at 915 MHz in (a) *XY*-plane, (b) *YZ*-plane and (c) *XZ*-plane.

The discrepancy between the simulated and measured radiation characteristics is attributed to the combined effects of possible small changes in the position of the internal components of the wristwatch assembly, measurement setup and losses in the ferrite-beaded cable that was not included in simulation. The developed antenna has a measured peak realized gain of -4.9 dBi and a radiation efficiency of 15.9 % at 915 MHz, compared to -4.14 dBi and 19.8 %, respectively for the simulated case. The measured peak realized gain is 0.76 dB and the radiation efficiency is 3.9 % less than the simulated case, most likely because of the previously described non-ideal measurement environment.

5.4.8 Performance Evaluation of the 915 MHz Antenna

Table 5.4 compares the key performance characteristics of the developed 915 MHz wristwatch antenna (row 10) with the state-of-the-art literature.

Table 5.4: Comparing on-phantom performance of the developed 915 MHz antenna with the literature.

A	B	C	D			E	F	G	H	I
Row	Ref.	Antenna Topology	Dimensions (mm)			f_0 (MHz)	-10 dB *BW* (MHz)	*Gain* (dBi) @ f_0	*h* (%) @f_0	*SAR* (W/kg) @f_0
			L	*W*	*h*					
1	[43]	Loop	40	30	10	920	180	NA	6.4	NA
2	[44]	Dipole	127	25	2	850	160	-8.3	7	3.75
3	[45]	Dipole	145	40	NA	900	160	NA	6.3	0.18
4	[42]	IFA[4]	93	37	5	780	105[1]	NA	7.9	NA
5	[46]	PIFA[4]	64.8	45.6	4.75	866	105	-4.4	26	0.78
6	[47]	Loop	201	56	0.2	900	100	-8[5]	NA	NA
7	[28]	PIFA[4]	44	28	1.6	915	55[1]	-6.09	NA	NA
8	[48]	Dipole[4]	220	10	0.25	922.5	44	-11.2	NA	NA
9	[49]	PIFA[4]	44	44	10	767	35[1]	-5.4	13	NA
10	**This Work**	**PIFA**	**48**	**41**	**2.3**	**915**	**30**	**-4.9**	**15.9**	**0.0019**
11	[50]	PIFA[5]	188	30	6	880	28	NA	83.7	NA
12	[116]	Helix	40	40	14.4	890	23	NA	NA	NA
13	[34]	Patch	86	25	1.6	915	19[3]	-6.87[5]	NA	NA
14	[36]	Helical	110	29	1.55	868	17	-13[5]	NA	NA
15	[37]	Monopole	100	15	0.6	911	14	-5.35	NA	NA
16	[38]	Monopole	40	15	1.8	911	7.5	-5.86	NA	NA
17	[39]	IFA[4]	45	30	5.5	846	7[5]	NA	14.8	NA
18	[40]	PIFA[4]	$\pi \times 25^2 \times 5$			402.5	5.2[2,3]	-12	3.6	NA
19	[30]	PIFA	$\pi \times 25^2 \times 5$			402.5	4.22[2,3]	-9.2	6.9	NA
20	[41]	Loop[5]	50	35	3	868	3.5	-1.44	NA	0.0002
21	[35]	Spiral[5]	$\pi \times 16^2$			915	3[3]	-1.04	NA	NA
22	[117]	PIFA	76.1	13.6	9.5	866	NA	-6.6	8.6	NA
23	[118]	Patch[5]	120	29	0.64	867	NA	-13	NA	NA
24	[119]	PIFA	90	20	3	923	NA	-5	NA	NA

This table is sorted in decreasing order of -10 dB bandwidth in column F

Important Notes:

[1] Antenna requires the use of an impedance matching network

[2] Only the -6 dB impedance bandwidth is reported

[3] Antenna does not meet the -10 dB bandwidth requirements for the targeted band

[4] Antenna was fully integrated in a wristwatch device

[5] Only simulated results are reported

NA = Information not reported

From Table 5.4, it can be seen that the antenna developed in this work is realized in one of the most compact form factors and well meets the minimum required -10 dB impedance bandwidth of 26 MHz for 915 MHz band operation. The comparison table show that the antennas in rows 1 to 9 have a -10 dB bandwidth more than 30 MHz, but those antennas achieve a wider bandwidth at the cost of either reduced radiation performance or using an impedance matching network or a large size antenna. On the contrary, the compact antenna developed in this work has achieved a -10 dB bandwidth of 30 MHz with simultaneously improved peak realized gain of -4.9 dBi and a radiation efficiency of 15.7 % at 915 MHz compared to the literature. In addition, for 1 mW input power, the developed antenna demonstrates one of the lowest SAR figures in the literature.

5.5 Development of an 868 MHz Wristwatch-Integrated Antenna

In Europe, many emerging LoRaWAN wireless technologies such as LoRa and SigFox operate in the 868 MHz (863-870 MHz) Industrial, Scientific and Medical (ISM) band [64]. To satisfy the Sub-GHz wireless communication requirements in Europe, in this section, the development of an 868 MHz antenna and its integration into a wristwatch wireless sensor device is presented. The developed 868 MHz antenna was integrated within a similar wristwatch enclosure case, as described previously in this chapter for the 915 MHz antenna. For the proposed 868 MHz antenna, all design parameters were kept the same as that of the 915 MHz antenna described earlier in this chapter, except for the two changes: (a) The flexible polyimide substrate was removed and the antenna structure was directly printed on the wristwatch enclosure using laser direct structuring (LDS) technology and (b) The 915 MHz antenna was tuned for 868 MHz operation using an impedance matching network, as described in [53].

5.5.1 Prototype Fabrication of the 868 MHz Antenna

The proposed 868 MHz antenna was fabricated using an LPKF laser direct structuring (LDS) technology [153], available within the Tyndall Microsystems Packaging Laboratory [154]. For antenna fabrication, the LDS technology was chosen because of its associated advantages such as low fabrication cost, easy integration into the enclosure structure and because it eliminated the need for additional flexible PCB [153].

The fabrication of the proposed antenna prototype using the LDS technology was completed in the following steps:

1. *3D part fabrication or selection:* The 3D part/object on which the metal has to be printed can be fabricated using standard 3D printers. The commercially available thermoplastic parts, such as metals, plastics, glass, FR-4, can also be used. For the proposed antenna, the antenna structure was printed on an acrylonitrile styrene acrylate (ASA) thermoplastic wristwatch enclosure from OKW enclosures [144].
2. *Part coating with ProtoPaint LDS epoxy:* The wristwatch plastic enclosure was covered with the LPKF ProtoPaint LDS epoxy layer. LPKF ProtoPaint LDS is an adhesive spray paint that makes plastic surfaces suitable for laser direct structuring [153, 155].
3. *Laser direct structuring*: The LPKF laser system creates an outline of the conductive pattern of the design. In this step, the laser removes some of the epoxy material and forms a rough surface to which the copper can firmly adhere during metallization.
4. *Metallization*: This step involves the electroless copper plating of the region exposed by laser etching. The scanning electron microscope (SEM) photograph of the antenna track (in cross-section view) deposited during the metallization process is illustrated in Figure 5.28 and the photograph of the antenna printed in the wristwatch enclosure is shown in Figure 5.29.

The LDS fabrication work was carried out by the Tyndall Microsystems Packaging Laboratory group. Additional information available regarding the LDS process steps have been published in [53], where more details regarding the metallization process are provided. Unfortunately, the electrical characteristics of the electroplated LDS metal layer were not measured during this work but would be a valuable addition for future work.

With respect to the line thickness of the LDS metallization, the average thickness has been calculated as 17.6 μm. The skin depth at 915 MHz has also been calculated at 2.18 μm, assuming that the electroplated metal layer has a conductivity close to that of copper, $\sigma = 5.8 \times 10^7$ S/m. Therefore, the electroplated metal has a thickness of approximately eight times the skin depth, that is sufficient to minimize skin effect losses at 915 MHz.

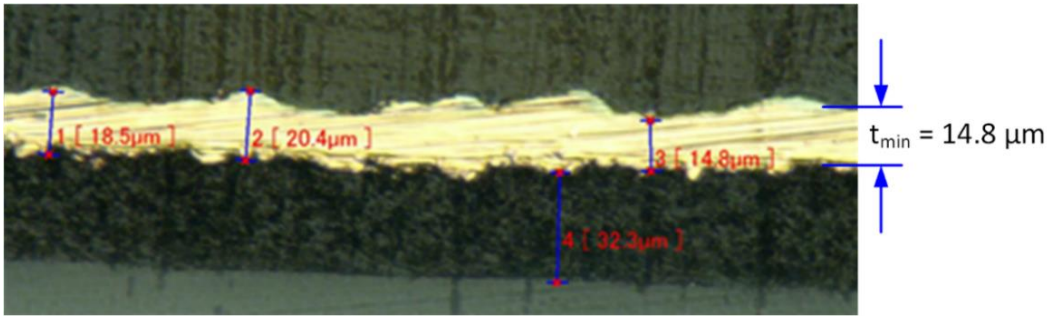


Figure 5.28: Cross section-view of the metallization of the antenna track.

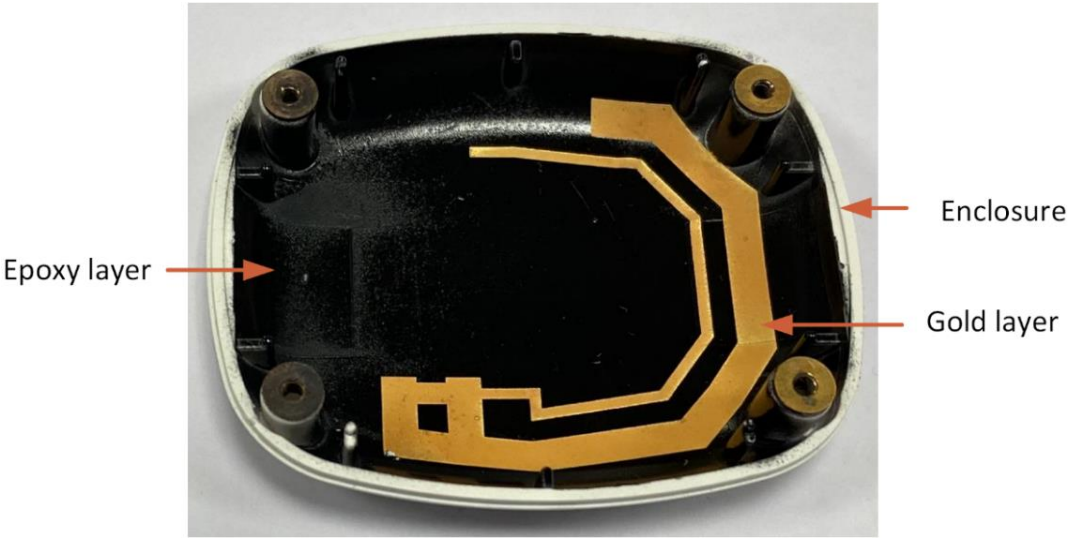


Figure 5.29: Photograph of the proposed laser direct structuring (LDS) printed antenna.

As shown in Figure 5.28, the minimum (t_{min}) and maximum (t_{max}) thickness of the electroplated copper is 14.8 µm and 20.4 µm, respectively. As LDS printing involved a manual coating of the plastic enclosure using an adhesive spray painting, this variation in the metal thickness of the order of approximately 5 µm is expected.

5.5.2 Measurements of the 868 MHz Antenna

In this section, the measured impedance and radiation characteristics of the proposed 868 MHz wristwatch-integrated antenna are described. Similar to the 915 MHz wristwatch-integrated antenna, the measurements of the 868 MHz antenna were performed after placing the wristwatch assembly on a commercial SHO-GFPC-V1 phantom arm [145]. First, the impedance characteristics of the antenna were measured using a Rohde and Schwarz *ZVRE* vector network analyzer (VNA) [61]. In Figure 5.30, the measured S_{11} response of the antenna is illustrated.

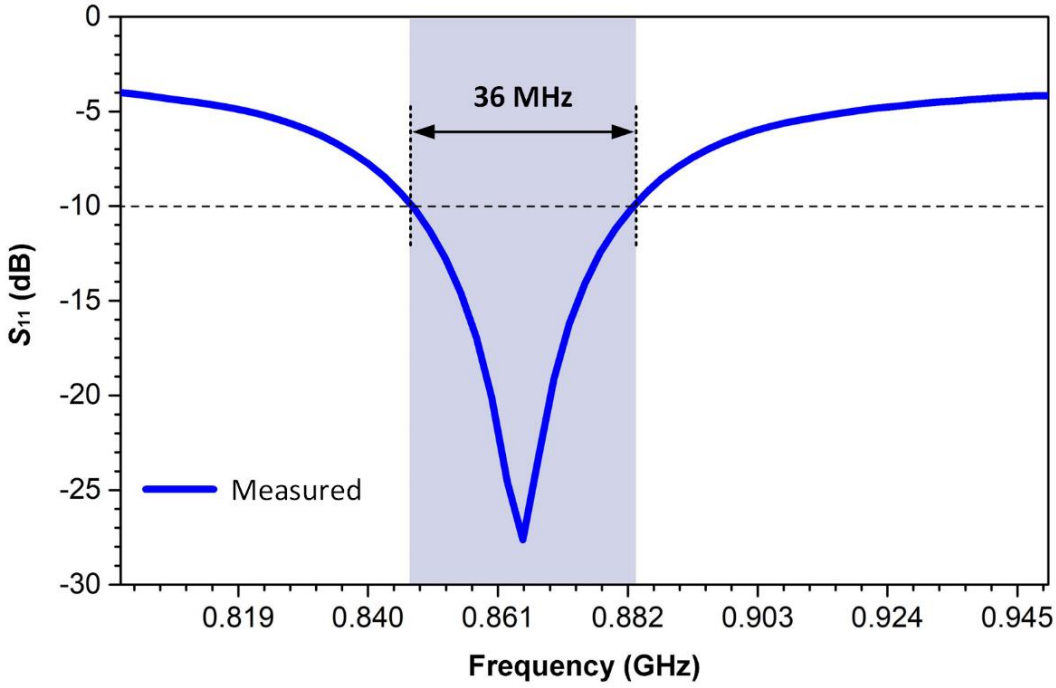


Figure 5.30: Measured S_{11} response of the proposed 868 MHz antenna.

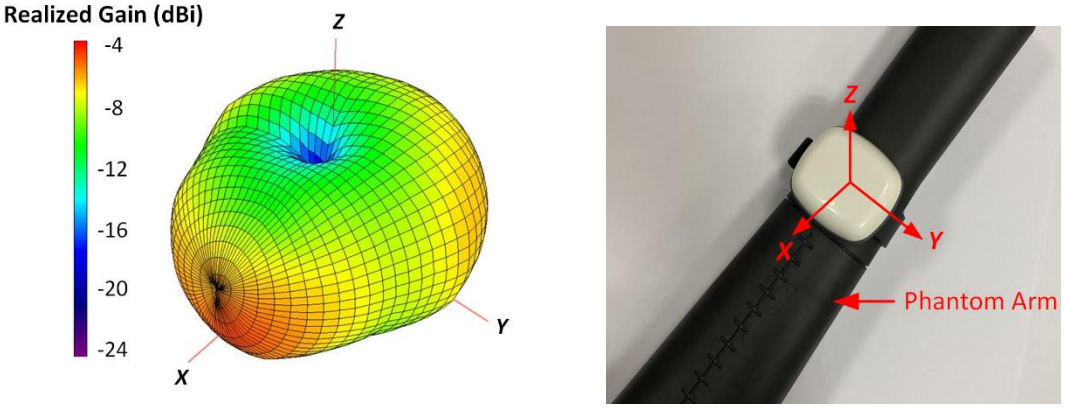


Figure 5.31: (a) Measured antenna realized gain (3D) at 868 MHz, (b) Coordinate system of the wristwatch device placed on a phantom arm.

The measured prototype antenna is resonant at 868 MHz with a −10 dB impedance bandwidth of 36 MHz. This impedance bandwidth figure is five times higher than the minimum required impedance bandwidth specification of 7 MHz (863–870 MHz) at the 868 MHz band [64].

Secondly, the 3D radiation characteristics of the wristwatch device under test (DUT) were measured in an AMS-8050 antenna measurement system [63]. In Figure 5.31(a), the measured 3D realized gain pattern of the developed antenna at 868 MHz is shown.

The coordinate system of the wristwatch device placed on a phantom arm is also shown in Figure 5.31(b). In the *XY*-plane, the antenna is characterized as a PIFA-like radiation characteristic with an omnidirectional radiation pattern [40]. The antenna exhibits nulls along the z-axis in the *YZ*- and *XZ*-planes. These radiation nulls are expected due to the shielding effect of the finite PIFA ground planes of the radio and motherboard PCBs and the absorption of the radiated energy by the phantom arm along the *Z*-axis. The on-phantom prototype antenna demonstrated a measured peak realized gain of -4.86 dBi and a radiation efficiency of 14.53 % at 868 MHz.

5.5.3 Performance Evaluation of the 868 MHz Antenna

In Table 5.5, the key performance characteristics of the 868 MHz LDS printed antenna (row 9) developed in this work is compared against the Sub-GHz wrist-worn antennas reported in the literature.

Table 5.5: Comparing on-phantom performance of the developed 868 MHz LDS printed antenna with the literature.

A	B	C	D			E	F	G	H	I
Row	Ref.	Antenna Topology	Dimensions (mm)			f_0 (MHz)	-10 dB *BW* (MHz)	*Gain* (dBi) @ f_0	*h* (%) @f_0	*SAR* (W/kg) @f_0
			L	*W*	*h*					
1	[43]	Loop	40	30	10	920	180	NA	6.4	NA
2	[44]	Dipole	127	25	2	850	160	-8.3	7	3.75
3	[45]	Dipole	145	40	NA	900	160	NA	6.3	0.18
4	[42]	IFA[4]	93	37	5	780	105[1]	NA	7.9	NA
5	[46]	PIFA[4]	64.8	45.6	4.75	866	105[6]	-4.4	26	0.78
6	[47]	Loop	201	56	0.2	900	100	-8[5]	NA	NA
7	[28]	PIFA[4]	44	28	1.6	915	55[1]	-6.09	NA	NA
8	[48]	Dipole[4]	220	10	0.25	922.5	44	-11.2	NA	NA
9	**This Work**	**PIFA**	**48**	**41**	**2.3**	**868**	**36[1]**	**-4.86**	**14.5**	**0.0027**
10	[49]	PIFA[4]	44	44	10	767	35[1,6]	-5.4	13	NA
11	[50]	PIFA[5]	188	30	6	880	28	NA	83.7	NA
12	[116]	Helix	40	40	14.4	890	23	NA	NA	NA
13	[34]	Patch	86	25	1.6	915	19[3]	-6.87[5]	NA	NA
14	[36]	Helical	110	29	1.55	868	17	-13[5]	NA	NA
15	[37]	Monopole	100	15	0.6	911	14	-5.35	NA	NA
16	[38]	Monopole	40	15	1.8	911	7.5	-5.86	NA	NA
17	[39]	IFA[4]	45	30	5.5	846	7[5]	NA	14.8	NA
18	[40]	PIFA[4]	$\pi \times 25^2 \times 5$			402.5	5.2[2,3]	-12	3.6	NA
19	[30]	PIFA	$\pi \times 25^2 \times 5$			402.5	4.22[2,3]	-9.2	6.9	NA
20	[41]	Loop[5]	50	35	3	868	3.5	-1.44	NA	0.0002
21	[35]	Spiral[5]	$\pi \times 16^2$			915	3[3]	-1.04	NA	NA
22	[117]	PIFA	76.1	13.6	9.5	866	NA	-6.6	8.6	NA
23	[118]	Patch[5]	120	29	0.64	867	NA	-13	NA	NA
24	[119]	PIFA	90	20	3	923	NA	-5	NA	NA

This table is sorted in decreasing order of -10 dB bandwidth in column F

Important Notes:

[1] Antenna requires the use of an impedance matching network

[2] Only the -6 dB impedance bandwidth is reported

[3] Antenna does not meet the -10 dB bandwidth requirements for the targeted band

[4] Antenna was fully integrated in a wristwatch device

[5] Only simulated results are reported

[6] Antenna fabricated using LDS technology

NA = Information not reported

As shown in Table 5.5, the impedance and radiation performance characteristics of the antenna [53] developed in this work compares well with the literature. As shown in the table, two Sub-GHz wristwatch antennas [46, 49], which are fabricated using LDS technology are found in the literature. It is observed that the antenna developed in this work is the most compact antenna design, and achieves the second highest bandwidth, peak realized gain and radiation efficiency for any LDS printed Sub-GHz wrist-worn antennas in the literature.

5.5.4 System Implementation and Clinical Trials

The developed 868 MHz antenna was integrated into a prototype wristwatch wireless sensor device and clinical trials were performed at Mercy University Hospital, Cork, Ireland [156] after ethics approval had been obtained from the university authorities. The details of the system implementation and clinical trials are described in [53]. The clinical trials were successfully conducted on 24 patients over a period of four weeks, and under the supervision of clinical staff. Each trial took approximately 3 minutes to measure the SpO_2 and heart rate of a patient. In Figure 5.32, the devices used in the clinical trials are shown, such as a gateway, an optical biosensor, a smartphone, and the developed wristwatch sensor device are illustrated.



Figure 5.32: Clinical trial test devices.

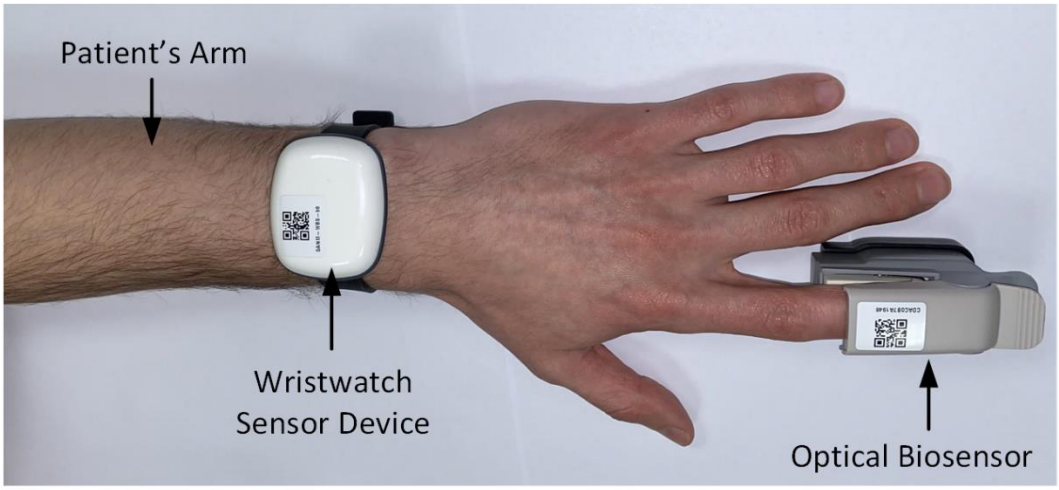


Figure 5.33: Wristwatch sensor device worn by a patient in a clinical setting.

The gateway works as a communication link between the wristwatch sensor platform and the smartphone app. The details of the architecture and the internal components of the gateway is described in detail in [53]. The clinical trials also employ an existing optical biosensor device, which can wirelessly connect to the smartphone application. Figure 5.33 illustrates the SpO_2 and heart rate measurement setup on a patient's arm using the developed wristwatch sensor device as well as the existing optical biosensor in a clinical setting. The test protocol used in the clinical trials specified that the arm should be parallel to the ground, as the patient would usually be sitting or lying down.

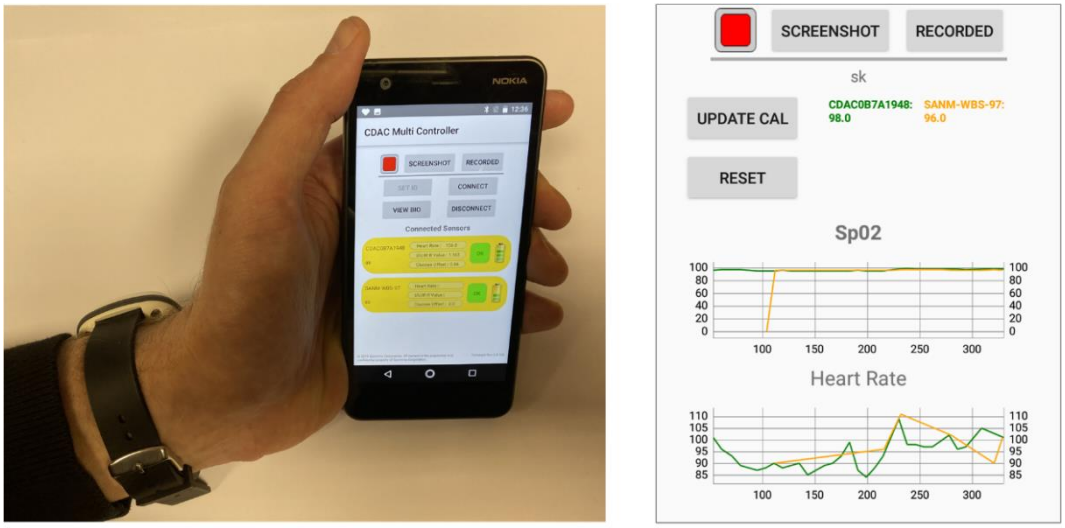


Figure 5.34: Smartphone application for SpO2 and heart rate measurements (a) smartphone app in a user's hand, (b) screenshot of the measured plots.

This position is recommended because the accuracy of the SpO_2 and heart rate measurement is heavily impacted by motion artefacts, which are likely to have a significant influence on the quality of the measured data [157].

The sensor data measured by the wristwatch device were compared against the optical biosensor data. Figure 5.34(a) shows the smartphone app in a user's hand, showing that both the sensor devices (wristwatch sensor and optical biosensor) are connected. The plots of the measured SpO_2 and HR sensor data on the smartphone app are shown in Figure 5.34(b). The green curves represent the SpO_2- and HR-measured values by the wristwatch device, and the yellow curves represent the optical biosensor-measured data. It can be seen that the measurement results from the developed sensor wristwatch device are in close agreement with the results from the optical biosensor device.

5.6 Conclusions

In this chapter, the design and development of two Sub-GHz band PIFA-type wristwatch-integrated antennas has been described. For both antennas, a dual-radiator approach was implemented to enhance the impedance bandwidth and radiation performance. In the first iteration, a novel design for a compact 915 MHz antenna integrated within a wristwatch wireless sensor device was developed to meet the Sub-GHz band wireless communication requirements in North America. The compact 915 MHz antenna was fabricated using a low cost flexible polyimide substrate. In addition, an equivalent circuit model of the proposed antenna was also developed to predict the impedance response of the antenna. The developed 915 MHz antenna is published in [52] and represented one of the most compact sized (48 mm × 41 mm × 2.3 mm) wristwatch-integrated antennas that has achieved a -10 dB impedance bandwidth of at least 30 MHz, with simultaneously improved peak realized gain of -4.9 dBi and a radiation efficiency of 15.9 % when compared to the Sub-GHz wrist-worn antennas in the literature.

In a second iteration, the above 915 MHz antenna was optimized for 868 MHz operation to meet the Sub-GHz band wireless communication requirements in Europe [64]. The 868 MHz antenna structure was printed on the surface of a wristwatch enclosure using laser direct structuring (LDS) technology and was fully integrated into a wristwatch wireless sensor device.

The developed 868 MHz wristwatch antenna is published in [53] and represents the most compact antenna design fabricated using LDS technology and demonstrated the second highest -10 dB impedance bandwidth (36 MHz), peak realized gain (-4.86 dBi) and radiation efficiency (14.5 %) for any LDS printed Sub-GHz wrist-worn antennas in the literature.

In addition, both 915 MHz and 868 MHz antennas demonstrated low SAR values of less than 0.08 % of the maximum permissible SAR limit for wrist tissue [80, 109], making the antenna suitable for a wide range of wrist-worn wireless applications. In the next chapter, the feed structure of the 915 MHz antenna [52] has further been optimized to significantly enhance the impedance bandwidth of the antenna.

Chapter 6: A Bandwidth Enhanced 915 MHz Wristwatch Antenna using an Optimized Feed Structure

6.1 Background

In Chapter 5, two new wristwatch-integrated compact antennas operating at 915 MHz [52] and 868 MHz [53] bands were described. The 915 MHz antenna presented in Chapter 5 has achieved a -10 dB impedance bandwidth of 30 MHz, which is slightly greater than the required impedance bandwidth of 26 MHz (902-928 MHz) for 915 MHz band operation [55]. The antenna presented in this chapter is based around a novel design methodology, which aims at significantly enhancing the impedance bandwidth when compared to the previous 915 MHz antenna described in Chapter 5.

Similar to the previous antenna [52], the antenna developed in this work incorporates two radiating elements. However, to enhance the impedance bandwidth, the feed structure for the two radiating elements is modified. With the optimized feed, the new antenna excites two closely located resonant frequencies that can be independently tuned to maximize the impedance bandwidth of the antenna. The excitation of two adjacent resonant frequencies for impedance bandwidth enhancement has not been previously reported for Sub-GHz wristwatch antennas in the literature, which is one of the novel aspects of this work.

Furthermore, an equivalent circuit model for the proposed antenna design is derived to explain the impedance bandwidth enhancement mechanism. Another contribution of this work is the development of an equivalent transmission line model for the proposed antenna to accurately predict the antenna impedance characteristics with greatly reduced computation time compared to EM simulation. The key results presented in this chapter have been published in [54].

6.2 Antenna Design

The target wristwatch device for the antenna developed in this work is the same off-the-shelf wristwatch enclosure [144] as has been described in Chapter 5, Section 5.2. The geometry of the proposed antenna is shown in Figure 6.1(a). The antenna is a variant of a planar inverted-F antenna (PIFA) topology and consists of two radiating elements, denoted Rad_1 and Rad_2. The antenna is printed on a low-cost 0.13 mm thick flexible polyimide substrate with a copper thickness t_{CU} = 0.018 mm. The polyimide substrate has dimensions of L (48 mm) × W (41 mm) and has a measured ε_r = 3.1 and $tan\delta$ = 0.0245 at 915 MHz [87].

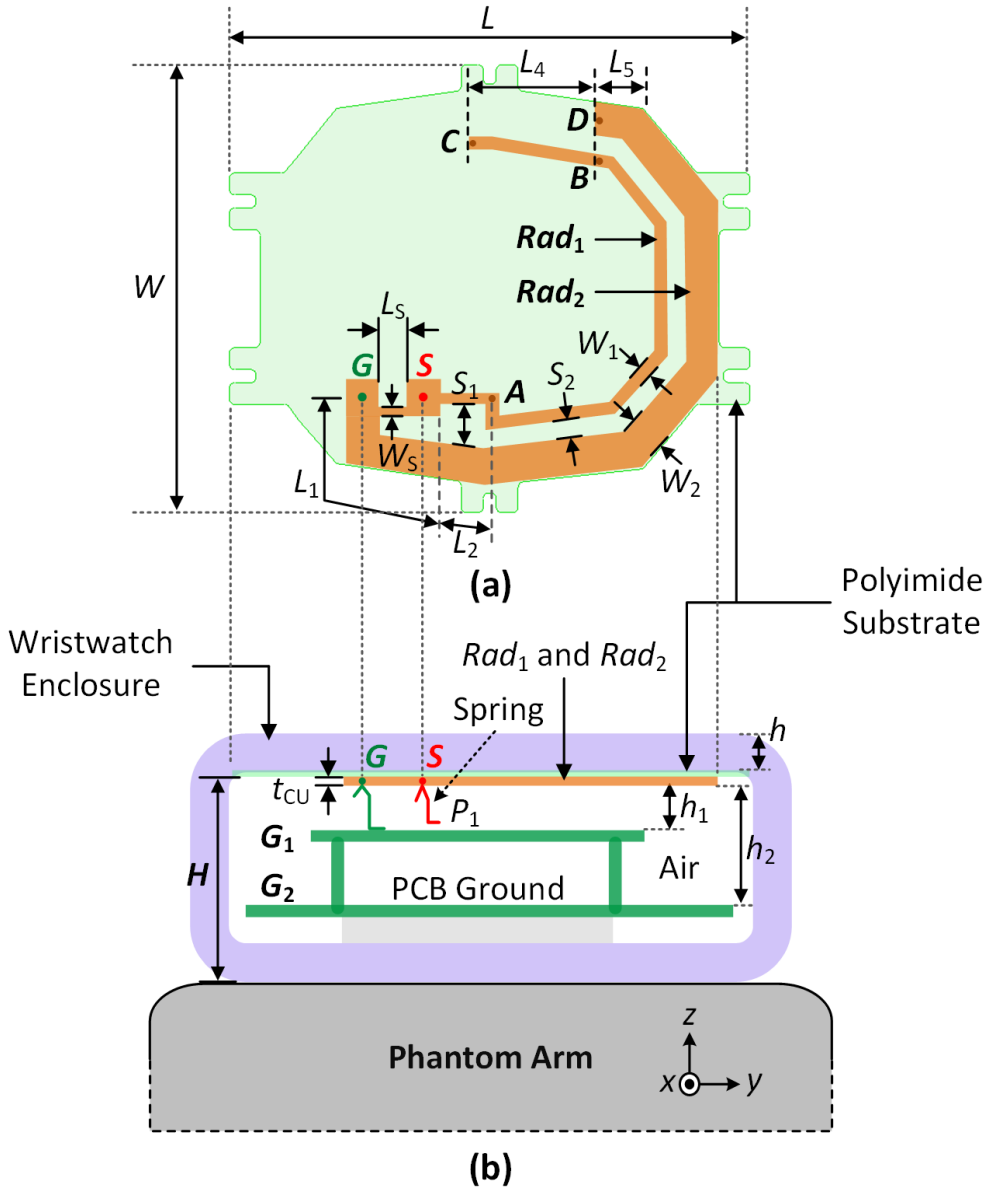


Figure 6.1: Geometry of the proposed wristwatch-integrated antenna placed on a phantom arm.

The antenna is integrated into a complete, integrated wristwatch assembly, where the bottom surface of the plastic enclosure is placed on the top surface of a commercial SPEAG SHO-GFPC-V1 phantom arm model from Speag [145]. The dielectric properties of the phantom arm model are described in Chapter 5, Section 5.4.1. The antenna structure is integrated within the wristwatch enclosure and placed above the ground planes. As shown in Figure 6.1(b), the ground planes are implemented using two PCB assemblies, denoted G_1 and G_2. As shown in Figure 6.1, via contact springs, element Rad_1 is excited at port P_1 using a 50 Ω unbalanced feed coaxial cable with a signal at point *S* and element Rad_2 is connected to ground at point *G*. The section between points *S* and *G* implements a shunt inductive element that is used to balance the distributed capacitance of elements Rad_1 that is in close proximity to ground planes (G_1 and G_2) of the PCBs beneath [146].

6.3 Antenna Simulations

This section presents the simulated results of the proposed antenna using both circuit and full-wave electromagnetic (EM) simulations. The circuit simulations of the proposed antenna were carried out using AWR Microwave Office [148] and the EM simulations were performed using ANSYS HFSS [137]. First, an equivalent circuit model is developed to explain the impedance bandwidth enhancement methodology. The impedance and radiation performance of the antenna obtained from EM simulations are then presented. A new transmission line (TL) model of the proposed antenna is also developed to study the impact of key antenna parameters on the resonant response with greatly reduced computation time when compared to the EM model.

6.3.1 Optimization of Feed Structure for Bandwidth Enhancement

The proposed antenna design extends the previous work [52] described in Chapter 5, with a key focus on significantly improving the impedance bandwidth of the antenna. As shown in Figure 6.2(a), the 915 MHz wristwatch antenna previously presented in Chapter 5 has two radiating elements, denoted Rad_1 and Rad_2, where both the elements are excited from the same feed point *S*.

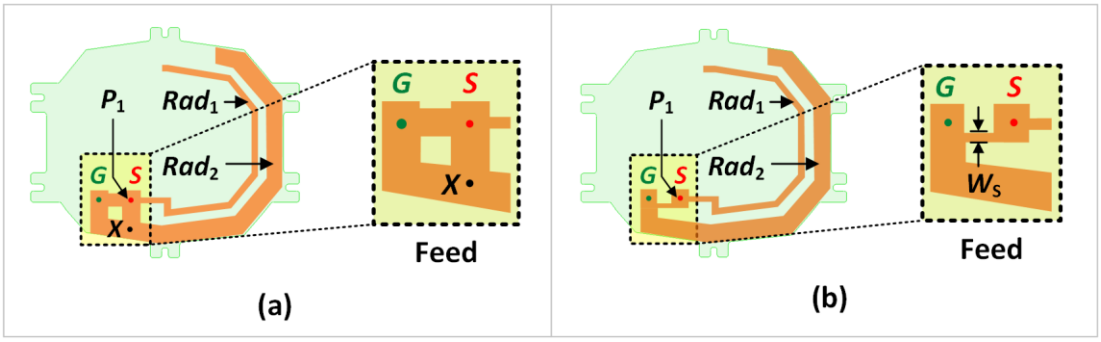


Figure 6.2: (a) Antenna topology presented in Chapter 5 [52], (b) Proposed antenna topology with optimized feed developed in this work.

The key advance of the proposed new antenna described in this chapter over the previous antenna in [52] is the optimization of the feed structure. The proposed antenna topology with the optimised feed structure is shown in Figure 6.2(b), where element Rad_1 is excited directly from the feed point *S* and element Rad_2 is connected directly to ground *G* and is excited via mutual inductive coupling with element Rad_1. In addition, for the proposed antenna the width W_S of the inductive shunt section between points *S* and *G* is also reduced to improve the impedance matching of the antenna. With the optimized feed structure, the new antenna achieves a significant improvement in the impedance bandwidth, as described below.

6.3.1.1 Equivalent Circuit Model of the Proposed Antenna

The impedance bandwidth enhancement of the proposed antenna can be explained by developing an equivalent circuit model of the antenna, as shown in Figure 6.3.

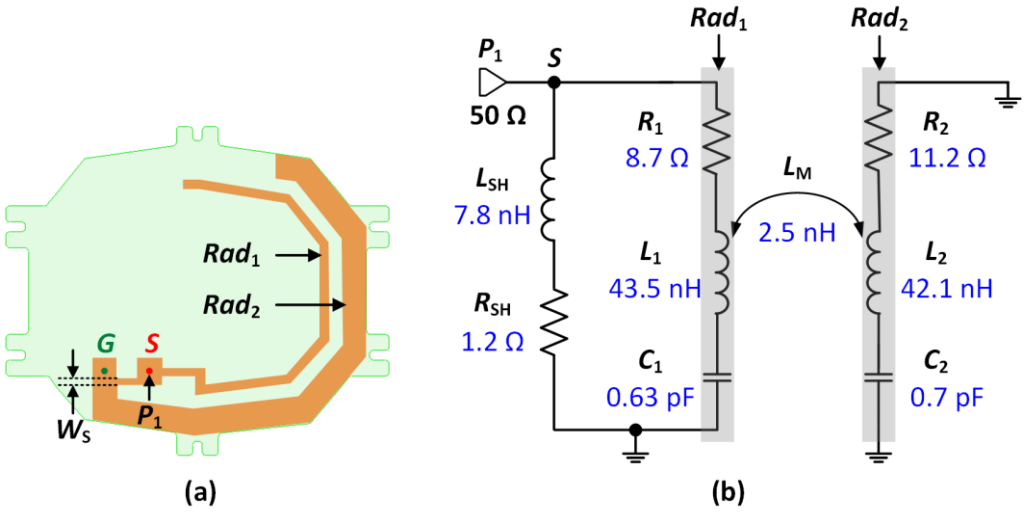


Figure 6.3: (a) Geometry of the proposed antenna, (b) Equivalent circuit model.

The proposed antenna topology shown in Figure 6.3(a) can be represented by an equivalent circuit model shown in Figure 6.3(b). The first series $R_1L_1C_1$ branch represents element Rad_1 and the second series $R_2L_2C_2$ branch represents element Rad_2. The third branch L_{SH} with resistance R_{SH} represents the shunt inductive section between excitation points S and ground G. Element Rad_2 is grounded and inductively coupled to element Rad_1 via mutual inductance L_M. The equivalent circuit component values shown in Figure 6.3(b) were derived through optimization against measured S_{11} data (measurements described in Section 6.4 of this chapter) in AWR Microwave Office [148]. The equivalent circuit model in Figure 6.3(b) is known to have two resonant frequencies, denoted f_L and f_H [158].

Figure 6.4 compares the measured and circuit model simulated S_{11} response of the antenna proposed in this work as well as of the 915 MHz antenna previously described in Chapter 5. The S_{11} response for the equivalent circuit models agrees well with the respective measured responses. As shown in Figure 6.4, the antenna proposed in this work is resonant at two frequencies, namely the lower resonant frequency, f_L = 908 MHz and the upper resonant frequency, f_H = 938 MHz with a -10 dB impedance bandwidth of 62 MHz.

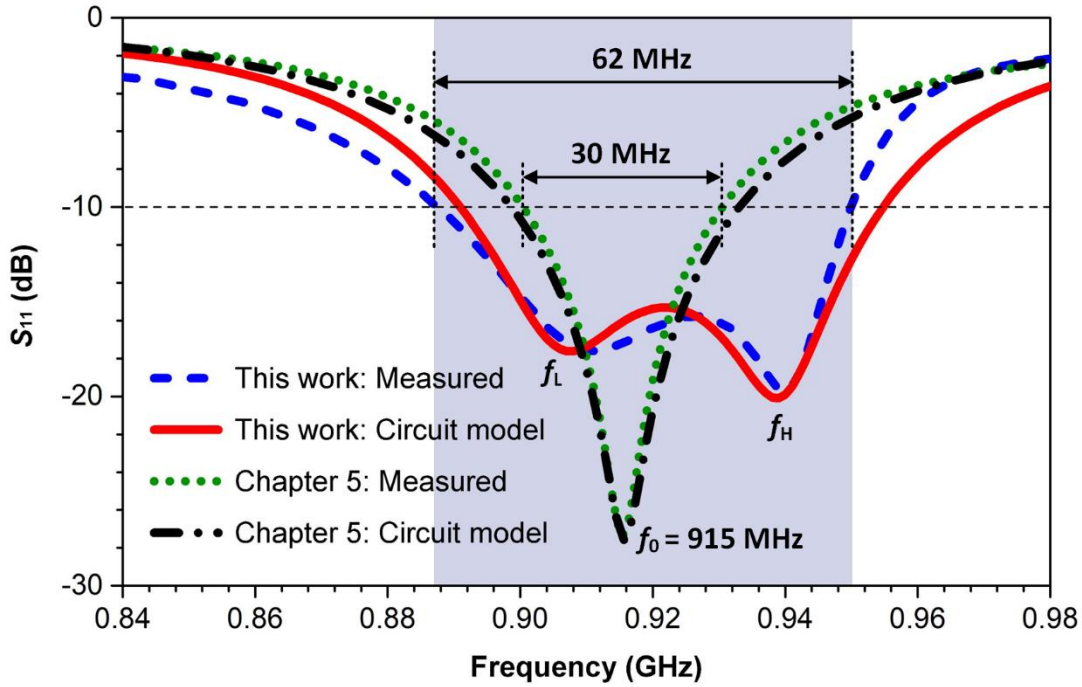


Figure 6.4: Simulated S_{11} response showing the impedance bandwidth enhancement.

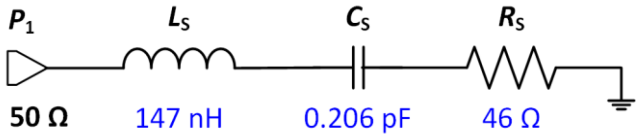


Figure 6.5: Single-branch equivalent circuit model for the 915 MHz antenna in Chapter 5.

By comparison, the antenna described in Chapter 5 is modelled as a single-branch series $R_SL_SC_S$ circuit, as shown in Figure 6.5, with only one resonant frequency $f_0 = 1/\left(2\pi\sqrt{L_SC_S}\right) = 914.6$ MHz ≈ 915 MHz. The detailed equivalent circuit model analysis of the previous antenna is described in Chapter 5, Section 5.4.2. Figure 6.4 also includes the S_{11} response for the antenna described in Chapter 5 to illustrate the impedance bandwidth enhancement achieved. As shown in Figure 6.4, the previous antenna has achieved a -10 dB impedance bandwidth of 30 MHz. However, as shown in Figure 6.4, with the optimized feed structure, the antenna proposed in this work is resonant at two frequencies f_L and f_H and therefore enabled a -10 dB impedance bandwidth enhancement of more than 107 % when compared to the previous 915 MHz antenna [52].

6.3.2 Equivalent Transmission Line (TL) Model of the Proposed Antenna

To enable rapid computation of the impedance characteristics, a transmission line (TL) model was developed using AWR Microwave Office [148]. The equivalent TL model is illustrated in Figure 6.6(b). This TL model uses an inverted microstrip transmission line topology whose physical characteristics are derived from the antenna geometry shown in Figure 6.6(a). Element Rad_1 extends between points S and C via A and B, and is modelled as a series combination of transmission lines T_2, T_3 and T_4. Similarly, element Rad_2 extends between points G and D, and is modelled as a series combination of transmission lines T_1, T_2, T_3 and T_5.

As shown in Figure 6.6(b), the antenna is fed at point S using a 50 Ω coaxial cable of length L_C = 50 mm, denoted T_{COAX}. The coaxial cable represents a lossy transmission line (0.0833 dB/m) and the dielectric insulator between inner conductor and grounded shield has a relative permittivity, ε_r = 1.7 [148]. The shunt inductive section between points S and G in Figure 6.6(a) is modelled as a lumped inductor denoted L_{SH} in the equivalent TL model. Parameters S_1 and S_2 represent the separation between elements Rad_1 and Rad_2, as defined in the coupled transmission lines T_2 and T_3.

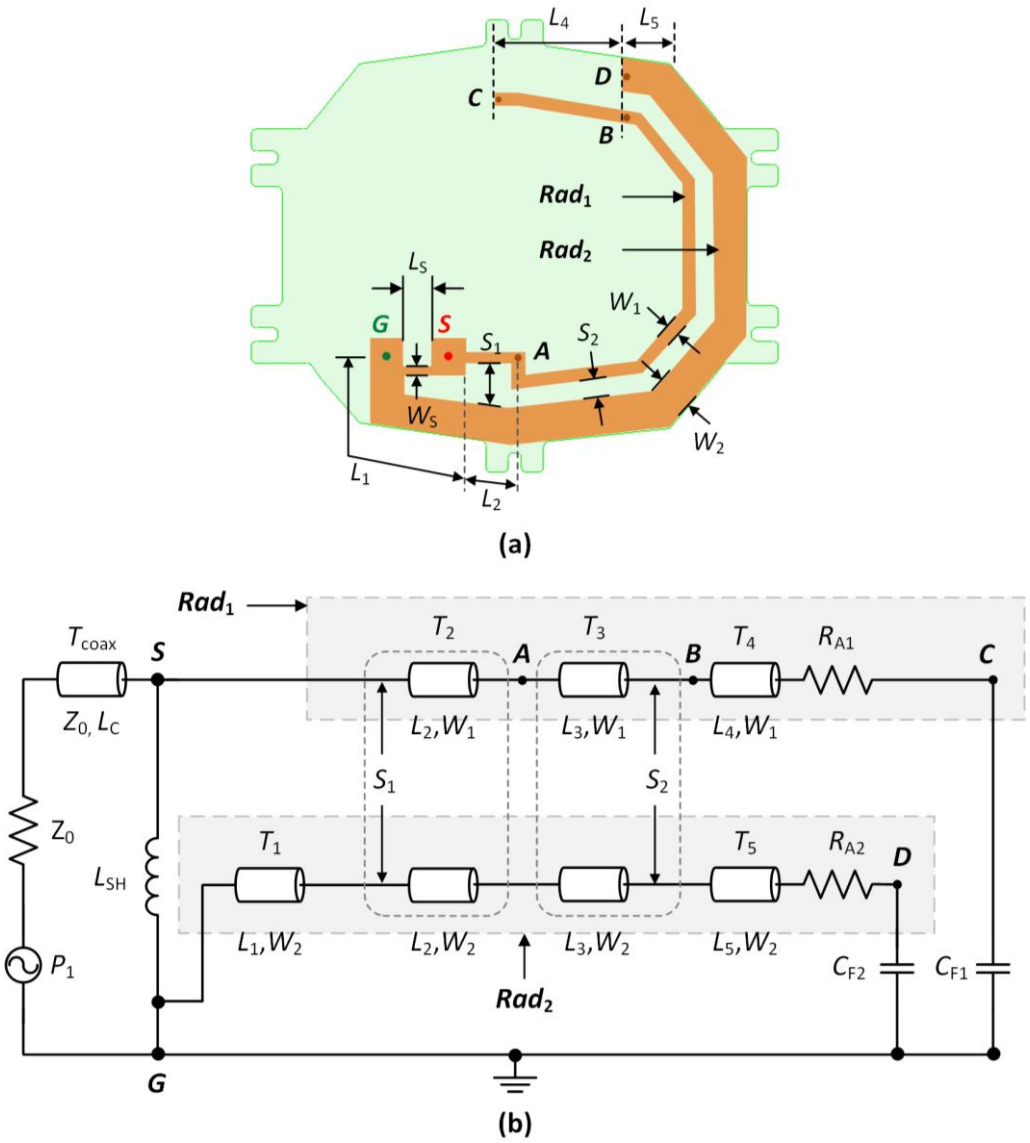


Figure 6.6: (a) proposed antenna geometry, (b) Equivalent transmission line (TL) model.

Furthermore, two capacitances C_{F1} and C_{F2} are included to account for the end capacitances of element Rad_1 and Rad_2 with respect to ground [159]. The radiation resistance, ohmic losses and dielectric losses associated with elements Rad_1 and Rad_2 are modelled using lumped elements R_{A1} and R_{A2}.

The antenna is modelled using a lossless inverted microstrip line, as shown in Figure 6.7. In order to model the dielectric properties of the inverted microstrip line, an effective relative electrical permittivity (ε_{eff}) is defined. This is required to account for the fact that the radiated fields from the antenna propagate both in the dielectric region of the enclosure (ε_r = 2.9) and in air [160].

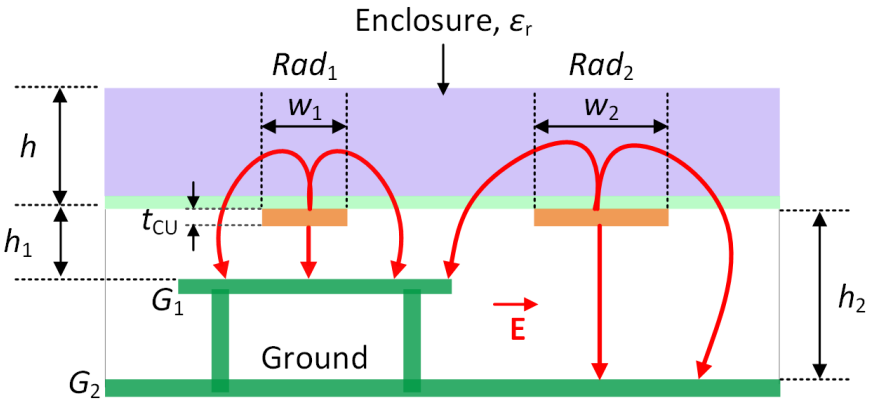


Figure 6.7: Inverted microstrip topology.

The ε_{eff} value of the inverted microstrip line for element Rad_1 is calculated using equation (6.1) given in [160], where w_1 is defined as the width of Rad_1, h is enclosure thickness, h_1 is the height of Rad_1 from ground G_1, and ε_r is the relative electrical permittivity of the plastic enclosure.

$$\varepsilon_{eff} = \left[1 + (h/h_1)\left(A_1 - B_1 ln(w_1/h_1)\right)\left(\sqrt{\varepsilon_r} - 1\right)\right]^2 \tag{6.1}$$

where,

$$A_1 = [0.5173 - 0.1515\ ln(h/h_1)]^2, \tag{6.2}$$

$$B_1 = [0.3092 - 0.1047\ ln(h/h_1)]^2. \tag{6.3}$$

Using equation (6.1), for ε_r = 2.9 (measured), h = 1.5 mm, h_1 = 2.3 mm, w_1 = 1 mm, the ε_{eff} value for element Rad_1 was calculated to be 1.45. Note that the above calculation holds true for calculating ε_{eff} for element Rad_2 also. For element Rad_2, width w_2 = 3 mm, height from ground h_2 = 7.5 mm, h = 1.5 mm and ε_r = 2.9, the ε_{eff} value for element Rad_2 was calculated to be 1.23. As the distance from elements Rad_1 and Rad_2 to ground G_1 is much less (5.2 mm) than the distance to G_2, as depicted in Figure 6.7, the E-field density is greater in this region and more fields pass through the enclosure material than in air. Therefore, a value of ε_{eff} = 1.45 has been chosen for the TL model simulations.

6.3.2.1 Parametric Analysis using Transmission Line (TL) Model

In this section, a parametric analysis is performed using the TL model described in the previous section to study the key antenna parameters that affect the impedance response with the goal of maximizing the impedance bandwidth.

The starting values for the physical parameters of the TL model were determined from the final design parameters obtained from the EM simulation of the previous 915 MHz antenna [52] described in Chapter 5. The starting values for the lumped parameters (R_{A1}, R_{A2}, C_{F1} and C_{F2}) were derived experimentally by comparing the S_{11} responses of the TL model and measured data of the proposed antenna (measurements described in Section 6.4 of this chapter). Note that for the parametric analysis, only one parameter is varied at a time while the other parameters are kept constant, as tabulated in Table 6.1 at the end of this section.

Figure 6.8 shows the S_{11} response when the shunt inductance parameter, L_{SH} is varied. The starting value of L_{SH} was derived from the EM simulation of the previous antenna [52]. It can be seen that inductance L_{SH} primarily affects the upper resonant frequency or f_H response. This is expected because L_{SH} mainly affects the impedance matching of element Rad_1 as it is added in shunt with the feed to balance the capacitance of element Rad_1 that is in close proximity to ground. Also, as increasing L_{SH} increases the effective inductance of element Rad_1, f_H gradually decreases with increasing the value of L_{SH} [161]. Therefore, parameter L_{SH} enables the impedance matching and the bandwidth adjustment of the antenna. The final value for L_{SH} is selected to be 5 nH.

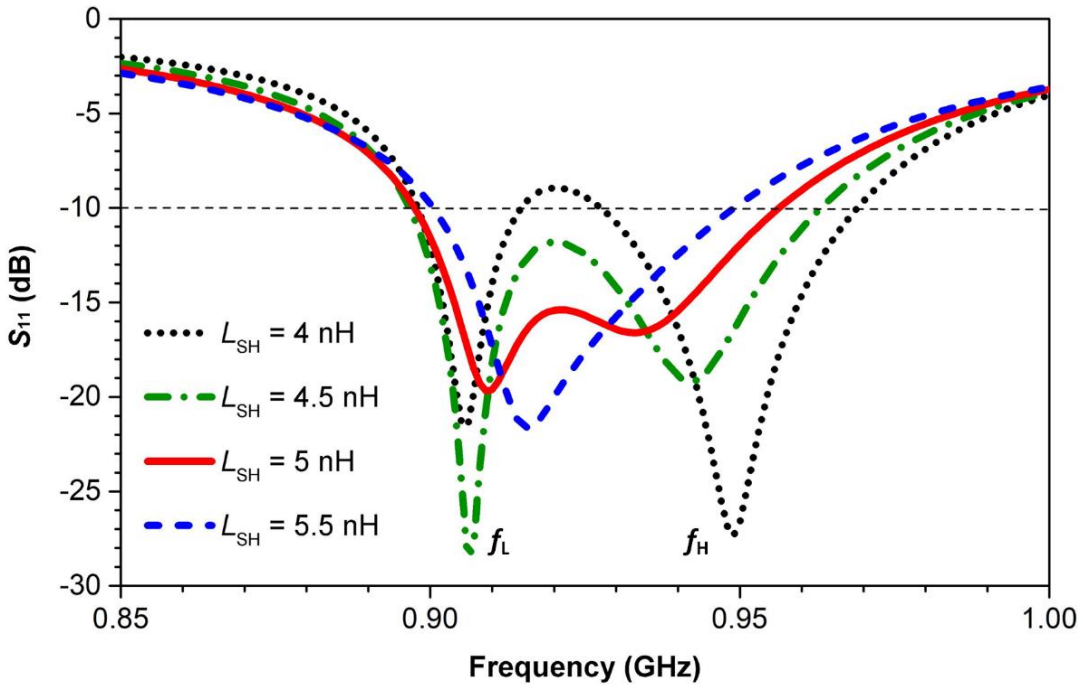


Figure 6.8: Simulated TL model S_{11} response for varying L_{SH}.

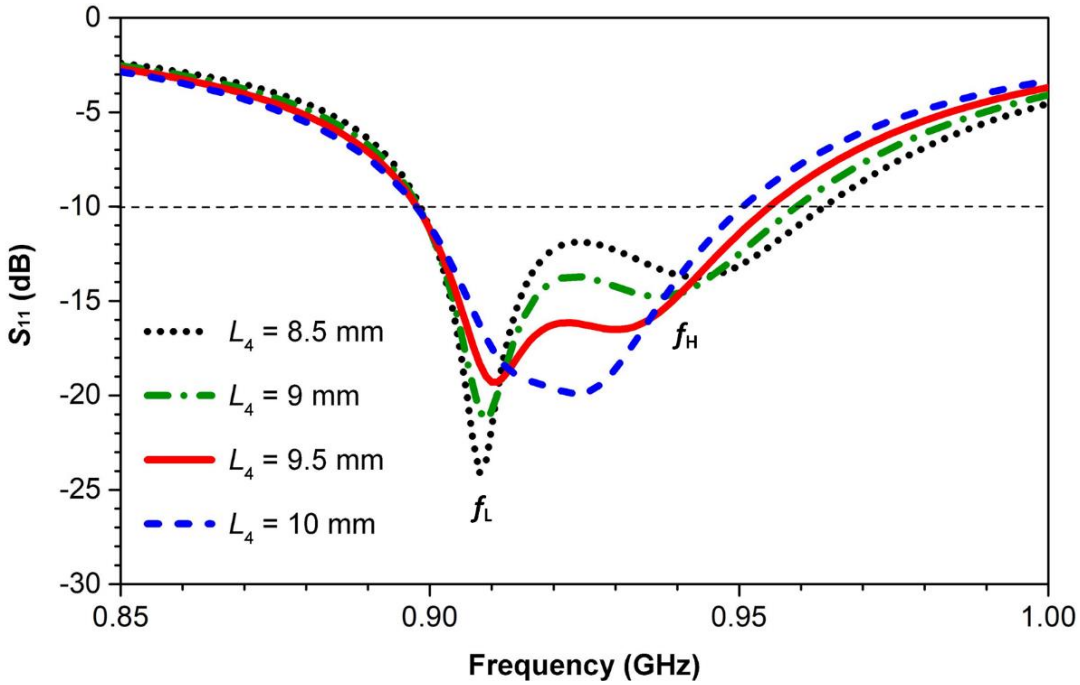


Figure 6.9: Simulated TL model S_{11} response for varying L_4.

Figure 6.9 shows the S_{11} response of the antenna to varying the parameter L_4 that represents the end length of element Rad_1. The resonance at f_H is created by element Rad_1, and the resonance at f_L is created by element Rad_2. Because, parameter L_4 adjusts the total length of element Rad_1, it mainly controls the f_H response. Increasing L_4 leads to a decrease in f_H, because the electrical length of element Rad_1 increases with increasing length L_4, leading to a reduction in f_H. In addition, varying length L_4 also has an influence on the input impedance of the antenna, and so affects the S_{11} magnitude. Thus, length L_4 enables matching of the input impedance and controls the impedance bandwidth of the antenna. The final value for L_4 is selected to be 9.5 mm because for this value the S_{11} response has an optimal compromise for wider impedance bandwidth along with impedance matching at both f_L and f_H.

In Figure 6.10, the S_{11} response of the antenna for a varying parameter L_5 or the end length of element Rad_2 is shown. Parameter L_5 determines the total electrical length of element Rad_2 and mainly controls the resonant response at f_L. Element Rad_2 has a total electrical length longer than element Rad_1, and thus Rad_2 is resonant at f_L. As expected, increasing length L_5 leads to a reduction in f_L.

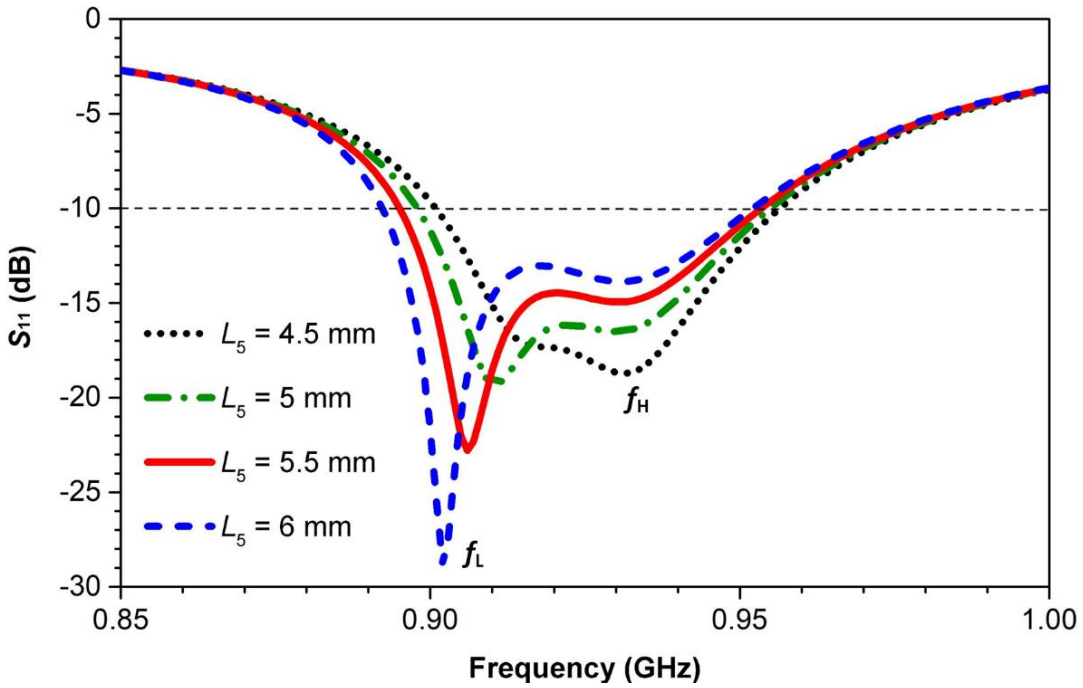


Figure 6.10: Simulated TL model S_{11} response for varying L_5.

Increasing length L_5 improves the impedance bandwidth of the antenna as it enables adjustment of f_L and the magnitude of S_{11} at f_L. The final value for L_5 is selected to be 5 mm, because this provides a wider impedance bandwidth along with impedance matching at both f_L and f_H.

Table 6.1: Final Optimized TL Parameters of the Proposed Antenna.

Parameter Name	Value (mm)	Parameter Name	Value
L_1	11.6	h_1	2.3 mm
L_2	6	h_2	7.5 mm
L_3	45	S_1	3.2 mm
L_4	9.5	S_2	2 mm
L_5	5	R_{A1}	120 Ω
L_S	2.5	R_{A2}	54 Ω
L_C	50	Z_0	50 Ω
W_1	1	C_{F1}	0.23 pF
W_2	3	C_{F2}	0.275 pF
h	1.5	L_{SH}	5 nH
t_{CU}	0.018		

The parametric study provided a better understanding of how to control impedance matching and tune f_L and f_H to improve the impedance bandwidth response of the antenna. The final optimized TL design parameters that maximize the impedance bandwidth of the proposed antenna are listed in Table 6.1.

6.3.3 Electromagnetic (EM) Simulations of the Proposed Antenna

The EM simulations of the proposed antenna were performed using ANSYS HFSS [137]. The final optimized physical parameters of the proposed antenna are listed in Table 6.2.

Table 6.2: Final optimized EM model parameters of the proposed antenna.

Parameter Name	Value (mm)	Parameter Name	Value (mm)
L_1	10.5	h	1.5
L_2	5	h_1	2.3
L_4	11	h_2	7.5
L_5	5	S_1	3.2
L_S	2.5	S_2	2
W_1	1	H	13.5
W_2	3	t_{CU}	0.018

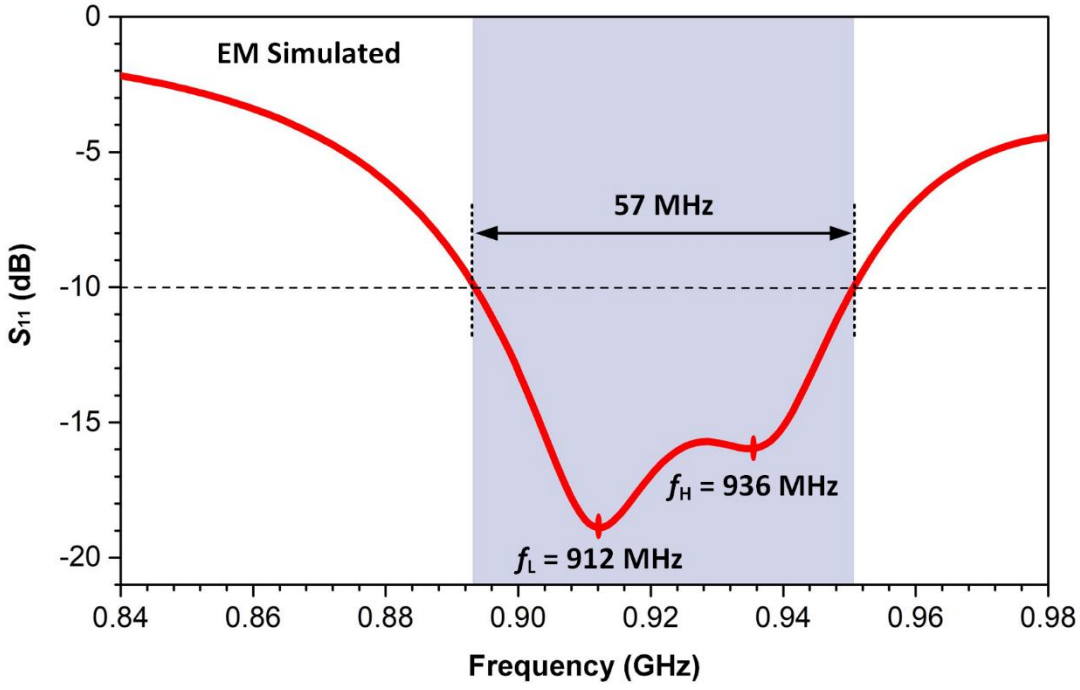


Figure 6.11: EM Simulated S_{11} response of the proposed antenna.

The simulated S_{11} response of the antenna obtained from the EM model is shown in Figure 6.11. It can be seen that the proposed antenna is resonant at two frequencies, denoted f_L = 912 MHz and f_H = 936 MHz. These resonant frequencies can be independently tuned to maximize the impedance bandwidth of the antenna.

As summarized in Table 6.3, the EM model provides S_{11} response of the antenna in 8:34 hours or 30840 seconds. However, the equivalent TL model described in the previous section has enabled impedance response analysis in a greatly reduced computation time of 0.03 seconds. Note that both EM and TL model simulations were performed using a computer with a 64 GB RAM, 3.41 GHz 4 Cores i7 processor and a 64-bit operating system.

Table 6.3: Comparing EM and TL models S_{11} computation time.

Antenna Modelling type	Simulation time (in seconds)
EM model	30840
TL model	0.03

6.3.3.1 Surface Current Distribution

It was described earlier in EM simulation that the proposed antenna has a dual-resonant response with f_L = 912 MHz and f_H = 936 MHz. In Figure 6.12(a) the simulated surface current distribution at f_L = 912 MHz is illustrated. Large magnitude currents are observed on element Rad_2 compared to Rad_1, which signifies that element Rad_2 is resonant at 912 MHz. The simulated surface current at f_H = 936 MHz is illustrated in Figure 6.12(b), and large magnitude currents on element Rad_1 shows that element Rad_1 is resonant at 936 MHz. Furthermore, at both 912 MHz and 936 MHz, large current flow is observed at point *a* along the shunt inductive tuning path across the antenna feed between the signal (*S*) and ground (*G*) contacts. This is expected due to the low impedance path between points *S* and *G*.

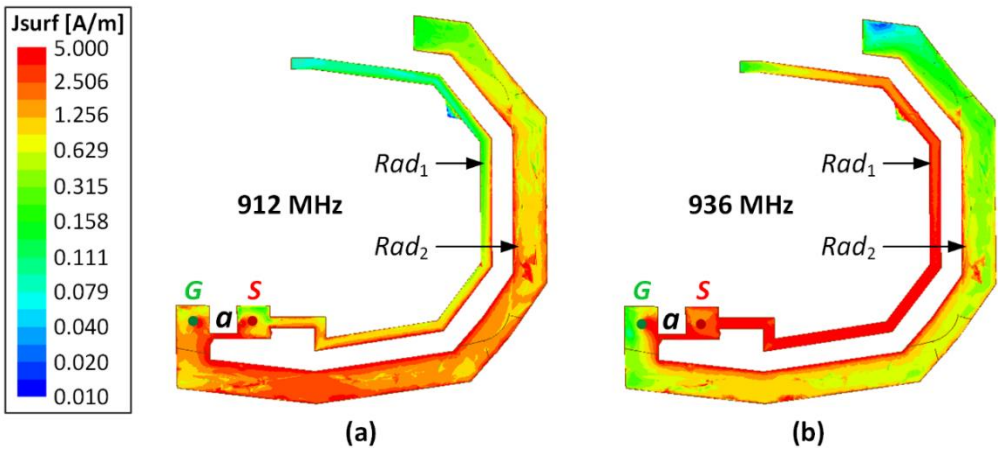


Figure 6.12: Surface current distribution at (a) 912 MHz and (b) 936 MHz.

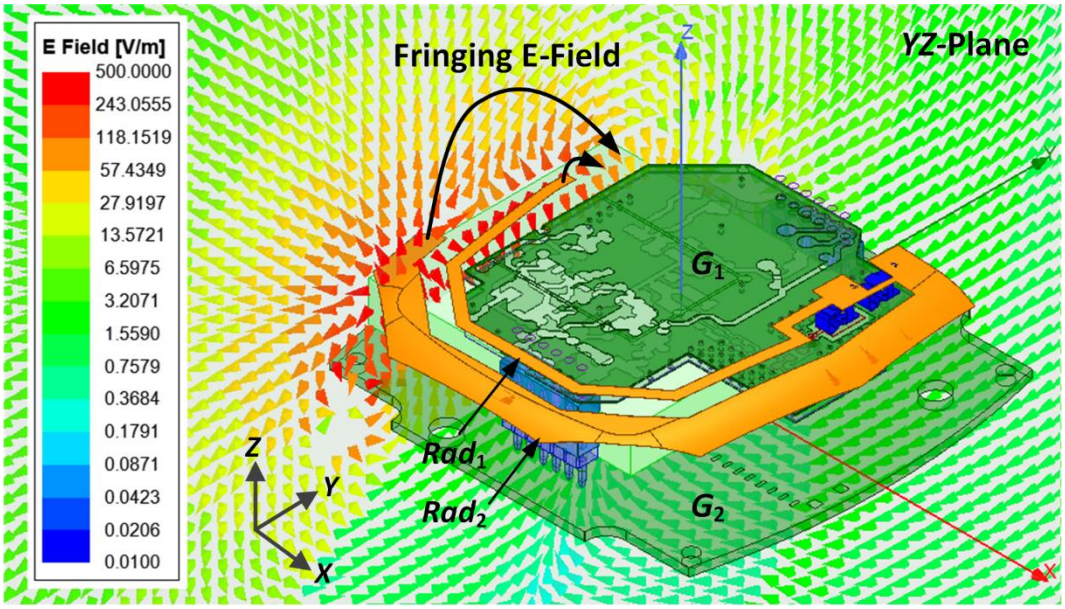


Figure 6.13: E-field distribution in the *YZ*-plane at 915 MHz.

6.3.3.2 Radiation Mechanism of the proposed antenna

To explain the radiation mechanism of the proposed antenna, the E-field distribution in the *YZ*-plane is investigated. In Figure 6.13, the E-field distributions in the YZ-plane (passing through the ends of elements Rad_1 and Rad_2) at 915 MHz are illustrated. Large magnitude E-fields emerge from the open *ends* of both radiating elements and terminate at the ground planes. This is due to fringing field close to the ends of both elements that are the main source of radiation for the antenna [149-152].

6.3.3.3 *Simulated 3D Radiation Pattern of the Proposed Antenna*

Figure 6.14 illustrates the simulated 3D realized gain radiation pattern of the proposed antenna at 915 MHz. The radiation pattern is consistent with the pattern of a PIFA antenna [40] and the finite ground planes G_1 and G_2 of the PIFA minimizes the power radiation towards the phantom arm. The antenna has omnidirectional radiation characteristics in the *XY*-plane. In the *YZ*- and XZ-planes, the antenna has radiation nulls, which are expected due to the shielding effect of the finite PIFA ground planes in combination with body absorption along the *Z*-axis. As shown in Figure 6.14, the proposed antenna has a simulated peak realized gain of -4.46 dBi at 915 MHz.

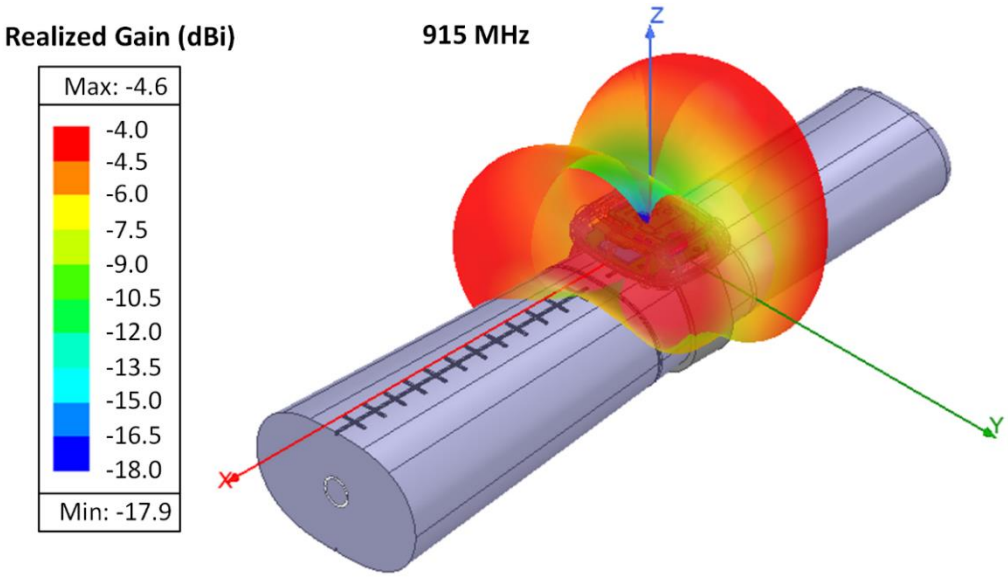


Figure 6.14: Simulated 3D Realized Gain radiation pattern at 915 MHz.

6.3.3.4 *Specific Absorption Rate (SAR) Evaluation*

The Specific Absorption Rate (SAR) [29, 80] parameter is a measure of the rate at which power is absorbed by the human body when exposed to electromagnetic (EM) radiation [78]. The simulated SAR level for the proposed antenna was evaluated on a Speag SHO-GFPC-V1 phantom arm [145]. According to the Federal Communications Commission (FCC) [109] and International Commission on Non-Ionizing Radiation Protection (ICNIRP) guidelines [80], for limbs, the standard SAR exposure level should not exceed 4.0 W/kg, averaged over 10 g of tissue mass.

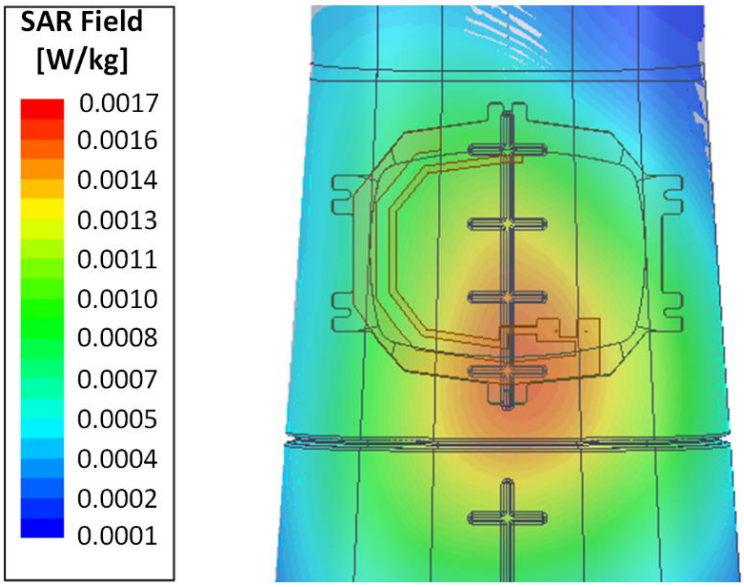


Figure 6.15: Simulated SAR distribution on the phantom arm at 915 MHz.

As shown in Figure 6.15, for an input power of 1 mW, an EM simulated peak SAR value of 0.0017 W/kg at 915 MHz is obtained. This simulated SAR value is less than 0.05 % of the SAR limit of 4 W/kg for general public limb-wearable applications [80, 109]. The finite ground planes (G_1 and G_2) of the antenna reduce the backward radiation towards the human wrist [40, 65]. Therefore, the shielding provided by the ground planes is critical in achieving a low SAR figure.

The EM simulated performance characteristics of the proposed antenna for the final design parameters listed in Table 6.2 are summarized in Table 6.4.

Table 6.4: The EM simulated performance summary of the proposed 915 MHz antenna.

-10 dB impedance bandwidth (MHz)	Peak realized gain at 915 MHz (dBi)	Radiation Efficiency at 915 MHz (%)	SAR at 915 MHz at 1 mW (W/kg)
57	-4.46	15.9	0.0017

6.4 Antenna Measurements

To validate the antenna design, the proposed antenna with the physical dimensions obtained from the EM simulation was fabricated and its characteristics were measured. A photograph of the fabricated antenna that is attached to a wristwatch enclosure is shown in Figure 6.16.

Furthermore, in Figure 6.17, a photograph of the internal components of the wristwatch device such as sensor assembly, radio PCB (G_1) with 50 Ω coaxial cable, motherboard PCB (G_2) with an attached battery, screws and the prototype antenna is illustrated.

For conducting the impedance and radiation measurements, the fabricated antenna and all internal components were integrated inside the wristwatch device or device under test (DUT). All the measurements of the DUT were performed after placing the wristwatch device on a Speag SHO-GFPC-V1 phantom arm [145]. The S_{11} response of the antenna was measured using an Anritsu MS2038C vector network analyzer [62].

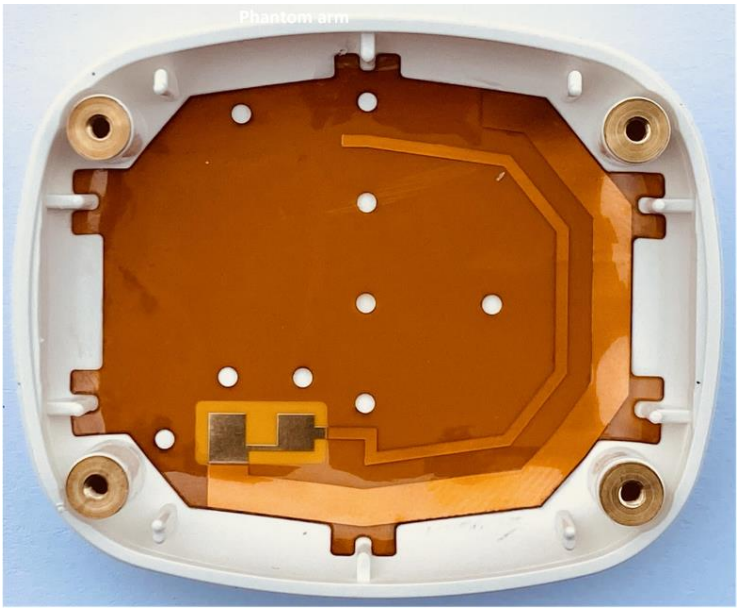


Figure 6.16: Photograph of the fabricated antenna.

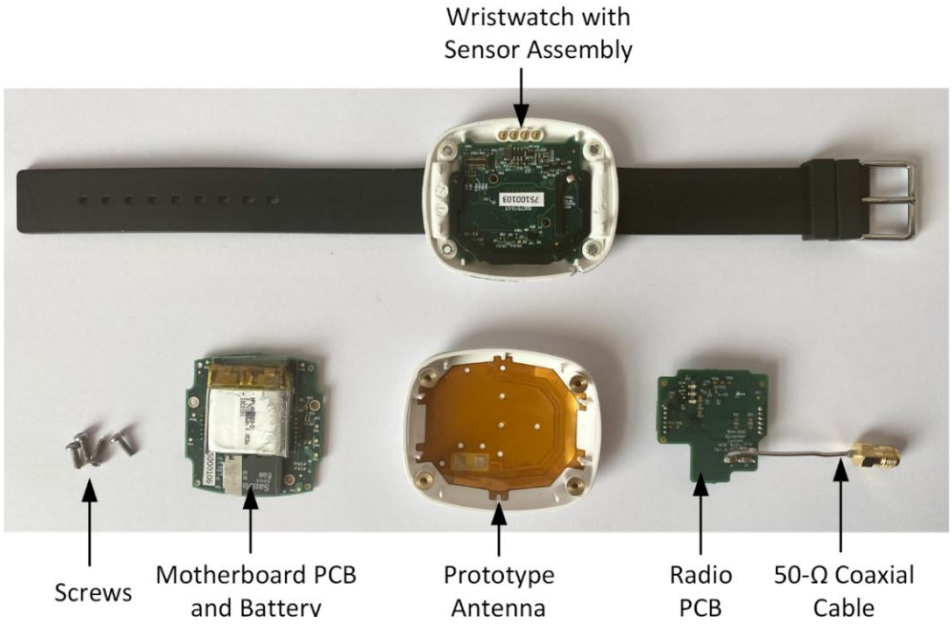


Figure 6.17: Internal components of the wristwatch device.

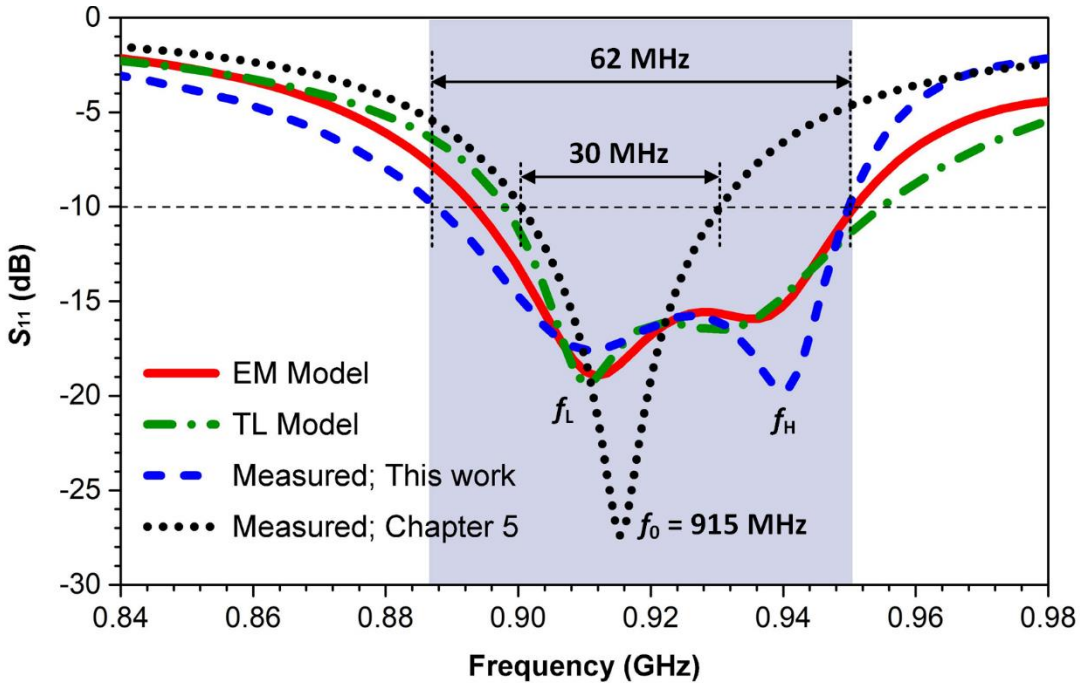


Figure 6.18: Simulated (TL and EM models) and measured S_{11} response of the antenna.

Figure 6.18 compares the measured and simulated S_{11} responses obtained from the TL and EM models for the proposed antenna and the measured S_{11} response for the 915 MHz antenna presented in Chapter 5. For the proposed antenna, both simulated and measured S_{11} responses are shown to be resonant at two frequencies, f_L and f_H, corresponding to elements Rad_2 and Rad_1, respectively. The proposed antenna achieves a measured -10 dB impedance bandwidth of 62 MHz, which is approximately 2.4 times the minimum required bandwidth of 26 MHz for 915 MHz operation.

For the 915 MHz antenna in Chapter 5, a measured -10 dB impedance bandwidth of 30 MHz was demonstrated. On the other hand, the proposed antenna exhibits a measured -10 dB impedance bandwidth of 62 MHz, which is 107 % higher than the previous antenna. A slight discrepancy in the simulated and measured responses is attributed to the combined effects of small changes in the position of the internal components of the wristwatch assembly, measurement setup and losses in the ferrite-beaded cable used in the measurement.

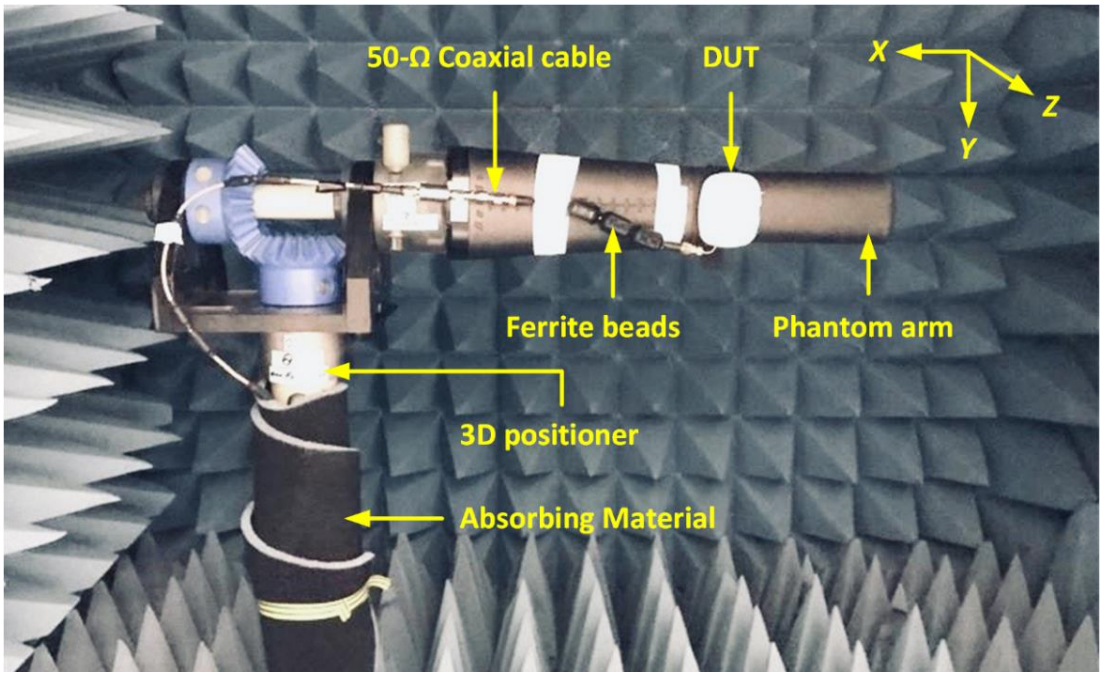


Figure 6.19: Device under test (DUT) measurement setup in an AMS-8050 anechoic chamber.

Figure 6.19 shows the anechoic chamber measurement setup of the DUT in an AMS-8050 antenna measurement system [63]. The rotation of the DUT in the anechoic chamber is controlled using the 3D positioner. The DUT was placed on an Speag phantom arm [145] and was supported on a mounting fixture. The antenna is excited using an unbalanced 50 Ω coaxial cable. Since the coaxial cable can affect the antenna radiation properties, multiple ferrite beads have been incorporated in the measurement setup to suppress the effects of coaxial cable currents on the antenna radiation characteristics. As shown in Figure 6.19, the coaxial cable runs along the 3D positioner and an EM radiation absorbing material has been used to cover the coaxial cable to minimize the effects of the cable on the radiation characteristics of the antenna.

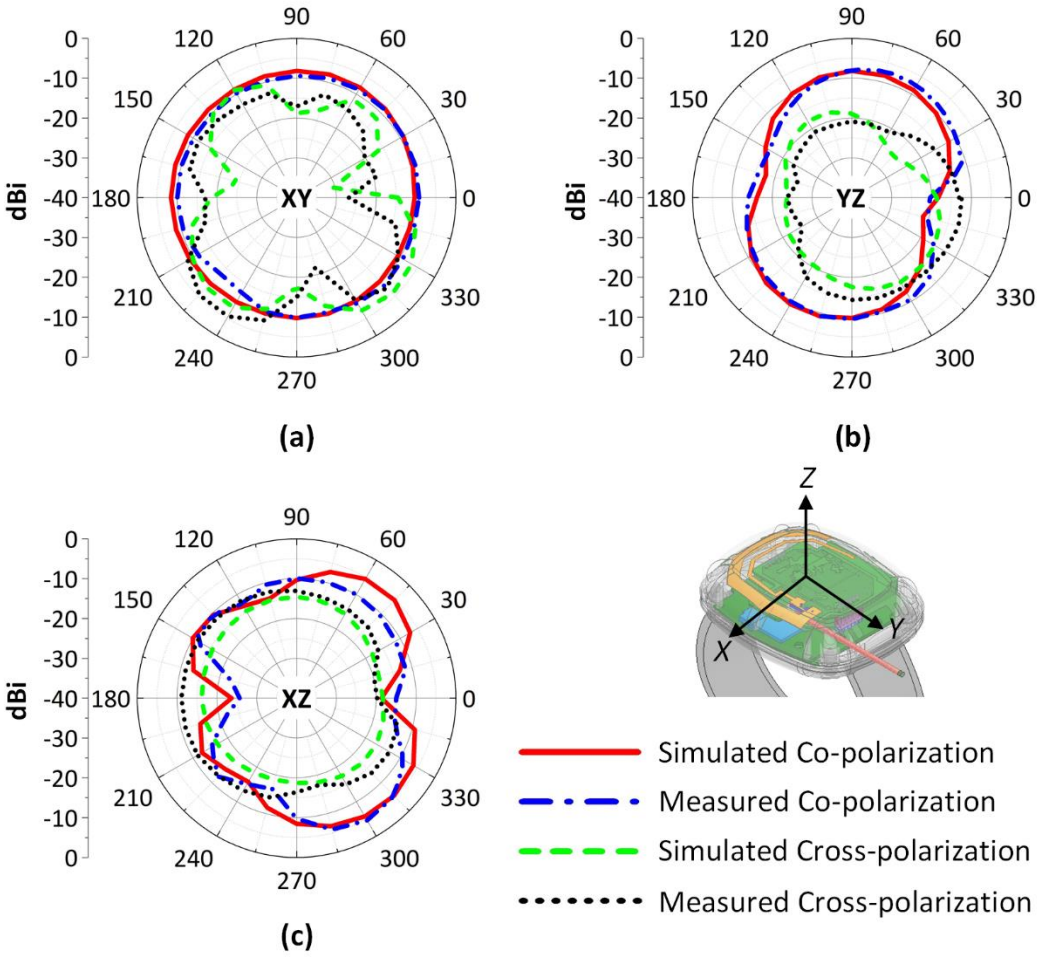


Figure 6.20: Simulated and measured radiation patterns of the antenna at 915 MHz: (a) *XY*-plane, (b) *YZ*-plane and (c) *XZ*-plane.

In Figure 6.20, the simulated and measured radiation characteristics of the proposed antenna in three principal planes *XY, YZ* and *XZ* at 915 MHz are illustrated. As shown in Figure 6.20(a), for the co-polarized case the antenna has an omnidirectional radiation pattern in the *XY*-plane, where the simulated and measured co-polarized radiation patterns correlate well in the *XY*-plane. The radiation patterns in the *YZ*- and *XZ*-planes are respectively illustrated in Figure 6.20(b) and (c). The co-polarized radiation patterns exhibit nulls in the YZ- and XZ-planes. The presence of the radiation nulls can be explained by taking into account the shielding effect of the antenna's finite ground planes and the energy absorption by the phantom arm. A slight discrepancy in the simulated and measured radiation characteristics in the *YZ*- and *XZ*-planes is attributed to the combined effects of possible small changes in the position of the internal components of the wristwatch assembly, measurement setup and losses in the ferrite-beaded cable that was not included in simulation.

At 915 MHz, the on-phantom prototype antenna exhibits a measured peak realized gain of -4.6 dBi and a simulated radiation efficiency of 15.9 %.

6.5 Performance Evaluation of the Proposed Antenna

Table 6.5 on the next page shows a performance comparison of the developed wristwatch antenna (row 7) with previously reported wrist-worn antennas to identify the performance improvements that the developed antenna has enabled compared with other works in this research area.

Table 6.5*:* Comparing on-phantom performance of the developed antenna with the literature.

A	B	C	D			E	F	G	H	I
Row	Ref.	Antenna Topology	Dimensions (mm)			f_0 (MHz)	-10 dB *BW* (MHz)	*Gain* (dBi) @ f_0	*h* (%) @f_0	*SAR* (W/kg) @f_0
			L	*W*	*h*					
1	[43]	Loop	40	30	10	920	180	NA	6.4	NA
2	[44]	Dipole	127	25	2	850	160	-8.3	7	3.75
3	[45]	Dipole	145	40	NA	900	160	NA	6.3	0.18
4	[42]	IFA[4]	93	37	5	780	105[1]	NA	7.9	NA
5	[46]	PIFA[4]	64.8	45.6	4.75	866	105	-4.4	26	0.78
6	[47]	Loop	201	56	0.2	900	100	-8[5]	NA	NA
7	**This Work**	**PIFA**	**48**	**41**	**2.3**	**915**	**62**	**-4.6**	**17.8**	**0.0017**
8	[28]	PIFA[4]	44	28	1.6	915	55[1]	-6.09	NA	NA
9	[48]	Dipole[4]	220	10	0.25	922.5	44	-11.2	NA	NA
10	[49]	PIFA[4]	44	44	10	767	35[1]	-5.4	13	NA
11	[50]	PIFA[5]	188	30	6	880	28	NA	83.7	NA
12	[116]	Helix	40	40	14.4	890	23	NA	NA	NA
13	[34]	Patch	86	25	1.6	915	19[3]	-6.87[5]	NA	NA
14	[36]	Helical	110	29	1.55	868	17	-13[5]	NA	NA
15	[37]	Monopole	100	15	0.6	911	14	-5.35	NA	NA
16	[38]	Monopole	40	15	1.8	911	7.5	-5.86	NA	NA
17	[39]	IFA[4]	45	30	5.5	846	7[5]	NA	14.8	NA
18	[40]	PIFA[4]	$\pi \times 25^2 \times 5$			402.5	5.2[2,3]	-12	3.6	NA
19	[30]	PIFA	$\pi \times 25^2 \times 5$			402.5	4.22[2,3]	-9.2	6.9	NA
20	[41]	Loop[5]	50	35	3	868	3.5	-1.44	NA	0.0002
21	[35]	Spiral[5]	$\pi \times 16^2$			915	3[3]	-1.04	NA	NA
22	[117]	PIFA	76.1	13.6	9.5	866	NA	-6.6	8.6	NA
23	[118]	Patch[5]	120	29	0.64	867	NA	-13	NA	NA
24	[119]	PIFA	90	20	3	923	NA	-5	NA	NA

This table is sorted in decreasing order of -10 dB bandwidth in column F

Important Notes:

[1] Antenna requires the use of an impedance matching network

[2] Only the -6 dB impedance bandwidth is reported

[3] Antenna does not meet the -10 dB bandwidth requirements for the targeted band

[4] Antenna was fully integrated in a wristwatch device

[5] Only simulated results are reported

NA = Information not reported

In Table 6.5 (row 7), the impedance and radiation performance of the antenna developed in this work is summarized. The developed antenna has achieved a -10 dB impedance bandwidth of 62 MHz in the most compact sized wristwatch form factor in the literature. At the same time, the developed antenna has demonstrated a competitive high peak realized gain and radiation efficiency performance.

6.6 Conclusions

This chapter has presented the design and modelling of a new bandwidth enhanced 915 MHz wristwatch antenna developed to meet the system requirements associated with a wristwatch sized wireless sensing system. The antenna design described in this chapter incorporates two mutually coupled radiating elements and achieved a measured 107 % improvement in the -10 dB impedance bandwidth when compared to the previous antenna [52] described in Chapter 5. This bandwidth enhancement was achieved by optimizing the feed structure of the previous antenna to enable the excitation of two closely located resonant frequencies that can be independently tuned to maximize the impedance bandwidth.

The measured on-phantom prototype antenna achieved a -10 dB impedance bandwidth of 62 MHz which is more than double the minimum required impedance bandwidth of 26 MHz for the 915 MHz band operation [55]. Furthermore, the developed antenna is published in [54] and represents the most compact wristwatch-integrated antenna that achieves a -10 dB impedance bandwidth of more than 60 MHz, as well as with improved peak realized gain (greater than -5 dBi) and radiation efficiency (greater than 17 %) when compared to the state-of-the-art Sub-GHz wrist-worn antennas.

A conceptual equivalent circuit model for the proposed antenna was derived to explain the impedance bandwidth enhancement achieved. Another key contribution of this work is the development of a novel equivalent transmission line (TL) model to accurately predict the impedance characteristics with greatly improved speed compared to EM simulation (the simulation time was reduced from hours to seconds). In addition, for 1 mW input power, the simulated peak SAR value of less than 0.05 % of the maximum permissible limit is demonstrated, making the proposed antenna suitable for wireless wristwatch devices. The results of the antenna presented in this chapter have been published in [54].

Chapter 7: Conclusions and Future Work

This chapter summarizes the research work conducted and described in this thesis. The key focus of this thesis was to design new Sub-GHz wristwatch antennas with improved impedance bandwidth performance when compared to the state-of-the-art reported in the literature. In the last decade, the Sub-GHz bands have received increased interest for internet-of-things (IoT) applications due to emerging wireless technologies such as long-range wide-area network (LoRaWAN) [15] and SigFox [16]. Use of the Sub-GHz bands has potential for increased wireless communication range with low power consumption and increased battery life when compared with 2.45 GHz-based technologies, such as Bluetooth and Wi-Fi. The identified advantages of wireless communications at Sub-GHz bands were a key motivation for selecting Sub-GHz frequencies for IoT wristwatch applications. However, the design of antennas for Sub-GHz bands is challenging due to the practical size constraints of wristwatch devices. The high level of integration required for such wristwatch devices results in the need for electrically small antenna designs that have limited impedance bandwidth and radiation performance. Another key challenge is the presence of the human body in the immediate vicinity of the antenna. The electromagnetic (EM) coupling between the antenna and human body can lead to antenna impedance mismatch and losses of radiated antenna power by absorption in human tissue [32, 33].

In Chapter 3 of this thesis, several gaps in current state-of-the-art relating to the limited impedance bandwidth of Sub-GHz wristwatch antennas were identified. Based on the literature review, a hypothesis was formulated that involved the use of a dual-radiator approach to enhance impedance bandwidth performance for wristwatch antennas compared to that reported in the literature.

7.1 Contributions to the state-of-the-art

This thesis aimed at addressing the aforementioned impedance bandwidth related challenges and developing novel Sub-GHz wristwatch-integrated antennas in a highly constrained form factor. The major contributions of this thesis include the development of four new Sub-GHz wristwatch-integrated antennas [51-54], with the impedance and radiation characteristics of the developed antennas summarized in Table 7.1.

Table 7.1: Performance summary of the Sub-GHz wristwatch antennas developed in this thesis.

Ref.	f_0 (MHz)	*-10 dB BW** (MHz)	G_R** (dBi) @ f_0	*Efficiency h* (%) @ f_0	*SAR* (W/kg) @ f_0	Key Contributions
[51]	915	28.3	-0.57	46.8	0.0034	Dual-radiator. Highest G_R. Second highest *h*.
[52]	915	30	-4.9	15.9	0.0019	Dual-radiator. Compact size. Simultaneously improved *BW*, G_R and *h* compared to the literature.
[53]	868	36	-4.86	14.5	0.0027	Second highest *BW*, G_R and *h* using LDS technology. Most compact LDS printed.
[54]	915	62	-4.6	17.8	0.0017	Dual-resonant response. 107 % BW enhancement compared to [52]. Transmission line model.

*BW** = -10 dB impedance bandwidth, G_R** = Peak realized gain at f_0.

In Chapter 4 [51], the design and development of a novel bandwidth enhanced 915 MHz planar inverted-F antenna (PIFA) was presented. For this antenna, a dual-radiator approach was used to improve the impedance bandwidth and radiation performance of the antenna. The dual-radiator approach was not reported previously in the literature for Sub-GHz wristwatch antennas. The developed antenna demonstrated the highest peak realized gain and the second highest radiation efficiency for Sub-GHz wristwatch antennas reported in the literature.

Chapter 5 [52, 53] presented the development of two new bandwidth enhanced wristwatch-integrated compact PIFA antennas operating in the 915 MHz and 868 MHz bands. The 915 MHz antenna was fabricated using a low cost flexible polyimide substrate and the 868 MHz antenna was directly printed on the surface of a wristwatch enclosure using laser direct structuring (LDS) technology. The 915 MHz antenna featured one of the most compact (48 mm × 41 mm × 2.3 mm) antenna designs when compared to state-of-the-art Sub-GHz wrist-worn antennas with a -10 dB impedance bandwidth of 30 MHz, a peak realized gain of -4.9 dBi and a radiation efficiency of 15.7 % at 915 MHz. The 868 MHz antenna is the most compact LDS printed Sub-GHz wristwatch antenna in the literature. In addition, the measurements on the 868 MHz prototype antenna demonstrated the second highest -10 dB impedance bandwidth, the second highest peak realized gain as well as the second highest radiation efficiency for LDS printed Sub-GHz wristwatch antennas reported in the literature.

For the antenna presented in Chapter 6 [54], the feed structure of the flexible 915 MHz antenna described in Chapter 5 [52] was optimized to enable the excitation of two closely located resonant frequencies that could be independently tuned to maximize the impedance bandwidth by 107 % compared to the antenna described in [52]. With a -10 dB impedance bandwidth greater than 60 MHz, the developed antenna is the most compact sized design for Sub-GHz wristwatch-integrated antennas in the literature. The radiation performance of the antenna in [54] is similar to that reported in [52]. The excitation of two adjacent resonant frequencies is a novel bandwidth enhancement approach, which is not reported previously for Sub-GHz wristwatch antennas in the literature. Another key contribution of this work includes the development of a new equivalent transmission line (TL) model of the antenna to rapidly predict the antenna impedance characteristics. The TL model requires greatly reduced computation time (0.03 seconds) when compared to EM simulation that requires 8:34 hours.

Furthermore, all the developed wristwatch antennas presented in this thesis have obtained a low specific absorption rate (SAR) of less than 0.1 % of the maximum permissible SAR limit of 4 W/kg averaged over 10 g of wrist tissue [80, 109], making the developed antennas suitable for a wide range of wristwatch-based wireless applications. The peer-reviewed journal and conference publications that have emanated from this research work are listed at the end of this chapter.

7.2 Future Work

The work presented in this thesis suggests several potential areas for further research and investigation. The identified research areas that could be explored further in the future include the following:

1) Another research direction that is worth considering for antenna research is the development of improved equivalent circuit models for antennas such as those presented in this thesis. In comparison to EM methods, equivalent circuit models derived from the antenna physical parameters would be a valuable antenna design tool and would help provide enhanced insight and intuition on how to improve the impedance response of the antennas. The antennas developed in this thesis used two radiating elements and with the derived equivalent circuit model, the mutual coupling between the radiating elements could further be investigated with the aim to further improve the antenna performance. Furthermore, similar to the equivalent circuit-based characteristic mode analysis approach taken in [162], further circuit model analysis could be performed to predict the radiation performance of the antennas.
2) Depending on the regulations and geographical region, different Sub-GHz frequencies have been allocated in different regions or countries, such as 915 MHz in North America, 868 MHz in Europe and 433 MHz in Asia [163]. However, using a separate antenna for each operating frequency within a compact wristwatch device is not practical due to volume constraints [164]. A frequency reconfigurable or tunable antenna could enable switching the operating frequency to the desired frequency and the use of such a reconfigurable antenna could thus reduce the required footprint and associated cost of a wireless wristwatch device. As an example, PIN diode or varactor diodes could be used as RF switches to adjust the effective length of an antenna [165] to achieve frequency reconfigurability for an antenna. However, reconfigurable antennas have not been a key focus of research for Sub-GHz wristwatch antennas and future research could include the design and development of such reconfigurable antennas for future wireless wristwatch devices.

3) Future work could also focus on the design of multi-band wristwatch antennas with the goal to cover several Sub-GHz frequency bands, such as 433 MHz, 868 MHz and 915 MHz using a single antenna. For example, the dual-radiator antenna demonstrated in Chapter 6 can be further optimized to cover 868 MHz and 915 MHz bands. In addition, a third radiating element could also be incorporated in the design to simultaneously cover 433 MHz, 868 MHz and 915 MHz bands, similar to a triple-band Sub-GHz antenna described in [166].
4) For the 868 MHz LDS printed antenna presented in Chapter 5, the electrical characteristics of the electroplated LDS metal layer were not measured in this thesis work but would be a valuable addition for future work.

The following are the peer-reviewed publications that have emanated from the research work presented in this thesis:

Journal Publications:

[P1] S. Kumar, R. Newberry, T. Hannon, J. Barton, M. Rodencal, M. Pigeon, W. G. Scanlon, B. O'Flynn, and J. L. Buckley, "A Bandwidth-Enhanced Sub-GHz Wristwatch Antenna Using an Optimized Feed Structure," *IEEE Antennas and Wireless Propagation Letters,* vol. 20, no. 8, pp. 1389-1393, 2021.

[P2] S. Kumar, J. L. Buckley, J. Barton, M. Pigeon, R. Newberry, M. Rodencal, A. Hajzeraj, T. Hannon, K. Rogers, D. Casey, D. O'Sullivan, and B. O'Flynn, "A Wristwatch-Based Wireless Sensor Platform for IoT Health Monitoring Applications," *MDPI Sensors Journal,* vol. 20, no. 6, p. 1675, 2020.

Conference Publications:

[P3] S. Kumar, J. L. Buckley, J. Barton, R. Newberry, G. Dunlop, M. Rodencal, C. Webster, M. Pigeon, W. G. Scanlon, and B. O'Flynn, "A 915 MHz Wristwatch-Integrated Antenna for Wireless Health Monitoring," in *2020 14th European Conference on Antennas and Propagation (EuCAP)*, 2020, pp. 1-5.

[P4] S. Kumar, J. L. Buckley, J. Barton, R. Newberry, G. Dunlop, M. Rodencal, C. Webster, and B. O'Flynn, "A Bandwidth Enhanced 915 MHz Antenna for IoT Wrist-Watch Applications," in *2019 13th European Conference on Antennas and Propagation (EuCAP)*, 2019, pp. 1-5.

Bibliography

[1] R. Khan, S. U. Khan, R. Zaheer, and S. Khan, "Future Internet: The Internet of Things Architecture, Possible Applications and Key Challenges," in *2012 10th International Conference on Frontiers of Information Technology*, 2012, pp. 257-260.

[2] *Nurse Station, (Accessed on 6 May 2021)*. Available: https://pngtree.com/so/hospital-icons

[3] M. E. E. E. Alahi, N. Pereira-Ishak, S. C. Mukhopadhyay, and L. Burkitt, "An Internet-of-Things Enabled Smart Sensing System for Nitrate Monitoring," *IEEE Internet of Things Journal,* vol. 5, no. 6, pp. 4409-4417, 2018.

[4] G.-Z. Yang, *Body Sensor Networks*, 2 ed. London: Springer-Verlag, 2014.

[5] P. Sundaravadivel, E. Kougianos, S. P. Mohanty, and M. K. Ganapathiraju, "Everything You Wanted to Know about Smart Health Care: Evaluating the Different Technologies and Components of the Internet of Things for Better Health," *IEEE Consumer Electronics Magazine,* vol. 7, no. 1, pp. 18-28, 2018.

[6] J. W. Kim, J. H. Lim, S. M. Moon, and B. Jang, "Collecting Health Lifelog Data From Smartwatch Users in a Privacy-Preserving Manner," *IEEE Transactions on Consumer Electronics,* vol. 65, no. 3, pp. 369-378, 2019.

[7] E. G. Zimbelman and R. F. Keefe, "Development and validation of smartwatch-based activity recognition models for rigging crew workers on cable logging operations," *PLOS ONE,* vol. 16, no. 5, p. e0250624, 2021.

[8] J. S. Park, S. Robinovitch, and W. S. Kim, "A Wireless Wristband Accelerometer for Monitoring of Rubber Band Exercises," *IEEE Sensors Journal,* vol. 16, no. 5, pp. 1143-1150, 2016.

[9] T. M. Fernández-Caramés and P. Fraga-Lamas, "Towards The Internet of Smart Clothing: A Review on IoT Wearables and Garments for Creating Intelligent Connected E-Textiles," *Electronics,* vol. 7, no. 12, p. 405, 2018.

[10] W. Chang, L. Chen, and Y. Chiou, "Design and Implementation of a Drowsiness-Fatigue-Detection System Based on Wearable Smart Glasses to Increase Road Safety," *IEEE Transactions on Consumer Electronics,* vol. 64, no. 4, pp. 461-469, 2018.

[11] T.-C. Lu, C.-M. Fu, M. H.-M. Ma, C.-C. Fang, and A. M. Turner, "Healthcare Applications of Smart Watches. A Systematic Review," (in eng), *Applied clinical informatics,* vol. 7, no. 3, pp. 850-869, 2016.

[12] H. Yu, S. Cang, and Y. Wang, "A review of sensor selection, sensor devices and sensor deployment for wearable sensor-based human activity recognition systems," in *2016 10th International Conference on Software, Knowledge, Information Management & Applications (SKIMA)*, 2016, pp. 250-257.

[13] *Statista: The global wearables market is all about the wrist, (Accessed on 16 February 2021)*. Available: https://www.statista.com/chart/3370/wearable-device-forecast/

[14] N. Azmi, L. M. Kamarudin, M. Mahmuddin, A. Zakaria, A. Y. M. Shakaff, S. Khatun, K. Kamarudin, and M. N. Morshed, "Interference issues and mitigation method in WSN 2.4GHz ISM band: A survey," in *2014 2nd International Conference on Electronic Design (ICED)*, 2014, pp. 403-408.

[15] *LoRa Alliance, (Accessed on 28 October 2021)*. Available: https://lora-alliance.org/

[16] *Sigfox, (Accessed on 28 October 2021)*. Available: https://www.sigfox.com/en

[17] S. Popli, R. K. Jha, and S. Jain, "A Survey on Energy Efficient Narrowband Internet of Things (NBIoT): Architecture, Application and Challenges," *IEEE Access,* vol. 7, pp. 16739-16776, 2019.

[18] E. De Poorter, J. Hoebeke, M. Strobbe, I. Moerman, S. Latré, M. Weyn, B. Lannoo, and J. Famaey, "Sub-GHz LPWAN Network Coexistence, Management and Virtualization: An Overview and Open Research Challenges," *Wireless Personal Communications,* vol. 95, no. 1, pp. 187-213, 2017/07/01 2017.

[19] S. Aust, R. V. Prasad, and I. G. M. M. Niemegeers, "IEEE 802.11ah: Advantages in standards and further challenges for sub 1 GHz Wi-Fi," in *2012 IEEE International Conference on Communications (ICC)*, 2012, pp. 6885-6889.

[20] J. A. Richards, *Radio Wave Propagation: An Introduction for the Non-Specialist*. Springer-Verlag Berlin Heidelberg, 2008.

[21] I. F. Akyildiz, W. Su, Y. Sankarasubramaniam, and E. Cayirci, "Wireless sensor networks: a survey," *Computer Networks,* vol. 38, no. 4, pp. 393-422, 2002/03/15/ 2002.

[22] H. Karvonen, M. Hämäläinen, J. Iinatti, and C. Pomalaza-Ráez, "Coexistence of wireless technologies in medical scenarios," in *2017 European Conference on Networks and Communications (EuCNC)*, 2017, pp. 1-5.

[23] R. Cavallari, F. Martelli, R. Rosini, C. Buratti, and R. Verdone, "A Survey on Wireless Body Area Networks: Technologies and Design Challenges," *IEEE Communications Surveys & Tutorials,* vol. 16, no. 3, pp. 1635-1657, 2014.

[24] "ETSI EN 300 220-2 V3.2.1 (2018-04), ," *Short Range Devices (SRD) operating in the frequency range 25 MHz to 1 000 MHz; Part 2: Harmonised Standard for access to radio spectrum for non specific radio equipment* pp. 1–50, 2018.

[25] S. Aust, R. V. Prasad, and I. G. M. M. Niemegeers, "Performance evaluation of Sub 1 GHz wireless sensor networks for the smart grid," in *37th Annual IEEE Conference on Local Computer Networks*, 2012, pp. 292-295.

[26] F. Wu, C. Qiu, T. Wu, and M. R. Yuce, "Edge-Based Hybrid System Implementation for Long-Range Safety and Healthcare IoT Applications," *IEEE Internet of Things Journal,* pp. 1-1, 2021.

[27] K. N. Paracha, S. K. A. Rahim, P. J. Soh, and M. Khalily, "Wearable Antennas: A Review of Materials, Structures, and Innovative Features for Autonomous Communication and Sensing," *IEEE Access,* vol. 7, pp. 56694-56712, 2019.

[28] A. Di Serio, J. Buckley, J. Barton, R. Newberry, M. Rodencal, G. Dunlop, and B. O'Flynn, "Potential of Sub-GHz Wireless for Future IoT Wearables and Design of Compact 915 MHz Antenna," *Sensors,* vol. 18, no. 1, p. 22, 2018.

[29] D. Wu and S. W. Cheung, "A Cavity-Backed Annular Slot Antenna With High Efficiency for Smartwatches With Metallic Housing," *IEEE Transactions on Antennas and Propagation,* vol. 65, no. 7, pp. 3756-3761, 2017.

[30] H. Hamouda, P. L. Thuc, R. Staraj, and G. Kossiavas, "Dualband MICS/WIFI small antenna for portable applications in telemedicine," in *2013 IEEE Antennas and Propagation Society International Symposium (APSURSI)*, 2013, pp. 2081-2082.

[31] R. Harrington, "Effect of antenna size on gain, bandwidth, and efficiency," *Journal of Research of the National Bureau of Standards, Section D: Radio Propagation,* p. 1, 1960.

[32] M. I. Hossain, M. R. I. Faruque, and M. T. Islam, "Investigation of hand impact on PIFA performances and SAR in human head," *Journal of Applied Research and Technology,* vol. 13, no. 4, pp. 447-453, 2015/08/01/ 2015.

[33] A. Alomainy, Y. Hao, and D. M. Davenport, "Parametric Study of Wearable Antennas with Varying Distances from the Body and Different On-Body Positions," in *2007 IET Seminar on Antennas and Propagation for Body-Centric Wireless Communications*, 2007, pp. 84-89.

[34] G.-L. Huang, C.-Y.-D. Sim, S.-Y. Liang, W.-S. Liao, and T. Yuan, "Low-Profile Flexible UHF RFID Tag Design for Wristbands Applications," *Wireless Communications and Mobile Computing,* vol. 2018, p. 9482919, 2018/06/07 2018.

[35] D. Wang, Y. J. Zhang, and M. S. Tong, "A wearable UHF RFID tag antenna with Archimedean spiral strips," in *2017 Progress in Electromagnetics Research Symposium - Fall (PIERS - FALL)*, 2017, pp. 1849-1852.

[36] S. Lopez-Soriano and J. Parron, "Design of a Small-Size, Low-Profile, and Low-Cost Normal-Mode Helical Antenna for UHF RFID Wristbands," *IEEE Antennas and Wireless Propagation Letters,* vol. 16, pp. 2074-2077, 2017.

[37] J. Park and J. Woo, "Microstrip Line Monopole Antenna for the Wearable Applications," in *2008 38th European Microwave Conference*, 2008, pp. 1277-1279.

[38] J. Park and J. Woo, "Miniaturization of microstrip line monopole antenna for the wearable applications," in *2008 Asia-Pacific Microwave Conference*, 2008, pp. 1-4.

[39] J. Chen, M. Berg, H. Y. Amin, and A. Pärssinen, "Effect of small wearable device antenna location on its impedance, bandwidth potential and radiation efficiency," in *Loughborough Antennas & Propagation Conference (LAPC 2017)*, 2017, pp. 1-5.

[40] H. Hamouda, P. L. Thuc, R. Staraj, and G. Kossiavas, "Small antenna embedded in a wrist-watch for application in telemedicine," in *The 8th European Conference on Antennas and Propagation (EuCAP 2014)*, 2014, pp. 876-879.

[41] M. Feliziani and F. Maradei, "Antenna design of a UHF RFID tag for human tracking avoiding spurious emission," in *2012 IEEE International Symposium on Electromagnetic Compatibility*, 2012, pp. 245-248.

[42] J. Chen, M. Berg, V. Somero, H. Y. Amin, and A. Pärssinen, "A multiple antenna system design for wearable device using theory of characteristic mode," in *12th European Conference on Antennas and Propagation (EuCAP 2018)*, 2018, pp. 1-5.

[43] C. Hong and S. Yeh, "Cellular antenna design with metallic housing for wearable device," in *2016 IEEE 5th Asia-Pacific Conference on Antennas and Propagation (APCAP)*, 2016, pp. 419-420.

[44] J. R. Flores-Cuadras, J. L. Medina-Monroy, R. A. Chavez-Perez, and H. Lobato-Morales, "Novel ultra-wideband flexible antenna for wearable wrist worn devices with 4G LTE communications," *Microwave and Optical Technology Letters,* vol. 59, no. 4, pp. 777-783, 2017.

[45] K. Zhao, Z. Ying, and S. He, "Antenna designs of smart watch for cellular communications by using metal belt," in *2015 9th European Conference on Antennas and Propagation (EuCAP)*, 2015, pp. 1-5.

[46] M.-A. Chung, "Embedded 3D multi-band antenna with ETS process technology covering LTE/WCDMA/ISM band operations in a smart wrist wearable wireless mobile communication device design," *IET Microwaves, Antennas & Propagation,* vol. 14, no. 1, pp. 93-100, 2020.

[47] Y. Jia, L. Liu, J. Hu, and L. Xu, "Miniaturized wearable watch antenna for wristband applications," in *2019 IEEE MTT-S International Microwave Biomedical Conference (IMBioC)*, 2019, vol. 1, pp. 1-3.

[48] T. Pumpoung, P. Wongsiritorn, C. Phongcharoenpanich, and S. Kosulvit, "UHF-RFID Tag Antenna Using T-Matching and Double-Ended Rectangular Loop Techniques for Wristband Applications," in *Theory and Applications of Applied Electromagnetics*, Cham, 2016, pp. 97-107: Springer International Publishing.

[49] S.-W. Su and Y.-T. Hsieh, "Integrated LDS antenna for B13 and B4/B3/B2/B1 LTE operation in smartwatch," *Microwave and Optical Technology Letters,* vol. 59, no. 4, pp. 869-873, 2017.

[50] G. Xu, Z. Zhijun, C. Wenhua, F. Zhenghe, M. F. Iskander, and Z. An-Ping, "A novel wrist wear dual-band diversity antenna," in *2009 IEEE Antennas and Propagation Society International Symposium*, 2009, pp. 1-4.

[51] S. Kumar, J. L. Buckley, J. Barton, R. Newberry, G. Dunlop, M. Rodencal, C. Webster, and B. O'Flynn, "A Bandwidth Enhanced 915 MHz Antenna for IoT Wrist-Watch Applications," in *2019 13th European Conference on Antennas and Propagation (EuCAP)*, 2019, pp. 1-5.

[52] S. Kumar, J. L. Buckley, J. Barton, R. Newberry, G. Dunlop, M. Rodencal, C. Webster, M. Pigeon, W. G. Scanlon, and B. O'Flynn, "A 915 MHz Wristwatch-Integrated Antenna for Wireless Health Monitoring," in *2020 14th European Conference on Antennas and Propagation (EuCAP)*, 2020, pp. 1-5.

[53] S. Kumar, J. L. Buckley, J. Barton, M. Pigeon, R. Newberry, M. Rodencal, A. Hajzeraj, T. Hannon, K. Rogers, D. Casey, D. O'Sullivan, and B. O'Flynn, "A Wristwatch-Based Wireless Sensor Platform for IoT Health Monitoring Applications," *Sensors,* vol. 20, no. 6, p. 1675, 2020.

[54] S. Kumar, R. Newberry, T. Hannon, J. Barton, M. Rodencal, M. Pigeon, W. G. Scanlon, B. O'Flynn, and J. L. Buckley, "A Bandwidth-Enhanced Sub-GHz Wristwatch Antenna Using an Optimized Feed Structure," *IEEE Antennas and Wireless Propagation Letters,* vol. 20, no. 8, pp. 1389-1393, 2021.

[55] "IEEE Standard for Low-Rate Wireless Networks," *IEEE Std 802.15.4-2015 (Revision of IEEE Std 802.15.4-2011),* pp. 1-709, 2016.

[56] "IEEE standard for definitions of terms for antennas, ," *IEEE Std 145-2013 (Revision of IEEE Std 145-1993),* pp. 1–50, 2013.

[57] C. A. Balanis, *Antenna theory: Analysis and design*. New York: John Wiley & Sons, 2005.

[58] W. L. Stutzman, *Antenna Theory and Design*, 2 ed. John Wiley & Sons, Inc., 2012.

[59] D. M. Pozar, *Microwave Engineering*. John Wiley & Sons, 2012.

[60] T. H. Lee, *The Design of CMOS Radio-Frequency Integrated Circuits*, 2 ed. Cambridge: Cambridge University Press, 2009.

[61] *Rohde & Schwarz ZVRE vector network analyzer, (Accessed on 26 April 2021)*. Available: https://www.rohde-schwarz.com/home_48230.html

[62] *Anritsu MS2038C vector network analyzer, (Accessed on 10 June 2021)*. Available: https://www.anritsu.com/en-us/test-measurement/products/ms2038c

[63] *ETS-LINDGREN: AMS-8050 Antenna Measurement System, (Accessed on 17 March 2021)*. Available: http://www.ets-lindgren.com/

[64] M. Lauridsen, B. Vejlgaard, I. Z. Kovacs, H. Nguyen, and P. Mogensen, "Interference Measurements in the European 868 MHz ISM Band with Focus on LoRa and SigFox," in *2017 IEEE Wireless Communications and Networking Conference (WCNC)*, 2017, pp. 1-6.

[65] V. F. Fusco, *Foundations of Antenna Theory and Techniques*. Pearson, 2005.

[66] K. Fujimoto and H. Morishita, *Modern small antennas*. New York: Cambridge University Press, 2013.

[67] H. A. Wheeler, "Fundamental Limitations of Small Antennas," *Proceedings of the IRE,* vol. 35, no. 12, pp. 1479-1484, 1947.

[68] G. C. Duree Jr, *Optics for dummies*. John Wiley & Sons, 2011.

[69] W. A. Davis, T. Yang, E. D. Caswell, and W. L. Stutzman, "Fundamental limits on antenna size: a new limit," *IET Microwaves, Antennas & Propagation*, vol. 5, no. 11, pp. 1297-1302

[70] H. Wheeler, "Small antennas," *IEEE Transactions on Antennas and Propagation,* vol. 23, no. 4, pp. 462-469, 1975.

[71] J. S. McLean, "A re-examination of the fundamental limits on the radiation Q of electrically small antennas," *IEEE Transactions on Antennas and Propagation,* vol. 44, no. 5, p. 672, 1996.

[72] J. D. Kraus, *Antennas For All Applications*, 3 ed. Tata McGraw-Hill, 2002.

[73] A. K. Skrivervik, J. Zurcher, O. Staub, and J. R. Mosig, "PCS antenna design: the challenge of miniaturization," *IEEE Antennas and Propagation Magazine,* vol. 43, no. 4, pp. 12-27, 2001.

[74] Y. Huang, "Radiation Efficiency Measurements of Small Antennas," in *Handbook of Antenna Technologies*, Z. N. Chen, D. Liu, H. Nakano, X. Qing, and T. Zwick, Eds. Singapore: Springer Singapore, 2016, pp. 2165-2189.

[75] *Texas Instruments: Link Budget, ISM-Band and Short Range Device Antennas, (Accessed on 12 November 2021)*. Available: https://www.ti.com/lit/an/swra046a/swra046a.pdf

[76] *Microchip Sub-GHz AT86RF212B radio transceiver, (Accessed on 28 October 2021)* Available: https://www.microchip.com/wwwproducts/en/AT86RF212B

[77] E. Kopp, "Link budgets -- a comparison of satellite and terrestrial cellular and wireless budgets," in *30th AIAA International Communications Satellite System Conference (ICSSC)*.

[78] "IEEE Recommended Practice for Measurements and Computations of Radio Frequency Electromagnetic Fields With Respect to Human Exposure to Such Fields,100 kHz-300 GHz," *IEEE Std C95.3-2002 (Revision of IEEE Std C95.3-1991),* pp. i-126, 2002.

[79] "IEEE Standard for Safety Levels with Respect to Human Exposure to Radio Frequency Electromagnetic Fields, 3 kHz to 300 GHz," *IEEE Std C95.1, 1999 Edition,* pp. 1-83, 1999.

[80] "Icnirp guidelines for limiting exposure to electromagnetic fields (100 KHz to 300 GHz," *Health Phys.,* vol. 118(5), pp. 483–524, 2020.

[81] *Speag: DASY SAR measurement Systems, (Accessed on 02 November 2021)*. Available: https://speag.swiss/products/dasy8/overview/

[82] Y. Qishan, O. P. Gandhi, M. Aronsson, and W. Ding, "An automated SAR measurement system for compliance testing of personal wireless devices," *IEEE Transactions on Electromagnetic Compatibility,* vol. 41, no. 3, pp. 234-245, 1999.

[83] J. C. Wang, E. G. Lim, M. Leach, Z. Wang, and K. L. Man, "Review of SAR Measurement Methods in Relation to Wearable Devices," *Engineering Letters,* Article vol. 24, no. 3, pp. 11-17, 2016.

[84] P. S. Hall, E. Lee, and C. T. P. Song, "Planar Inverted-F Antennas," in *Printed Antennas for Wireless Communications*, 2007, pp. 195-227.

[85] H. T. Chattha, Y. Huang, and Y. Lu, "PIFA Bandwidth Enhancement by Changing the Widths of Feed and Shorting Plates," *IEEE Antennas and Wireless Propagation Letters,* vol. 8, pp. 637-640, 2009.

[86] J. Baker-Jarvis, M. D. Janezic, P. D. Domich, and R. G. Geyer, "Analysis of an open-ended coaxial probe with lift-off for nondestructive testing," *IEEE Transactions on Instrumentation and Measurement,* vol. 43, no. 5, pp. 711-718, 1994.

[87] *Speag Dielectric Assessment Kit: DAK3.5-TL, (Accessed on 14 April 2021)* Available: https://speag.swiss/products/dak/overview/

[88] *Research and markets: Smart Wearable Market - Growth, Trends, COVID-19 Impact, and Forecasts (2021 - 2026), (Accessed on 4 June 2021)*. Available: https://www.researchandmarkets.com/reports/4769754/smart-wearable-market-growth-trends-covid-19

[89] *Apple Watch Series 6, (Accessed on 28 March 2021)*. Available: https://www.apple.com/in/apple-watch-series-6/

[90] *Huawei watch GT 2 Pro, (Accessed on 18 February 2021)*. Available: https://consumer.huawei.com/ie/wearables/watch-gt2-pro/

[91] *Garmin vivoactive 4, (Accessed on 18 February 2021)*. Available: https://buy.garmin.com/en-IE/GB/p/643382

[92] *Fitbit sense, (Accessed on 18 February 2021)*. Available: https://www.fitbit.com/global/ie/products/smartwatches/sense

[93] *Samsung galaxy watch active, (Accessed on 28 March 2021)*. Available: https://www.samsung.com/in/microsite/galaxy-watch-active/

[94] *Fossil Gen 5, (Accessed on 28 March 2021)*. Available: https://www.fossil.com/en-us/smartwatches/learn-more/gen-5/

[95] S. Aras, T. Johnson, K. Cabulong, and C. Gniady, "GreenMonitor: Extending battery life for continuous heart rate monitoring in smartwatches," in *2015 17th International Conference on E-health Networking, Application & Services (HealthCom)*, 2015, pp. 317-322.

[96] R. M. Al-Eidan, H. Al-Khalifa, and A. M. Al-Salman, "A Review of Wrist-Worn Wearable: Sensors, Models, and Challenges," *Journal of Sensors,* vol. 2018, p. 5853917, 2018/12/19 2018.

[97] R. Iqbal and A. Ahmad, "Wrist Band based on custom made antenna for passive NFC tag," in *European Wireless 2014; 20th European Wireless Conference*, 2014, pp. 1-6.

[98] A. J. Khalilabadi and A. Zadehgol, "An Ultra-thin Dual-Band Smart-watch Antenna Compatible with Several Wireless Bands," in *2018 IEEE International Symposium on Antennas and Propagation & USNC/URSI National Radio Science Meeting*, 2018, pp. 457-458.

[99] S. Y. Jun, A. Elibiary, B. Sanz-Izquierdo, L. Winchester, D. Bird, and A. McCleland, "3-D Printing of Conformal Antennas for Diversity Wrist Worn Applications," *IEEE Transactions on Components, Packaging and Manufacturing Technology,* vol. 8, no. 12, pp. 2227-2235, 2018.

[100] Y. Jin and J. Choi, "Bandwidth enhanced compact dual-band smart watch antenna for WLAN 2.4/5.2 GHz application," in *2017 International Applied Computational Electromagnetics Society Symposium (ACES)*, 2017, pp. 1-2.

[101] S. Woo, J. Baek, H. Park, D. Kim, and J. Choi, "Design of a compact UWB diversity antenna for WBAN wrist-watch applications," in *2013 Proceedings of the International Symposium on Antennas & Propagation*, 2013, vol. 02, pp. 1304-1306.

[102] B. Sanz-Izquierdo and J. Sungyun, "WLAN antenna on 3D printed bracelet and wrist phantom," in *2014 Loughborough Antennas and Propagation Conference (LAPC)*, 2014, pp. 372-375.

[103] S. Su and Y. Hsieh, "Integrated Metal-Frame Antenna for Smartwatch Wearable Device," *IEEE Transactions on Antennas and Propagation,* vol. 63, no. 7, pp. 3301-3305, 2015.

[104] Y. Yang and H. Chen, "Open slot antenna for smartwatch application," in *2016 IEEE 5th Asia-Pacific Conference on Antennas and Propagation (APCAP)*, 2016, pp. 41-42.

[105] C.-H. Wu, K.-L. Wong, Y.-C. Lin, and S.-W. Su, "Internal shorted monopole antenna for the watch-type wireless communication device for Bluetooth operation," *Microwave and Optical Technology Letters,* vol. 49, no. 4, pp. 942-946, 2007.

[106] H. Hamouda, P. L. Thuc, R. Staraj, and G. Kossiavas, "A two curved PIFA system for MIMO application," in *2013 7th European Conference on Antennas and Propagation (EuCAP)*, 2013, pp. 1200-1203.

[107] M.-A. Chung and C.-F. Yang, "Built-in antenna design for 2.4 GHz ISM band and GPS operations in a wrist-worn wireless communication device," *IET Microwaves, Antennas & Propagation,* vol. 10, no. 12, pp. 1285-1291, 2016.

[108] L. Quan and S. Zhongxiang, "Inverted microstrip-fed cavity-backed slot antennas," *IEEE Antennas and Wireless Propagation Letters,* vol. 1, pp. 98-101, 2002.

[109] "Evaluating compliance with fcc guidelines for human exposure to radio frequency electromagnetic fields, supplement c (edition 01-01) to oet bulletin 65 (edition 97-01)," *Federal Communications Commission Washington, D.C. 20554, USA,* 2001.

[110] G. A. Casula, A. Michel, P. Nepa, G. Montisci, and G. Mazzarella, "Robustness of Wearable UHF-Band PIFAs to Human-Body Proximity," *IEEE Transactions on Antennas and Propagation,* vol. 64, no. 5, pp. 2050-2055, 2016.

[111] V. K. Palukuru, A. Pekonen, V. Pynttäri, R. Mäkinen, J. Hagberg, and H. Jantunen, "An inkjet-printed inverted-F antenna for 2.4-GHz wrist applications," *Microwave and Optical Technology Letters,* vol. 51, no. 12, pp. 2936-2938, 2009.

[112] Y. Chen and T. Ku, "A Low-Profile Wearable Antenna Using a Miniature High Impedance Surface for Smartwatch Applications," *IEEE Antennas and Wireless Propagation Letters,* vol. 15, pp. 1144-1147, 2016.

[113] W. Dingliang, H. Yang, W. Hanyang, and Z. Hai, "A wearable antenna design using a high impedance surface for all-metal smartwatch applications," in *2017 International Workshop on Antenna Technology: Small Antennas, Innovative Structures, and Applications (iWAT)*, 2017, pp. 274-276.

[114] H. M. Anderson, "Wrist Watch Weather Radio, (Patent no. 4480253)," *United States Patent,* 1984.

[115] J. H. Lee, S. H. Lee, D. Kim, and C. W. Jung, "Transparent dual-band monopole antenna using a μ-metal mesh on the rear glass of an automobile for frequency modulation/digital media broadcasting service receiving," *Microwave and Optical Technology Letters,* vol. 61, no. 2, pp. 503-508, 2019.

[116] B. Xu, Y. Li, and Y. Kim, "Classification of Finger Movements Based on Reflection Coefficient Variations of a Body-Worn Electrically Small Antenna," *IEEE Antennas and Wireless Propagation Letters,* vol. 16, pp. 1812-1815, 2017.

[117] L. Catarinucci, F. P. Chietera, and R. Colella, "Permittivity-Customizable Ceramic-Doped Silicone Substrates Shaped With 3-D-Printed Molds to Design Flexible and Conformal Antennas," *IEEE Transactions on Antennas and Propagation,* vol. 68, no. 6, pp. 4967-4972, 2020.

[118] S. López-Soriano and J. Parrón, "Wearable RFID tag antenna for healthcare applications," in *2015 IEEE-APS Topical Conference on Antennas and Propagation in Wireless Communications (APWC)*, 2015, pp. 287-290.

[119] W. Ng, Y. Lee, E. Lim, and B. Chung, "Design of a Compact PIFA Tag Antenna for Wearable Electronics," in *2018 IEEE 38th International Electronics Manufacturing Technology Conference (IEMT)*, 2018, pp. 1-4.

[120] *LoRa Alliance: RP002-1.0.2 LoRaWAN® Regional Parameters, (Accessed on 15 Novemver 2021)*. Available: https://lora-alliance.org/resource_hub/rp2-102-lorawan-regional-parameters/

[121] P. Pongpaibool, "A study on performance of UHF RFID tags in a package for animal traceability application," in *2008 5th International Conference on Electrical Engineering/Electronics, Computer, Telecommunications and Information Technology*, 2008, vol. 2, pp. 741-744.

[122] C. Song, Y. Huang, J. Zhou, P. Carter, S. Yuan, Q. Xu, and Z. Fei, "Matching Network Elimination in Broadband Rectennas for High-Efficiency Wireless Power Transfer and Energy Harvesting," *IEEE Transactions on Industrial Electronics,* vol. 64, no. 5, pp. 3950-3961, 2017.

[123] G. R. Hoch, P. Nayeri, and A. Elsherbeni, "Bandwidth enhancement of dipole antennas using parasitic elements," in *2015 31st International Review of Progress in Applied Computational Electromagnetics (ACES)*, 2015, pp. 1-2.

[124] C. Laohapensaeng, C. Free, and K. M. Lum, "Printed strip monopole antenna with the parasitic elements on the circular ground plane," in *IWAT 2005. IEEE International Workshop on Antenna Technology: Small Antennas and Novel Metamaterials, 2005.*, 2005, pp. 371-374.

[125] H. T. Chattha, Y. Huang, Y. Lu, and X. Zhu, "Further bandwidth enhancement of PIFA by adding a parasitic element," in *2009 Loughborough Antennas & Propagation Conference*, 2009, pp. 213-216.

[126] B. Reeder and A. David, "Health at hand: A systematic review of smart watch uses for health and wellness," *Journal of Biomedical Informatics,* vol. 63, pp. 269-276, 2016/10/01/ 2016.

[127] E. Jovanov, "Preliminary analysis of the use of smartwatches for longitudinal health monitoring," in *2015 37th Annual International Conference of the IEEE Engineering in Medicine and Biology Society (EMBC)*, 2015, pp. 865-868.

[128] J. S. Seybold, "Communication Systems and the Link Budget," in *Introduction to RF Propagation*: John Wiley & Sons, 2005, pp. 66-86.

[129] *ABS Plastic Enclosure, (Accessed on 15 July 2021)*. Available: http://www.hammondmfg.com/pdf/1551F.pdf

[130] A. H. a. T. Kiikka. *Premix: Optimizing RF Properties of Injection Molded Plastic Parts, (Accessed on 16 March 2021)*. Available: https://www.premixgroup.com/

[131] *Indexsar IXB-060 phantom column, (Accessed on 16 March 2021)*. Available: https://indexsar.com/product/phantom-columns-ixb-063-and-ixb-103/

[132] J. F. D. a. P. C. Servais. *Silicone rubber as cable insulation, Wire and Cable Symposium, U. S Army Signal Corps, 1967, (Accessed on 16 March 2021)*.

[133] H. T. Chattha, Y. Huang, M. K. Ishfaq, and S. J. Boyes, "Bandwidth enhancement techniques for planar inverted-F antenna," *IET Microwaves, Antennas & Propagation*, vol. 5, no. 15, pp. 1872-1879Available: https://digital-library.theiet.org/content/journals/10.1049/iet-map.2010.0505

[134] P. Lindberg, L. Morton, A. Kaikkonen, S. Cheng, and P. Hallbjorner, "Technique of Ground Size Tuning for Isolation Between Monopoles in Compact Wireless Terminals," *IEEE Transactions on Antennas and Propagation,* vol. 60, no. 11, pp. 5488-5491, 2012.

[135] S. M. A. Nezhad and H. R. Hassani, "A Novel Triband E-Shaped Printed Monopole Antenna for MIMO Application," *IEEE Antennas and Wireless Propagation Letters,* vol. 9, pp. 576-579, 2010.

[136] Y. Wang, M. Lee, and S. Chung, "Two PIFA-Related Miniaturized Dual-Band Antennas," *IEEE Transactions on Antennas and Propagation,* vol. 55, no. 3, pp. 805-811, 2007.

[137] *Ansys HFSS, (Accessed on 26 April 2021)*. Available: https://www.ansys.com/products/electronics/ansys-hfss

[138] K. Girish and K. P. Ray, *Broadband Microstrip Antennas*. Artech, 2002, p. 1.

[139] K. P. Ray, P. V. Anob, R. Kapur, and G. Kumar, "Broadband planar rectangular monopole antennas," *Microwave and Optical Technology Letters,* vol. 28, no. 1, pp. 55-59, 2001.

[140] T. Kim, U. Kim, and J. Choi, "Design of a compact UHF RFID tag antenna using an inductively coupled parasitic element," *Microwave and Optical Technology Letters,* vol. 53, no. 2, pp. 239-242, 2011.

[141] S. W. Lee, H. S. Jung, and Y. J. Sung, "A Reconfigurable Antenna for LTE/WWAN Mobile Handset Applications," *IEEE Antennas and Wireless Propagation Letters,* vol. 14, pp. 48-51, 2015.

[142] M.-G. Huang, Z.-M. Xie, and X.-Z. Lai, "A compact multiband PIFA for handheld RFID applications," *Microwave and Optical Technology Letters,* vol. 58, no. 8, pp. 1934-1937, 2016.

[143] *Bridgeport GX 480 System, (Accessed on 17 March 2021)*. Available: https://www.hardinge.com/ProductCatalog/Product/ProductId/173

[144] *OKW Enclosures, (Accessed on 26 April 2021)*. Available: https://www.okw.co.uk/en/Body-Case/B1606117.htm?ref=12684740-c3bc-11e5-8215-bc764e08a0ea

[145] *Speag phantom arm: SHO-GFPC-V1, (Accessed on 14 April 2021)* Available: https://speag.swiss/products/em-phantoms/overview-2/

[146] Y. Li, Z. Zhang, W. Chen, Z. Feng, and M. F. Iskander, "A Quadband Antenna With Reconfigurable Feedings," *IEEE Antennas and Wireless Propagation Letters,* vol. 8, pp. 1069-1071, 2009.

[147] S. Jeon and H. Kim, "Critical coupling of the inverted-F antenna by increasing effective inductance," *Microwave and Optical Technology Letters,* vol. 53, no. 4, pp. 737-740, 2011.

[148] *Cadence: AWR Microwave Office, (Accessed on 20 April 2021)*. Available: https://www.awr.com/

[149] K. Wong, C. Chang, and Y. Lin, "Printed PIFA EM Compatible With Nearby Conducting Elements," *IEEE Transactions on Antennas and Propagation,* vol. 55, no. 10, pp. 2919-2922, 2007.

[150] G. Augustin, Q. Rao, and T. A. Denidni, "Low-Profile Antennas," in *Handbook of Antenna Technologies*, Z. N. Chen, D. Liu, H. Nakano, X. Qing, and T. Zwick, Eds. Singapore: Springer Singapore, 2016, pp. 1557-1559.

[151] V. Antonchik and R. G. Vaughan, "Spatial Aspects of the Transmission Line Model for Rectangular PIFA," in *2007 Canadian Conference on Electrical and Computer Engineering*, 2007, pp. 808-811.

[152] G. H. Huff and J. J. McDonald, "A Spherical Inverted-F Antenna (SIFA)," *IEEE Antennas and Wireless Propagation Letters,* vol. 8, pp. 649-652, 2009.

[153] *LPKF: Laser Direct Structuring, (Accessed on 26 April 2021)*. Available: https://www.lpkf.com/en/industries-technologies/electronics-manufacturing/3d-mids-with-laser-direct-structuring-lds

[154] *LPKF Protolaser 3D System, Tyndall Microsystems Packaging Laboratory, (Accessed on 26 April 2021)* Available: https://www.tyndall.ie/micro-electronics-micro-systems-packaging

[155] S. Brinkhues, A. Kanthamneni, A. Brose, S. Majcherek, and B. Schmidt, "Investigation of adhesion strength of metallization on thermoplastic and ceramic substrates," in *2016 12th International Congress Molded Interconnect Devices (MID)*, 2016, pp. 1-6: IEEE.

[156] "Mercy University Hospital, Cork, Ireland , Available online:," *http://www.muh.ie/,* no. Accessed in March 2020.

[157] Y. Zhang, S. Song, R. Vullings, D. Biswas, N. Simões-Capela, N. van Helleputte, C. van Hoof, and W. Groenendaal, "Motion Artifact Reduction for Wrist-Worn Photoplethysmograph Sensors Based on Different Wavelengths," *Sensors,* vol. 19, no. 3, p. 673, 2019.

[158] X. Yu, A. El-Gouhary, and N. M. Neihart, "A Transformer-Based Dual-Coupled Triple-Mode CMOS LC-VCO," *IEEE Transactions on Microwave Theory and Techniques,* vol. 62, no. 9, pp. 2059-2070, 2014.

[159] J. L. Buckley, K. G. McCarthy, D. Gaetano, L. Loizou, B. O'Flynn, and C. O'Mathuna, "Design of a compact, fully-autonomous 433 MHz tunable antenna for wearable wireless sensor applications," *IET Microwaves, Antennas & Propagation,* vol. 11, no. 4, pp. 548-556, 2017.

[160] R. Garg, P. Bhartia, I. J. Bahl, and A. Ittipiboon, *Microstrip antenna design handbook*. Artech house, 2001.

[161] H. T. Chattha, Y. Huang, X. Zhu, and Y. Lu, "An Empirical Equation for Predicting the Resonant Frequency of Planar Inverted-F Antennas," *IEEE Antennas and Wireless Propagation Letters,* vol. 8, pp. 856-860, 2009.

[162] J. J. Adams and J. T. Bernhard, "Broadband Equivalent Circuit Models for Antenna Impedances and Fields Using Characteristic Modes," *IEEE Transactions on Antennas and Propagation,* vol. 61, no. 8, pp. 3985-3994, 2013.

[163] K. Mekki, E. Bajic, F. Chaxel, and F. Meyer, "A comparative study of LPWAN technologies for large-scale IoT deployment," *ICT Express,* vol. 5, no. 1, pp. 1-7, 2019/03/01/ 2019.

[164] M. W. Young, S. Yong, and J. T. Bernhard, "A Miniaturized Frequency Reconfigurable Antenna With Single Bias, Dual Varactor Tuning," *IEEE Transactions on Antennas and Propagation,* vol. 63, no. 3, pp. 946-951, 2015.

[165] L. Tan, R. Wu, and Y. Poo, "Magnetically Reconfigurable SIW Antenna with Tunable Frequencies and Polarizations," *IEEE Transactions on Antennas and Propagation,* vol. 63, no. 6, pp. 2772-2776, 2015.

[166] S. Genovesi, A. Monorchio, and S. Saponara, "Compact Triple-Frequency Antenna for Sub-GHz Wireless Communications," *IEEE Antennas and Wireless Propagation Letters,* vol. 11, pp. 14-17, 2012.